



HAL
open science

Soil moisture estimation at high spatio-temporal resolution : a new approach based on the synergy of active-passive microwave observations and optical-thermal

Nitu Kumari Ojha

► **To cite this version:**

Nitu Kumari Ojha. Soil moisture estimation at high spatio-temporal resolution : a new approach based on the synergy of active-passive microwave observations and optical-thermal. Hydrology. Université Paul Sabatier - Toulouse III, 2021. English. NNT : 2021TOU30183 . tel-03651573

HAL Id: tel-03651573

<https://theses.hal.science/tel-03651573v1>

Submitted on 25 Apr 2022

HAL is a multi-disciplinary open access archive for the deposit and dissemination of scientific research documents, whether they are published or not. The documents may come from teaching and research institutions in France or abroad, or from public or private research centers.

L'archive ouverte pluridisciplinaire **HAL**, est destinée au dépôt et à la diffusion de documents scientifiques de niveau recherche, publiés ou non, émanant des établissements d'enseignement et de recherche français ou étrangers, des laboratoires publics ou privés.

THÈSE

En vue de l'obtention du
DOCTORAT DE L'UNIVERSITÉ DE TOULOUSE

Délivré par : *l'Université Toulouse 3 Paul Sabatier (UT3 Paul Sabatier)*

Présentée et soutenue le *15/11/2021* par :

Nitu Kumari OJHA

**Estimation de l'humidité du sol à haute résolution spatio-temporelle : une nouvelle
approche basée sur la synergie des observations micro-ondes actives/passives et
optiques/thermiques**

JURY

PIERRE-LOUIS FRISON	Maître de conférences	Rapporteur
MERCEDES MAGDALENA VALL-LLOSSERA	Professeur associé	Rapporteur
FERRAN MARIA-JOSÉ	Ingénieur de Recherche	Invité
ESCORIHUELA JEAN-LOUIS ROUJEAN	Directeur de recherche	Examineur
MEHREZ ZRIBI	Directeur de recherche	Examineur
NICOLAS BAGHDADI	Directeur de recherche	Examineur
OLIVIER MERLIN	Chargé de Recherche	Directeur de Thèse

École doctorale et spécialité :

SDU2E : Surfaces et Interfaces Continentales, Hydrologie

Unité de Recherche :

Centre d'Études Spatiales de la Biosphère (UMR 5126)

Directeur de Thèse :

Olivier MERLIN

Rapporteurs :

Pierre-Louis FRISON et Mercedes Magdalena VALL-LLOSSERA FERRAN

“The important thing is not to stop questioning. Curiosity has its own reason for existence. One cannot help but be in awe when he contemplates the mysteries of eternity, of life, of the marvelous structure of reality. It is enough if one tries merely to comprehend a little of this mystery each day.”

Albert Einstein

Acknowledgement

First, I would like to express my special gratitude towards my supervisor Olivier MERLIN for giving me an opportunity to work with him as a research engineer and then as a Doctoral candidate under his guidance. I would also like to thank him for his trust in me and his endless patience in elaborating minute details and answering my countless questions. His dedication, inspiration, and positive attitude towards research has given me positive vibes, confidence and motivated me to stay committed to the research problem. He is very supportive, kind, and helpful in all situations, and I thank him for understanding the situation and encouraging me during the uncertain COVID period. I learned a lot from him and I appreciate his hard work and the time he spent to provide proper research guidance.

I want to thank Maria Jose Escorihuela for her guidance and my numerous discussions helped me build a concrete groundwork for my thesis. I also like to thank her for giving me an excellent environment in isardSAT,Barcelona to work and share knowledge with other people. I also like to thank all the colleagues in isardSAT for being very welcoming, friendly and helpful.

In addition, I am thankful to the thesis committee (special thanks to Nemesio Jose Rodriguez-Fernandez and Christophe Suère) and jury members for their time and support in being a part of my thesis. Let me also thank all the staff in the administrative department - Emilie Bastie, Dominique Tarrisse, Laurence Keppel, Laura Leal, for all the support and help throughout my Doctoral studies.

I would like to acknowledge Ali MEHMOODI, whose guidance has motivated and inspired me to work harder. His wise words and positive attitude has been a guiding light for me at the time of uncertainty. I thank him for being nice to me while sharing the office and giving a good environment to work.

I would also like to express my special gratitude towards Yann KERR for giving me an opportunity to be a part of SMOS team and also to all the SMOS team members for their welcoming nature.

I wish to commend all the staff/researchers in CESBIO for their welcoming nature and giving me an excellent environment to work in. Special thanks to people for sharing morning coffee while drafting my thesis. I would like to thank my friends from CESBIO and Morocco (special thanks to El houssaine Bouras for the help) for the nice time we spent together.

Last but not the least, I thank my wonderful family - mother, father, Pretty, Pooja, Alankrita, and Shivanth, for being a part of this and their endless support and love, and motivating me to do better and building my confidence.

Abstract

SMOS and SMAP passive microwave sensors provide soil moisture (SM) data at 40 km resolution every 2-3 days globally, with a 0-5 cm sensing depth relevant for climatic and meteorological applications. However, SM data would be required at a higher (typically 100 m or finer) spatial resolution for many other regional (hydrology) or local (agriculture) applications. Optical/thermal and radar sensors can be used for retrieving SM proxies at such high spatial resolution, but both techniques have limitations. In particular, optical/thermal data are not available under clouds and underplant canopies. Moreover, radar data are sensitive to soil roughness and vegetation structure, which are challenging to characterize from outer space, and have a repeat cycle of at least six days, limiting the observations' temporal frequency.

In this context, the leading principle of the thesis is to propose a new approach that combines passive microwave, optical/thermal, and active microwave (radar) sensors for the first time to retrieve SM data at 100 m resolution on a daily temporal scale. Our assumption is first to rely on an existing disaggregation method (DISPATCH) of SMOS/SMAP SM data to meet the target resolution achieved by radars. DISPATCH is originally based on the soil evaporative efficiency (SEE) retrieved over partially vegetated pixels from 1 km resolution optical/thermal (typically MODIS) surface temperature and vegetation cover data. The disaggregated SM data is then combined with a radar-based SM retrieval method to exploit the sensing capabilities of the Sentinel-1 radars. Finally, the efficacy of the assimilation of satellite-based SM data in a soil water balance model is assessed in terms of SM predictions at the 100 m resolution and daily temporal scale.

As a first step, the DISPATCH algorithm is improved from its current version by mainly 1) extending its applicability to fully vegetated optical pixels using the temperature vegetation dryness index and an enhanced vegetation cover product, and 2) increasing the targeted downscaling resolution from 1 km to 100 m using Landsat (in addition to MODIS) optical/thermal data. The 100 m resolution disaggregated SM product is validated with in situ measurements collected over irrigated areas in Morocco, showing a daily spatial correlation in the range of 0.5-0.9.

As a second step, a new algorithm is built on a synergy between DISPATCH and radar 100 m resolution data. In practice, the DISPATCH SM product available on clear sky days is first used to calibrate a radar radiative transfer model in the direct mode. Then the calibrated radar radiative transfer model is used in the inverse mode to estimate SM at the spatio-temporal resolution of Sentinel-1. Results indicate a positive correlation between satellite and in situ measurements in the range of 0.66 to 0.81 for a vegetation index lower than 0.6.

As a third and final step, an optimal assimilation method is used to interpolate 100 m resolution SM data in time. The assimilation exercise is undertaken over irrigated crop fields in Spain. The analyzed SM product derived from the assimilation of 100 m resolution DISPATCH SM is

consistent with irrigation events. This approach can be readily applied over large areas, given that all the required input (remote sensing and meteorological) data are available globally.

Keywords: Soil moisture, Disaggregation, Synergy, Assimilation

Résumé

Les capteurs micro-ondes passifs SMOS et SMAP fournissent des données d’humidité du sol (SM) à une résolution d’environ 40 km avec un intervalle de 2 à 3 jours à l’échelle mondiale et une profondeur de détection de 0 à 5 cm. Ces données sont très pertinentes pour les applications climatiques et météorologiques. Cependant, pour les applications à échelle régionale (l’hydrologie) ou locales (l’agriculture), des données de SM à une haute résolution spatiale (typiquement 100 m ou plus fine) seraient nécessaires. Les données collectées par les capteurs optiques/thermiques et les radars peuvent fournir des indicateurs de SM à haute résolution spatiale, mais ces deux approches alternatives ont des limites. En particulier, les données optiques/thermiques ne sont pas disponibles sous les nuages et sous les couverts végétaux. Quant aux données radar, elles sont sensibles à la rugosité du sol et à la structure de la végétation, qui sont tous deux difficiles à caractériser depuis l’espace. De plus, la résolution temporelle de ces données est d’environ 6 jours.

Dans ce contexte, la ligne directrice de la thèse est de proposer une nouvelle approche qui combine pour la première fois des capteurs passifs micro-ondes, optiques/thermiques et actifs micro-ondes (radar) pour estimer SM sur de grandes étendues à une résolution de 100 m chaque jour. Notre hypothèse est d’abord de nous appuyer sur une méthode de désagrégation existante (DISPATCH) des données SMOS/SMAP pour atteindre la résolution cible obtenue par les radars. À l’origine, DISPATCH est basé sur l’efficacité d’évaporation du sol (SEE) estimée sur des pixels partiellement végétalisés à partir de données optiques/thermiques (généralement MODIS) de température de surface et de couverture végétale à résolution de 1 km. Les données désagrégées de SM sont ensuite combinées avec une méthode d’inversion de SM basée sur les données radar afin d’exploiter les capacités de détection des radars Sentinel-1. Enfin, les capacités de l’assimilation des données satellitaires de SM dans un modèle de bilan hydrique du sol sont évaluées en termes de prédiction de SM à une résolution de 100 m et à une échelle temporelle quotidienne.

Dans une première étape, l’algorithme DISPATCH est amélioré par rapport à sa version actuelle, principalement 1) en étendant son applicabilité aux pixels optiques entièrement végétalisés en utilisant l’indice de sécheresse de la végétation basé sur la température et un produit de couverture végétale amélioré, et 2) en augmentant la résolution de désagrégation de 1 km à 100 m en utilisant les données optiques/thermiques de Landsat (en plus de MODIS). Le produit de SM désagrégé à la résolution de 100 m est validé avec des mesures in situ collectées sur des zones irriguées au Maroc, indiquant une corrélation spatiale quotidienne variant de 0,5 à 0,9.

Dans un deuxième étape, un nouvel algorithme est construit en développant une synergie entre les données DISPATCH et radar à 100 m de résolution. En pratique, le produit SM issu de DISPATCH les jours de ciel clair est d’abord utilisé pour calibrer un modèle de transfert radiatif radar en mode direct. Ensuite, le modèle de transfert radiatif radar ainsi calibré est utilisé en mode inverse pour estimer SM à la résolution spatio-temporelle de Sentinel-1. Sur les sites de validation, les résultats indiquent une corrélation entre les mesures satellitaires et in situ, de

l'ordre de 0,66 à 0,81 pour un indice de végétation inférieur à 0,6.

Dans une troisième et dernière étape, une méthode d'assimilation optimale est utilisée pour interpoler dans le temps les données de SM à la résolution de 100 m. La dynamique du produit SM dérivé de l'assimilation de SM DISPATCH à 100 m de résolution est cohérente avec les événements d'irrigation. Cette approche peut être facilement appliquée sur de grandes zones, en considérant que toutes les données (télédétection et météorologique) requises en entrée sont disponibles à l'échelle globale.

Mots clés : Humidité du sol, Désagrégation, Synergie, Assimilation

Contents

Acknowledgement	iii
Abstract	vii
Résumé	ix
List of Figures	xiii
List of Tables	xv
Acronyms	xvii
Symbols	xix
1 Introduction	1
1.1 Context	2
1.1.1 Global changes	2
1.1.2 Dynamics of water resources in the Mediterranean region	3
1.1.3 Spatio-temporal variability of soil moisture	4
1.2 Soil moisture monitoring	6
1.2.1 In situ soil moisture	7
1.2.2 Dynamic models	9
1.2.3 Satellite information	10
1.2.4 Downscaling methods	17
1.3 Research objectives and outline of the thesis	18
1 Introduction (français)	21
1.1 Contexte	22
1.1.1 Changements globaux	22
1.1.2 Dynamique des ressources en eau dans la région méditerranéenne	23
1.1.3 Variabilité spatio-temporelle de l'humidité du sol	24
1.2 Suivi de l'humidité du sol	27
1.2.1 Mesure in situ de l'humidité du sol	27
1.2.2 Modèles dynamiques	29
1.2.3 Informations satellitaires	31
1.2.4 Méthodes de réduction d'échelle ou désagrégation de données	38
1.3 Objectifs de recherche et plan de la thèse	40

2	Study area	43
2.1	Introduction	44
2.1.1	Tensift basin, central Morocco	44
2.1.2	Ebro basin, northeastern Spain	46
2.1.3	Duro basin, northwestern Spain	47
2.1.4	Garonne basin, southwestern France	48
2.2	Conclusion	48
3	Disaggregation of passive microwave soil moisture using optical/thermal data	49
3.1	Introduction	50
3.2	Downscaling algorithm	50
3.3	C4DIS processor	54
3.4	Adaptation of C4DIS to other sensors	55
3.5	Conclusion	55
4	Extending the applicability of the disaggregation algorithm	57
4.1	Introduction	58
4.2	A new SM index for DISPATCH algorithm mainly in vegetated areas	59
4.3	New estimates of temperature endmembers in DISPATCH algorithm	60
4.4	A new vegetation index for DISPATCH algorithm mainly in vegetated areas	61
4.5	Conclusion	65
4.6	Article : Extending the Spatio-Temporal Applicability of DISPATCH Soil Moisture Downscaling Algorithm: A Study Case Using SMAP, MODIS and Sentinel-3 Data	66
5	How to further enhance the downscaling resolution	85
5.1	Introduction	86
5.2	Implementing a new DISPATCH algorithm at 100 m resolution	87
5.3	Practical algorithm to bridge the gap between SMAP and Landsat resolution	90
5.4	Selecting an optimal intermediate spatial resolution and evaluating DISPATCH at 100 m resolution	92
5.5	Conclusion	95
5.6	Article : Stepwise disaggregation of SMAP soil moisture at 100 m resolution using Landsat-7/8 data and a varying intermediate resolution	95
6	Building a synergy of disaggregated passive microwave soil moisture approach with radar-based retrieval approach	119
6.1	Introduction	120
6.2	A new radar-DISPATCH coupling method	120
6.3	Validation	123
6.4	Conclusion	125
6.5	Article : A calibration/disaggregation coupling scheme for retrieving soil moisture at high spatio-temporal resolution: synergy between SMAP passive microwave, MODIS/Landsat optical/thermal and Sentinel-1 radar data	126
7	High-resolution soil moisture data at the daily scale using dynamic surface model	151
7.1	Introduction	152
7.2	Method	153
7.2.1	Force restore model	153
7.2.2	Assimilation techniques	153

7.3	Results	155
7.4	Conclusion	158
8	General conclusions and perspectives	161
8.1	Summary of the main findings	162
8.2	Future researches on soil moisture monitoring and their applications	164
8	Conclusions générales et perspectives (français)	167
8.1	Résumé des principales conclusions	168
8.2	Recherches futures sur le suivi de l'humidité des sols et ses applications	170
	Bibliography	175

List of Figures

1.1	Human and natural forces affecting the global temperature. Source: U.S. Global change research program	2
1.2	Schematic representation of (a) water balance model and (b) energy balance model	5
1.3	Conceptual structure of the dependence of EF on SM. Source: (Seneviratne et al., 2010)	6
1.4	List of past and current passive microwave sensors until today.	12
1.5	List of past and current active microwave sensors till today. Source: UNAVCO .	13
1.6	List of past and current optical/thermal sensors until today. Source: Houborg et al. (2015)	15
1.7	Schematic diagram of the main research objective split into four successive steps.	19
1.1	Forces humaines et naturelles affectant la température globale. Source : Programme américain de recherche sur le changement global.	23
1.2	Représentation schématique du modèle de (a) bilan hydrique et (b) énergétique.	25
1.3	Structure conceptuelle de la dépendance de l'ET à SM.. Source: (Seneviratne et al., 2010)	26
1.4	Liste des capteurs micro-ondes passifs passés et actuels jusqu'à aujourd'hui . . .	33
1.5	Liste des capteurs micro-ondes actifs (ou radars) passés et actuels jusqu'à aujourd'hui. Source : UNAVCO	36
1.6	Liste des capteurs optiques/thermiques passés et actuels jusqu'à aujourd'hui. Source: Houborg et al. (2015)	37
1.7	Schéma de l'objectif principal de recherche divisé en quatre étapes successives. .	41
2.1	Study area including 1.Garonne Basin 2. Ebro Basin 3. Duero Basin 4. Tensift Basin	45
3.1	Visual representation of LST and fvg feature space graph and a trapezoid is drawn to divide the land surface into four different surface area: mainly bare soil (zone A), mainly dry and partially vegetated (zone B), mainly wet and partially vegetated (zone C) and mainly vegetated (zone D). Source: (Merlin et al., 2016)	52
3.2	Schematic diagram of C4DIS operational processor. Source: (Molero et al., 2016)	54
4.1	Illustration of the calculation of the temperature endmembers in Land surface temperature - fractional vegetation graph for zone A, B, C and D from <i>DISPATCH_{classic}</i> (left) and <i>DISPATCH_{veg-ext}</i> (right) algorithms for MODIS data at 1 km resolution.	61
4.2	Time series of the fractional vegetation cover derived from NDVI and EVI (left) and scatter plot between fractional vegetation covers (right) for ICOS (a,b); dry-land (c,d) and Rhemedus (e,f) areas.	64

5.1	<i>DISPATCH_{veg-ext}</i> and <i>DISPATCH_{100m}</i> algorithms calculate the wet and dry edges in Land surface temperature-fractional vegetation feature space for 100 m resolution Landsat data.	88
5.2	Landsat-derived SEE as a function of in situ SM superimposed with the SEE(SM) and SEE(LST) models for both linear and non-linear SEE models derived from <i>DISPATCH_{classic}</i> and <i>DISPATCH_{100m}</i> algorithms separately.	89
5.3	Flowchart of the two-step downscaling approach from 40 km resolution to 1 km (<i>DISPATCH_{veg-ext}</i>), from 1 km to ISR (aggregation to variable ISR), and from ISR to 100 m (<i>DISPATCH_{100m}</i>)	91
5.4	The LST-fvg feature space graph is represented for an ISR pixel of 30 km, 10 km, 3 km and 1 km for Landsat LST and fvg data at 100 m resolution.	92
5.5	Correlation coefficient (R), slope of the linear regression (slope), absolute mean bias (Absolute MB) and root mean square difference (RMSD) between 100 m resolution disaggregated and in situ SM for a range of ISR values (from 1 km to 30 km) for SMAP (left) and SMOS (right) data and for each sampling date separately.	93
6.1	The schematic diagram for developing a relationship between disaggregation and calibration scheme combines SMAP/SMOS SM, MODIS/Landsat optical/thermal, and Sentinel-1 radar data at various spatial resolutions to produce an SM product at the field scale at the temporal frequency of Sentinel-1.	123
6.2	Time series of the correlation coefficient and slope of the linear regression between estimated and in situ SM for both (empirical and semi-empirical) active radiative transfer model and two vegetation descriptors (NDVI and PR) separately where in situ SM datasets are used for the calibration.	125
7.1	Scatter plot between DISPATCH and in situ SM for the 1 km (left) and 100 m (right) resolution satellite data and for Foradada (top) and Agramunt (bottom) sites.	156
7.2	Time series of in situ SM, open loop predicted SM, re-analyzed SM using 1 km DISPATCH data and re-analyzed SM using 100 m DISPATCH data for Foradada (top) and Agramunt (bottom) sites.	157
7.3	Scatter plot between re-analyzed and in situ SM for the assimilation of 1 km (left) and 100 m (right) resolution DISPATCH products and for Foradada (top) and Agramunt (bottom) sites.	158

List of Tables

4.1	Statistical results in terms of correlation, slope, mean bias, RMSD between 1 km resolution disaggregated and in situ SM for <i>DISPATCH_{veg-ext}</i> algorithm using NDVI and EVI vegetation index separately.	63
5.1	Statistical results in terms of correlation coefficient (R), slope of the linear regression, absolute mean bias (MB) and root mean square difference (RMSD) between 100 m resolution disaggregated and in situ SM using an ISR set to 10 km (single grid) and SMAP and SMOS data as input separately.	94

Acronyms

- CATDS** Centre Aval de Traitement des Données SMOS C4DIS CATDS Level-4 Disaggregation processor. 50, 53, 58
- DEM** Digital Elevation Model. 53–56
- EASE** Equal-Area Scalable Earth. 53
- EF** Evaporative Fraction. xiii, 4, 6, 59
- ESA** European Space Agency. 55
- ET** Evapotranspiration. 4, 5, 16, 59
- EVI** Enhanced Vegetation Index. xiii, xv, 58, 61–65, 162
- ISMN** International Soil Moisture Network. 48
- ISR** Intermediate Spatial Resolution. xiv, xv, 86, 90–95, 163, 164
- LST** Land surface temperature. xiv, 16, 17, 58–60, 65, 86, 87, 89, 90, 92, 95, 162, 163, 165
- MODIS** Moderate Resolution Imaging Spectroradiometer. x, xiii, xiv, 16, 50, 53–61, 65, 66, 86, 90, 95, 121, 123, 155, 162, 163
- MYD11A1** MODIS/Aqua at 1km resoluition. 53
- NASA** National Aerounatics Space Agency. 12, 53
- NDVI** Normalized Vegetation Index. xiv, xv, 50, 51, 53–56, 58, 60–63, 65, 90, 95, 121, 123–126, 162–165
- RTM** Radiative Transfer Model. 121, 122, 126
- SEE** Soil Evaporative Efficiency. xiv, 50–53, 55, 59–61, 87, 89, 90, 95, 162, 164
- SLSTR** Sea andLand surface temperature radiometer. 55
- SM** Soil Moisture. x, xiii–xv, 4–14, 16–20, 38, 44–48, 57–60, 62, 63, 65, 86, 87, 89, 90, 92, 93, 95, 120–126, 152–159, 162–166
- SMAP** Soil Moisture Active Passive. x, xiv, xv, 50, 55, 57, 58, 60, 65, 66, 85, 87, 90, 93–95, 120, 121, 123, 126, 162–164

SMOS Soil Moisture and Ocean Salinity. xiv, xv, 11, 12, 17, 19, 20, 50, 51, 53–55, 58, 60, 65, 86, 87, 90, 93–95, 120, 121, 123, 162–164

TDR Time-domain reflectometry. 7, 8, 46–48

TVDI Temperature-Vegetation Dryness Index. 17, 58–61, 65, 162, 164

USGS United States Geological Survey. 53

WCM Water Cloud Model. 121

Symbols

ρ_B	Surface reflectance in blue band
ρ_R	Surface reflectance in red bands
ρ_w	Density of the water
ρ_{NIR}	Surface reflectance in near-infrared bands
$\sigma_{pol,empirical}$	Backscattering coefficient for the empirical radiative transfer model at a given polarisation
$\sigma_{pol,semi-empirical}$	Backscattering coefficient for the semi-empirical radiative transfer model at a given polarisation
$\sigma_{pol,soil}$	Backscattering coefficient from the soil contribution
$\sigma_{pol,veg}$	Backscattering coefficient for the vegetation contribution at a given polarisation
θ_1	Surface soil moisture
θ_{eq}	Surface soil moisture at equilibrium between the gravity and the capillary force
A_{pol}, B_{pol}	Coefficient parameters depends on vegetation characteristics
$a_{WCM}, b_{WCM}, c_{WCM}, d_{WCM}$	Coefficient parameters for semi-empirical radiative transfer model
C_1	Force coefficient in force and restore model
C_2	Restore coefficient in force and restore model
$DISPATCH_{100m}$	DISPATCH algorithm at 100 m resolution
$DISPATCH_{classic}$	DISPATCH algorithm at 1 km resolution implemented at C4DIS processor
$DISPATCH_{veg-ext}$	Extension of $DISPATCH_{classic}$ algorithm to include vegetated areas at 1 km
EVI_s	EVI in bare soil
EVI_v	EVI in full cover vegetation
EVI_{HR}	EVI at high resolution
f_{vgEVI}	Fractional vegetation calculated from EVI
f_{vgHR}	Fractional vegetation at high resolution

fvg_{NDVI} Fractional vegetation calculated from NDVI
 LST_{dry} Maximum land surface temperature value at a given fractional vegetation
 LST_{HR} Land surface temperature obtained from high resolution optical/thermal data
 LST_{wet} Minimum land surface temperature value at a given fractional vegetation
 $NDVI_{HR}$ NDVI values at high resolution
 $NDVI_s$ NDVI values at bare soil
 $NDVI_v$ NDVI values at full vegetation cover
 SEE_{HR} Soil evaporative efficiency at high resolution
 SEE_{LR} Soil evaporative efficiency at low resolution
 $SM_{empirical}$ Soil moisture at empirical radiative transfer model
 SM_{HR} Soil moisture at high resolution
 SM_{LR} Soil moisture at low resolution
 SM_p Soil moisture potential
 $SM_{semi-empirical}$ Soil moisture at semi-empirical radiative transfer model
 T_{pol}^2 Two way attenuation
 $T_{s,dry}$ Fully dry soil temperature
 $T_{s,HR}$ Soil temperature at high resolution
 $T_{s,wet}$ Fully wet soil temperature
 $TVDI_{HR}$ TVDI at high resolution obtained from optical/thermal data
 X^a Current estimate
 X^b modal estimate
 B Covariance matrix of the model
 d normalisation depth
 H Observation operator
 J Optimal weight derived by minimizing cost function between observation and the model
 K Kalman gain
 L Value for canopy background adjustment
 R Covariance matrix of the observation
 y observation from remote sensing data or ground data

Chapter 1

Introduction

Contents

1.1	Context	2
1.1.1	Global changes	2
1.1.2	Dynamics of water resources in the Mediterranean region	3
1.1.3	Spatio-temporal variability of soil moisture	4
1.2	Soil moisture monitoring	6
1.2.1	In situ soil moisture	7
1.2.2	Dynamic models	9
1.2.3	Satellite information	10
1.2.4	Downscaling methods	17
1.3	Research objectives and outline of the thesis	18

1.1 Context

1.1.1 Global changes

Water covers two-thirds of the earth's surface. In this, 97% of the earth's water is contained in the ocean as saltwater, and 2% of water is stored as fresh water in ice caps, glaciers, snowy mountain ranges, and only 1% are available for daily needs. Freshwater is stored in the soil, surface water, groundwater, lakes, rivers, and streams, among other places. Freshwater is required for all ecological and societal activities, including food and energy production, transportation, waste disposal, industrial development, and human health (Baron et al., 2002). Nonetheless, freshwater supplies are unevenly and randomly distributed, and some parts of the world are highly water-stressed (Chitonge, 2020). In the 20th century, freshwater demand increased due to the increase in the human population and living standards (Hinrichsen and Tacio, 2002). It is predicted that water demand will increase by 50% in 2050 (Leflaive, 2012) with the increase in population, water scarcity, and global climate change - making water supply and demand more problematic and uncertain (Hallegatte, 2009). Climate change in recent decades has been primarily caused by human activity, with only minor interference from natural cycles. Figure 1.1 shows the estimated human and natural influences on global temperature. Human activities like greenhouse gas emissions from fossil fuel combustion, deforestation, land-use change trigger climate change.

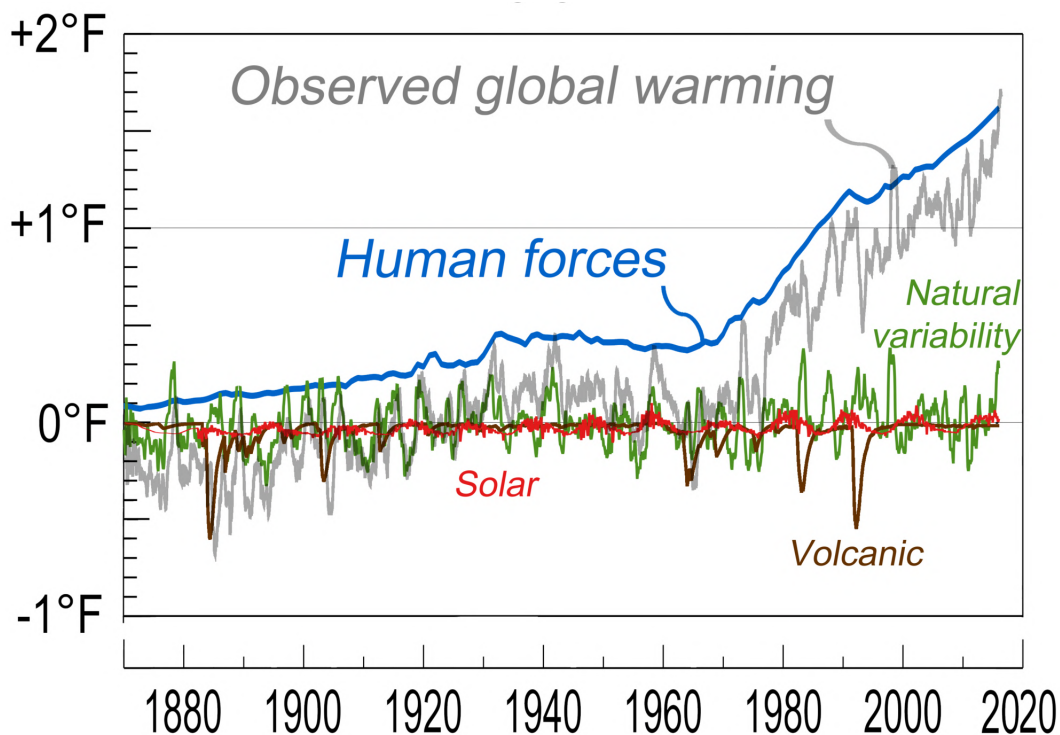


Figure 1.1: Human and natural forces affecting the global temperature. Source: U.S. Global change research program

The Mediterranean region is more prone to global climate change (Lionello and Scarascia, 2018). The Mediterranean region has shown a climate transition in the past (Tsimplis et al., 2006) and is now considered a global "hot-spot" for climate change (Giorgi, 2006), where a severe impact of climate change is predicted (Stocker et al., 2014). Climate change in the Mediterranean region

raises average annual temperatures by 1.5°C, exceeding current global warming trends (+1.1°C) (Cramer et al., 2018). Summer becomes warmer as temperatures rise, and heat waves become more frequent and severe (Kuglitsch et al., 2010; Jacob et al., 2014). In most places, particularly in the south, each degree increase in temperature reduces rainfall by 4% (Lionello and Scarascia, 2018). The increased temperature and decreased precipitation lead to severe drought conditions in the southern and eastern parts of the Mediterranean region (Lelieveld et al., 2012; Yves et al., 2020). Heatwaves and droughts influence socioeconomic activities, biodiversity, and public health (Fouillet et al., 2006). Due to climate change, the Mediterranean region is also considered a hot-spot for biodiversity change, losing at least 70% of its habitat (Myers, 1990).

Water availability in the Mediterranean region is likely to reduce by 2% to 15%, the most significant decrease globally (Schleussner et al., 2016). The decline in rainfall and changes in the precipitation regimes directly affect the water quantity that reaches the soil or surface runoff or discharge into the river. The increase in temperature and the change in other parameters such as solar radiation, wind speed, and humidity increase plants' transpiration process and the evaporation process from the soil and the water bodies. These changes affect river flows as well as the quality and quantity of the water resources and knowledge about dynamics of water resources at regional/local scale is necessary.

1.1.2 Dynamics of water resources in the Mediterranean region

It is essential to understand the distribution of water resources and the effect of climate change on water supply in the future, especially in the water-scarce regions. Understanding the impact of climate change on society is becoming more critical, particularly in water resource management. It is essential to understand the different environmental and human modifications responsible for the change in water resource management and hydrology, such as the impact of climate change on water balance, water runoff, change in land use and land cover, urbanization, and irrigation.

Water is limited in the Mediterranean region, and it mainly depends on the water runoff from the mountainous regions (Viviroli and Weingartner, 2004; de Jong et al., 2009). Mountains provide a significant portion of the overall runoff in Mediterranean areas, accounting for between 20% and 90% of total runoff (Viviroli et al., 2007). The increase in water demand also creates pressure on the mountainous region. Long-term climatic conditions are becoming more apparent and impacting the ecosystem of the Mediterranean mountains (Giorgi and Lionello, 2008), and hence the stability of the water supply is not maintained.

Land use and land cover (LULC) changes are the main characteristics of the Mediterranean landscape and environmental alteration. Land use affects the hydrological process through interception, evapotranspiration, infiltration, and runoff (Cosandey et al., 2005; Foley et al., 2005). Land cover changes have significantly affected hydrological response at the basin scale (Andréassian, 2004). Land-use change has been rapid during recent decades due to the rapid extension of urbanization and irrigation. The development of new irrigation and crops in Mediterranean lowland areas requires more water for consumption. The newly irrigated areas cover almost 10 million ha and consume a large volume of water. These areas are far from the river valleys, so water transport in these areas puts pressure on the complex infrastructure (reservoir and canals) and over-exploits groundwater.

The proper water resources management can fulfill the increase in demand of water supply at the regional scale. The water management strategies will benefit from continuous monitoring the

surface water status as a result of climate and LULC dynamics and change. Strong knowledge in different fields such as climate change, river regimes, hydrology, etc., helps develop a framework for water resource management.

1.1.3 Spatio-temporal variability of soil moisture

In this section, we define soil moisture, how it is linked with the water and energy budget of the surface, and how its measurement at various spatial and temporal scales will be helpful in water resource management and other applications. Soil moisture (SM) is the water content available in the unsaturated zone. SM is a key variable as it controls water and energy exchange from the land surface to the atmosphere and links the water and energy balance models (Figure 1.2 shows the water and energy balance models).

The water balance model is expressed as:

$$\frac{dW}{dt} = P - ET - R \quad (1.1)$$

where $\frac{dW}{dt}$ is the change in water content in a given soil layer, P is precipitation, ET is evapotranspiration, and R is surface runoff. Water is exchanged from the surface to the atmosphere via ET, and rainfall is partitioned into infiltration, and runoff in the water balance model. Both ET and runoff, as well as infiltration, are affected by the SM content.

The energy balance model is expressed as:

$$\frac{dQ}{dt} = R_{net} - H - \lambda * LE - G \quad (1.2)$$

where $\frac{dQ}{dt}$ is energy change in a given soil layer, H is sensible heat flux, $\lambda * LE$ is ET, G is surface heat flux, and R_{net} is net radiation. The land surface available energy is partitioned into sensible heat flux and latent heat flux. This partitioning is dependent on the SM in a transitional zone (Seneviratne et al., 2010).

It can be seen from equations 1.1 and 1.2 that both the energy and water balance model is coupled through ET.

ET is the result of a combination of evaporation and transpiration. Evaporation occurs when water evaporates from soil surfaces, while transpiration occurs when water evaporates from vegetation leaves. ET is an essential variable that controls the energy and mass exchange between the surface and the atmosphere. ET plays a vital role in flood (Bouilloud et al., 2010), rainfall forecast (Findell et al., 2011), drought forecast (Gao et al., 2011), and agriculture (Allen et al., 2005). As a result, knowledge of daily measurements of ET is essential.

A conceptual/theoretical framework is used to define the ET system as a function of SM (shown in Figure 1.3). SM limited condition and energy limited condition are the two ET systems characterized by the evaporative fraction (EF, which is the ratio of ET to the energy available at the surface) (Koster et al., 2004; Seneviratne et al., 2010). In SM limited conditions, SM values are below the critical SM value, and SM mainly controls ET. In energy-limited conditions, SM is above critical SM value, and ET is independent of SM and primarily influenced by the atmospheric demand. The critical SM ($SM_{critical}$) is defined as the SM between the SM at field capacity (SM_{fc} , above which water is not held against gravitational drainage) and SM at wilting point ($SM_{wilting}$ above which the water is retained too firmly by the soil matrix that it is not

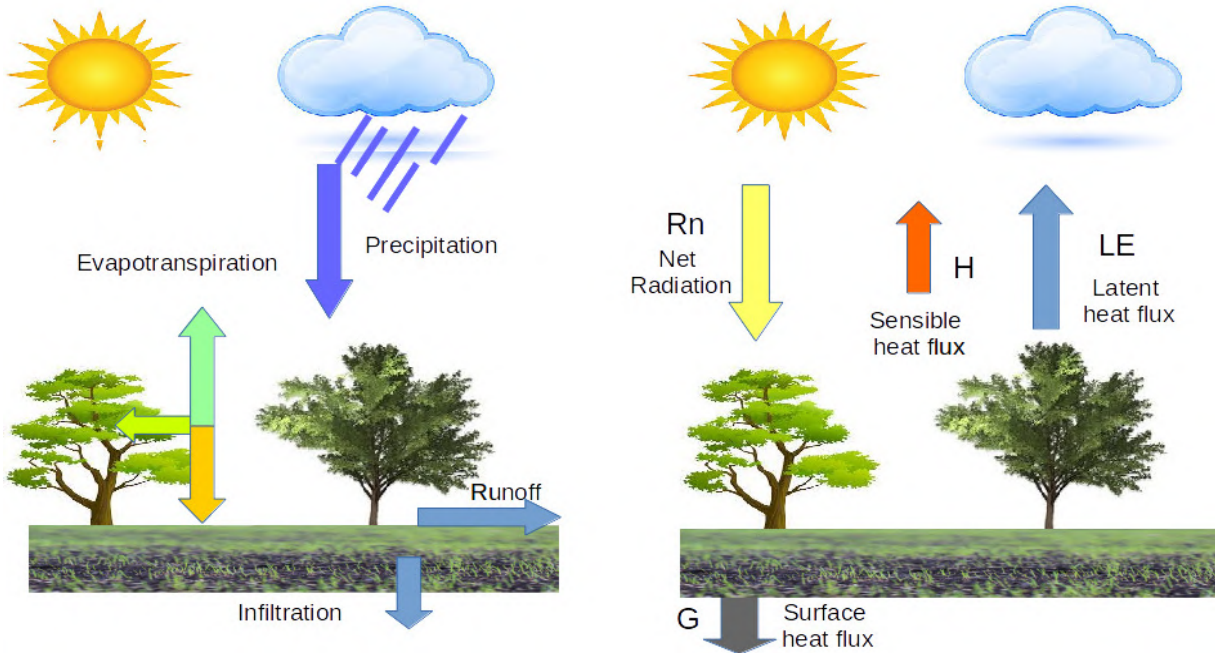


Figure 1.2: Schematic representation of (a) water balance model and (b) energy balance model

accessible to plants). The conceptual framework describes three SM modes based on the impact of SM on ET variability: wet ($SM > SM_{critical}$), dry ($SM < SM_{wilting}$), and transitional zone ($SM_{wilting} < SM < SM_{critical}$).

For instance, in first-generation land surface models, ET was estimated as a function of the SM simulated by the bucket model.

The importance of SM in ecohydrological and land surface processes is recognized by various researchers (Robinson et al., 2008; Seneviratne et al., 2010; Jung et al., 2010; Evaristo et al., 2015). SM varies greatly over vast spatio-temporal scales, with spatial scales ranging from a few centimeters to thousands of kilometers and time scale ranging from minutes to years. Many studies have investigated the spatial variability of SM at different ranges of scale such as field scale (Nielsen et al., 1973; Bell et al., 1980), catchment scale (Nielsen et al., 1973; Western et al., 2004), regional scale (Romshoo, 2004; Zhao et al., 2013) and continental scale (Entin et al., 2000; Li and Rodell, 2013). Western et al. (2002) examined several scaling strategies to relate the spatial variability of SM across spatial scales. Vanderlinden et al. (2012) analyzed the temporal variability of SM at different scales. They explored several interconnected elements such as soil, vegetation, topography, and climate that play an essential role in determining the temporal stability of SM.

It is essential to understand the features of SM patterns across space and time that reflect an integrated effect of various environmental factors on SM dynamics (Famiglietti et al., 2008; Brocca et al., 2010; Ochsner et al., 2013). Due to the complex interaction of SM with the surrounding environment with significant spatio-temporal variability, it is difficult to predict the temporal evolution of SM at any spatial scale, even with the knowledge of the fundamental process (Seneviratne et al., 2010; Vereecken et al., 2014). It is essential to determine the factors that control the spatio-temporal variability of SM and those that drive the evolution of SM spatio-temporal patterns at various scales. The factors affecting the spatio-temporal variability of SM at the

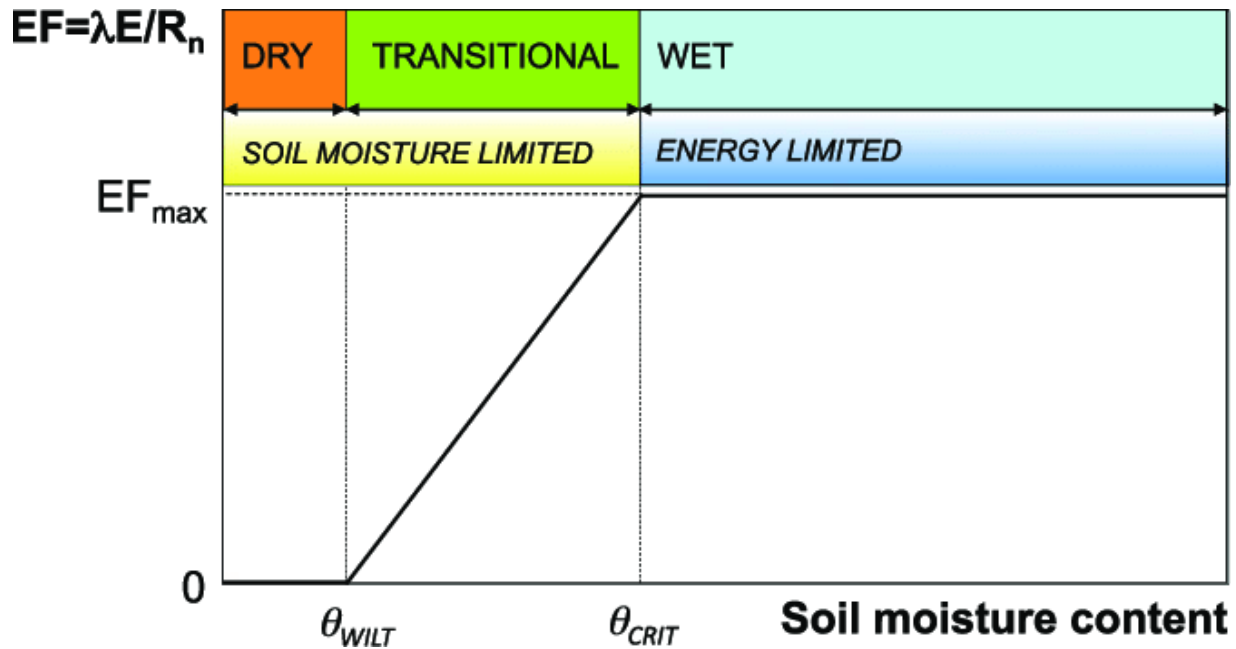


Figure 1.3: Conceptual structure of the dependence of EF on SM. Source: (Seneviratne et al., 2010)

field and regional scales are notably the soil characteristics, depth, vegetation dynamics, and topographical aspects (Mohanty and Skaggs, 2001; Teuling and Troch, 2005; Vereecken et al., 2014; Wang, 2014; Wang et al., 2015).

Different quantitative methods analyzed spatio-temporal variability and soil properties across a diverse range of scales. These methods are geostatistics, spectral and wavelet analysis, multifractal analysis, state-space analysis, and fuzzy-set analysis (Si, 2008; Molero et al., 2018). Currently, various new techniques are used to measure the SM spatial and temporal variability using in situ measurements, land surface or hydrological models, and remote sensing satellites. Those techniques are described in detail in the next section.

1.2 Soil moisture monitoring

Three broad ranges of methodologies can be used to estimate SM: in situ measurement, land surface modeling, and remote sensing. While in situ measurements have been and are still used as a reference for evaluating the other methods, they are limited by their spatial representativeness (Western et al., 2002). Given the physics, forcing data, and calibration parameters of soil water transfers at the soil-vegetation-atmosphere interface, land surface models can simulate SM continuously in time and space. Unfortunately, accurately determining the forcing data and model parameters is complex, and all models tend to diverge from reality after more or less running time. Remote sensing techniques have the unique asset of providing SM data at a range of spatial resolutions. The point is that they are subject to two main limitations: a low frequency of observations (smaller than 1 per day) and the uncertainty in remotely sensed data associated with the impact of disturbing factors specific to the wavelength used. Because each method has advantages and disadvantages, most studies combine SM information from in situ measurements, models, and remote sensing data.

1.2.1 In situ soil moisture

SM measurements are categorized into direct and indirect methods (Yoder et al., 1998). On the one hand, the direct method is used to measure the gravimetric soil water content, from which the volumetric SM is derived through the density of the soil sample. On the other hand, the indirect method estimates the volumetric soil water content by calibrating a function based on other measurable variables that vary with soil water content (Evelt and Parkin, 2005). Various direct and indirect ground measurement techniques for SM monitoring are discussed below:

Gravimetric method

The gravimetric method is an ancient and classical method to determine SM content. This is the oven-dry method most widely used for SM measurement (Schmugge et al., 1980). It is in particular used as the standard reference for calibration of other SM methods (Walker et al., 2004; Merlin et al., 2007). The wet soil sample is dried at 105°C until the constant weight of the soil sample is obtained. The gravimetric method measures SM as the ratio of the weight of water present in the soil to the weight of the soil sample. The weight of the water content is derived from the difference between the wet weight of the soil sample and the oven-dried weight. The gravimetric method gives the SM as a percentage of the dry weight of the soil. For calculating the volumetric water content, the gravimetric water volume is multiplied by the bulk density of the soil. The advantages of this technique : 1) robust, easy, and accurate, 2) sample acquisition is inexpensive, 3) SM content is easily calculated. However, the disadvantages of this technique : 1) SM estimation is difficult in heterogeneous soil, 2) this method is destructive and difficult to use for a long time 3) it is labor and time-intensive.

Dielectric technique

This is the most common technique due to its capability to monitor localized SM continuously in time at a relatively low cost. It estimates SM by measuring the soil dielectric constant. Since the dielectric constant of the liquid water is larger than the soil constitutes, the soil's total permittivity is governed by liquid water. Time-domain reflectometry (TDR) and frequency domain reflectometry (FDR) are the major techniques that use the soil's dielectric property for SM measurement.

TDR is widely used to measure SM content (Rao and Singh, 2011). It measures the propagation velocity of the electromagnetic wave in the soil and the dielectric constant as the amount of electrical energy in the substance. Soil water content is estimated by calibrating the function relating SM to the measured soil dielectric constant. The advantages of TDR : 1) it is non-destructive, less labor-intensive than the gravimetric method, easy to install 2) no specific calibration is required (Topp and Davis, 1985) 3) it provides an accurate result at a high temporal resolution (Chandler et al., 2004) 4) this technique is independent of the soil texture, temperature and soil content 5) this technique can be automated as it does not require daily maintenance and can be automatically regulated. The disadvantages of this technique : 1) high initial cost 2) limited applicability in highly saline soils (Ferrara and Flore, 2003) 3) specific calibration is required for bound water in organic soil, volcanic soil, etc.

FDR estimates the SM content from the signal frequency that varies according to the dielectric

constant of the soil. FDR uses a capacitor and the soil as a dielectric material to measure the SM content. The capacitor is connected with the oscillator to form an electrical circuit. The change in SM is estimated by the difference in the frequency of the operating circuit. The oscillatory frequency is restricted under a specific range to determine the resonant frequency. It gives the measurement of the water content in the soil (Muñoz-Carpena, 2004). The advantages of FDR : 1) it gives accurate results but requires specific site calibration, 2) applicable in highly saline soil conditions 3) flexibility in probe designers. The disadvantages of FDR : 1) higher sensitivity to temperature, bulk density, air gaps, and clay content limits the use of this method compared to TDR (Erlingsson et al., 2009), 2) restricted sphere of influence, 3) for reliable measurements, ensuring a good contact between the sensor and the soil is very critical.

Nuclear technique

The neutron scattering technique is an indirect way of determining the SM content. It estimates the SM by measuring the thermal or slow neutron density. The radioactive source emits high-energy fast neutrons into the soil, and they slow down when they collide with the same mass as a neutron (i.e., proton H+) and build a cloud of thermalized neutrons. The density of the thermalized neutron around the probe is proportional to the volume fraction of water present in the soil because water is the main source of hydrogen in the soil. The neutron probe is of two types: depth and surface probes. The depth probe is used to measure SM below the soil at a given depth, while the surface probe measures the soil water content in the uppermost layer of the soil (Schmugge et al., 1980). The advantages of nuclear technique : 1) it is more robust and accurate 2) it can detect the rapid and temporal change in the SM estimation 3) it measures a large soil volume, and also measure the SM profile at different depths 4) it is not affected by the soil salinity or the air gaps. The disadvantages : 1) the initial cost of the instrumentation is expensive, 2) a low degree of spatial resolution 3) the operator must take care to minimize the health risks.

Another nuclear-based technique is the gamma-ray attenuation technique. This is a radioactive technique that measures SM at a depth of 25 cm or less. This technique assumes that the scattering and absorption of gamma rays are related to density of the matter in their path. The specific gravity of the soil remains constant as the SM changes. The advantages of the gamma-ray attenuation technique : 1) is to provide temporal SM measurements at different depths 2) measurement is non-destructive 3) data can be obtained over small and horizontal distances. The disadvantages : 1) costly and difficult to use, 2) requires extreme care to reduce the risk of health hazards, and 3) being impacted by the significant variation in bulk density.

Tensiometer technique

A tensiometer measures the tension or the energy with which the soil holds water. SM can be derived from the soil water tension, given the soil's hydraulic properties. The tensiometer consists of a water-filled cylindrical tube with ceramic tips on the end and a vacuum gauge at the top. A tensiometer is installed into the soil at a depth at which the SM measurement is required. At this depth, the water in the tensiometer comes to an equilibrium with the surrounding soil. When the soil dries, the water is pulled out through the tip and creates tension on vacuum tubes. When the SM is wet, the stress is reduced, and it allows the water to enter into the vacuum tubes through the cylindrical tubes, and the vacuum is reduced. The pressure generated by the tensiometer is equivalent to the tension used by the plant to extract water from the soil. The advantages of the tensiometer technique : 1) easy to install and cost-effective, 2) SM distribution

information is obtained under both saturated and unsaturated soil conditions, 3) the equipment can be easily placed in the soil and provides continuous measurement of the soil with minimal disturbance and 4) use of ethylene glycol water solution makes the tensiometer suitable to be installed in the cold regions. The disadvantage : 1) unsuitable for dry soil 2) high maintenance is required 3) SM information can only be obtained within the water tension range of 0 to 85 centibar 4) the relationship between SM and the measured soil water tension is highly nonlinear.

1.2.2 Dynamic models

Land surface models describe the interactions between the land surface and the atmosphere, i.e., heat, energy, and water exchange. SM is simulated in time and space using a dynamic model that integrates the physics of the soil water transfers. It provides a boundary condition for the atmospheric model and plays an essential role in the numerical weather prediction and climate change projection system. It also plays a vital role in representing hydrological processes by modeling the interaction with the land surface and the atmosphere.

Land surface models can differ in representing the spatial variability of the SM, vegetation, topography, surface runoff, water storage, etc. They are categorized into three generations (Sellers et al., 1997; Pitman, 2003). The first generation of land surface models provides a straightforward representation that considers simple interactions with the land surface, atmosphere, or vegetation. Two examples of the first-generation models are given below.

Bucket model (Manabe, 1969) is the first simple land surface model used to model hydrological fluxes at a global scale. In this model, the soil layer has a fixed water capacity, constant soil depth, and soil properties. The basic principle of this model is that the bucket is filled with precipitation, and it will become empty with evaporation and runoff.

Force-restore model (Deardorff, 1978) based on the "force restore" method (Bhumralkar, 1975) was developed from an efficient time-dependent equation to estimate SM. The force and restore model usually involves two prognostic equations: surface or root zone layers, representing the evolution of the surface and root zone SM. It is the most popular SM prediction model because of its computation efficiency, and it employs a minimum number of prognostic variables and captures the most important physical processes.

Second and third-generation land surface models are formed by combining simple models to develop the complicated relationship between the land surface and the atmosphere at different scales in a more realistic manner. The more complex models can provide information about SM and other land surface and atmospheric variables such as surface temperature, precipitation, etc.

An example of a new generation land surface model is given by **Surface Externalisée (SURFEX)**, which is the surface model developed by Meteo France. The SURFEX model provides consistent stability of the land surface and atmosphere coupling. First, each surface grid box receives the air temperature, pressure, specific humidity, total precipitation, long and short wave radiation, chemical species, and aerosol concentration during a model timestamp. Then SURFEX computes the average flux for momentum, sensible heat, latent heat, chemical species, and aerosol and sends these quantities back to the atmosphere with the addition of radiative surface temperature, diffuse albedo, and surface emissivity. In SURFEX, each model grid box is represented by different surface coverage: soil and vegetation, urban areas, and water bodies (sea or ocean or lake). These surface coverages are obtained through the global ECOCLIMAP database

that combines land cover maps and satellite information. The SURFEX averages all the fluxes computed over soil and vegetation, urban, and water (sea or lake or ocean) by their respective fractions. All this information is used in the lower boundary condition for atmospheric radiation and turbulent flux. A different model represents each surface type. The SURFEX model consists of physical models such as ISBA for land surfaces, Town Energy Balance (TEB) for urban areas, and Flakes for lakes and oceans.

As the land surface component of SURFEX, Interaction between soil biosphere and atmosphere (ISBA) integrates the interaction between the land surface and atmosphere. ISBA includes several models that transfer energy and water into the soil, vegetation, surface hydrology, and snow. The ISBA model is built to reduce the complexity level by reducing the number of parameters while still representing the physics of the land-atmosphere interaction. ISBA is a simple land surface model that can use the 'force restore' method (Deardorff, 1977) to calculate the surface and mean soil temperature over time and the soil water budget (IBA-2L, (Noilhan and Planton, 1989)). In this model, the upper layer acts as a reservoir for the evaporation from the soil surface, and the single subsurface soil layer is used to model the mean water content from the root and the sub root zone layer. Standard ISBA-2 layer can also define the routing layer and include a third layer that distinguishes between the surface root and sub-root-zone soil water basins (ISBA-3L, (Boone et al., 1999)). ISBA was further modified to account for the atmospheric carbon dioxide concentration on the stomatal aperture (ISBA-Ags, (Calvet et al., 1998)). The standard ISBA model was updated to represent better the surface and the sub-grid runoff for hydrological applications (Habets et al., 1999).

The dynamic modeling used to estimate SM thus faces a compromise in terms of SM accuracy between the physics implemented in the model equations, the number of represented layers, the availability of the parameters, and forcing data needed as input to the model. In general, a simple model allows for sampling its entire parameter set and inferring an optimal calibration. However, it cannot replace sophisticated models that account for the complex relationships in soil and vegetation to produce more comprehensive results in different hydro-climatic conditions. The main advantage of simple models is that they require fewer input parameters, improving their calibration capabilities to reduce associated uncertainty in the output data.

1.2.3 Satellite information

SM is spatially variable, and the factors that affect the variability of SM are especially soil types, vegetation cover, climatic conditions, and topography. In situ measurements of SM are limited to the point scale at a particular location. Such point-based measurement cannot cover such a high variability of SM (Srivastava et al., 2013). Extrapolating such point scale measurements via geostatistical techniques (Qiu et al., 2001) is practically expensive, time-consuming, and complex, especially over heterogeneous land surfaces (Qin et al., 2013; Byun et al., 2014). Although the in situ SM measurement has more significant potential for SM estimation, it is impractical to measure the spatial and temporal SM variability at a regional and global scale.

The problem is solved by developing remote sensing techniques that can estimate SM from regional to global scale at a daily temporal scale. Microwave satellite observation from active and passive sensors is most suitable for retrieving SM (Schmugge et al., 2002; Mohanty et al., 2017). Microwave sensor cannot estimate SM directly, but it has a direct relationship between soil dielectric constant and water content. This section describes remote sensing techniques based on passive microwave, active microwave, and optical/thermal remote sensors, estimating SM over

large extents.

Passive microwave sensors

The earth continuously receives electromagnetic radiation from the sun. Some of the radiation gets absorbed/reflected or gets transmitted from the earth's surface. The energy absorbed is transformed into thermal energy and increases the temperature of the surface until it reaches thermodynamic equilibrium. In this state, all media radiate energy to keep the energy balance. Passive microwave sensors are susceptible and detect the emitted or radiated energy from the earth's surface at the wavelength of 1 to 30 cm, expressed as brightness temperature. The emitted energy absorbed by the passive microwave includes the contribution from the atmosphere, land surface, and the reflected radiation from the sky. The passive microwave can provide SM information as there is a significant difference between the dielectric constant of water (80) and soil (4). Soil texture and the variability in the temperature of soil and vegetation also affect the microwave spectrum's retrieval. The advantage of a passive microwave radiometer is that the cloud cover does not limit its weather conditions and is minor dependent on the daytime acquisition, and when vegetation is not present, SM is the dominant parameter affecting the received signal from passive microwave (Njoku and Entekhabi, 1996). The passive microwave is adequate for monitoring SM globally (Owen et al., 1998). Generally, the two-parameter retrieval technique has been used to retrieve SM and vegetation optical depth simultaneously. This technique is well suited for passive microwave observation using dual-polarization multi-frequency or multi-angular L-band observations (Peischl et al., 2014). Various passive microwave remote sensing satellites have been launched in the past 35 years (Chen et al., 2012). Some of the passive microwave sensors are shown in Figure 1.4.

Various microwave bands such as L, C, X, and K are used by radiometers. Currently, L-band is used to estimate SM because data at L band frequencies are sensitive to the SM through vegetation up to 5 kg/m^2 and can provide SM in all weather conditions. In contrast, other higher frequency (C, X, and K) bands are sensitive to vegetation but are more attenuated by the vegetation effect and are hence limited in applicability to areas of moderate vegetation ($< 3 \text{ kg/m}^2$). The L-band frequency gives the information from the top surface to a few centimeters of the soil surface ($\approx 5 \text{ cm}$) and is less affected by the Radio Frequency Interference (RFI). Note that sensors operating at lower frequencies (P-band) could also be used to obtain information more profoundly into the soil. However, the antenna size (increasing with the increase in wavelength) and the significant presence of RFI make it challenging to build a remote sensing satellite using P-band passive microwave.

Currently, two L-band missions, Soil Moisture Ocean Salinity (SMOS, (Kerr et al., 2010)) and Soil Moisture Active and Passive (SMAP, (Entekhabi et al., 2010)), are used to provide SM at a global scale and are used extensively in this thesis.

SMOS is the first L-band microwave satellite launched by the European Space Agency on 2nd November 2009. SMOS provides SM and ocean salinity data using a radiometer at a frequency of 1.4 GHz using a Microwave Imaging Radiometer with Aperture Synthesis (MIRAS) instrument. It provides SM images at 35 km spatial resolution with a temporal resolution of 1-3 days. SMOS has a sun-synchronous, quasi-circular orbit with an altitude of 758 km with an ascending (6 pm) and descending (6 am) overpass. SMOS is a 2-D interferometer, which provides the brightness temperature in horizontal and vertical polarisation at a range of incidence angles (ranging from 0 to 55 degrees). The SMOS algorithm uses a dual-polarised multi-incidence angle to separate

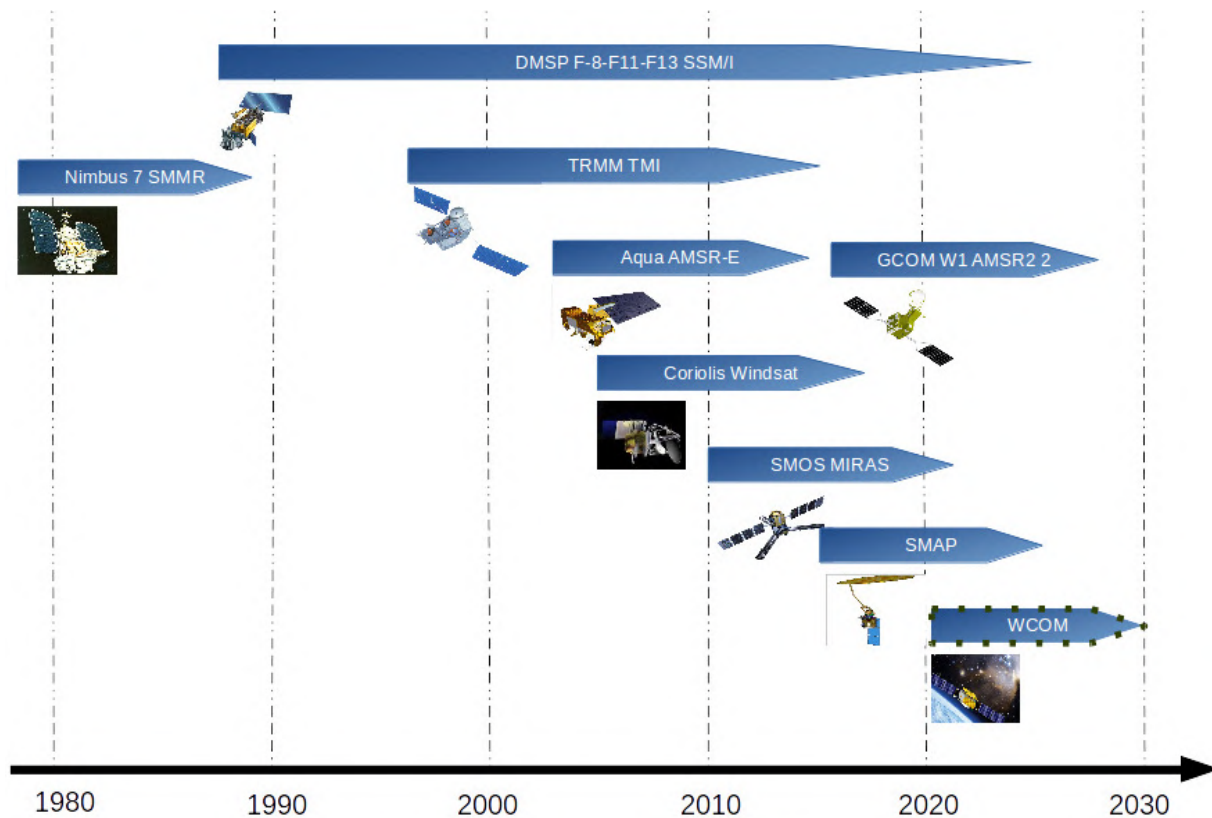


Figure 1.4: List of past and current passive microwave sensors until today.

the soil and vegetation contributions to land emissivity. SMOS provides SM products at Level 2 and Level 3. Along with the SM product, the SMOS mission provides ancillary data such as surface temperature, roughness parameter, and optical thickness at the top of the atmosphere. It provides a global SM product with a specified accuracy of $0.04 \text{ m}^3/\text{m}^3$ derived from the brightness temperature (Kerr et al., 2001). The validation experiment of the Level 2 SMOS product shows satisfying results in SM estimation over different ecosystems and different spatial scales. For example, validation studies have been performed in various areas such as South America (Escorihuela et al., 2012), Europe (Lacava et al., 2012; Srivastava et al., 2013; Petropoulos et al., 2014), Australia (Panciera et al., 2011; Peischl et al., 2014) and the United States (Jackson et al., 2011; Al Bitar et al., 2012) ranging from the continental scale (Dente et al., 2012; Zhao et al., 2014) to the catchment scale (Bircher et al., 2012; Srivastava et al., 2013).

SMAP is a L-band satellite launched by NASA on 31st January 2015. SMAP is designed to use active and passive microwave sensors by incorporating L-band radar (VV, HH, and HV polarizations) and L-band radiometer (V, H, and 3rd and 4th Stokes parameter polarizations). But due to the failure of the radar, currently, the SMAP radiometer mission provides SM data at 36 km spatial resolution on a revisit cycle of 3 days on a global scale. The SMAP satellite has a sun-synchronous polar orbit with an altitude of 658 km with a descending/ascending overpass at 6:00 a.m./p.m. local time. The SMAP mission provides SM products with a specified accuracy better than $0.04 \text{ m}^3/\text{m}^3$. Various validation results show satisfactory results for different spatial resolution SM products from SMAP (Vreugdenhil et al., 2013; Cai et al., 2017; Colliander et al., 2017a; Ma et al., 2017; Bhuiyan et al., 2018; Colliander et al., 2019). The SMAP mission currently provides SM on a 9 km resolution grid (Das et al., 2013) by interpolating the L-band

radiometer using the Backus-Gilbert method (Backus and Gilbert, 1970). The SMAP mission also combines the SMAP radiometer with Sentinel-1 radar to provide SM at 9 km and 3 km (Das et al., 2018), but this approach is limited by the requirement of having quasi-simultaneous overpass times of SMAP and Sentinel-1.

Active microwave sensors

Active microwave (or radar) satellites use their radiation source to illuminate the targeted objects and calculate the backscattering coefficient, the difference between the transmitted and received electromagnetic radiation. Active microwave sensors are divided into imaging (e.g., synthetic aperture radar (SAR)) and non-imaging instruments, including scatterometers and altimeters. The radar backscattering coefficient is related to SM because of the significant difference between the soil dielectric constant of dry soil and water, but the accuracy of the retrieved SM is affected by the soil roughness and vegetation biomass (Moran et al., 2004). Due to the complex connection between the backscattering coefficient and surface reflectivity, the complex structure of soil surface and vegetation has a significant impact on the measurements, and a simple procedure for removing those effects is challenging to develop. By considering the sensor configuration and surface parameters, various backscattering models have been developed over the past 30 years (a list of active microwave sensors is shown in Figure 1.5), categorized into three groups: physical or theoretical, empirical, and semi-empirical models.

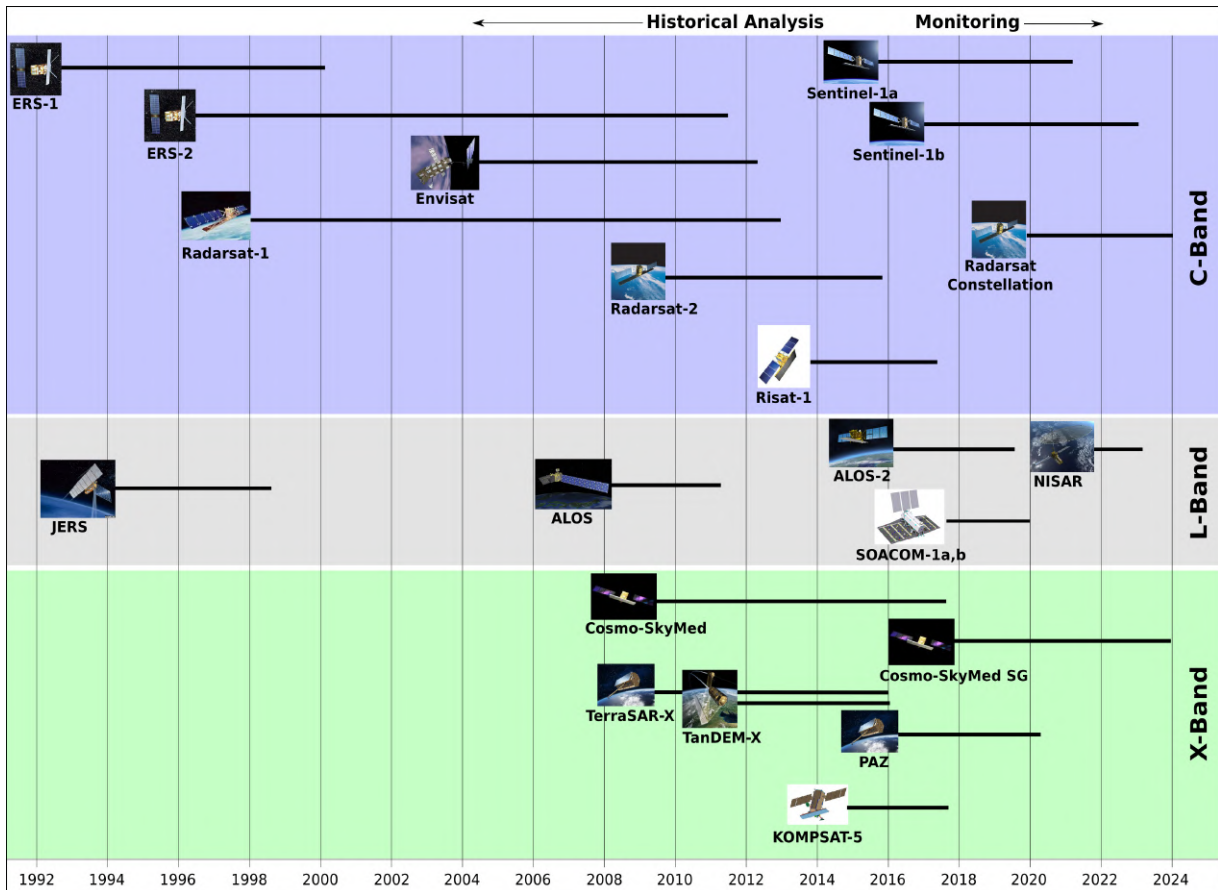


Figure 1.5: List of past and current active microwave sensors till today. Source: UNAVCO

Physical or theoretical models compute the radar backscattering coefficient in terms of dielectric constant and soil roughness by computing the interaction between microwave radiation and soil. In these models, the SM is estimated by the mathematical inversion of the backscattering coefficient. The advantage of the theoretical approach is that it is independent of the sensor's local site condition and typical features. It provides SM with high accuracy (Notarnicola and Solorza, 2014) and can be implemented in specific roughness conditions. The disadvantage is that it requires many input parameters that make the parameterization difficult and complex (Moran et al., 2004). This model also provides difficulty in describing the soil roughness (Zribi and Dechambre, 2003). The most commonly used physical model nowadays is the Integral Equation Model (IEM).

IEM (Fung et al., 1992) is a physical-based radiative transfer model that calculates dry soil's backscattering coefficient with given radar properties such as wavelength, polarization, surface characteristics such as dielectric constant, and surface roughness, and local incidence angle. This model is one of the widely used inversion models to estimate SM and surface roughness (Shi et al., 1997; Satalino et al., 2002; Zribi and Dechambre, 2003). Nonetheless, IEM shows difficulty over the natural surfaces due to the sensitivity of the models to the surface roughness parameters and the problem associated with their correct measurements (Zribi and Dechambre, 2003). This model neglects the scattering from the subsurface soil volume that may be important for the dry soil condition (Schanda, 1987). Therefore these models require very detailed knowledge of the surface roughness.

Consequently, empirical models are also used to derive the direct relationship between the radar backscattering coefficient and SM. The empirical studies are based on the experimental results associated with the experimental sites' surface conditions and radar parameters. Many empirical studies show a linear relation between radar backscattering coefficient and SM for specific sites where the SM ranges from 0.10 to 0.35 m^3/m^3 by assuming that roughness does not change between successive radar measurements (Zribi et al., 2005). This model directly relates radar backscattering to SM. However, this empirical-based approach requires specific datasets and implementation conditions, e.g., incidence angle, observation frequency, and surface roughness. Another limitation is that they need high-quality situ SM measurements to perform the calibration step, which is costly and challenging. In addition, those empirical models may not be valid outside the conditions for which they have been calibrated.

Intermediate between theoretical and fully empirical approaches, the semi-empirical models, combine the numerical radiative transfer model (physical model) and analyzed or experimental datasets (empirical model) to provide a simple relationship between surface properties and the physics of the backscattering mechanism. The model generally provides a good compromise between the theoretical model's complexity and the empirical model's simplicity. The advantage of this type of model is that it is site-independent and can be applied when there is little or no information of soil roughness available (Baghdadi et al., 2008). The most widely used semi-empirical model is the Oh model (Oh et al., 1992) and the water cloud model (Attema and Ulaby, 1978).

The water cloud model is a volume scattering model over the vegetated areas. This model was developed by assuming that the canopy "cloud" is made up of identical water droplets randomly distributed within the canopy. Due to its simplicity, it is most extensively used for SM estimation, especially over agricultural areas (Bindlish and Barros, 2001; Dabrowska-Zielinska et al., 2007; Baghdadi et al., 2017; Li and Wang, 2018). This model expresses the complex scattering characteristics in the vegetated areas and provides attenuation information from the vegetation

layer.

Optical/thermal remote sensing sensors

Visible/shortwave sensors depend on the sun as a source of illumination and use visible, near-infrared, and short wave infrared to image the earth's surface. Different objects observe and reflect differently at different wavelengths. Their spectral signature can differentiate the reflected objects in the remotely sensed image. Various optical/thermal sensors at different resolutions have been launched since the 1970s, as shown in Figure 1.6.

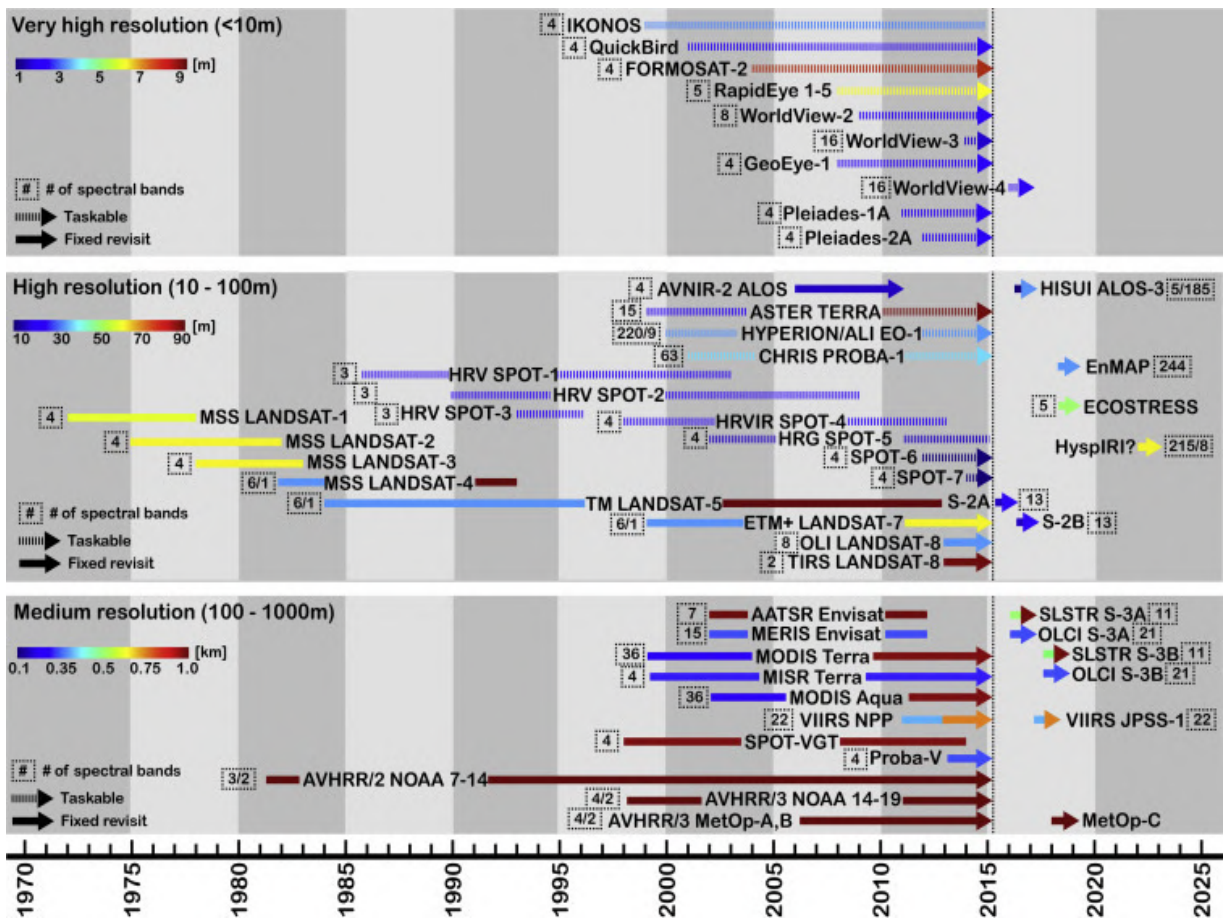


Figure 1.6: List of past and current optical/thermal sensors until today. Source: [Houborg et al. \(2015\)](#)

Visible/shortwave sensors depend on the sun as a source of illumination and use visible, near-infrared, and short wave infrared to image the earth's surface. Different objects observe and reflect differently at different wavelengths. Their spectral signature can differentiate the reflected objects in the remotely sensed image.

Optical remote sensing is classified based on the spectral bands:

1. Panchromatic uses a single band to record radiation for a longer wavelength. e.g. SPOT HRV-Pan, Ikonos Pan.

2. A multispectral sensor (multichannel detector) uses few spectral bands and records electromagnetic radiation in the narrow wavelength, e.g., Landsat MSS, Landsat TM, SPOT HRV-XS, Ikonos MS.

3. Superspectral sensor uses more than ten spectral bands and record electromagnetic radiation on the short wavelengths that enable the more exemplary spectral characteristics of the target to be captured, e.g., MODIS, MERIS

4. Hyperspectral sensor uses more than 100 spectral bands, and the precise spectral signature better classifies the objects and is used for different applications such as forestry, agriculture, etc., e.g., Airborne Visible Infrared Imaging Spectrometer (AVIRIS)

Several studies document an empirical relationship between soil surface reflectance and SM (Gao et al., 2013) and the non-linear relationship between SM and reflectance (Lobell and Asner, 2002; Nocita et al., 2013). The main disadvantage of the optical sensors for SM monitoring is that they have limited ability to penetrate clouds and are highly attenuated by the vegetation cover (Zhao and Li, 2013). In addition, soil reflectance measurements are strongly affected by the many physical properties of the soil, such as organic matter content, roughness, texture, angle of incidence, plant cover, etc. that makes the soil reflectance highly variable regardless of the SM. The relationship between soil reflectance and SM is only achieved when the model is fitted to specific soil types (Muller and Decamps, 2001). In general, reflected spectral information alone could not provide a viable solution to provide SM.

Thermal images use infrared sensors to detect the infrared radiation emitted from the earth's surface. This radiation is emitted from the warm earth's surface, and they are used in remote sensing satellites to measure the land and sea surface temperature. The amount of thermal radiation emitted by the objects depends on their temperature.

Since evaporation is the most efficient way to calculate the energy loss at the surface, there is a strong coupling between the land surface temperature (LST) and water availability in the water stress condition. Therefore the use of thermal data is the most appropriate way to access the actual evaporation and SM status at a suitable space and time scale (Boulet et al., 2007). In addition to this, thermal data have the advantage of detecting vegetation water stress information and water stress variability at field scale (Anderson et al., 2012). The residual method and the EF method are used to determine ET and SM using LST data.

The residual method estimates ET as the residual term in the energy surface model, defined as available energy at the surface minus the sensible heat flux. This approach is based on a single-pixel method to calculate ET for each pixel independently. Models that use this approach are, for instance, Two-Source Energy Balance (TSEB, (Norman et al., 1995)), Surface Energy Balance Model (SEBS, (Su, 2002)), and Two-Source Time Integrated Model (Anderson et al., 1997). The approach is computationally efficient and offers a reasonable estimate of ET with high accuracy over homogeneous areas. This approach requires ground measurements such as wind speed, humidity, vegetation height, air temperature, etc. However, due to the limited availability of ground measurements over the heterogeneous area, this model is rarely used to estimate ET and SM over large areas on operational application (Jiang and Islam, 2003).

The other range of methods to estimate ET and SM from LST data are based on EF. EF can be estimated from the optical/thermal image, where the LST in dry and wet conditions can be estimated from the LST and fractional vegetation cover data. This method is based on the contextual-based method that uses the heterogeneity of the land surface within the remotely

sensed LST image and uses the whole image to estimate EF at each pixel. Models that use this approach are Surface Energy Balance Index (SEBI, (Menenti et al., 1989)), Simplified Surface Energy Balance Index (S-SEBI, (Roerink et al., 2000)), Monosource Surface energy Balance Model (SEB-1S, (Merlin et al., 2013)), Vegetation Temperature Condition Index (VTCI, (Wan et al., 2004)), and Temperature Vegetation Dryness Index (TVDI, (Sandholt et al., 2002)).

Thermal infrared remote sensing can also be used to decouple the surface thermal properties from the ambient temperature (daily temperature cycle) by calculating the apparent thermal inertia (Qin et al., 2013; Lei et al., 2014). The thermal inertia depends on thermal conductivity and heat capacity, which increases with the SM (Olsen et al., 2013). So, a relationship is developed between the LST change and SM by measuring the amplitude of the daily temperature change. The relationship between the daily temperature change and SM is a function of soil type and limited to bare soil conditions (Van de Griend et al., 1985). Recent studies have shown that SM can be estimated over vegetated areas if the linear relationship is maintained between the ground flux and LST (Maltese et al., 2013a,b).

1.2.4 Downscaling methods

Remote sensing satellites monitor SM at a global scale with passive radiometry at L-band (SMOS and SMAP) but with a spatial resolution far from the requirement for many applications, including fine scale hydrological studies and basin-scale water and irrigation management. Hence to overcome the limitations of low resolution SM and provide SM at a higher spatial resolution, various downscaling methods have been proposed to disaggregate the passive microwave derived SM data. Peng et al. (2017) categorized the existing downscaling methods into three different types: 1) geo-information based 2) model-based 3) satellite-based.

1. Geo-information-based models use land surface parameters (such as vegetation attributes, topography, and soil characteristics) to downscale coarser resolution to fine resolution. The downscaling approach can be helpful at the field scale where the in situ information is available, but its applicability is limited at the coarser scale.

2. Model-based downscaling methods can be based on statistical, hydrological, or land surface models. The statistical model is computationally inexpensive and the best way to use the large historical data to make a statistical relationship. A statistical model is prevalent in climatology for future prediction. Various statistical downscaling models are developed to downscale SM at fine resolution: the wavelet coefficient (Kaheil et al., 2008) and fractal interpolation (Kim and Barros, 2002) are two examples. Another model-based approach uses a hydrological or land surface model to downscale low resolution to high resolution observation by linear regression (Low and Mauser 2008), bivariate distribution (Verhoest et al., 2015), and assimilation of coarser-resolution in land surface/hydrological models to provide fine-scale resolution. The model-based approach can be used to provide SM globally, but the main limitation is that the error in the model or the remotely-sensed observations fully contributes to the finer resolution of SM. It also depends on the availability of the information at the finer scale resolution, such as soil types, soil texture, precipitation and irrigation data, which somehow restricts its usefulness to provide SM data at high resolution on a global daily basis. Another major problem is developing a hydrological or land surface model to represent the physics and remote sensing observations with better robustness and accuracy.

3. Satellite-based downscaling methods are developed based on a synergy between coarse resolution satellite data and fine resolution satellite data to provide high resolution SM as described below :

a) Synergy between active and passive microwave data :

It is found that the L-band radiometer is very efficient in providing SM information more accurately as compared to other satellite information. Based on this concept, the low resolution L-band derived SM is disaggregated at high resolution using fine scale remotely sensed ancillary data. Especially the SMAP mission combines the L-band radiometer at low resolution with the Sentinel-1 radar to downscale SM at 3 km and 1 km. But the main limitation is that it depends on the quasi-simultaneous overpass time of the Sentinel-1 and SMAP data.

b) Synergy between optical/thermal and passive microwave data :

[Merlin et al. \(2013\)](#) developed the DISaggregation based on the Physical and Theoretical scale CHange (DISPATCH) algorithm that uses optical/thermal data as a SM proxy to downscale low resolution microwave SM data. The DISPATCH algorithm uses the evaporation-based method. DISPATCH is a physical and theoretical approach to disaggregate coarser microwave low resolution to provide high resolution SM. [Peng et al. \(2015\)](#) use the VTCI as the thermal-based SM proxy to downscale low resolution SM. VTCI is calculated from triangular/trapezoidal feature space from optical/thermal data at high resolution. [Fang et al. \(2013\)](#) use the thermal inertia relationship between daily temperature change and daily average SM by using SM at low resolution and optical/thermal data at high resolution. [Song et al. \(2013\)](#) downscale microwave brightness temperature using high-resolution optical/thermal data. Then, high-resolution brightness temperature is used to retrieve SM using a single-chain algorithm ([Jackson, 1993](#)).

1.3 Research objectives and outline of the thesis

For SM monitoring, in situ measurements and land surface modeling are useful as a localized reference for validation purposes and as a physical tool to extrapolate results in both space and time, respectively. However, both have substantial limitations related to the spatial representativeness of SM estimates. In this context, remote sensing techniques have a strong potential to provide SM estimates at various spatial scales, which are required in many applications, including meteorology and climatology, hydrology, and agriculture (e.g., irrigation scheduling, for instance). Spaceborne sensors based on passive microwave, active microwave, and optical/ thermal data can provide SM information at different spatial and temporal scales.

The remote sensing community generally acknowledges passive microwave at L-band as one of the most accurate techniques. However, on the order of several tens of kilometers, its spatial resolution is not adapted to most fine-scale hydrological and agricultural uses. Therefore, other non-optimal but complementary methods are investigated based on radar and/or optical/thermal data available at higher spatial resolution. Still, no approach combines the available multi-sensor (passive/active microwave/optical/thermal) data to exploit each technique's advantages efficiently. This thesis aims to develop an algorithm that combines multi-sensor/multi-resolution/multi-wavelength data to provide SM data with improved robustness and accuracy at high spatio-temporal resolution.

Based on this idea, the research proposed herein develops and evaluates a new algorithm and

methodology for SM monitoring. In particular, a synergy is investigated between the SMAP/SMOS passive microwave-derived SM data disaggregated using optical/thermal data (with DISPATCH downscaling algorithm) and the SM retrieved from radar data (with an active microwave radiative transfer model). To do this, three successive steps are identified to disaggregate the 40 km resolution SMOS/SMAP data at the 1 km resolution (step 1), to disaggregate the SMOS/SMAP data at the 100 m resolution (step 2), and to build a synergy at the 100 m resolution with active microwave data (step 3). As a final step, the disaggregated SM data are assimilated into a land surface model to improve the accuracy and the frequency of SM estimates. The main objectives of the research are illustrated in Figure 1.7.

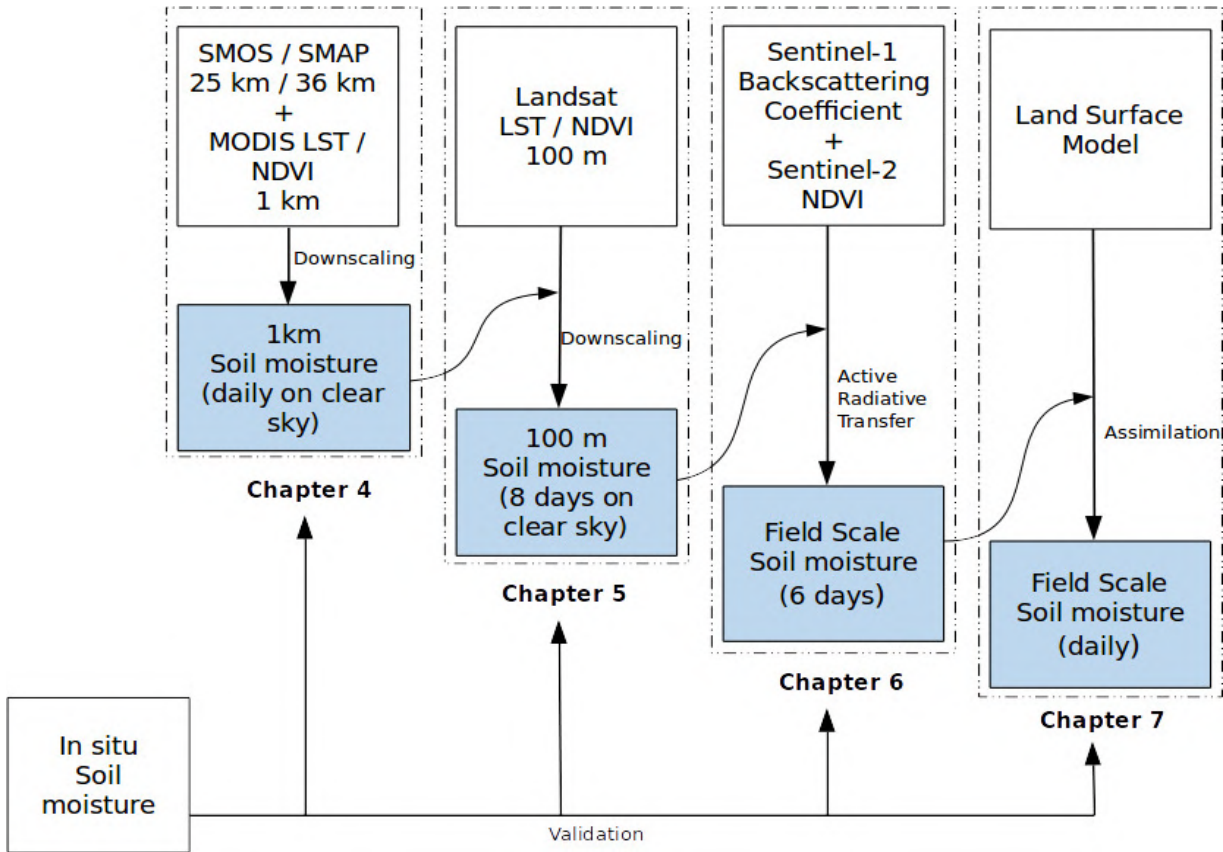


Figure 1.7: Schematic diagram of the main research objective split into four successive steps.

This research is expected to provide a new understanding of the advantage of the multi-sensor synergy and its applicability to provide SM at high spatio-temporal resolution. The algorithm used in this research is intended to be quite generic and could be applied for future upcoming remote sensing data.

In summary, the underlying scientific questions that this thesis proposes to address are:

- 1) How can we retrieve high-resolution SM data - which will be helpful for agriculture and hydrological purposes - meaning data at high spatial and temporal resolution (repeat cycle of a few days)?
- 2) Is it possible to provide high spatio-temporal resolution SM information from the readily

available remote sensing observations over different land covers?

3) What are the possible synergies between passive microwave, active microwave, and optical/thermal data for SM retrieval?

The thesis is organized to describe the approaches or algorithms implemented to combine and overcome limitations of passive microwave, active microwave, and optical/thermal observations, and the final objective is to provide SM at high spatio-temporal resolution with improved robustness and accuracy. In practice, the document is organized as follows:

Chapter 1 introduces the importance of SM from a broad perspective and discusses the availability and limitations of existing SM products derived from the different sensors and models at a range of resolutions.

Chapter 2 describes the study areas used for this research, i.e., the region selected for the analysis purpose within the Mediterranean region.

Chapter 3 gives a generic description of the DISPATCH downscaling algorithm used to provide SM at high resolution by downscaling the low resolution passive microwave-derived SM data using optical/thermal data. The downscaling algorithm is implemented globally to provide SM at 1 km resolution.

Chapter 4 presents the new implementation and improvement in the DISPATCH algorithm to increase the spatial coverage and improve the retrieved SM's accuracy. This chapter also presents a comparative qualitative and quantitative accuracy assessment with two different SM products at 1 km resolution.

Chapter 5 presents a new algorithm to provide SM data at 100 m resolution from the passive microwave observations at 40 km resolution using the DISPATCH algorithm. The two-step downscaling algorithm is used to disaggregate the SMOS/SMAP SM data at 100 m resolution.

Chapter 6 presents a new methodology that builds on a synergy between passive microwave, optical/thermal, and active microwave data sets. As a synergy strategy, radar model parameters are calibrated at the radar spatial resolution from the downscaled passive microwave-derived SM product. The algorithm is quite generic, and the main advantage is that it is independent of the in situ SM datasets for calibration purposes.

Chapter 7 investigates the usefulness of integrating SM products at high resolution into a land surface model to provide SM data at a daily field scale over an irrigated area. The approach is unique because the 100 m SM product is used to assess the sensitivity of the disaggregation-assimilation coupling scheme to irrigation, which is not included in the forcing data of the model.

Chapter 8 summarizes the research works and highlights their original contribution. It also opens a new path of future research avenues concerning SM monitoring from remote sensing and multiple applications.

Chapitre 1

Introduction (français)

Contents

1.1	Contexte	22
1.1.1	Changements globaux	22
1.1.2	Dynamique des ressources en eau dans la région méditerranéenne	23
1.1.3	Variabilité spatio-temporelle de l'humidité du sol	24
1.2	Suivi de l'humidité du sol	27
1.2.1	Mesure in situ de l'humidité du sol	27
1.2.2	Modèles dynamiques	29
1.2.3	Informations satellitaires	31
1.2.4	Méthodes de réduction d'échelle ou désagrégation de données	38
1.3	Objectifs de recherche et plan de la thèse	40

1.1 Contexte

1.1.1 Changements globaux

L'eau couvre les deux tiers de la surface de la terre. Ainsi, 97 % de l'eau de la terre est contenue dans les océans sous forme d'eau salée, et 2 % de l'eau est stockée sous forme d'eau douce dans les calottes glaciaires, les glaciers, les chaînes de montagnes enneigées, et seulement 1 % est disponible pour les besoins quotidiens. L'eau douce est stockée dans le sol, les eaux de surface, les eaux souterraines, les lacs, les rivières et les ruisseaux, entre autres. L'eau douce est nécessaire à toutes les activités écologiques et sociétales, notamment la production de nourriture et d'énergie, le transport, l'élimination des déchets, le développement industriel et la santé humaine (Baron et al., 2002). Néanmoins, les réserves d'eau douce sont réparties de manière inégale et aléatoire, et certaines régions du monde sont soumises à un stress hydrique important (Chitonge, 2020). Au cours du XXe siècle, la demande en eau douce a augmenté en raison de l'accroissement de la population humaine et de l'amélioration du niveau de vie (Hinrichsen and Tacio, 2002). On prévoit que la demande en eau augmentera de 50 % en 2050 (Leflaive, 2012) avec l'augmentation de la population, la pénurie d'eau et le changement climatique mondial - rendant l'offre et la demande en eau plus problématiques et incertaines (Hallegatte, 2009). Au cours des dernières décennies, le changement climatique a été principalement causé par l'activité humaine, les cycles naturels n'ayant qu'une incidence mineure. La Figure 1.1 montre les influences humaines et naturelles estimées sur la température globale. Les activités humaines, telles que les émissions de gaz à effet de serre provenant de la combustion de combustibles fossiles, la déforestation et le changement d'affectation des terres, sont à l'origine du changement climatique.

La région méditerranéenne est plus exposée au changement climatique mondial (Lionello and Scarascia, 2018). La région méditerranéenne a montré une transition climatique dans le passé (Tsimplis et al., 2006) et est maintenant considérée comme un "point chaud" mondial pour le changement climatique (Giorgi, 2006), où un impact sévère du changement climatique est prévu (Stocker et al., 2014). Le changement climatique dans la région méditerranéenne augmente les températures annuelles moyennes de 1,5°C, dépassant les tendances actuelles du réchauffement climatique (+1,1°C) (Cramer et al., 2018). L'été devient plus chaud à mesure que les températures augmentent, et les vagues de chaleur deviennent plus fréquentes et plus graves (Kuglitsch et al., 2010; Jacob et al., 2014). Dans la plupart des endroits, notamment dans le sud, chaque degré d'augmentation de la température réduit les précipitations de 4 % (Lionello and Scarascia, 2018). L'augmentation de la température et la diminution des précipitations entraînent de graves conditions de sécheresse dans les parties sud et est de la région méditerranéenne (Lieveld et al., 2012; Yves et al., 2020). Les vagues de chaleur et les sécheresses influencent les activités socio-économiques, la biodiversité et la santé publique (Fouillet et al., 2006). En raison du changement climatique, la région méditerranéenne est également considérée comme un point chaud pour le changement de la biodiversité, perdant au moins 70 % de son habitat (Myers, 1990).

La disponibilité de l'eau dans la région méditerranéenne est susceptible de diminuer de 2 % à 15 %, soit la diminution la plus importante au niveau mondial (Schleussner et al., 2016). La diminution des précipitations et les changements dans les régimes de précipitations affectent directement la quantité d'eau qui atteint le sol ou le ruissellement de surface ou le rejet dans la rivière. L'augmentation de la température et la modification d'autres paramètres tels que le rayonnement solaire, la vitesse du vent et l'humidité augmentent le processus de transpiration des plantes et le processus d'évaporation du sol et des masses d'eau. Ces changements affectent le débit des rivières, la qualité et la quantité des ressources en eau, et pour comprendre les facteurs

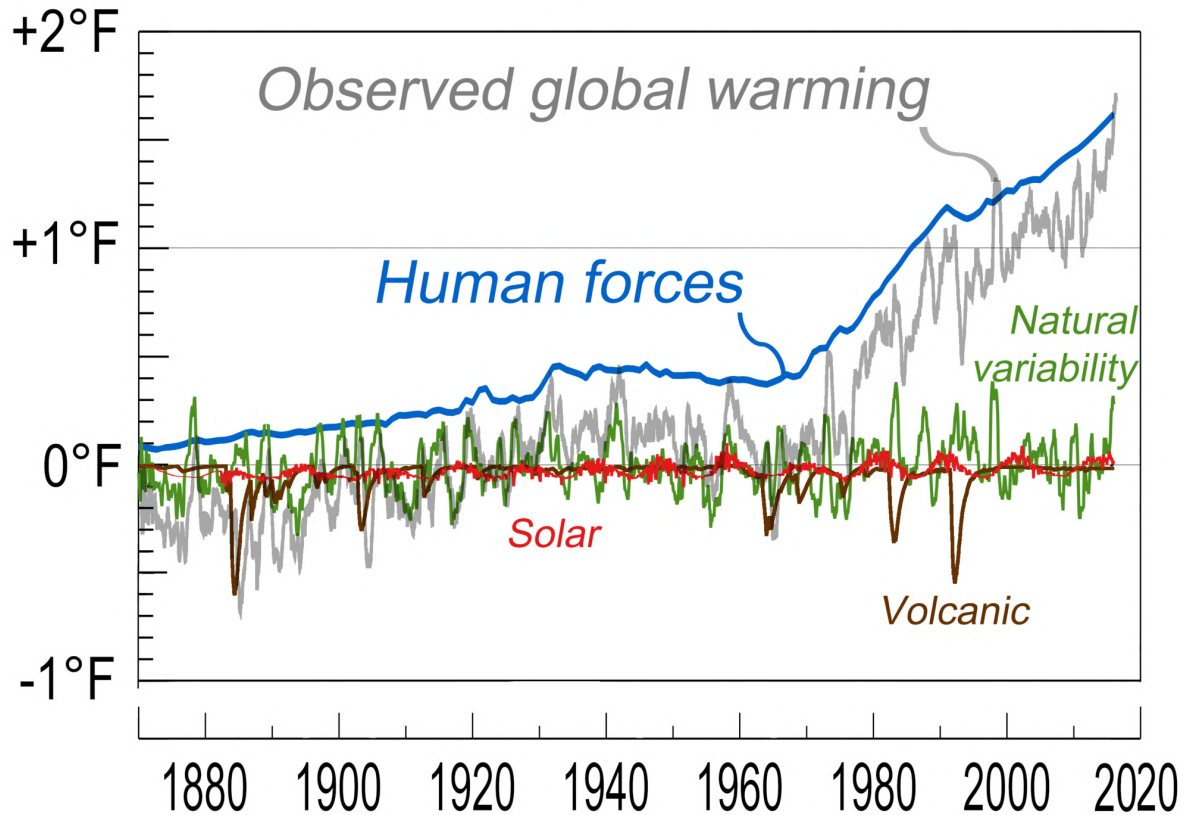


FIGURE 1.1 : Forces humaines et naturelles affectant la température globale. Source : Programme américain de recherche sur le changement global.

de ces changements, il est nécessaire de connaître la dynamique des ressources en eau à l'échelle régionale/locale.

1.1.2 Dynamique des ressources en eau dans la région méditerranéenne

Il est essentiel de comprendre la répartition des ressources en eau et l'effet du changement climatique sur la disponibilité de l'eau à l'avenir, en particulier dans les régions en manque d'eau. La compréhension de l'impact du changement climatique sur la société devient de plus en plus critique, notamment dans la gestion des ressources en eau. Il est primordial de comprendre les différentes modifications environnementales et humaines responsables du changement de la gestion des ressources en eau et de l'hydrologie, comme l'impact du changement climatique sur le bilan hydrique, le changement de l'utilisation et de la couverture des sols (LULC), l'urbanisation et l'irrigation.

La quantité d'eau est limitée dans la région méditerranéenne, et elle dépend principalement de l'écoulement des eaux provenant des régions montagneuses (Viviroli and Weingartner, 2004; de Jong et al., 2009). Les montagnes fournissent une part importante du ruissellement dans les zones méditerranéennes, représentant entre 20 et 90 % du ruissellement total (Viviroli et al., 2007). L'augmentation de la demande en eau crée également une pression sur les zones montagneuses. Les modifications des conditions climatiques à long terme deviennent plus apparentes et ont un impact sur l'écosystème des montagnes méditerranéennes (Giorgi and Lionello, 2008),

et donc la stabilité de l’approvisionnement en eau n’est pas maintenue.

Les changements de LULC sont les principales caractéristiques du paysage méditerranéen et de l’altération de l’environnement. L’utilisation des sols affecte les processus hydrologiques par l’interception, l’évapotranspiration, l’infiltration et le ruissellement (Cosandey et al., 2005; Foley et al., 2005). Les changements de la couverture terrestre ont considérablement affecté les réponses hydrologiques à l’échelle du bassin (Andréassian, 2004). Le changement d’utilisation des terres a été rapide au cours des dernières décennies en raison de l’extension rapide de l’urbanisation et de l’irrigation. Le développement de nouvelles zones d’irrigations et de cultures dans les zones de plaine méditerranéennes nécessite plus d’eau pour la consommation. Les zones nouvellement irriguées couvrent près de 10 millions d’hectares et consomment un grand volume d’eau. Ces zones étant éloignées des vallées fluviales, le transport de l’eau dans ces zones exerce une pression sur les infrastructures complexes (réservoirs et canaux) et surexploite les eaux souterraines.

Une gestion appropriée des ressources en eau peut répondre à l’augmentation de la demande d’approvisionnement en eau à l’échelle régionale. Les stratégies de gestion de l’eau doivent bénéficier d’une surveillance continue de l’état hydrique des sols résultant de la dynamique et des changements du climat et de LULC. De solides connaissances dans différents domaines tels que le changement climatique, les régimes fluviaux, l’hydrologie, etc. permettent de développer un cadre pour la gestion des ressources en eau.

1.1.3 Variabilité spatio-temporelle de l’humidité du sol

Nous définissons ici l’humidité du sol et expliquons comment cette variable est liée au bilan hydrique et énergétique de la surface, et comment sa mesure à différentes échelles spatiales et temporelles est essentielle pour la gestion des ressources en eau et d’autres applications. L’humidité du sol (SM) est la teneur en eau disponible dans la zone non saturée. L’humidité du sol est une variable clé en hydrologie car elle contrôle les échanges d’eau et d’énergie de la surface terrestre vers l’atmosphère et relie les modèles de bilan hydrique et énergétique (voir la Figure 1.2 qui présente les modèles de bilan hydrique et énergétique).

Le modèle de bilan hydrique est exprimé comme suit

$$\frac{dW}{dt} = P - ET - R \quad (1.1)$$

où $\frac{dW}{dt}$ est le changement de SM dans une couche de sol donnée, P est la précipitation, ET est l’évapotranspiration, et R est le ruissellement de surface. L’eau est échangée de la surface à l’atmosphère par l’ET, et les précipitations sont réparties en ET, infiltration et ruissellement dans le modèle de bilan hydrique. L’ET et le ruissellement, ainsi que l’infiltration, sont affectés par la teneur en SM.

Le modèle de bilan énergétique est exprimé comme suit

$$\frac{dQ}{dt} = R_{net} - H - \lambda * LE - G \quad (1.2)$$

où $\frac{dQ}{dt}$ est le changement d’énergie dans une couche de sol donnée, H est le flux de chaleur sensible, LE est l’ET, G est le flux de chaleur dans le sol, et R_{net} est le rayonnement net. L’énergie disponible à la surface du sol ($R_n - G$) est partitionnée en flux de chaleur sensible et flux de chaleur latente. Cette partition dépend de SM dans une zone de transition (Seneviratne et al., 2010).

Les équations 1.1 et 1.2 montrent que les bilans énergétique et hydrique sont couplés par le terme d'ET. L'ET est un processus combiné d'évaporation et de transpiration. L'évaporation se produit lorsque l'eau s'évapore des surfaces du sol, tandis que la transpiration se produit lorsque l'eau s'évapore des feuilles de la végétation. L'ET est une variable essentielle qui contrôle l'échange d'énergie et de masse entre la surface et l'atmosphère. L'ET joue un rôle essentiel dans la prévision des inondations (Bouilloud et al., 2010), des précipitations (Findell et al., 2011), de la sécheresse (Gao et al., 2011) et de l'agriculture (Allen et al., 2005). Par conséquent, la connaissance des mesures quotidiennes de l'ET est essentielle.

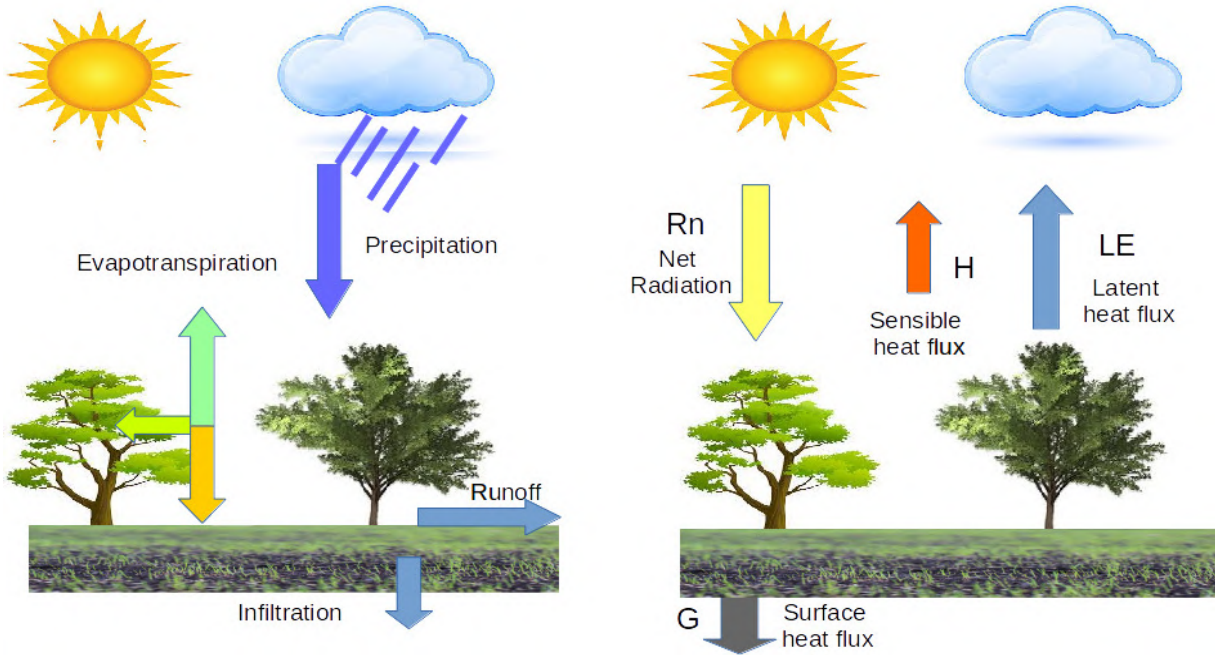


FIGURE 1.2 : Représentation schématique du modèle de (a) bilan hydrique et (b) énergétique.

Un cadre conceptuel/théorique est utilisé pour définir le système d'ET en fonction de SM (voir la Figure 1.3). Les conditions limitées par SM et les conditions limitées par l'énergie sont les deux systèmes d'ET caractérisés par la fraction évaporative (EF), qui est le rapport entre l'ET et l'énergie disponible à la surface (Koster et al., 2004; Seneviratne et al., 2010). Les valeurs de SM sont inférieures à la valeur critique de SM dans des conditions limitées en SM, et l'ET dépend principalement de SM. Inversement, les valeurs de SM sont supérieures à la valeur critique de SM dans des conditions limitées en énergie, et l'ET est indépendante de SM et contrôlée par la demande atmosphérique. La valeur critique de SM ($SM_{critical}$) est définie comme l'humidité entre SM à la capacité au champ (SM_{fc} , au-dessus duquel l'eau n'est pas retenue contre le drainage gravitationnel) et SM au point de flétrissement ($SM_{wilting}$, au-dessus duquel l'eau est retenue trop fermement par la matrice du sol qu'elle n'est pas accessible aux plantes). Le cadre conceptuel décrit trois modes de SM basés sur l'impact de SM sur la variabilité de l'ET : humide ($SM > SM_{critical}$), sec ($SM < SM_{wilting}$), et zone de transition ($SM_{wilting} < SM < SM_{critical}$). Par exemple, dans les modèles de surface terrestre de première génération, l'ET était estimée en fonction de la SM simulée par le modèle à réservoirs.

L'importance de SM dans les processus écohydrologiques et de surface terrestre est reconnue par diverses recherches (Robinson et al., 2008; Jung et al., 2010; Seneviratne et al., 2010; Evaristo

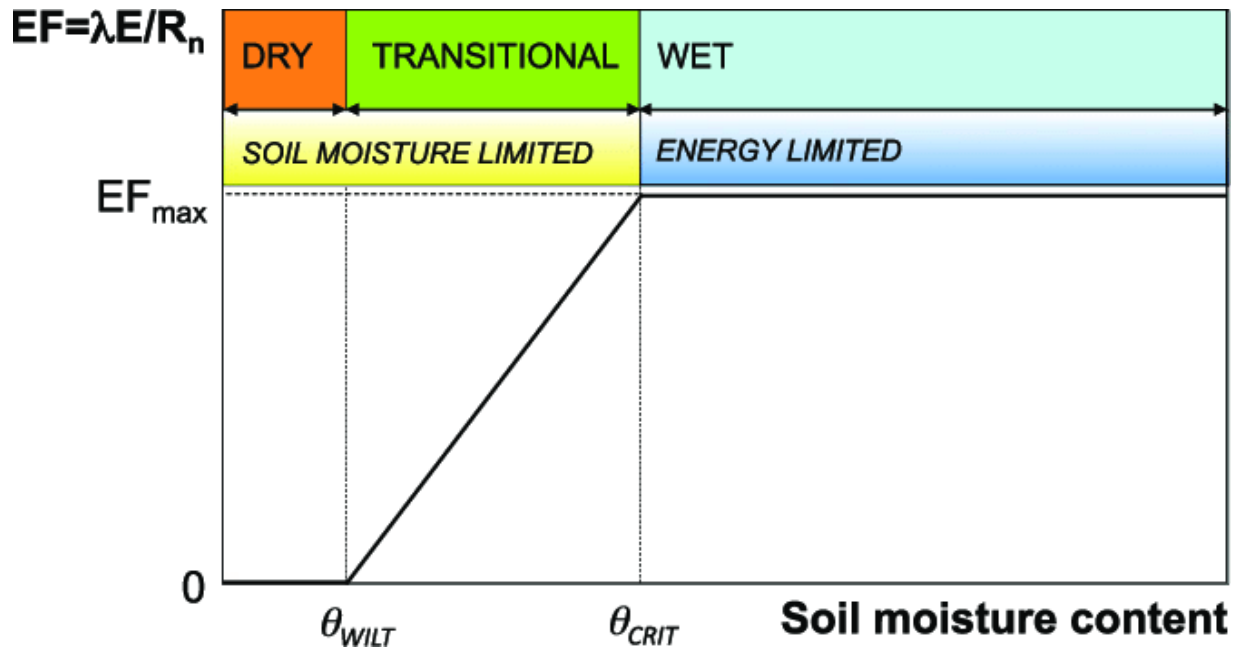


FIGURE 1.3 : Structure conceptuelle de la dépendance de l'ET à SM.. Source : (Seneviratne et al., 2010)

et al., 2015). SM varie fortement sur une très vaste plage d'échelles spatio-temporelles, avec des échelles spatiales allant de quelques centimètres à des milliers de kilomètres et des échelles temporelles allant de quelques minutes à des années. De nombreuses études ont examiné la variabilité spatiale de SM à différentes échelles telles que l'échelle de la parcelle (Nielsen et al., 1973; Bell et al., 1980), l'échelle du bassin versant (Nielsen et al., 1973; Western et al., 2004), l'échelle régionale (Romshoo, 2004; Zhao et al., 2013) et l'échelle continentale (Entin et al., 2000; Li and Rodell, 2013). Western et al. (2002) ont examiné plusieurs stratégies de mise à l'échelle pour mettre en relation la variabilité spatiale de SM à travers les échelles spatiales intégrées. Vanderlinden et al. (2012) ont analysé la variabilité temporelle de la SM à différentes échelles emboîtées. Ils ont exploré plusieurs éléments interconnectés tels que le sol, la végétation, la topographie et le climat qui jouent un rôle essentiel dans la détermination de la variabilité temporelle de SM.

Les variabilités de SM à travers l'espace et le temps reflètent un effet intégré de divers facteurs environnementaux (Famiglietti et al., 2008; Brocca et al., 2010; Ochsner et al., 2013). En raison de l'interaction complexe de SM avec le milieu environnant, avec une variabilité spatio-temporelle importante, il est difficile de prédire l'évolution temporelle du SM à n'importe quelle échelle spatiale, même avec la connaissance du processus fondamental (Seneviratne et al., 2010; Vereecken et al., 2014). Il est donc essentiel de déterminer les facteurs qui contrôlent la variabilité spatio-temporelle de SM à diverses échelles. Les facteurs qui affectent la variabilité spatio-temporelle de SM à l'échelle de la parcelle agricole et de la région sont notamment les caractéristiques et la profondeur du sol, la dynamique de la végétation et les aspects topographiques (Mohanty and Skaggs, 2001; Teuling and Troch, 2005; Vereecken et al., 2014; Wang, 2014; Wang et al., 2015)

Différentes méthodes quantitatives ont permis d'analyser la variabilité spatio-temporelle et les propriétés des sols à travers une gamme diverse d'échelles. Ces méthodes sont la géostatistique, l'analyse spectrale et par ondelettes, l'analyse multifractale, l'analyse de l'espace d'état et l'analyse par ensembles flous (Si, 2008; Molero et al., 2018). De manière déterministe, diverses tech-

niques sont utilisées pour estimer la variabilité spatiale et temporelle de SM à l'aide de mesures in situ, de modèles de surface terrestre ou hydrologiques, et de satellites de télédétection. Ces techniques sont décrites en détail dans la section suivante.

1.2 Suivi de l'humidité du sol

Trois grandes catégories de méthodes peuvent être utilisées pour estimer SM : les mesures in situ, la modélisation des surfaces et la télédétection. Si les mesures in situ ont été et sont toujours utilisées comme référence pour évaluer les autres méthodes, elles sont limitées par leur représentativité spatiale (Western et al., 2002). Compte tenu de la physique, des données de forçage et des paramètres de calibration des transferts d'eau du sol à l'interface sol-végétation-atmosphère, les modèles de surface terrestre peuvent simuler SM de façon continue dans le temps et l'espace. Malheureusement, la détermination précise des données de forçage et des paramètres du modèle est complexe, et tous les modèles ont tendance à diverger de la réalité après un temps de fonctionnement plus ou moins long. Les techniques de télédétection ont l'atout unique de fournir des données de SM sur une gamme de résolutions spatiales. Le fait est cependant qu'elles sont soumises à deux limitations principales : une faible fréquence d'observations (inférieure à 1 par jour) et l'incertitude des données de télédétection associée à l'impact des facteurs perturbateurs spécifiques à la longueur d'onde utilisée. Comme chaque méthode présente des avantages et des inconvénients, la plupart des études combinent les informations de SM provenant des mesures in situ, des modèles et des données de télédétection.

1.2.1 Mesure in situ de l'humidité du sol

La mesure de SM est classée en méthodes directes et indirectes (Yoder et al., 1998). D'une part, la méthode directe est utilisée pour mesurer la teneur en eau gravimétrique du sol, à partir de laquelle la SM volumétrique est dérivée connaissant la densité de l'échantillon de sol. D'autre part, la méthode indirecte estime la teneur en eau volumétrique du sol en calibrant une fonction basée sur d'autres variables mesurables qui varient avec la teneur en eau du sol (Evelt and Parkin, 2005). Les différentes techniques de mesure directe et indirecte du sol pour le suivi de SM sont présentées ci-dessous.

Méthode gravimétrique

La méthode gravimétrique est une méthode ancienne et classique pour déterminer la teneur en eau du sol. La méthode à l'étuve est la plus utilisée pour la mesure de SM (Schmugge et al., 1980). Elle est notamment utilisée comme référence standard pour la calibration des autres méthodes de SM (Walker et al., 2004; Merlin et al., 2007). L'échantillon de sol humide est séché à 105°C jusqu'à l'obtention d'un poids constant de l'échantillon de sol. La méthode gravimétrique mesure la SM comme le rapport entre le poids de l'eau présente dans le sol et le poids de l'échantillon de sol. Le poids de la teneur en eau est dérivé de la différence entre le poids humide de l'échantillon de sol et le poids séché au four. La méthode gravimétrique donne la valeur de SM en pourcentage du poids sec du sol. Pour calculer la teneur en eau volumétrique, le volume d'eau gravimétrique est multiplié par la densité apparente du sol.

Les avantages de cette technique sont 1) elle est robuste, facile et précise, 2) l'acquisition d'échantillons est peu coûteuse, 3) SM est facilement calculée. Cependant, les inconvénients de cette

technique sont : 1) l'estimation de la SM est difficile dans les sols hétérogènes, 2) cette méthode est destructive et difficile à utiliser sur une longue période 3) elle demande beaucoup de travail et de temps.

Technique diélectrique

Il s'agit de la technique la plus courante en raison de sa capacité à assurer un suivi localisé de SM de manière continue dans le temps pour un coût relativement faible. Elle estime la SM en mesurant la constante diélectrique du sol. Comme la constante diélectrique de l'eau liquide est plus grande que celle du sol, la permittivité totale du sol est régie par l'eau liquide. La réflectométrie dans le domaine temporel (TDR) et la réflectométrie dans le domaine fréquentiel (FDR) sont les principales techniques qui utilisent la propriété diélectrique du sol pour mesurer SM.

La TDR est largement utilisée pour mesurer SM (Rao and Singh, 2011). Elle mesure la vitesse de propagation de l'onde électromagnétique dans le sol et la constante diélectrique comme la quantité d'énergie électrique dans la substance. La teneur en eau du sol est estimée en calibrant la fonction reliant SM à la constante diélectrique du sol mesurée. Les avantages de la TDR sont les suivants : 1) elle n'est pas destructive, elle demande moins de travail que la méthode gravimétrique et elle est facile à installer ; 2) aucun étalonnage spécifique n'est nécessaire (Topp and Davis, 1985) ; 3) elle fournit un résultat précis à haute résolution temporelle (Chandler et al., 2004) ; 4) cette technique est indépendante de la texture, de la température et de la teneur en eau du sol ; 5) cette technique peut être automatisée car elle ne nécessite pas d'entretien quotidien et peut être régulée automatiquement. Les inconvénients de cette technique sont 1) un coût initial élevé, 2) une applicabilité limitée dans les sols hautement salins (Ferrara and Flore, 2003), 3) une calibration spécifique est nécessaire pour l'eau liée dans les sols organiques, les sols volcaniques, etc.

La FDR estime la teneur en SM à partir de la fréquence du signal qui varie en fonction de la constante diélectrique du sol. La FDR utilise un condensateur et le sol comme matériau diélectrique pour mesurer la teneur en SM. Le condensateur est connecté à l'oscillateur pour former un circuit électrique. La variation de la SM est estimée par la différence de fréquence du circuit de fonctionnement. La fréquence de l'oscillateur est limitée dans une plage spécifique pour déterminer la fréquence de résonance (Muñoz-Carpena, 2004). Les avantages de la FDR sont les suivants : 1) elle donne des résultats précis mais nécessite un étalonnage spécifique du site, 2) elle est applicable dans des conditions de sols hautement salins, 3) elle est flexible dans la conception des sondes. Les inconvénients de la FDR sont les suivants : 1) une plus grande sensibilité à la température, à la densité apparente, aux vides d'air et à la teneur en argile limite l'utilisation de cette méthode par rapport à la TDR (Erlingsson et al., 2009) ; 2) une sphère d'influence restreinte ; 3) pour des mesures fiables, il est très important d'assurer un bon contact entre le capteur et le sol.

Technique nucléaire

La technique de diffusion des neutrons est un moyen indirect pour déterminer la SM. Elle estime SM en mesurant la densité des neutrons thermiques ou lents. La source radioactive émet des neutrons rapides à haute énergie dans le sol, et ils ralentissent lorsqu'ils entrent en collision avec la même masse qu'un neutron (c'est-à-dire un proton H+) et construisent un nuage de neutrons thermalisés. La densité des neutrons thermalisés autour de la sonde est proportionnelle à la fraction volumique de l'eau présente dans le sol car l'eau est la principale source d'hydrogène dans le sol. Les sondes neutroniques sont de deux types : les sondes de profondeur et de surface. La

sonde de profondeur est utilisée pour mesurer la SM sous le sol à une profondeur donnée, tandis que la sonde de surface mesure la teneur en eau du sol dans la couche la plus superficielle du sol (Schmugge et al., 1980). Les avantages de la technique nucléaire sont les suivants : 1) elle est plus robuste ; 2) elle peut détecter les changements rapides et temporels dans l'estimation de la SM ; 3) elle mesure un grand volume de sol, et mesure également le profil de la SM à différentes profondeurs ; 4) elle n'est pas affectée par la salinité du sol ou les lames d'air. Les inconvénients sont 1) le coût initial de l'instrumentation est élevé, 2) un faible degré de résolution spatiale 3) l'opérateur doit veiller à minimiser les risques pour la santé.

Une autre technique basée sur le nucléaire est la technique d'atténuation des rayons gamma. Il s'agit d'une technique radioactive qui mesure la SM à une profondeur de 25 cm ou moins. Cette technique part du principe que la diffusion et l'absorption des rayons gamma sont liées à la densité de la matière se trouvant sur leur trajectoire. La densité spécifique du sol reste constante alors que SM change. Les avantages de la technique d'atténuation des rayons gamma sont 1) de fournir des mesures temporelles de la SM à différentes profondeurs, 2) la mesure est non-destructive, et 3) les données peuvent être obtenues sur de petites distances et horizontalement. Les inconvénients sont 1) la technique est coûteuse et difficile à utiliser, 2) elle nécessite une attention extrême pour réduire le risque de danger pour la santé, et 3) elle est impactée par la variation significative de la densité apparente.

Tensiométrie

Un tensiomètre mesure la tension ou l'énergie avec laquelle le sol retient l'eau. La SM peut être dérivée de la tension de l'eau du sol, étant donné les propriétés hydrauliques du sol. Le tensiomètre se compose d'un tube cylindrique rempli d'eau avec des embouts en céramique à l'extrémité et une jauge à vide au sommet. Le tensiomètre est installé dans le sol à la profondeur à laquelle la mesure de la SM est requise. À cette profondeur, l'eau contenue dans le tensiomètre est en équilibre avec le sol environnant. Lorsque le sol sèche, l'eau est extraite par la pointe et crée une tension sur les tubes à vide. Lorsque le sol est humide, la tension est réduite, et elle permet à l'eau de pénétrer dans les tubes à vide à travers les tubes cylindriques, et le vide est réduit. La pression générée par le tensiomètre est équivalente à la tension utilisée par la plante pour extraire l'eau du sol.

Les avantages de la technique du tensiomètre sont 1) il est facile à installer et rentable, 2) les informations sur la distribution de la SM sont obtenues dans des conditions de sol saturé et non saturé, 3) l'équipement peut être facilement placé dans le sol et fournit une mesure continue du sol avec une perturbation minimale et 4) l'utilisation d'une solution aqueuse d'éthylène glycol rend le tensiomètre approprié pour être installé dans les régions froides. Les inconvénients de cette technique sont les suivants : 1) elle ne convient pas aux sols secs ; 2) elle nécessite une maintenance importante ; 3) les informations relatives à la SM ne peuvent être obtenues que dans une plage de tension d'eau comprise entre 0 et 850 hPa ; 4) la relation entre SM et la tension d'eau du sol mesurée est non linéaire.

1.2.2 Modèles dynamiques

Les modèles de surface décrivent les interactions entre la surface terrestre et l'atmosphère, c'est-à-dire les échanges d'énergie et d'eau. SM est simulée dans le temps et l'espace à l'aide d'un modèle dynamique qui intègre la physique des transferts d'eau du sol. La modélisation de surface fournit

une condition limite pour le modèle atmosphérique et joue un rôle essentiel dans le système de prévision numérique du temps et de projection du changement climatique. Il joue également un rôle essentiel dans la représentation des processus hydrologiques en modélisant l'interaction avec la surface terrestre et l'atmosphère.

Les modèles de surface peuvent différer dans la représentation de la variabilité spatiale de SM, de la végétation, de la topographie, du ruissellement de surface, du stockage de l'eau, etc. Ils sont généralement classés en trois générations (Sellers et al., 1997; Pitman, 2003). La première génération de modèles de surface terrestre fournit une représentation directe qui considère des interactions simples avec la surface terrestre, la végétation et l'atmosphère. Deux exemples de modèles de première génération sont donnés ci-dessous.

Le modèle Bucket (Manabe, 1969) est le premier modèle simple de surface utilisé pour modéliser les flux hydrologiques à l'échelle globale. Dans ce modèle, la couche de sol a une capacité en eau fixe, une profondeur et des propriétés de sol constants. Le principe de base de ce modèle est que le réservoir du sol est rempli par les précipitations, et qu'il se vide avec l'évaporation et le ruissellement.

Le modèle Force-Restore (Deardorff, 1978) basé sur la méthode "force restore" (Bhumralkar, 1975) a été développé à partir d'une équation efficace dépendant du temps pour estimer le SM. Le modèle "force et restore" implique généralement deux équations pronostiques correspondant à une couche de surface du sol et la zone racinaire, représentant respectivement l'évolution de SM en surface et en zone racinaire. Il s'agit du modèle de prévision de la SM le plus populaire en raison de son efficacité de calcul. Il utilise de plus un nombre minimum de variables pronostiques et capture les processus physiques les plus importants.

Les modèles de surface de deuxième et troisième génération sont développés en combinant des modèles plus spécifiques afin de représenter de manière plus réaliste la relation complexe entre la surface terrestre et l'atmosphère à différentes échelles. Ces modèles plus complexes peuvent fournir des informations sur SM et d'autres variables de la surface terrestre et de l'atmosphère telles que la température de surface, les flux de surface, etc.

Un exemple de modèle de surface de nouvelle génération est donné par **Surface Externalisée (SURFEX)**, qui est le modèle de surface développé par Météo France. Le modèle SURFEX assure un couplage entre la surface terrestre et l'atmosphère. Tout d'abord, chaque maille de la surface reçoit la température de l'air, la pression, l'humidité spécifique, les précipitations totales, le rayonnement des ondes longues et courtes, les espèces chimiques et la concentration des aérosols pendant un horodatage du modèle. Ensuite, SURFEX calcule le flux moyen de la quantité de mouvement, de la chaleur sensible, de la chaleur latente, des espèces chimiques et des aérosols et renvoie ces quantités à l'atmosphère en y ajoutant la température radiative de la surface, l'albédo diffus et l'émissivité de la surface. Dans SURFEX, chaque maille du modèle est représentée par une couverture de surface différente : sol et végétation, zones urbaines et masses d'eau (mer ou océan ou lac). Ces couvertures de surface sont obtenues à partir de la base de données mondiale ECOCLIMAP qui combine des cartes de couverture des sols et des informations satellitaires. SURFEX fait la moyenne de tous les flux calculés sur le sol et la végétation, les zones urbaines, et l'eau (mer ou lac ou océan) par leurs fractions respectives. Toutes ces informations sont utilisées comme condition aux limites basses pour le rayonnement atmosphérique et le flux turbulent.

Dans SURFACE, un modèle différent représente chaque type de surface. Le modèle SURFEX

est en effet constitué de modèles physiques plus spécifiques tels que l'interaction entre le sol, la biosphère et l'atmosphère (ISBA) pour les surfaces terrestres, Town Energy Balance (TEB) pour les zones urbaines, et Flakes pour les lacs et les océans. ISBA comprend lui-même plusieurs modèles qui transfèrent l'énergie et l'eau dans le sol, la végétation, l'hydrologie de surface et la neige. Le modèle ISBA est construit pour limiter le niveau de complexité en réduisant le nombre de paramètres tout en représentant la physique de l'interaction terre-atmosphère. ISBA est un modèle simple de surface terrestre qui peut utiliser la méthode de "restauration de force" (Dardorff, 1977) pour calculer la température de surface et la température moyenne du sol au cours du temps ainsi que le bilan hydrique du sol (ISBA-2L, (Noilhan and Planton, 1989)). Dans ce modèle, la couche supérieure agit comme un réservoir pour l'évaporation de la surface du sol, et la seule couche de sol de subsurface est utilisée pour modéliser le contenu en eau moyen de la racine et de la couche de la zone sous-racinaire. La couche standard ISBA-2L peut également définir une couche d'acheminement et inclure une troisième couche qui distingue les bilans hydriques du sol de la surface et de la zone sous-racinaire (ISBA-3L, (Boone et al., 1999)). ISBA a encore été modifié pour tenir compte de la concentration de dioxyde de carbone atmosphérique sur l'ouverture des stomates (ISBA-Ags, (Calvet et al., 1998)). Le modèle standard ISBA a été mis à jour pour mieux représenter le ruissellement en surface pour les applications hydrologiques (Habets et al., 1999).

La modélisation dynamique utilisée pour estimer SM fait donc face à un compromis en termes de précision du SM entre la physique implémentée dans les équations du modèle, le nombre de couches représentées, et la disponibilité des paramètres et les données de forçage nécessaires en entrée du modèle. En général, un modèle simple permet d'échantillonner l'ensemble de ses paramètres et d'en déduire une calibration optimale. Cependant, il ne peut pas remplacer les modèles sophistiqués qui tiennent compte des relations complexes dans le sol et la végétation pour produire des résultats plus complets dans différentes conditions pédo-hydro-climatiques. Le principal avantage des modèles simples est qu'ils nécessitent moins de paramètres d'entrée, ce qui améliore leurs capacités de calibration et réduit par conséquent l'incertitude associée aux erreurs de calibration sur les données de sortie.

1.2.3 Informations satellitaires

La SM est variable dans l'espace, et les facteurs qui affectent la variabilité de la SM sont notamment les types de sol, la couverture végétale, les conditions climatiques et la topographie. Les mesures in situ de SM sont limitées à l'échelle du point à un endroit particulier. De telles mesures ponctuelles ne peuvent pas couvrir une si grande variabilité de SM (Srivastava et al., 2013). L'extrapolation de ces mesures ponctuelles par des techniques géostatistiques (Qiu et al., 2001) est coûteuse, longue et complexe, en particulier sur des surfaces terrestres hétérogènes (Qin et al., 2013; Byun et al., 2014). La mesure in situ n'est pas pratique pour mesurer la variabilité spatiale et temporelle de SM à l'échelle régionale et mondiale.

Le problème est résolu en développant des techniques de télédétection qui peuvent estimer SM de l'échelle régionale à l'échelle globale. L'observation par satellite à partir de capteurs micro-ondes actifs et passifs est la plus appropriée pour estimer SM (Schmugge et al., 2002; Mohanty et al., 2017). Les capteurs micro-ondes ne peuvent pas estimer directement SM, mais il existe une relation directe entre la constante diélectrique du sol et la teneur en eau. Cette section décrit les techniques de télédétection basées sur les capteurs micro-ondes passifs, micro-ondes actifs optiques/thermiques, permettant d'estimer SM sur de grandes étendues.

Capteurs micro-ondes passifs

La terre reçoit en permanence les rayonnements électromagnétiques du soleil. Une partie de ce rayonnement est absorbée/réfléchi ou transmise par la surface de la terre. L'énergie absorbée est transformée en énergie thermique et augmente la température de la surface jusqu'à ce qu'elle atteigne l'équilibre thermodynamique. Dans cet état, tous les milieux rayonnent de l'énergie pour maintenir l'équilibre énergétique. Les capteurs micro-ondes passifs sont très sensibles et détectent l'énergie émise ou rayonnée par la surface de la terre à la longueur d'onde de 1 à 30 cm, exprimée en température de brillance. L'énergie émise absorbée dans les micro-ondes comprend la contribution de l'atmosphère, de la surface terrestre et du rayonnement réfléchi par le ciel. Les micro-ondes passives peuvent fournir des informations sur SM car il existe une différence significative entre la constante diélectrique de l'eau (80) et celle du sol sec (4). La texture du sol et la variabilité de la température du sol et de la végétation affectent également l'extraction du spectre micro-onde. L'avantage d'un radiomètre micro-ondes est que la couverture nuageuse ne limite pas ses capacités d'observation, qui dépendent peu de l'heure d'acquisition. Lorsque la végétation n'est pas présente, SM est le paramètre dominant qui affecte le signal micro-onde reçu (Njoku and Entekhabi, 1996). Les micro-ondes passives sont adéquates pour assurer le suivi de SM à l'échelle globale (Owen et al., 1998). En général, la technique de récupération à deux paramètres a été utilisée pour inverser simultanément SM et l'épaisseur optique de la végétation. Cette technique est bien adaptée aux observations multi-fréquences à double polarisation ou multi-angulaires en bande L (Peischl et al., 2014). Divers satellites de télédétection à micro-ondes passives ont été lancés au cours des 35 dernières années (Chen et al., 2012). Certains des capteurs micro-ondes passifs sont présentés dans la Figure 1.4

Diverses bandes micro-ondes telles que L, C, X et K sont utilisées par les radiomètres. Actuellement, la bande L est utilisée pour estimer SM car les données aux fréquences de la bande L sont sensibles à SM y compris à travers la végétation jusqu'à 5 kg/m^2 et peuvent fournir une estimation de SM dans toutes les conditions météorologiques. En revanche, les bandes de fréquences plus élevées (C, X et K) sont davantage sensibles à la végétation. Les observations à ces fréquences sont donc plus atténuées par l'effet de la végétation et leur applicabilité est donc limitée aux zones de végétation modérée ($< 3 \text{ kg/m}^2$). La fréquence de la bande L donne une information sur la couche de quelques centimètres de la surface du sol (5 cm) et est moins affectée par l'interférence des fréquences radio (RFI) que les fréquences supérieures. Notez que les capteurs fonctionnant à des fréquences plus basses (bande P) pourraient également être utilisés pour obtenir des informations plus profondément dans le sol. Cependant, la taille de l'antenne (qui augmente avec la longueur d'onde) et la présence importante de RFI rendent difficile la construction d'un satellite de télédétection utilisant des micro-ondes passives en bande P.

Actuellement, deux missions en bande L, Soil Moisture Ocean Salinity (SMOS, (Kerr et al., 2010)) et Soil Moisture Active and Passive (SMAP, (Entekhabi et al., 2010)), sont utilisées pour fournir la SM à une échelle globale et sont largement utilisées dans cette thèse.

SMOS est le premier satellite micro-ondes en bande L lancé par l'Agence spatiale européenne le 2 novembre 2009. SMOS fournit des données de SM et de salinité des océans à l'aide d'un radiomètre à une fréquence de 1,4 GHz, utilisant un instrument MIRAS (Microwave Imaging Radiometer with Aperture Synthesis). Il fournit des images de SM à une résolution spatiale de 35 km avec une résolution temporelle de 1-3 jours. SMOS a une orbite quasi-circulaire héliosynchrone à une altitude de 758 km avec un passage ascendant (18 h) et descendant (6 h). SMOS

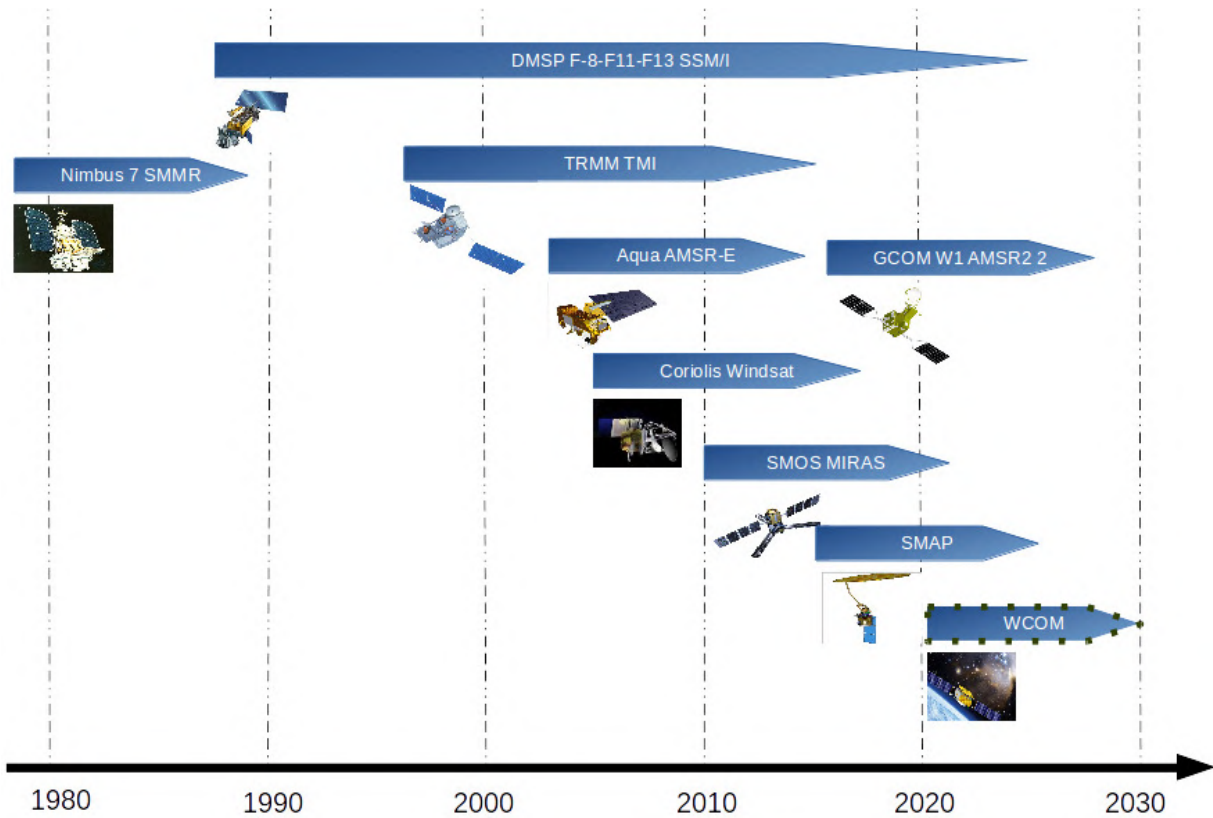


FIGURE 1.4 : Liste des capteurs micro-ondes passifs passés et actuels jusqu'à aujourd'hui

est un interféromètre 2-D, qui fournit la température de brillance en polarisation horizontale et verticale à une gamme d'angles d'incidence (allant de 0 à 55 degrés). L'algorithme SMOS utilise des angles d'incidence multiples à double polarisation pour séparer les contributions du sol et de la végétation de l'émissivité de la surface. SMOS fournit des produits SM de niveau 2 et de niveau 3. En plus du produit SM, la mission SMOS fournit des données auxiliaires telles que la température de surface, le paramètre de rugosité et l'épaisseur optique au sommet de l'atmosphère. Elle fournit à partir de la température de brillance mesurée un produit SM global avec une précision spécifiée de $0,04 \text{ m}^3/\text{m}^3$ (Kerr et al., 2001). L'expérience de validation du produit SMOS de niveau 2 montre des résultats satisfaisants dans l'estimation de SM sur différents écosystèmes et différentes échelles spatiales. Par exemple, des études de validation ont été réalisées dans diverses régions telles que l'Amérique du Sud (Escorihuela et al., 2012), l'Europe (Lacava et al., 2012; Srivastava et al., 2013; Petropoulos et al., 2014), l'Australie (Panciera et al., 2011; Peischl et al., 2014) et les États-Unis (Jackson et al., 2011; Al Bitar et al., 2012) allant de l'échelle continentale (Dente et al., 2012; Zhao et al., 2014) à l'échelle du bassin versant (Bircher et al., 2012; Srivastava et al., 2013).

SMAP est un satellite en bande L lancé par la NASA le 31 janvier 2015. SMAP est conçu pour utiliser des capteurs micro-ondes actifs et passifs en intégrant un radar en bande L (polarisations VV, HH et HV) et un radiomètre en bande L (polarisations V, H et 3e et 4e paramètres de Stokes). Mais en raison de la défaillance du radar, la mission radiométrique SMAP fournit actuellement des données SM à une résolution spatiale de 36 km sur un cycle de revisite de 3 jours à l'échelle mondiale. Le satellite SMAP a une orbite polaire héliosynchrone d'une altitude de 658 km avec un passage descendant/ascendant à 6 heures du matin/après midi, heure locale. La

mission SMAP fournit des produits SM avec une précision spécifiée meilleure que $0,04 \text{ m}^3/\text{m}^3$. Divers résultats de validation montrent des résultats satisfaisants pour différents produits SM de SMAP (Vreugdenhil et al., 2013; Colliander et al., 2017a; Cai et al., 2017; Ma et al., 2017; Bhuiyan et al., 2018; Colliander et al., 2019). La mission SMAP fournit également un produit SM sur une grille de résolution de 9 km (Das et al., 2013) en interpolant les données issus du radiomètre en bande L à l'aide de la méthode Backus-Gilbert (Backus and Gilbert, 1970). La mission SMAP combine également le radiomètre SMAP avec le radar Sentinel-1 pour fournir SM à 9 km et 3 km (Das et al., 2018), mais cette approche est limitée par la nécessité d'avoir des temps de passage quasi-simultanés de SMAP et Sentinel-1.

Capteurs micro-ondes actifs

Les capteurs micro-ondes actifs ou radars utilisent leur source de rayonnement pour illuminer les objets ciblés et calculer le coefficient de rétrodiffusion, c'est-à-dire la différence entre le rayonnement électromagnétique émis et reçu. Les radars sont divisés en instruments d'imagerie (par exemple, les radars à ouverture synthétique (SAR)) et en instruments non imageurs, notamment les diffusiomètres et les altimètres. Le coefficient de rétrodiffusion radar est lié à SM en raison de la différence significative entre la constante diélectrique du sol sec et celle de l'eau, mais la précision du SM récupéré est affectée par la rugosité du sol et la biomasse végétale (Moran et al., 2004). En raison du lien complexe entre le coefficient de rétrodiffusion et la réflectivité de la surface, la structure complexe de la surface du sol et de la végétation a un impact significatif sur les mesures, et il est difficile de développer une procédure simple pour éliminer ces effets. En tenant compte de la configuration du capteur et des paramètres de surface, divers modèles de rétrodiffusion ont été développés au cours des 30 dernières années (une liste de capteurs hyperfréquences actifs est présentée à la Figure 1.5), classés en trois groupes : modèles physiques ou théoriques, empiriques et semi-empiriques.

Les modèles physiques ou théoriques calculent le coefficient de rétrodiffusion radar en fonction de la constante diélectrique et de la rugosité du sol en calculant l'interaction entre le rayonnement micro-ondes et le sol. Dans ces modèles, SM est estimée par l'inversion mathématique du coefficient de rétrodiffusion. L'avantage de l'approche théorique est qu'elle est indépendante des conditions locales du site et des caractéristiques typiques du capteur. Elle fournit une valeur de SM avec une grande précision (Notarnicola and Solorza, 2014) et peut être mise en œuvre dans des conditions de rugosité spécifiques. L'inconvénient est qu'elle nécessite de nombreux paramètres d'entrée qui rendent le paramétrage difficile et complexe (Moran et al., 2004). Ce type de modèle présente également des difficultés pour décrire la rugosité du sol (Zribi and Dechambre, 2003).

Le modèle physique le plus utilisé de nos jours est le modèle d'équation intégrale (IEM). L'IEM (Fung et al., 1992) est un modèle de transfert radiatif basé sur la physique qui calcule le coefficient de rétrodiffusion du sol sec avec des propriétés radar données telles que la longueur d'onde, la polarisation, les caractéristiques de surface telles que la constante diélectrique, la rugosité de surface et l'angle d'incidence local. Ce modèle est l'un des modèles d'inversion les plus utilisés pour estimer la SM et la rugosité de surface (Shi et al., 1997; Satalino et al., 2002; Zribi and Dechambre, 2003). Néanmoins, l'IEM montre des difficultés sur les surfaces naturelles en raison de la sensibilité des modèles aux paramètres de rugosité de surface et du problème associé à leurs mesures correctes (Zribi and Dechambre, 2003). Ce modèle néglige la diffusion à partir du volume de sol de subsurface qui peut être importante pour les conditions de sol sec (Schanda, 1987). Par conséquent, ces modèles nécessitent une connaissance très détaillée de la rugosité de

la surface.

Des modèles empiriques sont également utilisés pour dériver la relation directe entre le coefficient de rétrodiffusion radar et le SM. Les études empiriques sont basées sur des résultats expérimentaux associés aux conditions de surface des sites expérimentaux et aux paramètres radar. De nombreuses études empiriques montrent une relation linéaire entre le coefficient de rétrodiffusion radar et le SM pour des sites spécifiques où le SM varie de 0,10 à 0,35 m^3/m^3 en supposant que la rugosité ne change pas entre les mesures radar successives (Zribi et al., 2005). Ce modèle relie directement la rétrodiffusion radar à la SM. Cependant, cette approche empirique nécessite des ensembles de données et des conditions de mise en œuvre spécifiques, par exemple, l'angle d'incidence, la fréquence d'observation et la rugosité de la surface. Une autre limitation est que cette approche nécessite des mesures de SM in situ de haute qualité pour effectuer l'étape de calibration, ce qui est coûteux et difficile. En outre, ces modèles empiriques peuvent ne pas être valables en dehors des conditions pour lesquelles ils ont été calibrés.

Intermédiaires entre les approches théoriques et totalement empiriques, les modèles semi-empiriques combinent le modèle numérique de transfert radiatif (modèle physique) et des ensembles de données analysées ou expérimentales (modèle empirique) pour fournir une relation simple entre les propriétés de surface et la physique du mécanisme de rétrodiffusion. Ce type de modèle offre généralement un bon compromis entre la complexité du modèle théorique et la simplicité du modèle empirique. L'avantage de ce type de modèle est qu'il est indépendant du site et peut être appliqué lorsque peu ou pas d'informations sur la rugosité du sol sont disponibles (Baghdadi et al., 2008). Le modèle semi-empirique le plus utilisé est le modèle de Oh (Oh et al., 1992) et le modèle de nuage d'eau (Attema and Ulaby, 1978).

n° Le modèle de nuage d'eau est un modèle de diffusion de volume sur les zones végétalisées. Ce modèle a été développé en supposant que le "nuage" de la canopée est constitué de gouttelettes d'eau identiques distribuées de manière aléatoire dans la canopée. En raison de sa simplicité, il est le plus utilisé pour l'estimation de SM, en particulier sur les zones agricoles (Bindlish and Barros, 2001; Dabrowska-Zielinska et al., 2007; Baghdadi et al., 2017; Li and Wang, 2018). Ce modèle exprime les caractéristiques complexes de diffusion dans les zones végétalisées et fournit des informations sur l'atténuation à partir de la couche de végétation.

Capteurs optiques/thermiques

capteurs visibles/à ondes courtes dépendent du soleil comme source d'éclairage et utilisent le visible, le proche infrarouge et l'infrarouge courtes longueurs d'onde pour obtenir des images de la surface de la terre. Différents objets observent et réfléchissent différemment à différentes longueurs d'onde. Leur signature spectrale permet de différencier les objets réfléchis dans l'image télédéteectée. Divers capteurs optiques/thermiques à différentes résolutions ont été lancés depuis les années 1970, comme le montre la Figure 1.6.

La télédétection optique est classée en fonction des bandes spectrales utilisées :

1. Le capteur panchromatique utilise une seule bande pour enregistrer le rayonnement sur une plus grande longueur d'onde, par exemple SPOT HRV-Pan, Ikonos Pan.
2. Un capteur multispectral est un détecteur multicanal qui utilise quelques bandes spectrales et enregistre le rayonnement électromagnétique dans la longueur d'onde étroite, par exemple, Landsat MSS, Landsat TM, SPOT HRV-XS, Ikonos MS.
3. Les instruments supraspectraux utilisent plus de dix bandes spectrales et enregistrent le rayon-

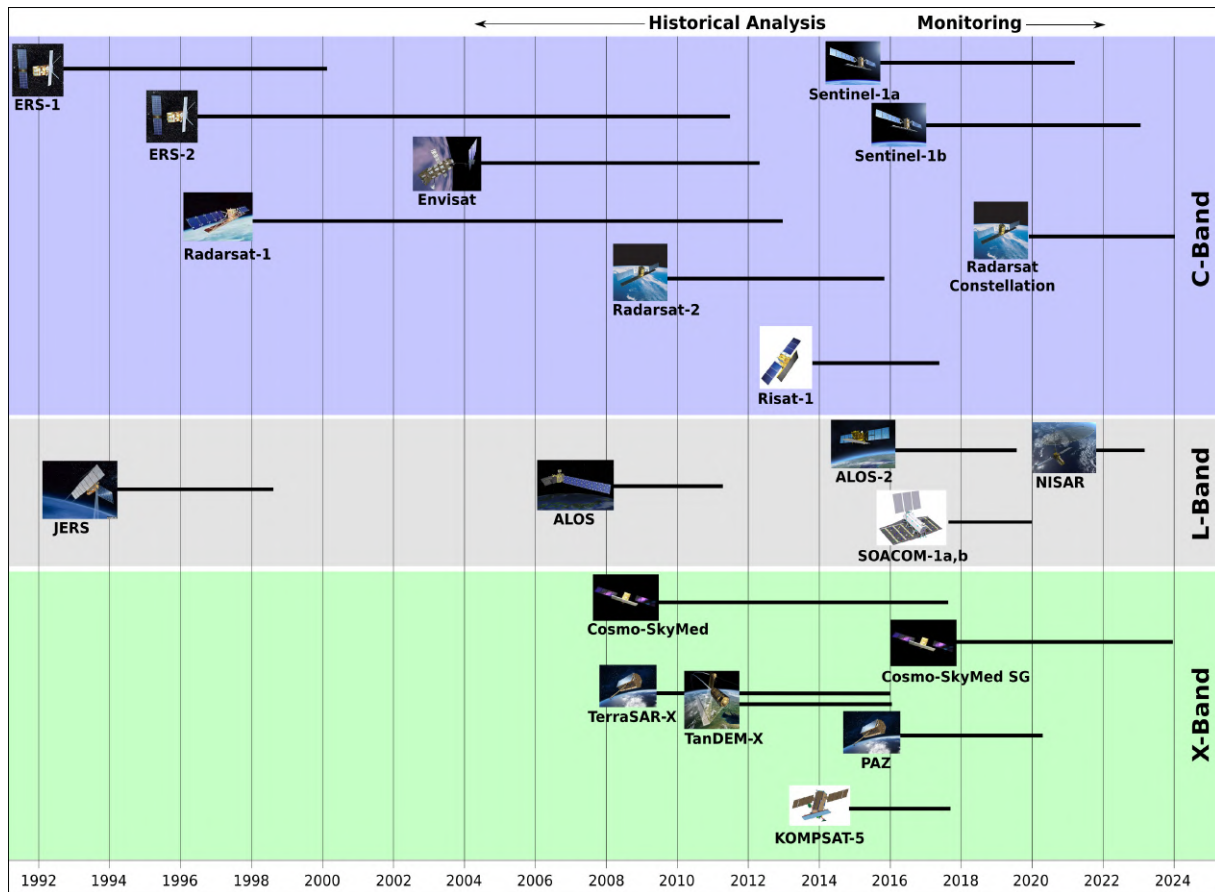


FIGURE 1.5 : Liste des capteurs micro-ondes actifs (ou radars) passés et actuels jusqu'à aujourd'hui. Source : UNAVCO

nement électromagnétique sur les courtes longueurs d'onde qui permettent de saisir les caractéristiques spectrales les plus exemplaires de la cible, par exemple MODIS, MERIS.

4. Les capteurs hyperspectraux utilisent plus de 100 bandes spectrales et la signature spectrale précise permet de mieux classifier les objets et est utilisée pour différentes applications telles que la foresterie, l'agriculture, etc.

Plusieurs études documentent une relation empirique entre la réflectance de la surface du sol et SM (Gao et al., 2013) et la relation non linéaire entre le SM et la réflectance (Lobell and Asner, 2002; Nocita et al., 2013). Le principal inconvénient des capteurs optiques pour le suivi de la SM est qu'ils ont une capacité limitée à pénétrer les nuages et sont fortement atténués par la couverture végétale (Zhao and Li, 2013). En outre, les mesures de réflectance du sol sont fortement affectées par les nombreuses propriétés physiques du sol, telles que la teneur en matière organique, la rugosité, la texture, l'angle d'incidence, la couverture végétale, etc. qui rend la réflectance du sol très variable indépendamment du SM. La relation entre la réflectance du sol et le SM n'est obtenue que lorsque le modèle est adapté à des types de sol spécifiques (Muller and Decamps, 2001). En général, l'information spectrale réfléchiée seule ne pourrait pas fournir une solution viable pour fournir des images de SM.

Les imageurs thermiques font également partie des instruments optiques. Ils utilisent des capteurs infrarouges pour détecter le rayonnement infrarouge émis par la surface de la terre. . Ils

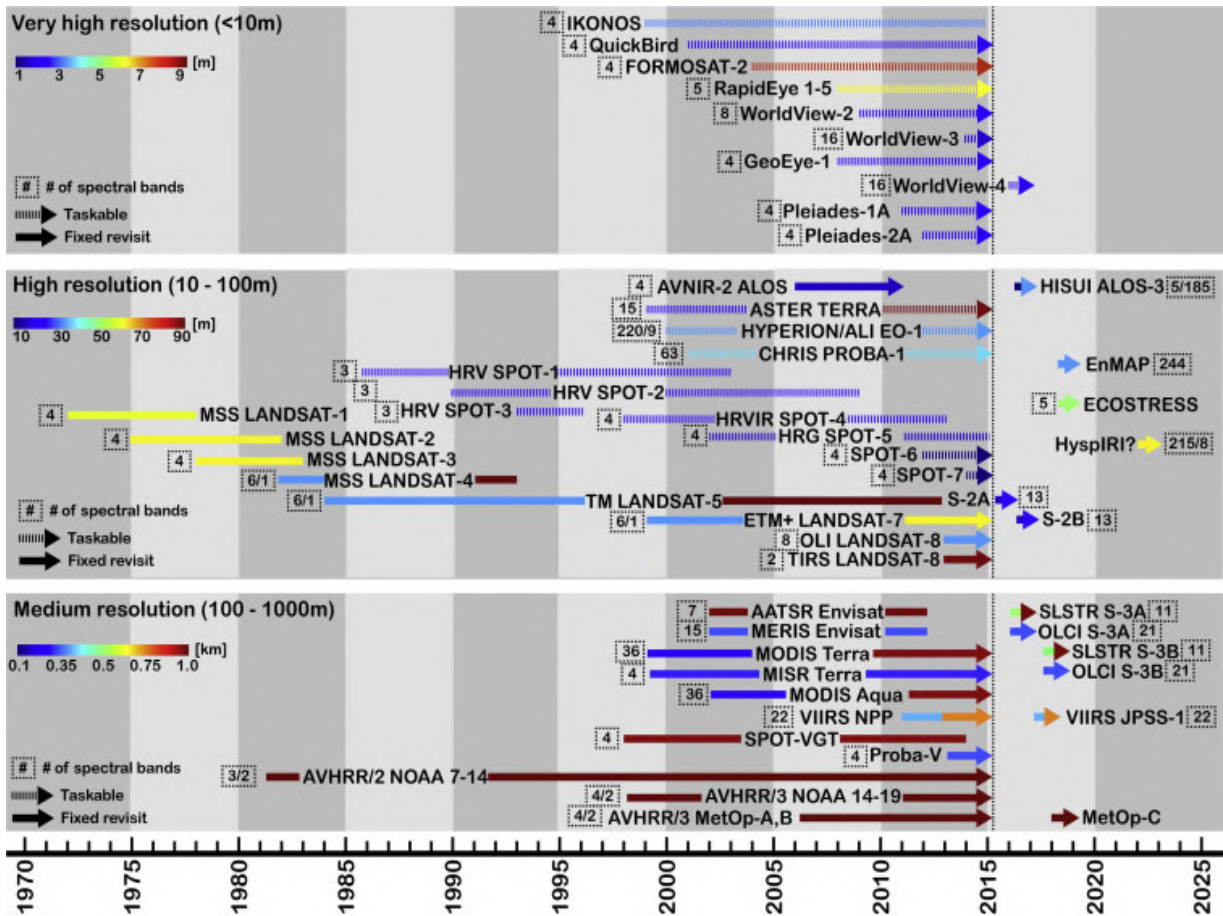


FIGURE 1.6 : Liste des capteurs optiques/thermiques passés et actuels jusqu'à aujourd'hui. Source : [Houborg et al. \(2015\)](#)

sont utilisés dans les satellites de télédétection pour mesurer la température de la surface de la terre et de la mer. La quantité de rayonnement thermique émise par les objets dépend de leur température.

L'évaporation étant le moyen le plus efficace de calculer la perte d'énergie à la surface, il existe un lien étroit entre la température de la surface terrestre (LST) et la disponibilité en eau du sol, notamment dans des conditions de stress hydrique. Par conséquent, l'utilisation de données thermiques est le moyen le plus approprié pour accéder à l'évaporation réelle et à l'état hydrique du sol (SM) à une échelle spatiale et temporelle appropriée ([Boulet et al., 2007](#)). En plus de cela, les données thermiques ont l'avantage de détecter les informations sur le stress hydrique de la végétation et la variabilité du stress hydrique à l'échelle du champ ([Anderson et al., 2012](#)).

La méthode résiduelle et la méthode EF sont toutes deux utilisées pour déterminer l'ET et SM en utilisant les données LST. La méthode résiduelle estime l'ET comme le terme résiduel du modèle de surface énergétique, défini comme l'énergie disponible à la surface moins le flux de chaleur sensible. Cette approche est basée sur une méthode à pixel unique pour calculer l'ET pour chaque pixel indépendamment. Les modèles qui utilisent cette approche sont, par exemple, le Two-Source Energy Balance (TSEB, ([Norman et al., 1995](#))), le Surface Energy Balance Model (SEBS, ([Su, 2002](#))), et le Two-Source Time Integrated Model ([Anderson et al., 1997](#)). Cette ap-

proche est efficace sur le plan informatique et offre une estimation raisonnable de l'ET avec une grande précision sur des zones homogènes. Cette approche nécessite des mesures au sol telles que la vitesse du vent, l'humidité, la hauteur de la végétation, la température de l'air, etc. Cependant, en raison de la disponibilité limitée des mesures au sol dans les zones hétérogènes, ce modèle est rarement utilisé pour estimer l'ET et la SM sur de grandes surfaces dans le cadre d'applications opérationnelles (Jiang and Islam, 2003).

L'autre gamme de méthodes d'estimation de l'ET et de la SM à partir des données LST est basée sur l'EF. L'EF peut être estimée à partir de l'image optique/thermique, où la LST en conditions sèches et humides peut être dérivée à partir de la LST observée et des données de couverture végétale. Cette méthode est basée sur la méthode contextuelle qui utilise l'hétérogénéité de la surface terrestre dans l'image LST télédéteectée et utilise l'image entière pour estimer l'EF à chaque pixel. Les modèles qui utilisent cette approche sont l'indice d'équilibre énergétique de surface (SEBI, (Menenti et al., 1989)), l'indice d'équilibre énergétique de surface simplifié (S-SEBI, (Roerink et al., 2000)), le modèle d'équilibre énergétique de surface monosource (SEB-1S, (Merlin et al., 2013)), l'indice de température et de condition de la végétation (VTCl, (Wan et al., 2004)) et l'indice de sécheresse de la végétation dérivée de la température (TVDI, (Sandholt et al., 2002)).

La télédétection infrarouge thermique peut également être utilisée pour découpler les propriétés thermiques de la surface de la température ambiante (cycle de température quotidien) en calculant l'inertie thermique apparente (Qin et al., 2013; Lei et al., 2014). L'inertie thermique dépend de la conductivité thermique et de la capacité thermique, qui augmente avec SM (Olsen et al., 2013). Ainsi, une relation est développée entre le changement de TCL et SM en mesurant l'amplitude du changement de température quotidien. La relation entre le changement de température quotidienne et la SM est fonction du type de sol et est limitée aux conditions de sol nu (Van de Griend et al., 1985). Recent studies have shown that SM can be estimated over vegetated areas if the linear. Des études récentes ont montré que la SM peut être estimée sur des zones végétalisées si la relation linéaire est maintenue entre le flux au sol et la LST (Maltese et al., 2013a,b).

1.2.4 Méthodes de réduction d'échelle ou désagrégation de données

Les satellites de télédétection assurent un suivi de la SM à l'échelle globale grâce à la radiométrie en bande L (SMOS et SMAP), mais avec une résolution spatiale qui est loin de répondre aux besoins de nombreuses applications, notamment les études hydrologiques à petite échelle et la gestion de l'eau et de l'irrigation à l'échelle du bassin. Par conséquent, pour surmonter les limites des données disponibles à basse résolution et fournir une SM à une résolution spatiale plus élevée, diverses méthodes de réduction d'échelle ont été proposées pour désagréger les données SM dérivées des micro-ondes passives. Peng et al. (2017) ont classé les méthodes de réduction d'échelle existantes en trois types différents : 1) basés sur la géo-information 2) basés sur des modèles 3) basés sur des satellites.

1) Les modèles basés sur la géo-information utilisent les paramètres de la surface terrestre (tels que les attributs de la végétation, la topographie et les caractéristiques du sol) pour réduire l'échelle d'une résolution plus grossière à une résolution fine. L'approche de réduction d'échelle peut être utile à l'échelle du champ où l'information in situ est disponible, mais son applicabilité est limitée à l'échelle la plus grossière.

2) Les méthodes de réduction d'échelle basées sur des modèles peuvent être basées sur des mo-

dèles statistiques, hydrologiques ou de surface terrestre. Le modèle statistique est peu coûteux en termes de calcul et constitue le meilleur moyen d'utiliser les grands jeux de données historiques pour établir une relation statistique. Un modèle statistique est prévalent en climatologie pour la prédiction future. Divers modèles statistiques de réduction d'échelle sont développés pour réduire l'échelle du SM à une résolution fine : le coefficient d'ondelette (Kaheil et al., 2008) et l'interpolation fractale (Kim and Barros, 2002) en sont deux exemples. Une autre approche basée sur la physique utilise un modèle hydrologique ou de surface terrestre pour désagréger l'observation basse résolution à haute résolution par régression linéaire (Low et Mauser 2008), distribution bivariée (Verhoest et al., 2015) et assimilation d'une résolution plus grossière dans les modèles de surface terrestre/hydrologiques pour fournir une résolution à fine échelle. L'approche basée sur les modèles peut être utilisée pour fournir une SM à l'échelle mondiale, mais la principale limitation est que l'erreur dans le modèle ou les observations télédéteectées contribue pleinement aux incertitudes sur les valeurs de SM à la résolution plus fine. Elle dépend également de la disponibilité des informations à l'échelle de résolution la plus fine, comme les types de sol, la texture du sol, les précipitations et les données d'irrigation, ce qui limite quelque peu son utilité pour fournir des données SM à haute résolution sur une base quotidienne globale. Un autre problème majeur est le développement d'un modèle hydrologique ou de surface terrestre pour représenter les observations physiques et de télédétection avec une meilleure robustesse et précision.

3) Basé sur les satellites : diverses méthodes de réduction d'échelle basées sur les satellites sont développées sur la base d'une synergie entre les données satellitaires de résolution grossière et les données satellitaires auxiliaires de résolution fine pour fournir des données SM à haute résolution, comme décrit ci-dessous.

a) Synergie entre les données micro-ondes actives et passives : on constate que le radiomètre en bande L est très efficace pour fournir des informations sur SM plus précises que les autres informations satellitaires. Sur la base de ce concept, le SM dérivé de la bande L à basse résolution est désagréé à haute résolution en utilisant des données auxiliaires de télédétection à fine échelle. En particulier, la mission SMAP combine le radiomètre en bande L à basse résolution avec le radar Sentinel-1 pour réduire l'échelle du SM à 3 km et 1 km. Mais la principale limitation est que cela dépend du temps de passage quasi-simultané des données Sentinel-1 et SMAP.

b) Synergie entre les données optiques/thermiques et les données micro-ondes passives :

Merlin et al. (2013) ont développé l'algorithme DISPATCH (DISaggregation based on the Physical and Theoretical scale CHange) qui utilise les données optiques/thermiques comme proxy de SM pour réduire l'échelle des données SM micro-ondes à basse résolution. L'algorithme DISPATCH utilise la méthode basée sur l'évaporation. DISPATCH est une approche physique et théorique pour désagréger les micro-ondes à résolution plus grossière afin de fournir une estimation de SM à haute résolution. Peng et al. (2015) utilisent le VTCI comme proxy thermique de la SM pour réduire l'échelle de la SM à basse résolution. Le VTCI est calculé à partir d'un espace caractéristique triangulaire/trapézoïdal à partir de données optiques/thermiques à haute résolution. Fang et al. (2013) utilisent la relation d'inertie thermique entre le changement de température quotidien et la SM moyenne quotidienne en utilisant la SM à basse résolution et les données optiques/thermiques à haute résolution. Song et al. (2013) réduisent l'échelle de la température de brillance des micro-ondes en utilisant des données optiques/thermiques à haute résolution. Ensuite, la température de brillance à haute résolution est utilisée pour récupérer la SM en utilisant un algorithme à chaîne unique (Jackson, 1993).

1.3 Objectifs de recherche et plan de la thèse

Pour le suivi de SM, les mesures in situ et la modélisation de la surface terrestre sont utiles comme référence localisée à des fins de validation et comme outil physique pour extrapoler les résultats dans l'espace et dans le temps, respectivement. Cependant, ces deux méthodes présentent des limites importantes liées à la représentativité spatiale des estimations de la SM. Dans ce contexte, les techniques de télédétection ont un fort potentiel pour fournir des estimations SM à diverses échelles spatiales, qui sont requises dans de nombreuses applications, y compris la météorologie et la climatologie, l'hydrologie et l'agriculture (par exemple, la programmation de l'irrigation). Les capteurs spatiaux basés sur les micro-ondes passives, les micro-ondes actives et les données optiques/thermiques peuvent fournir des informations sur SM à différentes échelles spatiales et temporelles. La communauté de la télédétection reconnaît généralement que les micro-ondes passives en bande L sont l'une des techniques les plus précises. Cependant, sa résolution spatiale, qui est de l'ordre de plusieurs dizaines de kilomètres, n'est pas adaptée à la plupart des utilisations hydrologiques et agricoles à échelle fine. C'est pourquoi d'autres méthodes non optimales mais complémentaires sont étudiées sur la base de données radar et/ou optiques/thermiques disponibles à plus haute résolution spatiale. Pourtant, aucune approche ne combine les données multi-capteurs (passive/active micro-ondes/optique/thermique) disponibles pour exploiter efficacement les avantages de chaque technique. Pour combler ce manque, cette thèse vise à développer un algorithme qui combine les données multi-capteurs/multi-résolution/multi-longueur d'onde afin de fournir des données de SM avec une robustesse et une précision améliorées à haute résolution spatio-temporelle.

Sur la base de cette idée, la recherche proposée ici développe et évalue un nouvel algorithme et une nouvelle méthodologie pour le suivi de SM. En particulier, une synergie est étudiée entre les données de SM dérivées des micro-ondes passives SMAP/SMOS désagrégées à l'aide de données optiques/thermiques (avec l'algorithme de réduction d'échelle DISPATCH) et le SM récupéré à partir de données radar (avec un modèle de transfert radiatif micro-onde actif). Pour ce faire, trois étapes successives sont identifiées pour désagréger les données SMOS/SMAP à 40 km de résolution à la résolution de 1 km (étape 1), pour désagréger les données SMOS/SMAP à la résolution de 100 m (étape 2), et pour construire une synergie à la résolution de 100 m avec les données micro-ondes actives (étape 3). Enfin, les données SM désagrégées sont assimilées dans un modèle de surface terrestre pour améliorer encore la précision et la fréquence des estimations SM. Les principaux objectifs de la recherche sont illustrés sur la Figure 1.7.

Ces travaux devraient permettre une nouvelle compréhension de l'avantage de la synergie multi-capteurs et de son applicabilité pour fournir un produit de SM à haute résolution spatio-temporelle. L'algorithme utilisé dans cette recherche est destiné à être assez générique et pourrait être appliqué aux futures données de télédétection. En résumé, les questions scientifiques sous-jacentes que ce projet de doctorat propose d'aborder sont les suivantes :

- 1) Comment pouvons-nous estimer SM à haute résolution – information utile en agriculture et hydrologie - c'est-à-dire inverser des données à haute résolution spatiale et temporelle (cycle de répétition de quelques jours) ?
- 2) Est-il possible de fournir des informations de SM à haute résolution spatio-temporelle à partir des observations de télédétection facilement disponibles sur différentes couvertures terrestres ?
- 3) Quelles sont les synergies possibles entre les micro-ondes passives, les micro-ondes actives et

les données optiques/thermiques pour l'extraction de la SM ?

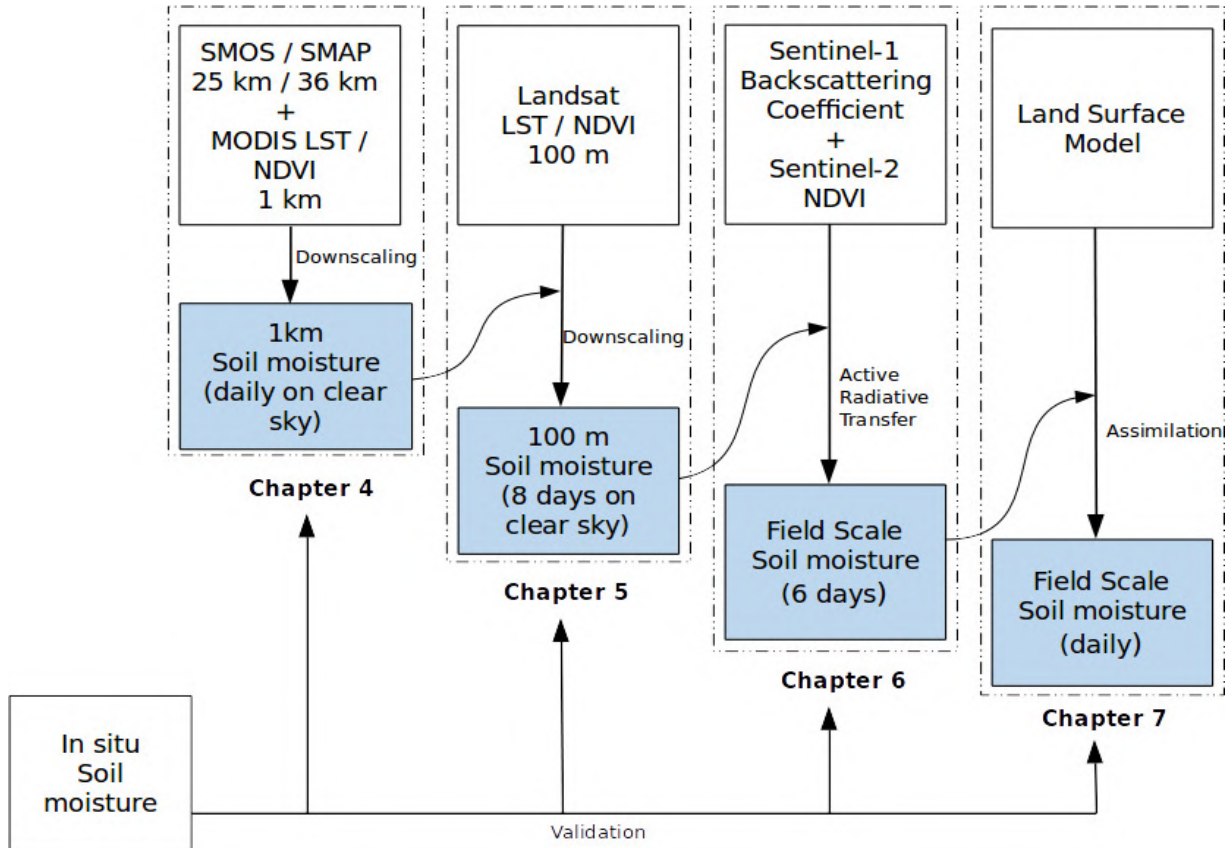


FIGURE 1.7 : Schéma de l'objectif principal de recherche divisé en quatre étapes successives.

La thèse est organisée de manière à décrire les approches ou les algorithmes mis en œuvre pour combiner et surmonter les limitations des observations micro-ondes passives, micro-ondes actives et optiques/thermiques, et l'objectif final est de fournir un SM à haute résolution spatio-temporelle avec une robustesse et une précision améliorées. En pratique, le document est organisé comme suit :

Le **Chapitre 1** présente l'importance du SM d'un point de vue général et discute la disponibilité et les limites des produits SM existants dérivés des différents capteurs et modèles sur une plage de résolutions.

Le **Chapitre 2** décrit les zones d'étude utilisées pour cette recherche, c'est-à-dire la région sélectionnée pour l'analyse dans la région méditerranéenne.

Le **Chapitre 3** donne une description générique de l'algorithme de réduction d'échelle DISPATCH utilisé pour fournir la SM à haute résolution en réduisant l'échelle des données SM à basse résolution dérivées des micro-ondes passives à l'aide de données optiques/thermiques. L'algorithme de réduction d'échelle est mis en œuvre pour fournir la SM en global à une résolution de 1 km.

Le **chapitre 4** présente la nouvelle mise en œuvre et l'amélioration de l'algorithme DISPATCH afin d'augmenter la couverture spatiale et d'améliorer la précision de la SM récupérée. Ce cha-

pitre présente également une évaluation comparative qualitative et quantitative de la précision avec deux autres produits de SM différents disponibles à la même résolution (1 km).

Le **Chapitre 5** présente un nouvel algorithme pour fournir des données de SM à une résolution de 100 m à partir des observations micro-ondes passives à une résolution de 40 km en utilisant l'algorithme DISPATCH. L'algorithme de réduction d'échelle en deux étapes est utilisé pour désagréger les données SM SMOS/SMAP à 100 m de résolution.

Le **Chapitre 6** présente une nouvelle méthodologie qui s'appuie sur une synergie entre les ensembles de données micro-ondes passives, optiques/thermiques et micro-ondes actives. Comme stratégie de cette synergie, les paramètres du modèle radar sont calibrés à la résolution spatiale du radar à partir du produit SM dérivé des micro-ondes passives à échelle réduite. L'algorithme est assez générique, et son principal avantage est qu'il est indépendant des ensembles de données SM in situ pour la calibration.

Le **Chapitre 7** étudie l'utilité de l'assimilation des produits de SM à haute résolution dans un modèle de surface terrestre pour fournir des données SM à l'échelle quotidienne sur une zone irriguée. Cette approche est unique car le produit SM à 100 m est utilisé pour évaluer la sensibilité du schéma de couplage désagrégation-assimilation à l'irrigation, qui n'est pas incluse dans les données de forçage du modèle.

Le **Chapitre 8** résume les travaux de recherche et souligne leur contribution originale. Il ouvre également de nouvelles voies de recherches futures concernant le suivi de SM à partir de la télédétection multi-capteurs et ses multiples applications.

Chapter 2

Study area

Contents

2.1	Introduction	44
2.1.1	Tensift basin, central Morocco	44
2.1.2	Ebro basin, northeastern Spain	46
2.1.3	Duro basin, northwestern Spain	47
2.1.4	Garonne basin, southwestern France	48
2.2	Conclusion	48

2.1 Introduction

The Mediterranean sea is surrounded by the Mediterranean region extending between 40°N and 30°N and covering around 4,300,300 km^2 . The area has a temperate climate (cooler) in the north and a subtropical climate (hot) in the south. The seasonal variability characterizes the climatic conditions in the Mediterranean region. Winter is cold and wet, and summer is hot and dry. For example, in summer, the mean temperature increases or decreases from north to south. The average winter precipitation is 30% of the total in the western and northern Mediterranean areas and 70% in the eastern and southern Mediterranean areas (Xoplaki et al., 2004). Such high spatial and temporal variability of temperature and precipitation occurs between the mid and tropical latitudes and is called a transitional climatic zone. The region is affected by tropical and subtropical subsystems and mid-latitude cyclones which also affect precipitation. The area shows sizable spatial variability due to its complex morphology, such as islands, mountains, basins, gulf, and many other meteorological factors that fully contribute to diverse spatial variability.

The main characteristic of the region is that it is densely populated, and due to this, it causes demographic pressure and anthropogenic effects that lead to environmental degradation. It is also strongly affected by climate change, which implies changes in the availability of water resources. Hydrological changes directly impact agricultural productivity, irrigation supply, energy use, and so on.

Agriculture is an important sector in the Mediterranean region that helps in sustainable economic development. However, the over-extraction of water for consumption degrades water quality, makes the water unavailable for irrigation, and leads to a water crisis (Pisinaras et al., 2010; Berahmani et al., 2012). In the semi-arid Mediterranean region, water scarcity is mainly due to its high population density, which leads to pressure on water resources and their use for irrigation.

The strong spatial (from north to south) and temporal (mainly seasonal) variabilities of the hydrological functioning within the Mediterranean region provide a distinct feature of soil moisture and ecosystem water stress dynamics. Therefore, the region offers a very peculiar interest in studying soil moisture's spatial distribution and evolution. This is especially true when considering the impact of natural (precipitation) and human-made (irrigation) forcing, which occur at a range of spatio-temporal scales. The thesis undertakes the methodological development for monitoring soil moisture (SM) over four basins (see Figure 2.1) in the Mediterranean region covering the climatic gradient from arid to temperate, presented in the following sections.

2.1.1 Tensift basin, central Morocco

The Tensift basin is located amid Morocco's western region, near Marrakech. It covers 20,450 km^2 , extending between latitudes 32°10' and 30°50' North and longitudes 9°25' and 7°12' West. The basin is bordered on the north by mountainous terrain, south by the high Atlas mountains, west by the Atlantic Ocean, and east by the Tensift drainage basin. The basin includes the Haouz plain and the high Atlas mountains. The Haouz plain was chosen as the study area. The climate on the Haouz plain is semi-arid, with cold winters and hot summers. The average annual precipitation is 250 mm, with an evaporative demand of 1600 mm.

Agriculture in this region is the principal source of economic growth and food security. In summer, due to hot climatic conditions, there is a tendency for irregular and intense rainfall. 87% of the area is rainfed, and the agricultural productivity depends on the rain. The demand for

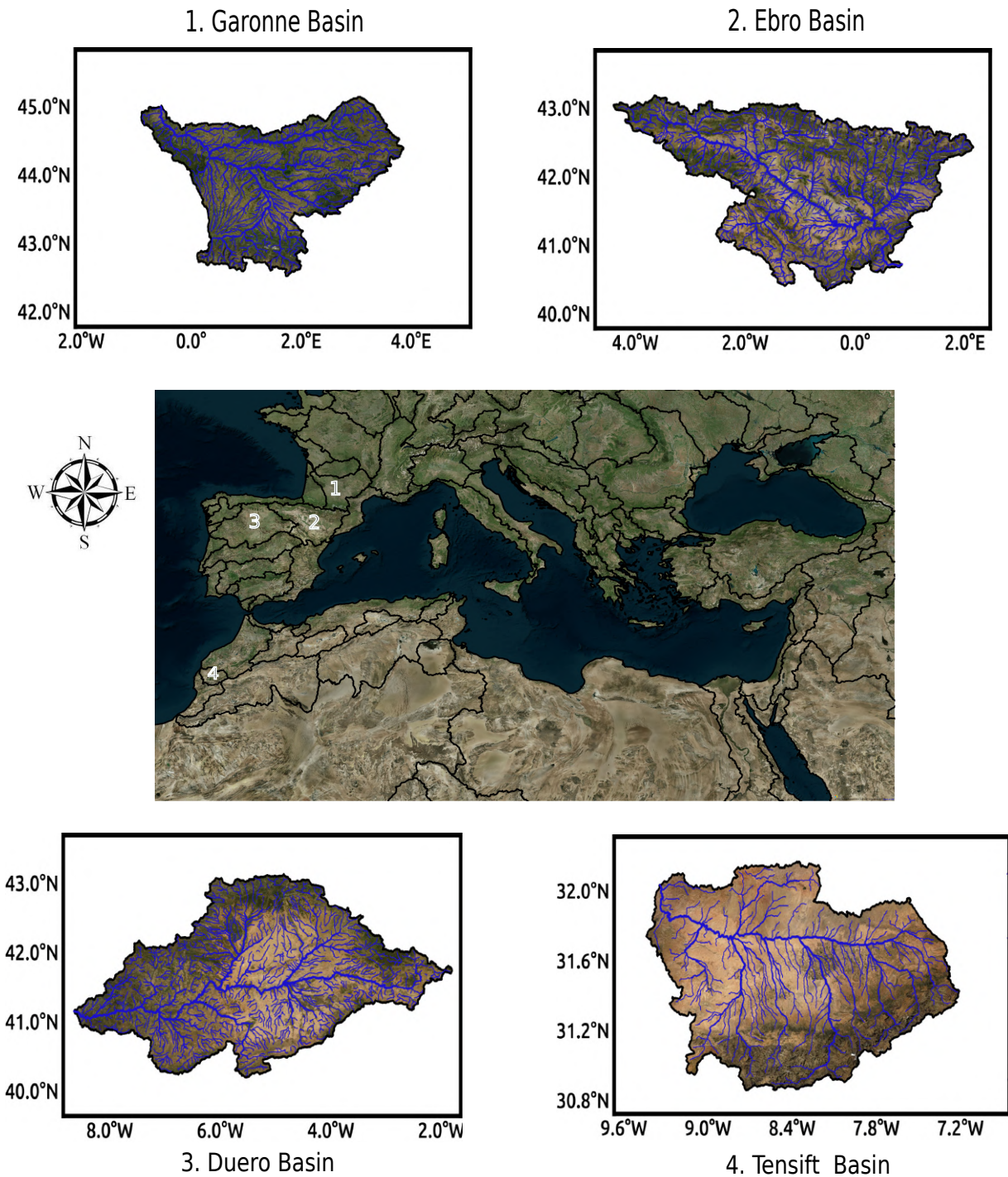


Figure 2.1: Study area including 1. Garonne Basin 2. Ebro Basin 3. Duero Basin 4. Tensift Basin

water irrigation will rise as the temperature rises in summer, putting pressure on the limited water resources. The dry period diminishes the impact of agriculture by 50 to 70% in rainfed areas. Water scarcity for irrigation reduces productivity and SM. Evapotranspiration rises due to warmer temperatures, resulting in lower agricultural yields and productivity.

The Tensift basin receives water from the high atlas range, basin transfer, and groundwater.

The high atlas range receives precipitation either in the form of snow or rain, and then the main river coming from the mountains drains the water into the basin through the Tensift river and its tributaries. The water supply from the basin uses different infrastructures and is categorized into the irrigation technique: Traditional irrigation technique where water is transferred through "seguis" consisting of small canals that divert the river's main flow into irrigated areas. Modern irrigation technique where water is transferred from the dam through the canal de Rocade and Lalla Takerkourst dam. Private irrigation technique where water is used from groundwater and puts higher pressure on the aquifer.

The R3 irrigated zone, Sidi Rahal site, and Chichaoua site are selected for the study over the Haouz plain. The R3 irrigated zone, Chichoua and Sidi Rahal study sites are 100 kilometers from Marrakesh in Morocco's Haouz plain. The soil texture is clayey for R3 irrigated zone, sandy for Sidhi Rahal and loamy clayey for the Chichaoua site. Wheat is the most widely grown crop for all the three sites.

In R3 irrigation district, crop fields have a typical size of 2-4 ha. Flood irrigation is used to cultivate the crop. Wheat is typically planted in November or December, with irrigation beginning in February and ending in April. A total of six irrigations are generally employed during the wheat crop's growth. Harvest is completed by May or June. Theta probes are used to manually collect SM at a depth of 0-5 cm. Then, the collected SM is calibrated using gravimetric measurements based on the soil samples collected for each sampling date. For each crop field, theta probes were utilized to measure the SM for ten discrete SM measurements. The in situ SM is collected at 5 cm for the five sampling days of year 14, 30, 38, 62, 78 for 2016.

In Chichaoua and Sidi Rahal a TDR sensor are used to collect the SM for every 30 min automatically. The gravimetric SM is used for the calibration of soil dielectric properties from the sensor. The in situ SM was collected at 5 cm from 2017 to 2018.

2.1.2 Ebro basin, northeastern Spain

The Ebro basin has a triangular structure with a coverage of 85,530 km². It is one of Spain's greatest hydrographic basins, accounting for 17.3% of the country's total surface area. The basin is surrounded on the west by the Pyrenees and Cantabrian mountains, north and east by the Catalan coastal range, and south by the Iberian massif. The middle of the Ebro basin area is flat and lies between the Pyrenees and the Iberian peninsula, which is called the Ebro depression. The average annual rainfall ranges from 3000 mm in the Pyrenees to less than 100 mm in the plain. Rainfall in the basin varies from year to year. The area in the Ebro depression has a Mediterranean climate (hot in summer and cold in winter) and the annual evapotranspiration in the Pyrenees is 600 mm and 800 mm in the central depression. The population density of this basin is 2.8 million. The population is heterogeneously distributed, and half of the population is situated in the central basin. The middle and lower parts of the Ebro basin are irrigated, and land cover is agricultural-type crops such as vineyards, maize, and orchards.

According to The Confederación Hidrográfica del Ebro (CHE, 2005), the annual water yield in the river basin is 18 km³, of which 12 km³ of water runoff to the sea. As a result, only 6 km³ of water is consumed. The majority of water taken from the Ebro basin is used for irrigation, with the remainder going to urban and other industrial uses and hydroelectric, thermal, and nuclear-generating facilities. Only 60% of the entire average mean runoff is stored in dams intended for

storage. Low precipitation and an increase in yearly temperature have resulted in a 15% decrease in precipitation and a 4% increase in temperature in the Pyrenees (López-Moreno et al., 2008). The different study areas used from the Ebro-basin are explained below in detail. The sites used in this study are Urgell, Agramunt, Fordada, in the north west of the basin and a dry land area in the south east.

Urgell has a Mediterranean climate, which is hot in the summer and cold in the winter. The annual precipitation averages 376 mm. An ancient flood irrigation technology and a new sprinkler or drip irrigation methods are used to irrigate the study area. The Segarra–Garrigues (SG) system, which aims to transform dry grounds into agricultural land, uses spray or drip irrigation. The area that is not included in the SG irrigation system plan stays dry. As a result, the irrigated region is bordered by unirrigated dryland. Irrigation is mostly done in the summer. The location was chosen because of its unique characteristics, e.g. fact that the area remains the same as the surrounding area during the winter, but the agricultural area becomes wet during the summer, while the surrounding area remains dry. The land is covered by agricultural crops, mainly corn, wheat, and alfalfa. The trees grown primarily in this region are olive trees, fruit trees, and vineyards.

Fordada and Agramunt sites are a part of SG system located at 41.866°N, 1.015°E and 41.782°N, 1.089°E. Fordada experimental field covers an area of 20 ha and Agramunt experimental field covers an area of 20.5 ha. The soil texture of Fordada is 41.5% sand, 42.3% silt, and 16.2% clay, and the soil texture of the Agramunt is 52.1% sand, 35.3% silt, and 12.6% clay. The area is irrigated with sprinkler irrigation, and the Agramunt area is irrigated with subsurface drippers. SM data collected for Agramunt and Fordada is 2015 and 2017, respectively.

The dryland experimental crop selected in the southern part of the basin is located in Tarragona province, Catalunya, east of Spain. The area has a semi-arid Mediterranean climate with annual average precipitation of 385 mm. The site has mainly rainfed crops, and the soil texture is clayey. TDR sensors are used to measure the SM at a depth of 5 cm. The network consists of 7 stations, and the SM is collected for six months from June to November 2019.

2.1.3 Duro basin, northwestern Spain

The basin is located north of the Iberian peninsula, with a total size of 97290 km^2 , 80% (78954 km^2) within the Spanish territory. The basin is depressed in the middle, and a mountainous region with an altitude of 2500 m surrounds most of the basin. The annual average rainfall varies from mountain to central depression. The yearly average rainfall in the mountain is 1000 mm, while the average rainfall is less than 400 mm in the central depression. The Mediterranean climate with a continental feature may be seen in the main central depression area. The land in the mountainous region is covered by forest, shrublands, grasslands, and the cropland area. This basin shows a transitional climate like the Ebro basin, i.e., summer is hot, and winter is cold.

The SM monitoring network named Rhemodus is located near the center of the Duro basin. The Rhemodus network is very dense and consists of 20 stations. Only 13 stations are used in this thesis. The network is located near the center of the Duro basin, west of Spain. The site has a semi-arid Mediterranean climate with annual average precipitation of 385 mm. The land cover of this network is rainfed croplands (78%), forests and pastures (13%), irrigated crops (5%), and vineyards (5%) (Sánchez et al., 2012). Soil texture is silty and clayey sand. TDR probes measure

the soil dielectric properties and the volumetric SM at a 0-5 cm depth. In situ SM measurement is collected from the International Soil Moisture Network (ISMN) for the time period of 2017.

2.1.4 Garonne basin, southwestern France

Garonne basin is located between the depressions of the Atlantic ocean and Mediterranean sea. The basin covers an area of 56000 km², located at 42°36 'N and 0°57' E. The basin is surrounded in the southeast by the Mediterranean Sea, on the west and south by the Pyrenees Mountains, and on the northeast by the Massif Central. The basin has a relatively flat surface and a low elevation. The basin is subjected to two climatic influences: one from the Atlantic Ocean, which is characterized by the western wind and heavy precipitation, and the other from the Mediterranean Sea, which is characterized by the hot and dry southeastern winds.

The climate varies with temperatures below freezing point in the mountains and rarely below freezing in the plains. In the mountainous terrain, forest and alpine grasslands cover the soil, while agriculture is practiced in the plain. The impact of agricultural practices on streamflow has been studied from a hydrological standpoint since 1983 in this basin. Because of the diverse environment, the area is vital from a hydrological standpoint. The average annual precipitation is 664 mm, with 1020 mm of potential evapotranspiration. The majority of the water is used in agriculture. The water quality is acceptable near the Pyrenees, but as it reaches the plain, it deteriorates due to extensive agricultural usage and other anthropogenic influences. Wheat, barley, corn, and fodder cultures are the crop types.

Auradé (43°3259N, 1°0622E) and Lamasquère (43°2947N, 1°1416E) sites are used in this thesis. Both study areas are located near Toulouse (south-west of France), separated by a distance of 12 km. The climate is temperate, with an average annual precipitation of 700 mm. Auradé soil texture is clay loam (20.6 percent sand, 47.1 percent loam, and 32.3 percent clay), while Lamasquère soil texture is clay (12.0% sand; 33.7% loam, and 54.3% clay). Both areas are covered by agricultural land. Winter wheat and sunflower are grown in the Auradé area, while winter wheat and wheat are grown in Lamasquère. Crop rotation techniques are used at both sites to cultivate crops. Both study areas are irrigated mainly covered by agricultural fields. For both, the study areas, the in situ measurements are collected over 2017 and 2018.

The SM is measured every 30 minutes with CS616 TDR probes (Campbell Scientific Inc., Logan, UT, USA) at depths of 0.05 m, 0.10 m, and 0.30 m. The volumetric SM is computed from the measured soil's dielectric permittivity and a site-specific calibration equation. [Tallec et al. \(2013\)](#) and [Béziat et al. \(2009\)](#) provide detailed information about the study area (2013).

2.2 Conclusion

The Mediterranean region is located in the transitional climatic zone, covering both wet and dry climatic conditions. The selected study areas include SM monitoring sites in four basins, one in Morocco (Tensift), two in Spain (Ebro, Duro), and one in France (Garonne). Those sites provide very heterogeneous conditions in terms of climate, soil type, hydrological functioning, and agricultural practices. They are thus very suitable to analyze the spatio-temporal variability of SM at a range of spatio-temporal resolutions and to test the SM monitoring methods in such conditions. Most of the experimental sites are agricultural, either rainfed or irrigated (according to various irrigation techniques), illustrating our effort in this thesis to retrieve SM at fine-scale, i.e., the crop field scale.

Chapter 3

Disaggregation of passive microwave soil moisture using optical/thermal data

Contents

3.1	Introduction	50
3.2	Downscaling algorithm	50
3.3	C4DIS processor	54
3.4	Adaptation of C4DIS to other sensors	55
3.5	Conclusion	55

3.1 Introduction

Nowadays, microwave radiometers are widely used for the estimation of soil moisture (SM) on a global basis. L-band radiometry is indeed widely accepted and optimal for SM estimation (Wagner et al., 2007). Based on this principle, two satellites were made operational - SMOS and SMAP - to provide SM data worldwide. Both satellites provide SM images at 40 km spatial resolution with a sensing depth of 5 cm. Such a coarse resolution is far from the requirement of most hydro-agricultural studies, which generally need SM data at a sub-kilometric scale (Walker and Houser, 2004). So in this context, disaggregation/downscaling approaches are used to improve the spatial resolution and to reduce the gap between the available low resolution and the required high resolution in SM data sets.

The methodological developments made in this thesis have been based on a downscaling algorithm named DISaggregation based on Physical and Theoretical scale CHange (DISPATCH). DISPATCH algorithm (Merlin et al., 2012, 2013) has been originally designed to disaggregate the 40 km resolution SMOS SM data to 1 km resolution using the optical/thermal data collected by MODIS aboard Aqua and Terra. The soil evaporative efficiency estimated at 1 km resolution from MODIS data is used to re-distribute the SM values at 1 km resolution within the 40 km resolution SMOS pixel. This is done given a relationship between SM and soil evaporative efficiency across scales, and a calibration of that model at the low resolution.

This chapter thus provides a brief and generic overview of the DISPATCH method, as well as its implementation at the quasi global scale by the Centre Aval de Traitement des Données SMOS (CATDS) in the SMOS French ground segment. The processor is named as CATDS Level-4 Disaggregation processor (C4DIS). While C4DIS was originally developed for SMOS and MODIS sensors, it can be adapted to other similar data. The adaptation of C4DIS to SMAP and Sentinel-3 data is also presented in this chapter.

3.2 Downscaling algorithm

The DISPATCH model relies on physical considerations because it provides a physical link between soil temperature, evaporation, and SM using a temperature-derived soil evaporation model. It also relies on a theoretical consideration because it uses mathematical tools such as Taylor series expansion and projection to develop a downscaling relationship between the low resolution SM and the targeted high resolution SM.

The downscaling algorithm captures the sub-pixel variability of SM at high spatial resolution within a low spatial resolution satellite image pixel. One key step is to estimate the soil evaporation rate from the optical/thermal data. In practice, the algorithm decouples the soil evaporation from the surface soil and the vegetation transpiration from the root-zone layer by separating the optical/thermal data into soil and vegetation components in the trapezoidal method. The LST/NDVI data are first used to calculate the soil evaporative efficiency (SEE, the ratio of actual to potential soil evaporation), generally constant during the day in cloud-free conditions. The calculated SEE is then used as a proxy for SM variability within the low-resolution pixel. The DISPATCH downscaling relationship establishes a link between SEE and SM to provide SM at high resolution, which is expressed as:

$$SM_{HR} = SM_{LR} + \left(\frac{\partial SEE}{\partial SM}\right)_{LR}^{-1} * (SEE_{HR} - SEE_{LR}) \quad (3.1)$$

where SM_{HR} is the disaggregated SM at high resolution, SM_{LR} is the SM derived at low resolution from L-band microwave data, SEE_{HR} is the SEE at high resolution, SEE_{LR} is aggregated value at low resolution and $\left(\frac{\partial SEE}{\partial SM}\right)_{LR}^{-1}$ is the inverse partial derivative of SEE model evaluated at low-resolution (around to low resolution SM observation).

The SEE used in the downscaling relationship of Equation 3.1 is calculated from the optical/thermal-derived LST and NDVI data. As mentioned before, SEE is used because, over partially vegetated pixels, it provides a strong correlation with SM, and it is relatively constant during daytime and in a clear sky. SEE shows a linear relationship with the soil surface temperature (Merlin et al., 2012). This behavior was verified using a physical-based two-source energy model (Merlin et al., 2016). SEE is hence written as:

$$SEE_{HR} = \frac{T_{s,dry} - T_{s,HR}}{T_{s,dry} - T_{s,wet}} \quad (3.2)$$

where $T_{s,HR}$ is the soil temperature at high resolution, $T_{s,dry}$ is the fully dry soil temperature with $SEE=0$, and $T_{s,wet}$ is the fully wet soil temperature with $SEE=1$. The temperature endmembers $T_{s,dry}$ and $T_{s,wet}$ are calculated from the LST-fvg feature space obtained by plotting LST as a function of the fvg (fvg, fractional vegetation cover obtained from the NDVI at high resolution).

The soil temperature at high resolution is calculated as the linear decomposition of LST into the soil and vegetation temperature using the trapezoid method (Merlin et al., 2012). It was suggested by Merlin et al. (2012) that retrieval of soil temperature is dependent on the vegetation temperature and is calculated by the hour-glass approach (Moran et al., 1994).

Soil temperature is thus expressed as:

$$T_{s,HR} = \frac{LST_{HR} - f_{vg,HR} * T_{v,HR}}{1 - f_{vg,HR}} \quad (3.3)$$

where LST_{HR} is the LST at high-resolution, $f_{vg,HR}$ is the fractional vegetation derived from NDVI data, and $T_{v,HR}$ is the vegetation temperature at high resolution. Fractional vegetation cover is expressed as:

$$f_{vg} = \frac{NDVI_{HR} - NDVI_s}{NDVI_v - NDVI_s} \quad (3.4)$$

where $NDVI_{HR}$ is the NDVI estimated at high resolution and $NDVI_s$ and $NDVI_v$ are the NDVI values at bare soil and NDVI values at full vegetation cover for a particular pixel. In DISPATCH, $NDVI_s$ and $NDVI_v$ are set to 0.15 and 0.90, respectively.

To better understand the retrieval of soil temperature from the LST-fvg feature space, Figure 3.1 illustrates the trapezoid drawn in the LST-fvg feature space and dividing the space into four different surface areas: bare soil areas, mainly dry and partially vegetated areas, mainly wet and partially vegetated areas and mainly vegetated areas named as zone A, B, C, and D. Note that the contextual method of Figure 3.1 assumes that the low-resolution pixel (let us say the 40 km resolution SMOS pixel) covers full SM conditions from residual to saturation and a range

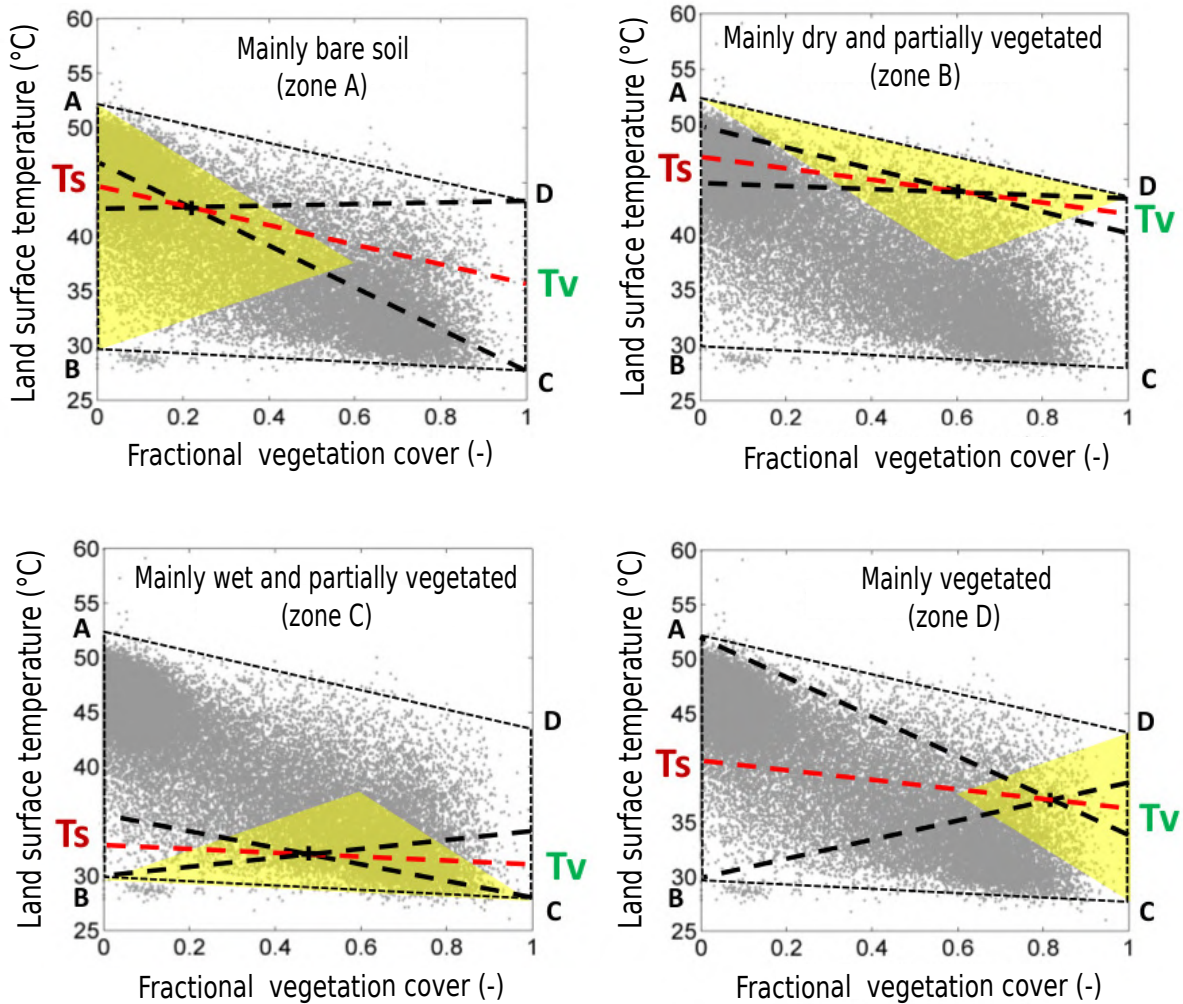


Figure 3.1: Visual representation of LST and fvg feature space graph and a trapezoid is drawn to divide the land surface into four different surface area: mainly bare soil (zone A), mainly dry and partially vegetated (zone B), mainly wet and partially vegetated (zone C) and mainly vegetated (zone D). Source: (Merlin et al., 2016)

of vegetation covers.

In zone A, the LST is mainly controlled by soil evaporation. It has an optimal sensitivity to SM. In contrast, in zone D, the LST is mainly controlled by vegetation transpiration with no significant sensitivity to surface SM. Zones B and C are mixed surfaces; the LST is controlled by both soil evaporation and vegetation transpiration. They have an intermediate sensitivity to SM.

The SEE is used as a proxy of SM in zones A, B, and C because of the sensitivity of soil temperature to SM in those zones. So, it means that the downscaling algorithm only applied to partially vegetated areas, which represents an essential limitation of the original version of DISPATCH.

Now SEE is used to develop a relationship with SM in the downscaling relationship of Equation 3.1 to account for the spatial variability of SM by considering that the SEE-SM relationship varies with soil type and atmospheric conditions. The SEE-SM relationship can be modeled as

linear or non-linear. According to (Merlin et al., 2013), linear relationship between SEE and SM is suitable for the downscaling at 1 km resolution and expressed as:

$$SEE_{LR} = \frac{SM_{LR}}{SM_p} \quad (3.5)$$

where SM_p is a SM parameter that depends on soil properties and atmospheric conditions. SM_p is calculated at the low-resolution pixel scale from SM and SEE estimated at low resolution.

Note that DISPATCH was also applied at 100 m resolution by using Landsat optical/thermal data instead of MODIS data (Merlin et al., 2013). At higher spatial resolution, the heterogeneity of the land surface increases, and it requires a more robust representation of the SEE-SM relationship. In fact, SEE(SM) shows a strongly non-linear behavior, which can be modeled by an exponential formulation (Komatsu, 2003). In that case, the SEE is expressed as:

$$SEE_{LR} = 1 - \exp\left(-\frac{SM_{LR}}{SM_p}\right) \quad (3.6)$$

Similarly to the linear case, SM_p is a SM parameter that can be estimated from SEE and SM estimates at low resolution.

Input data

Input data of DISPATCH are composed of high and low resolution data.

Low-resolution data:

DISPATCH uses SMOS Level-3 daily global soil moisture product (MIR CLF31A/D). SMOS provides a 40 km spatial resolution with a temporal coverage of 3 days at the equator with an ascending (6 a.m) and descending overpass (6 p.m). Level-3 soil moisture products are presented on the Equal-Area Scalable Earth (EASE) grid netCDF format, with a grid spacing of 25 x 25 km with a sensing depth of 5 cm.

High-resolution data:

DISPATCH uses high resolution ancillary data to downscale each low resolution pixel: the land surface temperature (LST) and normalized difference vegetation index (NDVI). Terra and Aqua satellites were launched in 1999 and 2002 by the National Aeronautics and Space Administration (NASA). MODIS provides data from 35 spectral bands - wavelengths ranging from 0.4 m to 14.4 m - with different spatial coverage of 250 m, 500 m, and 1 km. Terra and Aqua are sun-synchronous, polar orbit satellites that provide data with a temporal cycle of 1 to 3 days with an ascending node and an overpass time of 10:30 a.m (Terra) and 1:30 p.m (Aqua).

LST datasets were acquired at 1 km resolution from MODIS version 5, Level-3 Terra (MOD11A1), and Aqua (MYD11A1) daily data. NDVI datasets were obtained from MODIS version 5, Level-3 terra (CATDS), on 16-days interval of global vegetation indices at 1 km resolution. The DISPATCH method also uses as input the GTOPO30 product of the digital elevation model (DEM) to correct the elevation effect on the MODIS LST data. GTOPO30 is provided by the U.S. Geological Survey (USGS) EROS Data Center. The product has a grid spacing of 30 arc seconds, which approximately correspond to 1 km resolution.

3.3 C4DIS processor

C4DIS is the first operational processor based on the DISPATCH algorithm (Merlin et al., 2012, 2013, 2016). The processor provides SM products at 1 km resolution on a global daily basis only on the cloud-free condition and availability of the input data. A description of the schematic diagram of the C4DIS processor is provided in Figure 3.2.

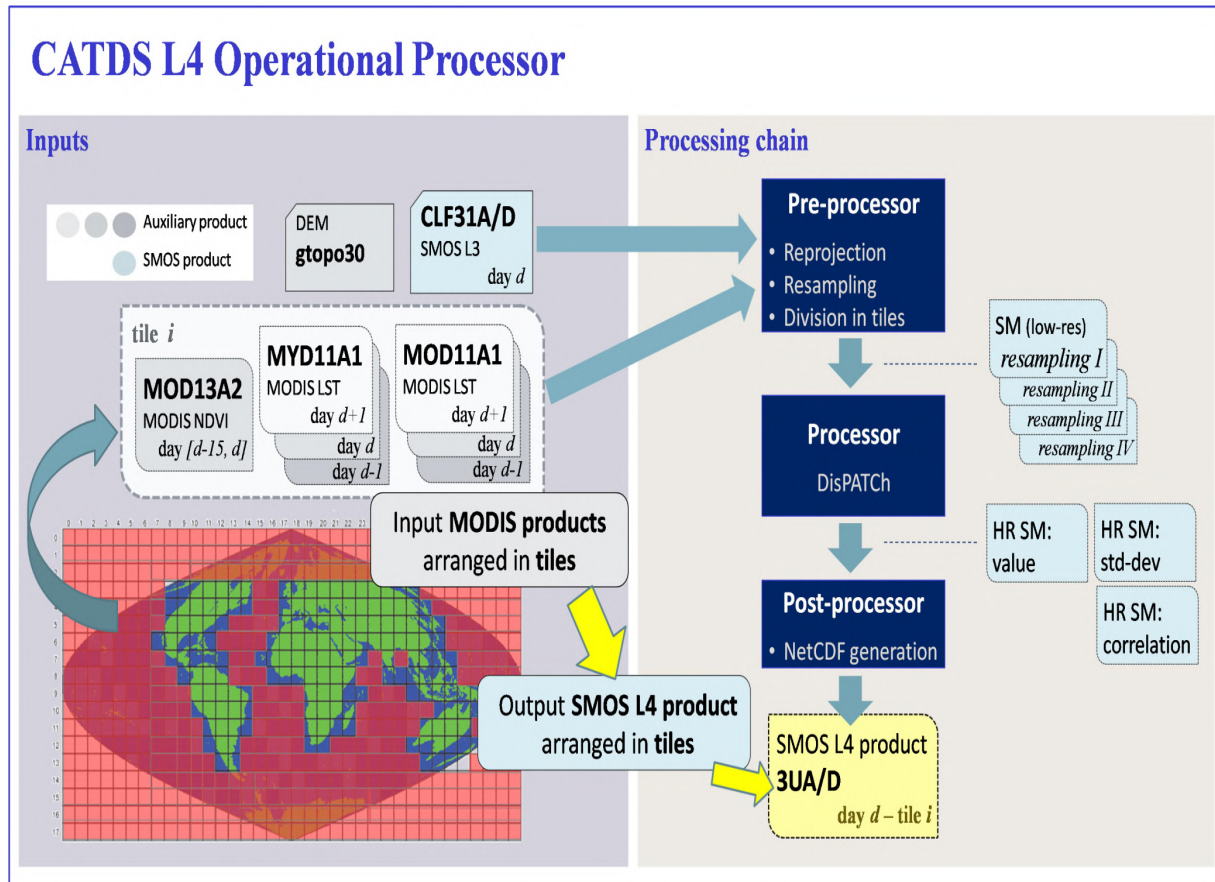


Figure 3.2: Schematic diagram of C4DIS operational processor. Source: (Molero et al., 2016)

The C4DIS processor is divided into two sections: inputs and processing chain. The processor requires 40 km resolution SMOS SM data, and 1 km resolution ancillary LST, and NDVI data from MODIS and DEM data from GTOPO30.

The input data to C4DIS include 40 km resolution SMOS products obtained by shifting the 40 km grid of half a grid resolution in east-west and north-south direction (the resampling of level-3 SMOS data is the double of its spatial resolution) for ascending and descending overpass separately; 6 MODIS LST products received for one day before, same day, and one day after for Aqua and Terra data separately. Each SMOS SM product is individually used for disaggregation using the 6 MODIS LST products (one day before, same day, and one day after), 1 NDVI product, and 1 DEM to produce 24 high-resolution SM products. The processor gives as output a single high-resolution SM product by compositing (averaging) the 24 individual output images.

The processing chain is subdivided into Preprocessing, Processor, and Post-processor steps.

Preprocessing includes the projection where all the input datasets are projected into a similar WGS 84 projection. Each low-resolution SMOS product is re-sampled to a 0.4° grid and high resolution data such as LST, NDVI, and DEM products into a 0.01° grid. All the gridded images for each day are gridded into the MODIS tile.

The processor selects a low resolution SMOS pixel and a high resolution LST pixel that falls within it and selects only the high-quality LST pixels i.e. with quality control equal to either 0 (best quality) or 17 with an estimated error on LST of less than 1 K. The high-quality LST pixels are used for the disaggregation of the SMOS pixel if $2/3$ of the SMOS pixel is in cloud-free condition.

The post-processor converts the output composited image back into netCDF format. Along with the high-resolution SM product, it also provides the standard deviation and count (number of elements within the disaggregation input data sets ensemble) to estimate the uncertainty of each disaggregated SM value. More detailed information about the C4DIS processor can be found in [Molero et al. \(2016\)](#).

3.4 Adaptation of C4DIS to other sensors

C4DIS processor is generic so that it can accept a large number of other input datasets at low resolution and high-resolution datasets. Other sensors such as SMAP and Sentinel-3 provided similar data to SMOS and MODIS respectively, and can therefore be used as alternative input data sets. SMAP is a L-band radiometer that provides global SM products at 40 km resolution with an interval of 1-3 days. SMAP is similar to SMOS as both are L-band passive microwave data have the same spatial and temporal resolutions. So, the plug-in has been developed only in the C4DIS input processor to accept the SMAP datasets.

A plug-in was also added for using high resolution Sentinel-3 LST data as an input to C4DIS. ESA launched the Sentinel-3 satellite in 2016. Sentinel-3 is a sun-synchronous polar orbit with an overpass time of 9:30 a.m. The thermal data collected from Sentinel-3 is based on Sea and Land surface temperature radiometer (SLSTR), a multichannel sensors consisting of 9 spectral bands and three thermal bands to derive LST with an accuracy of 1 K ([Sobrino et al., 2015](#)). Despite the earlier overpass and high accuracy of the data collection, it is similar to MODIS LST in terms of spatio-temporal resolution. It provides LST globally with a spatial resolution of 1 km and a revisit cycle 1-2 days.

The similarity of SMAP SM with SMOS SM and Sentinel-3 LST with MODIS LST allow us to check the performance and accuracy of 1 km SM product from different datasets. Moreover, the combination of all input data is expected to enhance the spatio-temporal coverage of the disaggregated SM data.

3.5 Conclusion

DISPATCH is a downscaling algorithm that disaggregates low resolution SMOS and SMAP SM data using the soil temperature data derived at high resolution from optical/thermal sensors. It uses a SEE model to represent a physical link between the evaporation rate and SM, and first-order Taylor series mathematical tools to link SEE and SM across scales. C4DIS is the operational processor that implements the DISPATCH algorithm on a global basis using SMOS

1-day CLF31A/D products and ancillary data composed of MODIS LST and NDVI products and GTOPO30 DEM data.

The SM output product at 1 km resolution was validated over the Australian region showing an accuracy of $0.04 \text{ m}^3/\text{m}^3$ in semi-arid and flat areas (Malbêteau et al., 2016; Molero et al., 2016). It should be noted that C4DIS SM products show better results in low vegetated areas, low topography, and moderate drainage. Especially the availability of DISPATCH disaggregated SM data is mainly constrained by cloud cover and vegetation cover. Moreover, the 1 km resolution is often too coarse for many applications including irrigation monitoring.

The limitations of the current DISPATCH SM product open a new path of research in the advancement of the SM products at 1 km and even finer resolutions. Further research is done to overcome the effects of cloud cover and to improve the applicability of DISPATCH algorithm over vegetated areas (described in **Chapter 4**) and to improve the spatial resolution to 100 m to be useful for agricultural purposes (described in **Chapter 5**).

Chapter 4

Extending the applicability of the disaggregation algorithm

Contents

4.1	Introduction	58
4.2	A new SM index for DISPATCH algorithm mainly in vegetated areas	59
4.3	New estimates of temperature endmembers in DISPATCH algorithm	60
4.4	A new vegetation index for DISPATCH algorithm mainly in vegetated areas	61
4.5	Conclusion	65
4.6	Article : Extending the Spatio-Temporal Applicability of DISPATCH Soil Moisture Downscaling Algorithm: A Study Case Using SMAP, MODIS and Sentinel-3 Data	66

4.1 Introduction

This chapter seeks to partially overcome two of the main limitations of DISPATCH algorithm, the disaggregation algorithm that was described in the previous **Chapter 3**. The CATDS Level-4 Disaggregation (C4DIS) processor based on the DISPATCH algorithm uses SMOS soil moisture (SM) at 40 km resolution and auxiliary data from MODIS and GTOPO30 to provide SM at 1 km daily on a global scale. The 1 km resolution disaggregated data set offers positive results, especially for arid and semi-arid areas (Merlin et al., 2012; Molero et al., 2016; Malbêteau et al., 2016; Mishra et al., 2018; Colliander et al., 2017b). However, the DISPATCH algorithm used in the C4DIS processor has two significant limitations: 1) it cannot provide SM estimates under fully vegetated areas, and 2) it cannot provide SM in the presence of cloud cover due the unavailability of optical/thermal data. Such constraints significantly reduce the spatio-temporal coverage of the optical-based disaggregated SM data. Hence, it inhibits its potential to be used where SM is required at high temporal coverage.

In practice, we propose to make three substantial changes in the DISPATCH algorithm: 1) the use of Temperature Vegetation Dryness Index (TVDI) approach in DISPATCH algorithm to calculate SM over fully vegetated areas by assuming that TVDI provides a link between surface SM and the root zone SM, 2) the use of Enhanced Vegetation Index (EVI) instead of Normalized Difference Vegetation Index (NDVI) to improve the robustness of the disaggregated SM over vegetated areas by assuming that EVI is more sensitive to the fully grown vegetation and corrects for inaccuracies and uncertainty due to atmospheric conditions and soil conditions, and 3) the use of Sentinel-3 land surface temperature (LST) as thermal data in DISPATCH algorithm instead of MODIS LST by assuming that Sentinel-3 data have less cloud cover due to earlier overpasses.

For brevity, the original DISPATCH algorithm is named $DISPATCH_{classic}$, and the improved DISPATCH algorithm is called $DISPATCH_{veg-ext}$. The modified algorithm is tested over 50 km *50 km areas mimicking three SMAP pixels in the southwest of France and northern Spain. The study area has a wide climatic spectrum - one temperate and two semi-arid regions. The study areas were chosen with the objectives 1) to evaluate the performance of the $DISPATCH_{veg-ext}$ algorithm over temperate and semi-arid regions 2) to assess the performance of $DISPATCH_{veg-ext}$ over different land cover types such as agricultural lands and drylands.

4.2 A new SM index for DISPATCH algorithm mainly in vegetated areas

In SM-limited regions, the spatial dynamics of evapotranspiration (ET) can be determined by the spatial dynamics of LST. The conceptual framework of an evaporative fraction can justify using temperature-derived SM proxies explained as the ratio of ET to available energy and its relationships with SM (Seneviratne et al., 2010).

It is reminded that the original version of DISPATCH uses the soil evaporative efficiency (SEE, ratio of actual to potential soil evaporation) as a SM index. SEE is supposedly more directly linked to the surface SM than EF (Merlin et al., 2012). SEE is estimated from the soil temperature retrieved from the feature space formed by plotting LST as a function of fractional vegetation cover (fvg). Different strategies to separate the soil and vegetation component temperatures are implemented in the four zones A, B, C, and D of the LST-fvg feature space. In zones A, B, and C, SEE can be used to estimate SM in this region because LST is controlled by soil evaporation. However, the SM is mainly controlled by vegetation transpiration in zone D, so SEE is no longer a relevant SM proxy. Hence *DISPATCH_{classic}*, which uses SEE, is only applied to regions that belong to zones A, B, and C of the LST-fvg feature space.

Therefore, a new SM index is required so that DISPATCH can also cover the regions that fall under zone D of the LST-fvg feature space. A choice is made to use the TVDI in place of SEE. TVDI provides water stress conditions over densely vegetated areas and can be used as a SM index in DISPATCH in these regions. Note that TVDI is derived from the vegetation temperature instead of the soil temperature, consistent with the sensitivity of LST to vegetation temperature in the vegetated pixels of zone D. The point is that TVDI is hence more sensitive to the root zone SM via vegetation temperature than to the surface SM via soil temperature. Consequently, an assumption is made to relate TVDI to the surface SM that the variability of surface SM is linked to the variability of root zone SM.

In practice, TVDI is expressed as:

$$TVDI_{HR} = \frac{LST_{dry} - LST_{HR}}{LST_{dry} - LST_{wet}} \quad (4.1)$$

where LST_{dry} and LST_{wet} are the dry and wet LST for a given fvg value, and LST_{HR} is the LST obtained from MODIS or Sentinel-3. TVDI values range from 0 to 1 where 0 represents dry edge (fully stress condition), and 1 represents wet edge (adequate water availability).

The main advantage of using TVDI over SEE is in providing vegetation water stress information over densely vegetated areas and then translating it into SM variabilities in the DISPATCH algorithm. In comparison, TVDI provides water stress conditions over densely vegetated areas and can be used as a soil moisture index in DISPATCH in these regions. The main concern with the use of TVDI is that it can show a non-linear relation between surface SM and root-zone SM (Albergel et al., 2008; Ford et al., 2013).

4.3 New estimates of temperature endmembers in DISPATCH algorithm

To the change of SM proxy in DISPATCH algorithm for zone D, an improvement was also proposed for estimating the temperature endmembers more accurately. It is reminded that temperature endmembers ($T_{s,max}$, $T_{s,min}$, $T_{v,max}$, $T_{v,min}$) are determined from the distribution of data points within the LST-fvg feature space using high-resolution MODIS (LST and NDVI) data within each 40 km resolution SMOS/SMAP pixel. An accurate estimation of temperature endmembers improves the DISPATCH algorithm's accuracy via SEE and TVDI, both dependent on those coarse-scale parameters. The description of the calculation of temperature endmembers used in $DISPATCH_{classic}$ can be found in (Molero et al., 2016).

The improvement suggested for the calculation of temperature endmembers in the $DISPATCH_{veg-ext}$ algorithm in this thesis are:

1. An offset is applied to the dry or wet edge so that the dry or wet edge line passes through maximum and minimum points within a given SMOS/SMAP pixel. It is assumed that all the data points in the LST-fvg graph should be below the dry edge and above the wet edge.
2. The maximum vegetation temperature is subjected to an extra constraint. If the maximum and minimum vegetation temperature is equal to or larger than half of the maximum to minimum soil temperature, then vegetation temperature is set to:

$$T_{v,max} = T_{v,min} + 0.5 * (T_{s,max} - T_{s,min}) \quad (4.2)$$

The temperature endmembers derived from $DISPATCH_{classic}$ (left) and $DISPATCH_{veg-ext}$ algorithm (right) for a given SMOS/SMAP pixel are shown in Figure 4.1 for visual analysis. It is observed that the $DISPATCH_{veg-ext}$ algorithm includes all the LST pixels within the polygon, whereas in $DISPATCH_{classic}$, some LST pixel values are above the dry edge. Moreover, the polygon size is increased in the $DISPATCH_{veg-ext}$ algorithm, and all LST points are inside the polygon envelope compared to $DISPATCH_{classic}$.

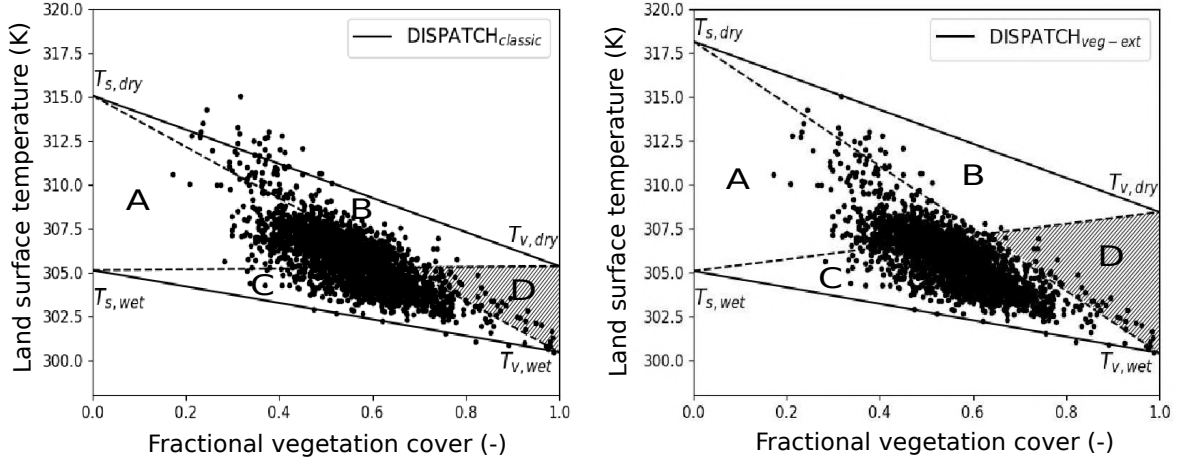


Figure 4.1: Illustration of the calculation of the temperature endmembers in Land surface temperature - fractional vegetation graph for zone A, B, C and D from $DISPATCH_{classic}$ (left) and $DISPATCH_{veg-ext}$ (right) algorithms for MODIS data at 1 km resolution.

4.4 A new vegetation index for DISPATCH algorithm mainly in vegetated areas

A comparison study is undertaken to assess the usefulness of EVI within DISPATCH. MODIS optical data are routinely used to monitor canopy structure, vegetation greenness and leaf area index. The MODIS product named MOD13 is contains two vegetation indices: NDVI and EVI. NDVI and EVI vegetation indices provide a global coverage of the vegetation at 1 km resolution with a temporal cycle of 16 days. NDVI vegetation index is used in the $DISPATCH_{classic}$ algorithm to estimate the fvg used in the derivation of SEE and TVDI.

NDVI is expressed as:

$$NDVI = \frac{\rho_{NIR} - \rho_R}{\rho_{NIR} + \rho_R} \quad (4.3)$$

where ρ_{NIR} and ρ_R the surface reflectances in near-infrared and red bands. fvg is computed from NDVI (Cleugh et al., 2007) as:

$$fvg_{NDVI} = \frac{NDVI_{HR} - NDVI_s}{NDVI_v - NDVI_s} \quad (4.4)$$

where $NDVI_{HR}$ is the NDVI at high-resolution, $NDVI_s$ is the NDVI in bare soil condition, and $NDVI_v$ is the NDVI at full cover vegetation. According to Gutman and Ignatov (1998), $NDVI_s$ and $NDVI_v$ values can be set to 0.15 and 0.90, respectively.

The limitation of NDVI is that it gets saturated in fully grown vegetation (Gitelson, 2004) and is very sensitive to the canopy background condition (Huete et al., 2002). In addition to this, NDVI gets affected by the atmospheric noise (Liu and Huete, 1995) and shows non-linear behavior like ratio-based indices (Jiang et al., 2006). In contrast, EVI does not get saturated in high canopy conditions, decouples the canopy background signal (Huete et al., 2002), is not affected by the background soil condition, and reduces the influence of the atmospheric effect (Matsushita et al.,

2007).

EVI is expressed as:

$$EVI = \frac{G * \rho_{NIR} - \rho_R}{\rho_{NIR} + C_1 * \rho_B - C_2 * \rho_B} + L \quad (4.5)$$

where G is the gain factor, C_1 and C_2 are the coefficients for aerosol correction, ρ_B is blue band surface reflectance, and L is the canopy background adjustment.

Similar to NDVI, the fvg calculated from EVI is expressed as:

$$fvg_{EVI} = \frac{EVI_{HR} - EVI_s}{EVI_v - EVI_s} \quad (4.6)$$

where EVI_{HR} is the EVI at high-resolution, EVI_s is the EVI in bare soil condition, and EVI_v is the EVI at full cover vegetation. Here, EVI_s is set to 0.05 and EVI_v to 0.95 (Mu et al., 2007).

Time series and scatter plot drawn between fvg of NDVI and EVI over three areas ICOS Network, Rhemedus, dryland areas shown in Figure 4.2. In the plots, EVI shows smoother dynamics in time series than NDVI because of the reduced atmospheric effect in EVI. The scatter plot is presented here to study the spatial impact of different soil types. The relative difference between them can be more significant in dryland areas. The vineyard mainly surrounds the dryland area, so a substantial rise is not observed in the middle of the season. Both vegetation indexes behave differently in different regions based on the soil type, canopy structure, and meteorological condition. EVI and NDVI vegetation indices are used separately to evaluate the SM accuracy and performance in the DISPATCH algorithm (evaluation results reported in Table 4.1) over the three different study areas. It can be observed that mean bias (MB) and root mean square difference (RMSD) between the disaggregated and in situ SM are relatively similar while using different vegetation indices in the DISPATCH algorithm. It is observed that the inclusion of EVI slightly improves the performance over the temperate and semi-arid region with an increased temporal correlation in ICOS network (agricultural land) of 7% and 1 to 4% for Rhemedus and dryland areas. The increase in temporal correlation with the use of EVI is explained by the higher the sensitivity of EVI to fvg over densely vegetated areas. Hence, EVI can improve the accuracy and performance of the DISPATCH algorithm for different climatic conditions such as semi-arid and temperate and other land cover types agricultural and dryland areas.

Network	Site	Year	DISPATCH _{veg-ext} (NDVI)					DISPATCH _{veg-ext} (EVI)				
			NR	R (-)	Slope (-)	MB (m ³ /m ³)	RMSD (m ³ /m ³)	NR	R (-)	Slope (-)	MB (m ³ /m ³)	RMSD (m ³ /m ³)
ICOS	Auradé	2017	148	0.40	0.52	0.08	0.10	148	0.42	0.54	0.08	0.10
		2018	141	0.36	0.54	0.10	0.14	141	0.39	0.58	0.08	0.10
	Lamasquère	2017	150	0.40	0.69	0.04	0.08	150	0.40	0.67	0.04	0.08
		2018	140	0.43	0.50	0.07	0.10	140	0.43	0.54	0.06	0.10
		All	145	0.40	0.56	0.07	0.11	145	0.41	0.58	0.07	0.11
Dryland	BA	2019	56	0.65	0.65	0	0.04	56	0.71	0.66	0.01	0.04
	GA		56	0.62	0.75	0.01	0.05	56	0.64	0.74	0.01	0.05
	HA1		53	0.77	1.07	0.02	0.05	53	0.80	0.98	0.02	0.05
	HA2		53	0.79	0.84	0.05	0.06	53	0.80	0.78	0.05	0.06
	PM		54	0.68	0.89	0.01	0.04	54	0.68	0.82	0	0.04
	All	54	0.70	0.84	0.02	0.05	54	0.73	0.80	0.02	0.05	
RHEMEDUS	K13	2017	157	0.44	0.40	0.11	0.13	157	0.43	0.39	0.11	0.12
	K10		160	0.43	1.28	-0.02	0.07	160	0.43	1.27	-0.02	0.06
	M05		161	0.70	1.06	0	0.05	161	0.71	1.04	0	0.04
	N09		161	0.50	0.48	0.08	0.10	161	0.50	0.48	0.08	0.10
	I06		176	0.59	3.61	-0.08	0.10	176	0.59	3.51	-0.08	0.10
	M09		162	0.41	0.51	0.06	0.08	162	0.41	0.50	0.06	0.08
	F06		176	0.51	0.47	0.06	0.09	176	0.53	0.47	0.06	0.09
	H13		180	0.79	1.75	0.02	0.06	180	0.79	1.72	0.02	0.06
	I03		179	0.67	1.88	-0.01	0.05	179	0.68	1.84	-0.01	0.05
	O07		161	0.62	0.94	-0.03	0.05	161	0.63	0.93	-0.03	0.05
	K04		179	0.77	2.95	-0.07	0.08	179	0.77	2.87	-0.07	0.08
	L07		160	0.45	0.41	0.10	0.11	160	0.46	0.42	0.10	0.11
	F11		177	0.77	1.37	-0.04	0.06	177	0.77	1.35	-0.04	0.06
	All	168	0.59	1.32	0.01	0.08	168	0.59	1.29	0.01	0.08	

Table 4.1: Statistical results in terms of correlation, slope, mean bias, RMSD between 1 km resolution disaggregated and in situ SM for *DISPATCH_{veg-ext}* algorithm using NDVI and EVI vegetation index separately.

*NR: Number of retrieval

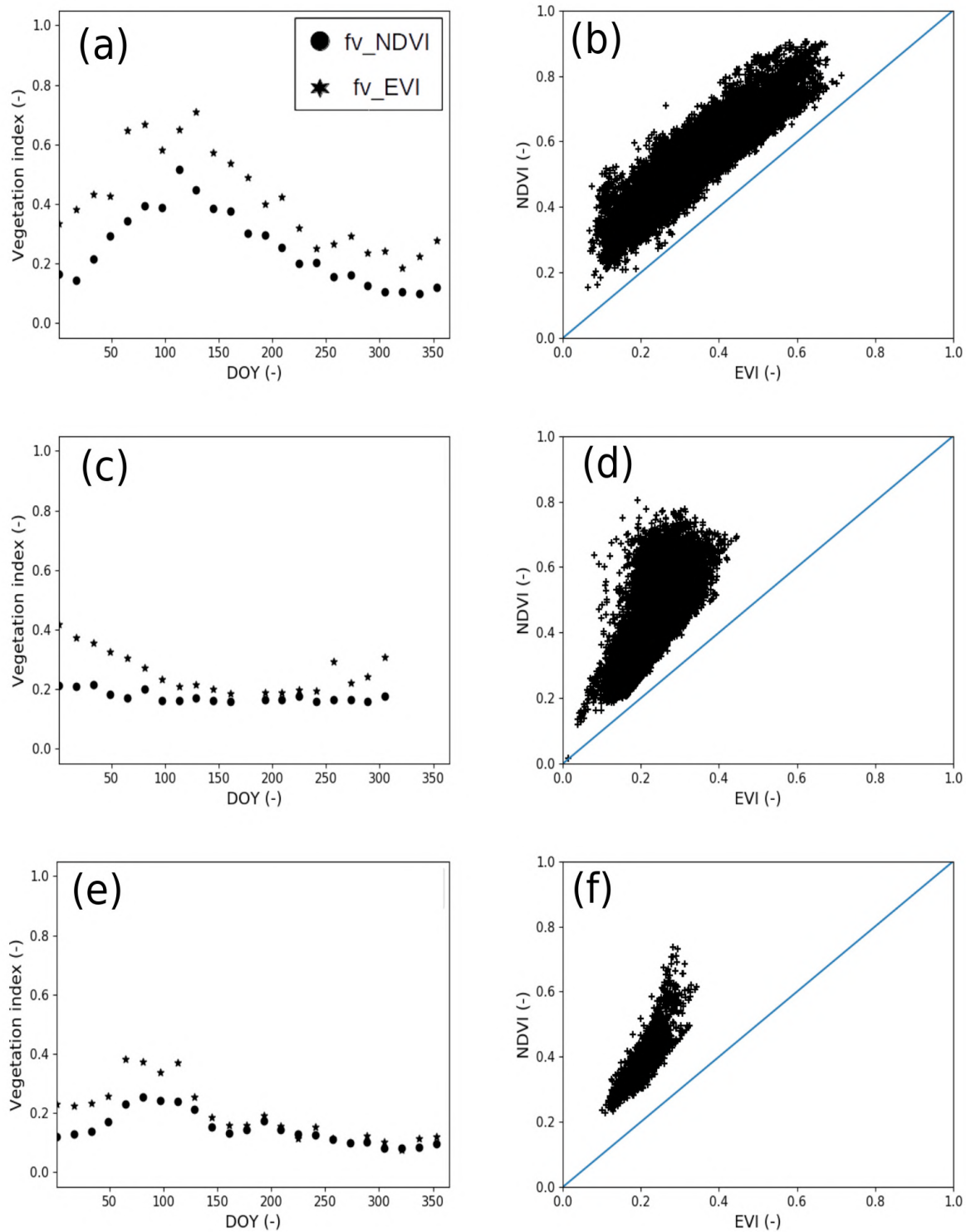


Figure 4.2: Time series of the fractional vegetation cover derived from NDVI and EVI (left) and scatter plot between fractional vegetation covers (right) for ICOS (a,b); dryland (c,d) and Rhemedus (e,f) areas.

4.5 Conclusion

DISPATCH is one downscaling algorithm that uses a thermal-derived SM proxy to disaggregate passive microwave SM data to higher resolutions. The DISPATCH algorithm uses SMOS or SMAP SM product and MODIS LST/NDVI data to downscale the 40 km resolution SM data at 1 km resolution. The original DISPATCH algorithm named *DISPATCH_{classic}* is only applicable to partially vegetated areas and under cloud-free conditions.

A new extension for the *DISPATCH_{classic}* algorithm - that uses TVDI to include the vegetated areas and the calculation of temperature endmembers - is proposed in this chapter and named *DISPATCH_{veg-ext}*. In this improved algorithm, EVI is used instead of NDVI to enhance the robustness of disaggregation over vegetated areas. Sentinel-3 datasets are also used to increase the spatial coverage of the DISPATCH data set and partially overcome the limitation of cloud cover thanks to the earlier overpass of the Sentinel-3.

Both (*DISPATCH_{classic}* and *DISPATCH_{veg-ext}*) algorithms are tested over one temperate site of the South of France (Aurade and Lamasquere) and two semi-arid regions (Rhemedus and dryland areas). When using Sentinel-3 instead of MODIS, the visual interpretation of downscaled product for the *DISPATCH_{veg-ext}* algorithm shows a 58-86% increase in spatial coverage for the whole MODIS tile and 6-9% over the temperate site and 3-6% over semi-arid zones. The use of EVI improves the performance by 7% over the temperate region and 1-4% over the semi-arid region without degrading the accuracy of the downscaled SM product. The significant increase in the spatio-temporal coverage of the DISPATCH data set will be an asset for building synergies with other remotely sensed data with different revisit times and observations capabilities (**Chapter 5** and **Chapter 6**) and assimilation studies (**Chapter 7**).

4.6 Article : Extending the Spatio-Temporal Applicability of DISPATCH Soil Moisture Downscaling Algorithm: A Study Case Using SMAP, MODIS and Sentinel-3 Data

1. Ojha, N., Merlin, O., Suere, C. and Escorihuela, M.J., 2021. Extending the Spatio-Temporal Applicability of DISPATCH Soil Moisture Downscaling Algorithm: A Study Case Using SMAP, MODIS and Sentinel-3 Data. *Frontiers in Environmental Science*, 9, p.40.



Extending the Spatio-Temporal Applicability of DISPATCH Soil Moisture Downscaling Algorithm: A Study Case Using SMAP, MODIS and Sentinel-3 Data

Nitu Ojha^{1*}, Olivier Merlin¹, Christophe Suere¹ and Maria José Escorihuela²

¹CESBIO, Université de Toulouse, CNES/CNRS/INRA/IRD/UPS, Toulouse, France, ²isardSAT S.L, Parc Tecnologic Barcelona Activa, Barcelona, Spain

OPEN ACCESS

Edited by:

Zheng Duan,
Lund University, Sweden

Reviewed by:

Lingmei Jiang,
Beijing Normal University, China
Yawei Wang,
Ludwig Maximilian University of
Munich, Germany

*Correspondence:

Nitu Ojha
ojhan@cesbio.cnes.fr

Specialty section:

This article was submitted to
Environmental Informatics
and Remote Sensing,
a section of the journal
Frontiers in Environmental Science

Received: 24 April 2020

Accepted: 01 February 2021

Published: 16 March 2021

Citation:

Ojha N, Merlin O, Suere C and
Escorihuela MJ (2021) Extending the
Spatio-Temporal Applicability of
DISPATCH Soil Moisture Downscaling
Algorithm: A Study Case Using SMAP,
MODIS and Sentinel-3 Data.
Front. Environ. Sci. 9:555216.
doi: 10.3389/fenvs.2021.555216

DISPATCH is a disaggregation algorithm of the low-resolution soil moisture (SM) estimates derived from passive microwave observations. It provides disaggregated SM data at typically 1 km resolution by using the soil evaporative efficiency (SEE) estimated from optical/thermal data collected around solar noon. DISPATCH is based on the relationship between the evapo-transpiration rate and the surface SM under non-energy-limited conditions and hence is well adapted for semi-arid regions with generally low cloud cover and sparse vegetation. The objective of this paper is to extend the spatio-temporal coverage of DISPATCH data by 1) including more densely vegetated areas and 2) assessing the usefulness of thermal data collected earlier in the morning. Especially, we evaluate the performance of the Temperature Vegetation Dryness Index (TVDI) instead of SEE in the DISPATCH algorithm over vegetated areas (called vegetation-extended DISPATCH) and we quantify the increase in coverage using Sentinel-3 (overpass at around 09:30 am) instead of MODIS (overpass at around 10:30 am and 1:30 pm for Terra and Aqua, respectively) data. In this study, DISPATCH is applied to 36 km resolution Soil Moisture Active and Passive SM data over three 50 km by 50 km areas in Spain and France to assess the effectiveness of the approach over temperate and semi-arid regions. The use of TVDI within DISPATCH increases the coverage of disaggregated images by 9 and 14% over the temperate and semi-arid sites, respectively. Moreover, including the vegetated pixels in the validation areas increases the overall correlation between satellite and *in situ* SM from 0.36 to 0.43 and from 0.41 to 0.79 for the temperate and semi-arid regions, respectively. The use of Sentinel-3 can increase the spatio-temporal coverage by up to 44% over the considered MODIS tile, while the overlapping disaggregated data sets derived from Sentinel-3 and MODIS land surface temperature data are strongly correlated (around 0.7). Additionally, the correlation between satellite and *in situ* SM is significantly better for DISPATCH (0.39–0.80) than for the Copernicus Sentinel-1-based (–0.03 to 0.69) and SMAP/S1 (0.37–0.74) product over the three studies (temperate and semi-arid) areas, with an increase in yearly valid retrievals for the vegetation-extended DISPATCH algorithm.

Keywords: soil moisture, DISPATCH, TVDI, EVI, SMAP, Sentinel-3

1 INTRODUCTION

Soil moisture (SM) is an important element in the hydrologic cycle, especially influencing precipitation, infiltration, and runoff (Hamlet et al., 2007). SM is thus useful for different applications such as meteorology (Dirmeyer, 2000), climatology (Douville, 2004), hydrology (Chen et al., 2011) and agriculture (Guéris and Duke, 2000). SM has a very high spatio-temporal variability and to approximate such a variability of SM, *in situ* measurements are not applicable on a global basis. Instead remote sensing techniques have a strong potential to provide SM estimates at multiple scales globally.

Currently, L-band radiometry is acknowledged as one of the most efficient technique to retrieve the surface SM on a global scale. Based on L-band radiometer, Soil Moisture and Ocean Salinity (SMOS, Kerr et al., 2012) satellite was launched by European Space Agency (ESA) on November 2, 2009 and Soil Moisture Active Passive (SMAP, Entekhabi et al., 2010) was launched by National Aeronautics and Space Administration (NASA) on January 31, 2015. Both satellites provide SM at a sensing depth of 3–5 cm with a spatial resolution of about 40 km and a revisit cycle of about 3 days on a global basis. Since L-band emission is highly sensitive to SM and relatively less sensitive to soil roughness and vegetation optical-depth (Wigneron et al., 2017), it can be used to derive SM with high precision.

Passive (including L-band) microwave-derived SM products are regularly evaluated and are found to be suitable for hydro-climatic applications (Wanders et al., 2014; Lievens et al., 2015). But for most of the hydrological and agricultural purposes, SM data are required at a much higher (i.e., at least kilometeric) spatial resolution. Active microwave (e.g., Synthetic Aperture Radar) can be used to derive SM at kilometeric or sub-kilometeric spatial resolution (Wegmuller and Werner, 1997; Bauer-Marschallinger et al., 2018). However, the major disadvantage of the radar techniques is the high sensitivity of the surface backscatter to disturbing factors such as notably vegetation structure (Waite and MacDonald, 1971), soil roughness (Verhoest et al., 2008) and topography (Atwood et al., 2014). Consequently, to overcome the limitation of both microwave techniques, various researches have been done in the past to combine active and passive microwave data (Narayan et al., 2006; Piles et al., 2009; Das et al., 2010). In particular, based on this technique, NASA recently developed a method that provides SM at 9 and 3 km resolution from SMAP data (Jagdhuber et al., 2017; Lievens et al., 2017; Das et al., 2018).

Alternatively, optical/thermal sensors such as Moderate resolution Imaging Spectroradiometer (MODIS) are extensively used to retrieve SM proxies from land surface temperature (LST) and normalized vegetation index (NDVI) (Peng et al., 2015a; Zhang and Zhou, 2016). The triangle (Carlson, 2007) or trapezoid (Moran et al., 1994) method is built by assuming that it covers the sensitivity of LST for fully vegetated areas and bare soil conditions. The fully dry and well-watered surface conditions can be determined as edges of the LST-NDVI feature space. Based on the LST-NDVI approach, various moisture index methods have been proposed like the crop water stress index (CWSI, Moran et al., 1994), the vegetation

condition index (VCI, Kogan, 1995), the normalized difference water index (NDWI, Gao, 1996) and the temperature vegetation dryness index (TVDI) (Sandholt et al., 2002). The TVDI in particular is a land surface dryness index used to calculate water-stress condition.

Further, an optical-derived SM proxy is used to disaggregate passive microwave derived SM data by establishing a link between LST and SM through the evapotranspiration process (Merlin et al., 2005; Kim and Hogue, 2012; Peng et al., 2015a; Peng et al., 2015b). Based on this, the DISPATCH method (Merlin et al., 2012; Merlin et al., 2013) was developed. DISPATCH estimates the soil evaporative efficiency (SEE, defined as the ratio of actual to potential soil evaporation) from optical/thermal data and expresses the disaggregated SM through a downscaling relationship between the SM observed at low resolution (LR) and the SEE derived at high resolution (HR). Given that SEE has a mostly linear relationship with soil temperature (Merlin et al., 2013), SEE is estimated as the optical-derived soil temperature normalized by its maximum and minimum values corresponding to dry and wet soil conditions in the LST-NDVI feature space (Merlin et al., 2012). For routine application of DISPATCH, the C4DIS processor was implemented at the Centre Aval de Traitement des données SMOS (CATDS) as a level-4 SM product (Molero et al., 2016). C4DIS processor provides SM at 1 km resolution product on a daily-global basis using LR SMOS SM and HR MODIS data. The C4DIS was recently adapted to integrate SMAP and Sentinel-3 data in replacement of SMOS and MODIS data, respectively.

Various researches have shown that the application of DISPATCH to SMAP or SMOS data provides a 1 km resolution SM product with satisfying accuracy in arid and semi-arid regions (Malbêteau et al., 2016; Molero et al., 2016; Colliander et al., 2017; Mishra et al., 2018). However DISPATCH, like all the optical-based SM disaggregation methods, has two main intrinsic limitations: 1) the soil surface temperature that is related to the surface (0–5 cm) SM cannot be retrieved underneath the vegetation cover and 2) optical/thermal data are unavailable in cloudy conditions. Such constraints significantly reduce the spatio-temporal coverage of optical-disaggregated SM images, which potentially hinders several applications requiring data at high temporal frequency.

In this context, the paper aims to partly overcome the above mentioned limitations by testing three significant changes in the DISPATCH algorithm. Firstly, over densely vegetated pixels, the DISPATCH downscaling relationship is implemented using the TVDI (Sandholt et al., 2002), by assuming over those areas a link between the surface SM (as sensed by SMOS/SMAP) and the TVDI-derived root zone SM. Secondly, the enhanced vegetation index (EVI) is used in place of NDVI to improve the robustness of disaggregated SM over vegetated region. In fact, EVI is expected to be more sensitive to vegetation density and to correct for inaccuracies due to atmospheric and soil conditions. Thirdly, Sentinel-3 LST is tested as input to DISPATCH in place of MODIS LST by assuming that an earlier optical/thermal observation is generally less affected by clouds (Georgiana Stefan et al., 2018).

The main objective of this paper is therefore to improve the spatio-temporal coverage and the robustness over vegetated areas of the 1 km resolution of DISPATCH SM. The approach is applied to SMAP SM data and tested over three 50 km by 50 km study areas in France and Spain with one temperate and two semi-arid regions. Results of the new vegetation-extended DISPATCH algorithm is assessed against *in situ* measurements collected in all three study areas, as well as against the 1 km resolution, Copernicus SM data derived from Sentinel-1 radar data and SMAP/S1 data derived from Sentinel-1 and SMAP.

2 MATERIALS AND METHODS

2.1 Study Area and *In Situ* Data

Three study areas of 50 km by 50 km are selected in the South-West of France (ICOS sites), and in the West (REMEDHUS sites) and East (dryland sites) of Spain (location is shown in **Figure 1**). The extent of each study area is defined in order to encompass at least one SMAP pixel and to represent the sub-pixel variability at the 1 km resolution. The main objective for the selection of study areas is two-fold 1) to evaluate the performance of DISPATCH under different climatic conditions including temperate and semi-arid, and 2) to evaluate the performance of DISPATCH over different land cover types such as agricultural land and dryland areas. A detailed description of the SM monitoring sites within each of the three study areas is provided below.

- i) ICOS network (South-West of France): It includes Auradé (43°32′58.81 N, 01°06′22.08 E) and Lamasquère (43°50′05 N, 01°24′19 E), which are located near Toulouse at a distance of 12 km from each other. The study area has temperate climatic conditions with an annual average precipitation of 700 mm. The land is mainly covered by agricultural field. Soil texture is clay loam for Auradé with clay and sand contents of 32.3 and 20.6%, respectively, while soil texture for Lamasquère is clay with clay and sand fraction contents of 54 and 12%, respectively. SM is measured by CS616 (Campbell Scientific Inc., Logan, UT, USA) probes at depths of 0.05, 0.10, and 0.30 m. CS616 probe uses soil dielectric permittivity to measure the volumetric soil water content. The *in situ* SM data collected at 5 cm depth for years 2017 and 2018 are used in this study. Detailed information about field instrumentation and agricultural practices can be found in Béziat et al. (2009) and Tallec et al. (2013).
- ii) REMEDHUS network (West of Spain): REMEDHUS is a very dense network, consisting of 20 stations located near the center of Duero basin (41.1–41.5°N, 5.1–5.7°W). The study area has semi-arid Mediterranean climate with an annual average precipitation 385 mm. In this paper 13 stations are used. The land is mainly covered by croplands, shrublands, forests and pasture. Soil type is silty and clayey sand. SM is measured by a dielectric sensor (hydra probe and Stevens water monitoring system), which measures the volumetric SM at a depth of 0.00–0.05 m. The *in situ* SM collected for 2017 are used in this study is obtained from the International Soil Moisture Network (ISMN) (Dorigo et al., 2011).
- iii) Dryland sites (East of Spain): Dryland areas are selected from the Tarragona province of Catalunya, Spain. Land is mainly covered

by rainfed crops. Soil texture of this area is clayey. The monitoring network consists of seven stations. SM is measured at a depth of 5 cm by Teros sensor 10. The *in situ* SM data collected from June to November 2019 are used in this study. The dryland sites area exhibits a semi-arid Mediterranean climate, which is dry and warm in summer and cold and wet in winter. The average annual precipitation is 385 mm with an elevation of 700–900 m above sea level.

2.2 Remote Sensing Data

2.2.1 SMAP SM Data

SMAP is a L-band satellite mission, launched in January 2015, that combines 1 km resolution radar and 36 km resolution radiometer observations to provide SM at 9 km resolution. But due to improper functioning of SMAP radar, currently SMAP provides SM at 36 km resolution (radiometer) on a global-daily basis. SMAP satellite has a near-polar sun-synchronous orbit with an altitude of 658 km. The SMAP swath is about 1,000 km width with a revisit cycle of 2–3 days. In this paper, SMAP level-3 daily SM product (named as L3SMP A/D, version 005) with an ascending and descending overpass of 6 pm/6 am is used separately as an input to DISPATCH algorithm. These products are in HDF format and cylindrically projected on the EASE grid version 2.0. SMAP data can be downloaded from <https://nsidc.org/data/SPL3SMP/versions/5>. In addition to this, SMAP/S1 (named as L2_SM_SP) provides SM at 1 km resolution is used for the statistical analysis with DISPATCH data. SMAP/S1 use Sentinel-1A and Sentinel-1B to disaggregate SMAP (~36 km) data at 1 km resolution.

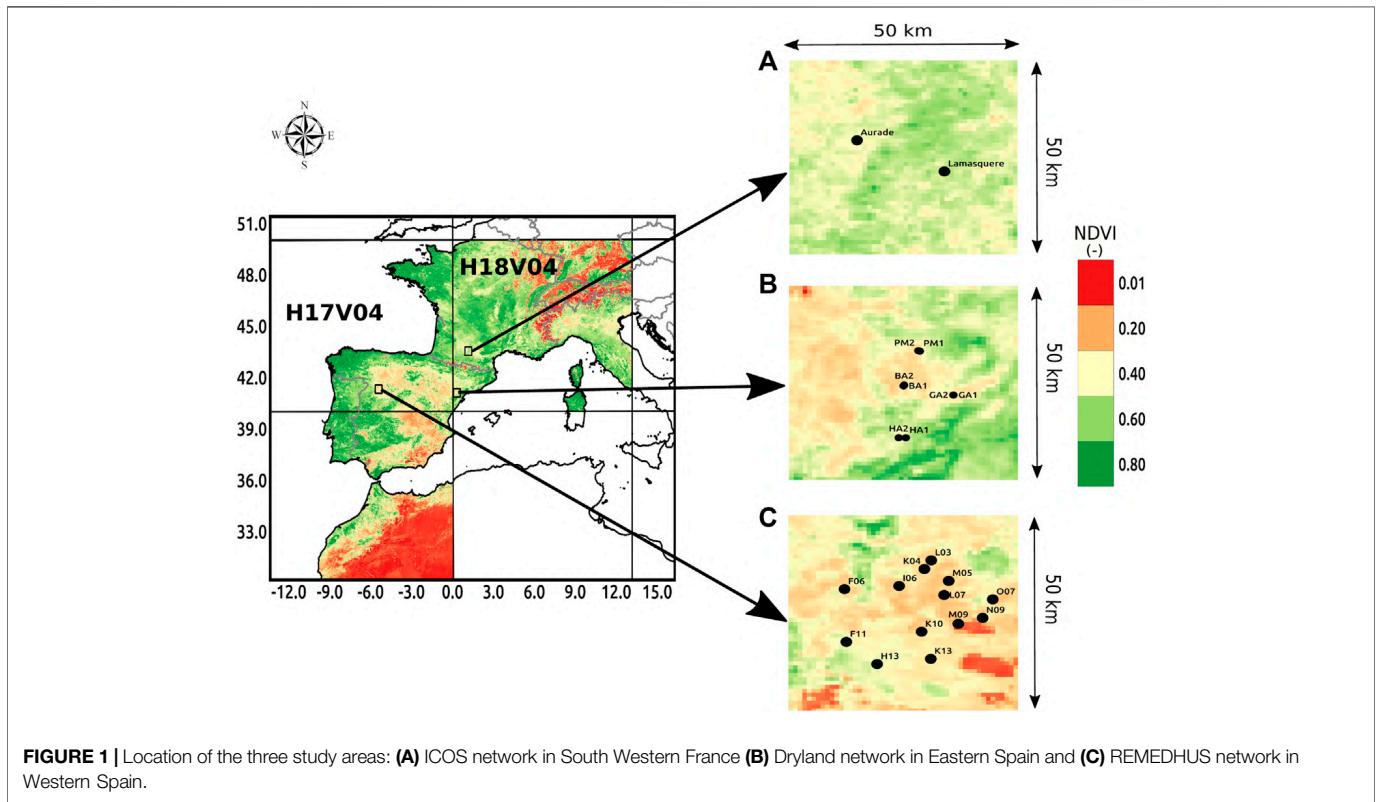
2.2.2 MODIS Optical Data

The C4DIS processor presented in Molero et al. (2016) uses the MODIS version 6 optical/thermal data. The Terra overpass (10:30 am)—named as MOD11A- and Aqua overpass (1:30 pm)—named as MYD11A1—gives 1 km resolution LST data on a daily basis. In DISPATCH algorithm, 6 MODIS LST products (1 day before, same day and 1 day after the SMAP overpass) are used as an input for each SMAP ascending and descending overpass. MODIS version 6 MOD13 is used to monitor canopy structure, leaf area index and vegetation greenness extent, and contains two vegetation indices—NDVI and EVI—as sub-datasets. MODIS NDVI and EVI products provide data continuously at 1 km spatial and 16-day temporal resolution for global vegetation coverage. NDVI is used in the original DISPATCH algorithm for disaggregation of SM at HR (Merlin et al., 2012). NDVI is defined as:

$$NDVI = \frac{\rho_{NIR} - \rho_R}{\rho_{NIR} + \rho_R} \quad (1)$$

where ρ_{NIR} and ρ_R are the surface reflectances from MODIS near infrared and red bands, respectively.

The main limitation of NDVI is that it is very sensitive to canopy background (Huete et al., 2002) and gets saturated in conditions of high biomass (Gitelson, 2004). Another limitation is that it shows a non-linear behavior like ratio-based indices (Jiang et al., 2006) and is affected by atmospheric noise (Liu and Huete,



1995). EVI was thus developed to improve the sensitivity to high biomass conditions. It also decouples the canopy background signal (Huete et al., 2002) and reduces atmospheric influence (Matsushita et al., 2007). EVI is computed as:

$$EVI = \frac{G * \rho_{NIR} - \rho_R}{\rho_{NIR} + C_1 * \rho_B - C_2 * \rho_B} + L \quad (2)$$

where, ρ_B is the surface reflectance from blue band, L is the canopy background adjustment, C_1 and C_2 are the coefficients for aerosol correction and G is the gain factor.

DISPATCH relies on the fractional vegetation cover (f_{vg}) derived from the vegetation index. Cleugh et al. (2007) calculated f_{vg} from NDVI:

$$f_{vgNDVI} = \frac{NDVI_{HR} - NDVI_s}{NDVI_v - NDVI_s} \quad (3)$$

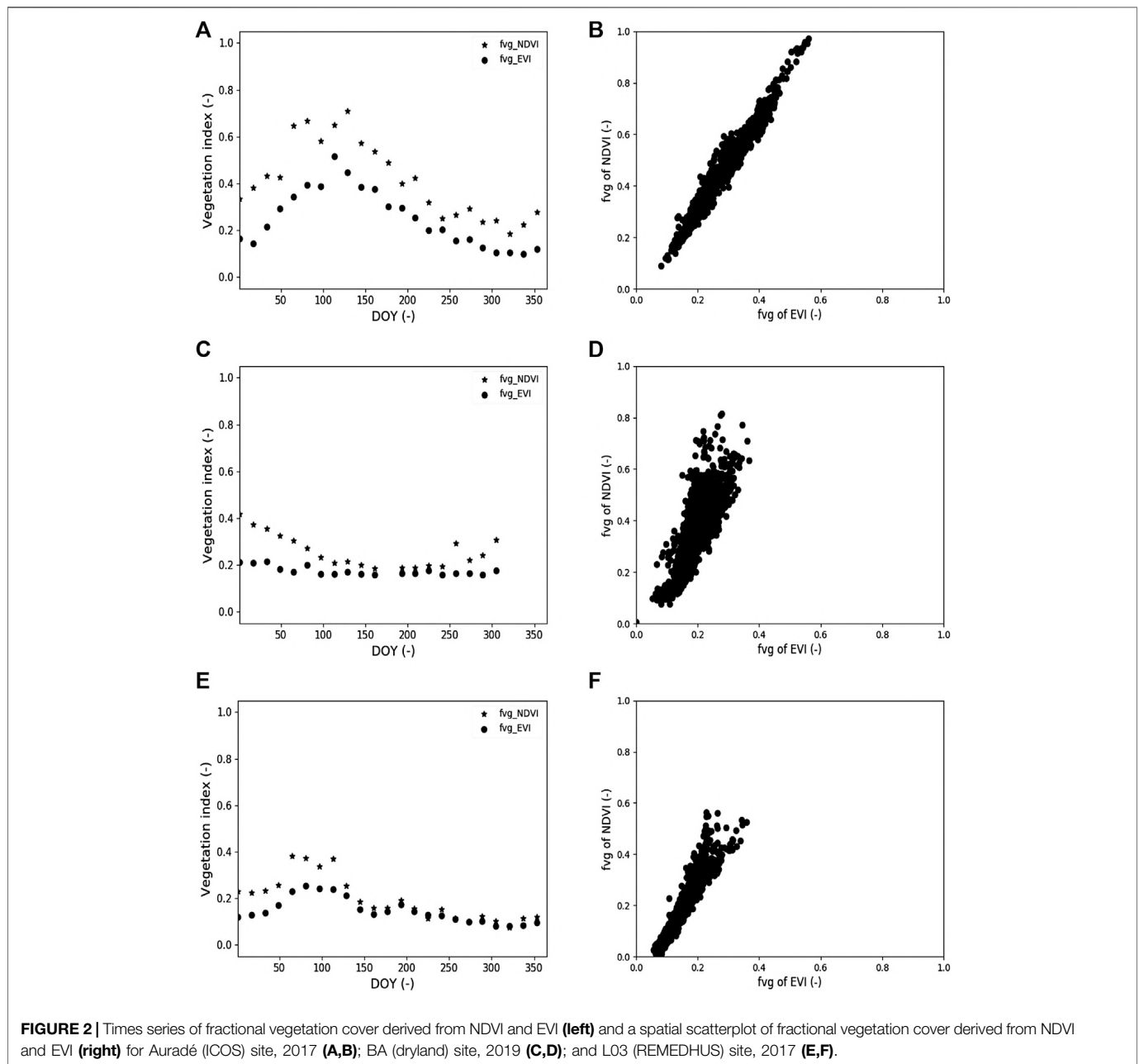
where $NDVI_{HR}$ is the MODIS NDVI at 1 km resolution, $NDVI_s$ is NDVI at bare soil and $NDVI_v$ is NDVI at full vegetation cover. Here $NDVI_s$ and $NDVI_v$ are set to 0.15 and 0.90, respectively (Gutman and Ignatov, 1998).

Similarly, f_{vg} can be estimated from EVI:

$$f_{vgEVI} = \frac{EVI_{HR} - EVI_s}{EVI_v - EVI_s} \quad (4)$$

where EVI_{HR} is the MODIS EVI at 1 km resolution, EVI_s is EVI at bare soil and EVI_v is EVI at full vegetation cover. Here EVI_s and EVI_v are set to 0.05 and 0.95, respectively (Mu et al., 2007).

EVI aims to provide a VI with reduced sensitivity to (daily) atmospheric effects and to (constant) background soil effects, while no such correction for soil or atmospheric effects is undertaken for NDVI. The time series and scatter plot comparisons between NDVI and EVI are hence presented to visually assess the possible artifacts in the temporal and in spatial pattern in NDVI that may occur due to atmospheric disruptive effects and/or to the background soil variability between study areas. **Figure 2** presents the time series of the 1 km resolution fractional vegetation cover derived from NDVI and EVI at Auradé site (ICOS study area), BA (dryland area) and F11 (REMEDHUS network study area) (left side) and also presents the scatter plot comparison of both fractional vegetation cover estimates extracted over ICOS, dryland, and REMEDHUS study areas (right side). The time series evolution in **Figure 2** observed a relatively smoother dynamics of EVI compared to NDVI, suggesting that the atmospheric effects are reduced in EVI data. The effect of different soil types is observed in the spatial scatter plot of **Figure 2** (right side) between the fractional vegetation cover derived from NDVI and EVI over each of the three study areas. Relative differences are more significant over the dryland sites. Since the dryland sites are covered by vineyards, a big jump of NDVI is not observed in the middle of the season. It is therefore observed that NDVI and EVI behave differently in different areas depending on meteorological conditions, canopy structure and soil type. This is the rationale for evaluating the performance of DISPATCH using EVI and NDVI vegetation indices separately for different regions.



2.2.3 Sentinel-3 Optical Data

Sentinel-3 satellite was launched by ESA in February 2016. Sentinel-3 has a sun-synchronous polar orbit with an altitude of 815 km and an overpass at 09:30 a.m. The LST Sentinel-3 product is derived from data collected by the Sea and Land Surface Temperature Radiometer (SLSTR) instrument. SLSTR is a multi-channel radiometer with nine spectral bands including three thermal bands, which are used to derive LST from the split-window method with an accuracy better than 1 K (Sobrino et al., 2015). Despite the earlier overpass of Sentinel-3 and the expected enhanced accuracy of Sentinel-3 LST data, SLSTR LST data are pretty similar to MODIS LST data in terms of spatio-temporal resolution: 1 km resolution with 1- or 2-day revisit time. In this

paper, the daily Sentinel-3 LST product named SL2LST downloaded from <https://scihub.copernicus.eu> is used as input to DISPATCH algorithm in place of MODIS LST. In the DISPATCH algorithm, three Sentinel-3 LST images are used (1 day before, same day, and 1 day after) as input for each SMAP ascending and descending overpass. Note that in this application, the NDVI/EVI data are still derived from MODIS to focus on the DISPATCH output differences associated with the input data of (MODIS or Sentinel-3) LST.

2.2.4 DEM Data

ETOPO 30 digital elevation model (DEM) data at 30 arc second resolution are used to correct the 1 km resolution MODIS/Sentinel-3 LST for topographic effects, before its use for SEE/

TVDI estimates within DISPATCH (Merlin et al., 2013). The DEM can be downloaded from <https://lta.cr.usgs.gov/GTOPO30>.

2.2.5 Copernicus Sentinel-1 SM Product

Copernicus global land service provides a SM product over Europe at 1 km resolution from 2016. The change detection method from Technological University of Vienna (TU-Wien) is used to derive daily relative SM estimates from the C-band Sentinel-1 backscatter time series collected in Interferometric Wide Swath (IW) and VV-polarization mode (Bauer-Marschallinger et al., 2018). In practice, the Copernicus Sentinel-1 relative SM (expressed in percentage from 0 to 100%) is derived from the angle-normalized backscattering coefficient linearly scaled between wet and dry conditions at each location individually. Data can be downloaded at <https://land.copernicus.eu/global/products/ssm>.

For comparing the performance of Copernicus and DISPATCH SM data sets at the validation sites, the Copernicus relative SM is converted into volumetric SM from the extreme SM values estimated at the site level using texture information:

$$SM_{S1} = SM_{min} + (SM_{max} - SM_{min}) * RSM_{S1} \quad (5)$$

Where SM_{S1} is the re-scaled SM (m^3/m^3), RSM_{S1} is the relative SM value (%) of Copernicus Sentinel-1 SM, and SM_{max} (m^3/m^3) and SM_{min} (m^3/m^3) are the SM at saturation and the residual SM estimated from pedotransfer functions in Cosby et al. (1984) and Brisson and Perrier (1991), respectively (Merlin et al., 2016).

2.3 DISPATCH

2.3.1 General Equations

The DISPATCH downscaling equation relies on HR optical-derived SM proxy (SEE in the current version of DISPATCH) to disaggregate LR (SMOS or SMAP) SM at HR:

$$SM_{HR} = SM_{LR} + \left(\frac{\delta SEE}{\delta SM} \right)_{LR}^{-1} * (SEE_{HR} - SEE_{LR}) \quad (6)$$

where SM_{HR} is the disaggregated SM at HR, SM_{LR} is the SM at LR observed by SMAP, SEE_{HR} is the SEE at HR derived from MODIS and/or Sentinel-3 data, SEE_{LR} serves as the aggregated HR SEE at LR and $(\delta SEE / \delta SM)_{LR}^{-1}$ is the inverse of the partial derivate of SEE(SM) at LR. In Eq. 6, SEE is expressed as:

$$SEE_{HR} = \frac{T_{s,max} - T_{s,HR}}{T_{s,max} - T_{s,min}} \quad (7)$$

where $T_{s,max}$ is the soil surface temperature at HR, and $T_{s,max}$ and $T_{s,min}$ are the soil temperature in fully dry (SEE = 0) and water-saturated (SEE = 1) conditions, respectively. Soil temperature endmembers $T_{s,max}$ and $T_{s,min}$ are estimated from the extreme LST values observed within the LST- f_{vg} feature space obtained with MODIS or Sentinel-3 data. The soil temperature in Eq. 7 is obtained from the linear decomposition of LST into soil and vegetation temperature using the trapezoid method (Merlin et al., 2012):

$$T_{s,HR} = \frac{LST_{HR} - f_{vg,HR} * T_{v,HR}}{1 - f_{vg,HR}} \quad (8)$$

where, LST_{HR} is the HR LST derived from MODIS or Sentinel-3 data, $f_{vg,HR}$ is the HR fractional vegetation cover derived from MODIS data and $T_{v,HR}$ is the HR vegetation temperature bounded by its maximum ($T_{v,max}$) and minimum value ($T_{v,min}$).

As fully described in Merlin et al. (2012), the retrieval of soil temperature in Eq. 8 depends on the estimation of vegetation temperature, which depends on the location of the associated HR pixel in the LST- f_{vg} feature space. As illustrated in Figure 3A, the LST- f_{vg} feature space is divided in four zones A, B, C, and D. In zone D, where the LST is mainly controlled by the vegetation temperature, the retrieved soil temperature is assumed to be constant meaning that SEE is uniform with the SMOS/SMAP pixel and the downscaling relationship is not applied. In summary, the use of SEE in the downscaling relationship of Eq. 6 implies that disaggregation is only possible in zones A, B, and C. No disaggregated SM value is provided by DISPATCH for the HR pixels located in zone D.

Note that Eq. 6 is applied to all SMOS/SMAP pixels over which the cloud cover percentage is lower than a given threshold (named the cloud cover threshold) set to 33% in the current DISPATCH version. Under cloud cover, the SEE values are set to the average SEE within the LR pixel, but no disaggregated SM value is provided.

More details on the DISPATCH method are provided in Merlin et al. (2012) and Merlin et al. (2013). Note that the original DISPATCH algorithm as described by the above equations and implemented in the current C4DIS processor (Molero et al., 2016) is named DISPATCH_{classic} in this paper.

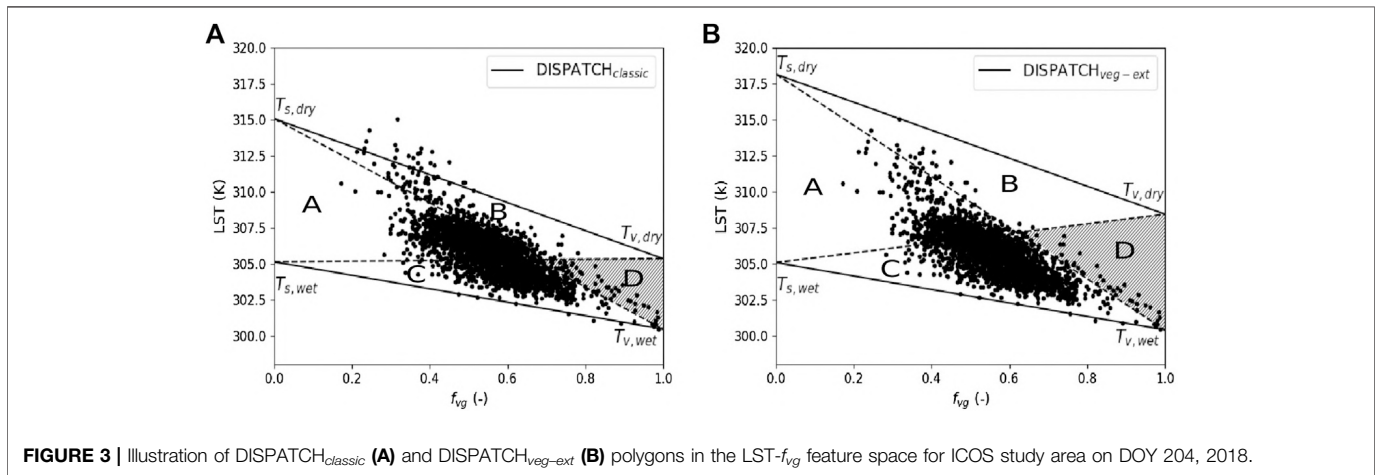
2.4 The Vegetation-Extended DISPATCH Version (DISPATCH_{veg-ext})

The objective of the new DISPATCH version is to apply the downscaling relationship of Eq. 6 to zone D, where the variability of LST for a given f_{vg} value is mainly attributed to the vegetation temperature. DISPATCH_{veg-ext} is thus an extension of DISPATCH_{classic} algorithm to densely vegetated areas. The main difference between DISPATCH_{classic} and DISPATCH_{veg-ext} is that SEE is replaced by TVDI in zone D of the LST- f_{vg} feature space. TVDI is hence used in the DISPATCH_{veg-ext} algorithm to calculate the disaggregated SM over vegetated pixels where transpiration is dominant (over the soil evaporation). By using TDVI instead of SEE, we are making an implicit assumption that the surface SM is linked to the root zone SM (Kumar et al., 2009).

TVDI is defined as

$$TVDI_{HR} = \frac{LST_{max} - LST_{HR}}{LST_{max} - LST_{min}} \quad (9)$$

where, LST_{min} and LST_{max} are defined as the minimum and maximum LST the wet and dry edge and LST_{HR} is the observed LST within a given MODIS/Sentinel-3 pixel. TVDI provides values in the range of 0–1, where 1 represents a wet edge (adequate water availability for vegetation) and 0 represents a dry edge (vegetation water stress condition).



2.5 Estimating Temperature Endmembers

It is reminded that DISPATCH_{classic} operates only on zones A, B, C of the LST- f_{vg} feature space where the soil temperature can be retrieved but DISPATCH_{veg-ext} algorithm additionally operates on zone D where vegetation temperature is dominant. Replacing SEE by TVDI in Eq. 6 thus involves modifying the algorithm for estimating temperature endmembers. SEE is more sensitive to the surface soil moisture via the soil temperature retrieved over bare or partially vegetated pixels, while TVDI is more sensitive to the root zone soil moisture via the vegetation temperature retrieved over vegetated pixels. As a matter of fact, SEE cannot be retrieved from satellite over densely vegetated areas. Therefore, TVDI has the advantage over SEE to provide vegetation water stress information over densely vegetated areas that can be translated into soil moisture variabilities within DISPATCH. However, the main issue with the use of TVDI instead of SEE is the link between the root zone soil moisture (information provided by TVDI) and the surface soil moisture (as retrieved from SMAP), which might not be linear (Albergel et al., 2008; Ford et al., 2013).

Figure 3 gives an illustration of the temperature endmembers retrieved from the DISPATCH_{classic} (A) and DISPATCH_{veg-ext} (B) algorithms for a given date within a given SMAP pixel. In this example, the SMAP pixel over the ICOS study area was selected. Note that the values of temperature endmembers are calibrated and will be different for each SMAP pixel and for each SMAP overpass time. Visually, it is observed from the graph in Figure 3B that the polygonal envelop for DISPATCH_{veg-ext} includes all pixel LST values (represented by black dots). This is not the case for DISPATCH_{classic} as illustrated in the graph of Figure 3A where several pixel LST values are clearly located above the dry edge. Moreover, if we consider zone D uniquely (represented by a grey area), the pixel LST values that come under zone D are discarded from the disaggregation in DISPATCH_{classic} (Figure 3A), whereas the pixel LST values in zone D are included for disaggregation in DISPATCH_{veg-ext} (Figure 3B). The DISPATCH_{veg-ext} algorithm thus extends the applicability of

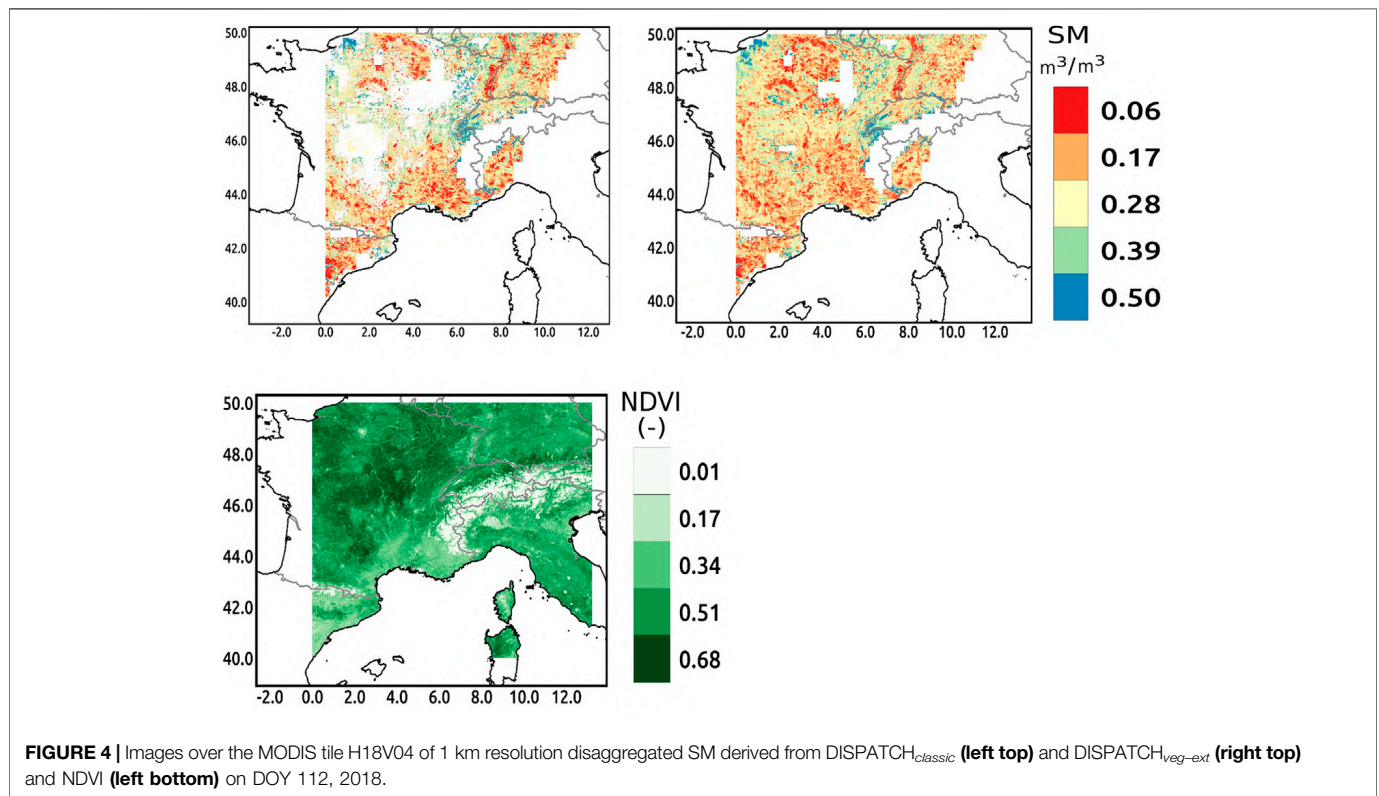
DISPATCH to zone D as well as improves the robustness of dry/wet edges determination. The main difference between DISPATCH_{classic} and DISPATCH_{veg-ext} for estimating temperature endmembers is two-fold: 1) instead of using directly the maximum and minimum observed LST values (DISPATCH_{classic}) to determine respectively the dry bare soil and wet full cover vertices, DISPATCH_{veg-ext} iteratively ensures that most of the data points are kept within the polygon, and 2) the maximum to minimum vegetation temperature difference is forced to be equal to or larger than half the maximum to minimum soil temperature difference. The rationale behind the second requirement is that the maximum to minimum soil temperature difference and the maximum to minimum vegetation temperature difference should be rather close from the energy budget perspective (Stefan et al., 2015; Yang et al., 2015). It has been demonstrated that the uncertainty in dry and wet boundaries is reduced and the accuracy in the associated SM proxies is increased when the second requirement is satisfied.

In practice, the new algorithm for estimating $T_{s,min}$, $T_{s,max}$, $T_{v,min}$, and $T_{v,max}$ is accomplished in three successive steps:

- (1) First guess estimates of temperature endmembers are provided by DISPATCH_{classic} algorithm (Figure 3A for illustration).
- (2) An offset is applied to the first guess dry (wet) edge to make it pass through the point corresponding to the maximum (minimum) observed LST.
- (3) An additional constraint is applied to the maximum vegetation temperature. In case the maximum to minimum vegetation temperature difference is lower than half the maximum to minimum soil temperature difference, the final maximum temperature is set to:

$$T_{v,max} = T_{v,min} + 0.5 * (T_{s,max} - T_{s,min}) \quad (10)$$

The above requirement is especially useful over relatively wet SMOS/SMAP pixels where water-stressed vegetation conditions do not occur, i.e., where the first guess maximum vegetation temperature is not sufficiently representative.



3 RESULTS

In this section, the DISPATCH_{veg-ext} algorithm is evaluated over the study sites and its performance is assessed compared to the DISPATCH_{classic} algorithm and to the Copernicus Sentinel-1-based SM retrieval method. DISPATCH_{veg-ext} is run in different modes with the use of MODIS EVI instead of MODIS NDVI, and the use of Sentinel-3 LST instead of MODIS LST. The objective is to quantify the potential increase in the spatial coverage of DISPATCH data and its accuracy over vegetated regions under temperate and semi-arid conditions.

3.1 Evaluating the Spatio-Temporal Coverage of DISPATCH_{veg-ext} Dataset

DISPATCH_{classic} and DISPATCH_{veg-ext} algorithms are run with the same input data to compare the spatial extent of their 1 km resolution disaggregated SM output. Readers are reminded that DISPATCH_{veg-ext} is an extension of the DISPATCH_{classic} algorithm to include vegetated areas (disaggregation is undertaken in all zones in the LST- feature space, including zone D). **Figure 4** illustrates the visual comparison of 1 km resolution disaggregated SM images obtained after running DISPATCH_{classic} and DISPATCH_{veg-ext} algorithms on DOY 112 for 2018 over the H18V04 MODIS tile. Note that there are multiple void regions in the output of DISPATCH_{classic} disaggregated SM. These void regions appear in the output images when the corresponding input pixels belong to zone D (densely vegetated areas). The DISPATCH_{classic} disaggregation

algorithm does not give disaggregated SM values over those areas. On the other hand, DISPATCH_{veg-ext} disaggregated image fills the void region attributed to vegetation cover by using TVDI in DISPATCH algorithm. The void regions are still visible in the output of DISPATCH_{veg-ext} image. Note that SMAP does not retrieve SM at high altitude which is covered by snow such as alps and pyrenees (O'Neill et al., 2018). Due to this, there is no SM retrieval in this region and the regions remains void. The void regions in high altitude are consistently observed across DISPATCH_{classic}, DISPATCH_{veg-ext} and NDVI images.

Different cloud cover thresholds (10, 30, 50 and 70%) are also used separately in DISPATCH_{veg-ext} and DISPATCH_{classic} algorithms to examine the effect on the spatial coverage of valid pixels. Such a comparison is made on a yearly basis (2017) over distinct spatial extents: the MODIS tiles H17V04 and H18V04 and the 50 km by 50 km REMEDHUS, ICOS, and dryland study areas. From **Table 1** it is observed that there is an overall increase in the percentage of valid pixels in DISPATCH_{veg-ext} disaggregated SM. The increase is about 3–6% in semi-arid areas and 6–9% in the temperate area as compared to DISPATCH_{classic} for different cloud-free threshold values. The increase in coverage is more evident in temperate sites because agricultural areas generally have a larger NDVI than semi-arid/dryland areas. For the MODIS tile extent, the relative increase in coverage over vegetated areas (from 58 to 86% depending on the cloud cover threshold) is very significant. The threshold values of cloud cover have a rather small effect

TABLE 1 | Percentage of valid pixels within the 1 km resolution disaggregated SM images using DISPATCH_{classic} and DISPATCH_{veg-ext} algorithm for i) the entire MODIS tile extent H18V04, ii) the union of both semi-arid areas and iii) the temperate study area separately, for different cloud cover thresholds in 2017.

Cloud cover threshold	MODIS tile extent (H18V04)		Both semi-arid study areas		Temperate study area	
	DISPATCH _{classic}	DISPATCH _{veg-ext}	DISPATCH _{classic}	DISPATCH _{veg-ext}	DISPATCH _{classic}	DISPATCH _{veg-ext}
%	%	%	%	%	%	%
70	12	19	39	40	36	38
50	11	18	37	38	33	36
30	10	16	34	36	31	33
10	7	13	28	29	28	30
All	10.00	16.50	34.50	35.75	32.00	34.25

TABLE 2 | Statistical results in terms of correlation (R), slope of the linear regression (Slope), mean bias (MB), RMSD between 1 km resolution disaggregated and *in situ* SM for (NDVI-based) DISPATCH_{classic} and DISPATCH_{veg-ext} algorithm.

Network	Site	Year	DISPATCH _{classic}					DISPATCH _{veg-ext} (NDVI)				
			NR	R (-)	Slope (-)	MB (m ³ /m ³)	RMSD (m ³ /m ³)	NR	R (-)	Slope (-)	MB (m ³ /m ³)	RMSD (m ³ /m ³)
ICOS	Auradé	2017	139	0.35	0.51	0.08	0.11	148	0.40	0.52	0.08	0.10
		2018	131	0.33	0.57	0.10	0.15	141	0.36	0.54	0.10	0.14
	Lamasquère	2017	140	0.37	0.76	0.04	0.09	150	0.40	0.69	0.04	0.08
		2018	124	0.42	0.57	0.06	0.10	140	0.43	0.50	0.07	0.10
		All	134	0.37	0.60	0.07	0.11	145	0.40	0.56	0.07	0.11
Dryland	BA	2019	55	0.65	0.73	0	0.04	56	0.65	0.65	0	0.04
			56	0.59	0.78	0	0.06	56	0.62	0.75	0.01	0.05
			53	0.78	1.28	0.03	0.07	53	0.77	1.07	0.02	0.05
			53	0.81	1.04	0.07	0.08	53	0.79	0.84	0.05	0.06
			54	0.66	0.96	0.01	0.05	54	0.68	0.89	0.01	0.04
		All	54	0.70	0.96	0.02	0.06	54	0.70	0.84	0.02	0.05
RHEMEDUS	K13	2017	145	0.39	0.40	0.12	0.13	157	0.44	0.40	0.11	0.13
			146	0.42	1.41	-0.02	0.07	160	0.43	1.28	-0.02	0.07
			147	0.67	1.10	0.01	0.05	161	0.70	1.06	0	0.05
			147	0.46	0.47	0.09	0.10	161	0.50	0.48	0.08	0.10
			166	0.57	3.88	-0.08	0.11	176	0.59	3.61	-0.08	0.10
			148	0.35	0.47	0.06	0.08	162	0.41	0.51	0.06	0.08
			166	0.45	0.45	0.07	0.10	176	0.51	0.47	0.06	0.09
			168	0.78	1.89	0.01	0.07	180	0.79	1.75	0.02	0.06
			165	0.65	2.07	-0.01	0.06	179	0.67	1.88	-0.01	0.05
			147	0.54	0.92	-0.04	0.06	161	0.62	0.94	-0.03	0.05
			165	0.78	3.32	-0.07	0.08	179	0.77	2.95	-0.07	0.08
			146	0.37	0.39	0.10	0.12	160	0.45	0.41	0.10	0.11
			165	0.76	1.48	-0.04	0.07	177	0.77	1.37	-0.04	0.06
					All	155	0.55	1.40	0.02	0.09	168	0.59

NR, Number of retrieval.

at the 50 km by 50 km scale for both DISPATCH algorithms. However, a significant improvement can be seen over the entire MODIS tile extent.

Statistical results of correlation (R), slope of the linear regression (Slope), mean bias (MB), and root mean square difference (RMSD) between disaggregated and *in situ* SM with DISPATCH_{classic} and DISPATCH_{veg-ext} algorithm are calculated separately and presented in **Table 2**. The overall temporal correlation of DISPATCH_{veg-ext} SM is in the range of 0.40–0.70, compared to 0.37–0.70 for the DISPATCH_{classic} case. The slight increase in the temporal correlation over

vegetated areas is mainly attributed to the increase in the spatio-temporal coverage of DISPATCH_{veg-ext} SM data set associated with the inclusion of vegetated areas. The MB and RMSD values remain approximately the same for both algorithms, with a maximum difference of 0.02 m³/m³. This indicates that the inclusion of vegetated areas in DISPATCH algorithm using the TVDI approach does not degrade the disaggregation performance. It is also observed that the slope of the linear regression between disaggregated and *in situ* SM is more stable for the new algorithm because of the modified calculation of temperature endmembers.

TABLE 3 | Statistical results in terms of correlation (R), slope of the linear regression (Slope), mean bias (MB) and RMSD between EVI-based DISPATCH_{veg-ext} 1 km resolution satellite product and *in situ* SM.

Network	Site	Year	DISPATCH _{veg-ext} (EVI)				
			NR	R (-)	Slope (-)	MB (m ³ /m ³)	RMSD (m ³ /m ³)
ICOS	Auradé	2017	148	0.42	0.54	0.08	0.10
		2018	141	0.39	0.58	0.08	0.10
	Lamasquère	2017	150	0.40	0.67	0.04	0.08
		2018	140	0.43	0.54	0.06	0.10
		All	145	0.41	0.58	0.07	0.11
Dryland	BA	2019	56	0.71	0.66	0.01	0.04
		GA	56	0.64	0.74	0.01	0.05
		HA1	53	0.80	0.98	0.02	0.05
		HA2	53	0.80	0.78	0.05	0.06
		PM	54	0.68	0.82	0	0.04
RHEMEDUS	K13	All	54	0.73	0.80	0.02	0.05
		2017	157	0.43	0.39	0.11	0.12
		K10	160	0.43	1.27	-0.02	0.06
		M05	161	0.71	1.04	0	0.04
		N09	161	0.50	0.48	0.08	0.10
		I06	176	0.59	3.51	-0.08	0.10
		M09	162	0.41	0.50	0.06	0.08
		F06	176	0.53	0.47	0.06	0.09
		H13	180	0.79	1.72	0.02	0.06
		L03	179	0.68	1.84	-0.01	0.05
		O07	161	0.63	0.93	-0.03	0.05
		K04	179	0.77	2.87	-0.07	0.08
		L07	160	0.46	0.42	0.10	0.11
F11	177	0.77	1.35	-0.04	0.06		
All	168	0.59	1.29	0.01	0.08		

NR, Number of retrieval.

3.2 Improving the Robustness of DISPATCH Over Vegetated Pixels

The robustness of the DISPATCH_{veg-ext} algorithm over vegetated areas is further tested by using NDVI and EVI vegetation indices as input. The analysis is done by comparing the NDVI-based DISPATCH_{veg-ext} (Table 2) and EVI-based DISPATCH_{veg-ext} (Table 3) performance in terms of correlation (R), slope of the linear regression (Slope), mean bias (MB) and RMSD between disaggregated and *in situ* SM. The overall (all sites) temporal

correlation of disaggregated SM vs. *in situ* SM ranges from 0.41 to 0.73 as compared to 0.40–0.70 for the EVI and NDVI case, respectively.

The inclusion of EVI improves the performance of the DISPATCH algorithm over the temperate and semi-arid study areas. Note that the overall percentage increase—as compared to the NDVI-based DISPATCH SM—in temporal correlation for the ICOS network (agricultural land) is 7% and for REMEDHUS and dryland networks is 1 and 4%. The increase in temporal correlation of disaggregated SM using EVI over agricultural areas is attributed to the sensitivity of EVI to f_{vg} over densely vegetated areas, which fosters the accuracy of the trapezoid approach. It is also observed that semi-arid areas exhibit a small increase in temporal correlation. One may hypothesize that the use of EVI in place of NDVI reduces the effect of the variability of soil color and of atmospheric noise. The mean bias (MB) and RMSD between disaggregated and *in situ* SM mostly remain the same for both algorithms, which indicates that the inclusion of EVI in place of NDVI in the DISPATCH algorithm does not degrade the performance of DISPATCH algorithm. Rather, the use of EVI improves the performance of the DISPATCH algorithm for different climatic conditions such as temperate and semi-arid areas and different land cover types such as agricultural and dryland areas.

3.3 Reducing the Impact of Clouds on DISPATCH Dataset by Using Sentinel-3 LST Data

Cloud cover strongly limits the availability of optical/thermal data. The non-availability of optical/thermal data at HR is the main reason for voids in DISPATCH disaggregated SM products. The cloud cover generally differs according to the time of day. Hence, in spite of having the same spatial and temporal resolution, MODIS LST and Sentinel-3 LST data sets may be affected by clouds differently. The cloud mask applied to the MODIS LST images extracts the LST pixels with quality control (QC) equal to 0 or 17, which corresponds to an uncertainty in LST lower than 1 K and a maximum emissivity error equal to 0.01 and 0.02, respectively. The cloud mask applied to the Sentinel-3

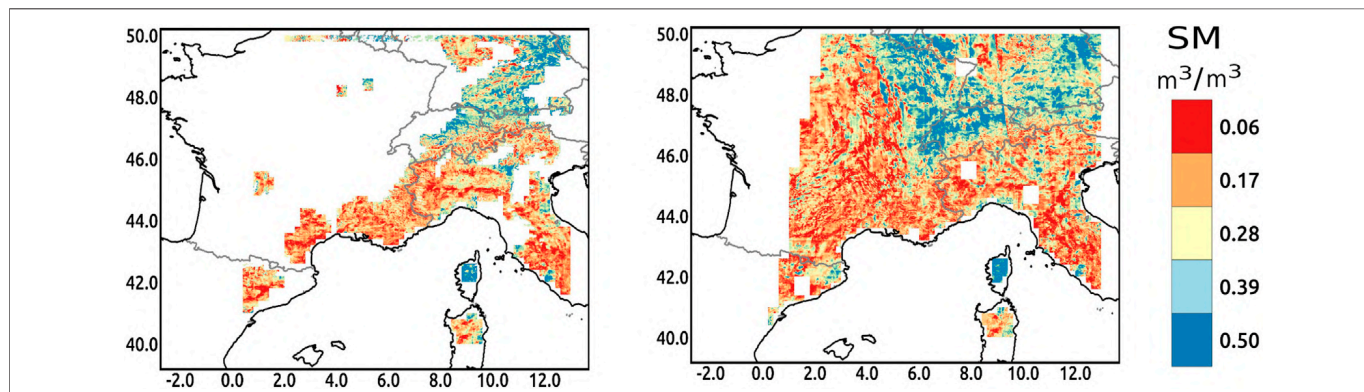
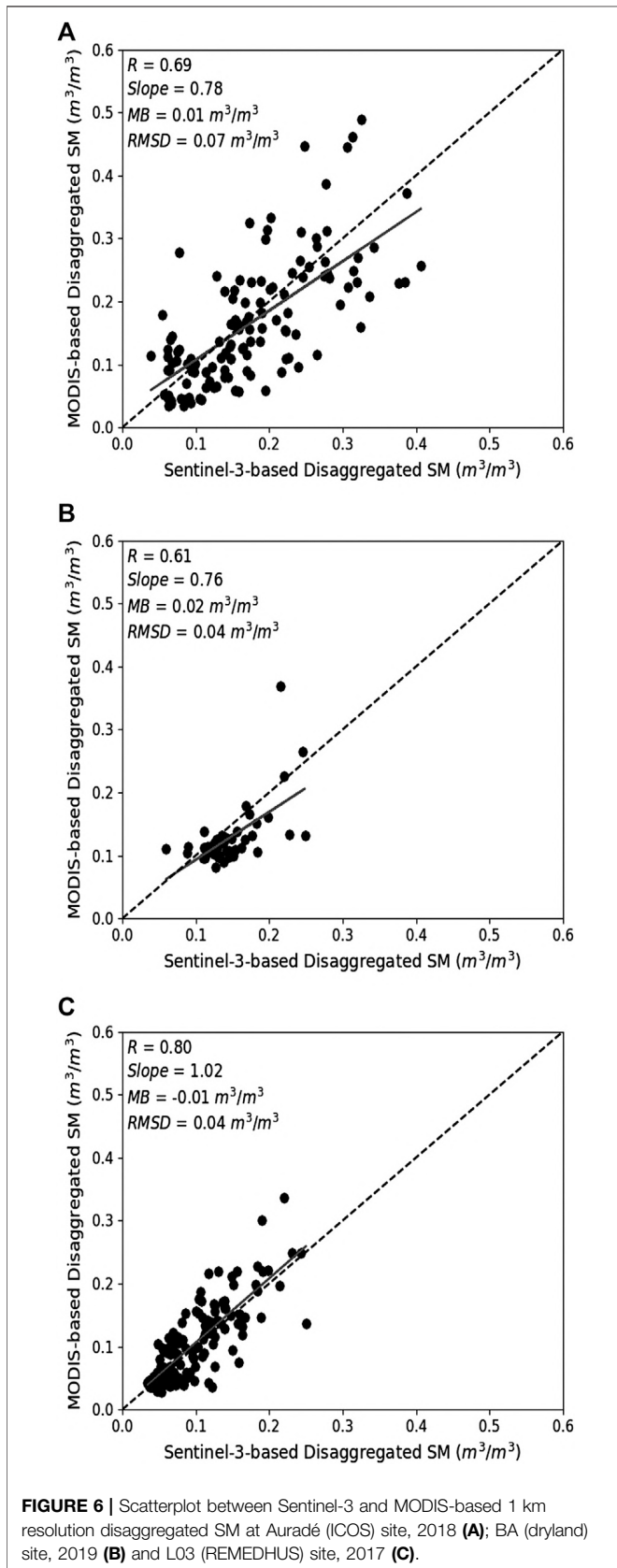


FIGURE 5 | DISPATCH_{veg-ext} 1 km resolution SM images for MODIS (left) and Sentinel-3 (right) LST input data on DOY 204, 2018.



LST images extracts the LST pixels with a QC equal to 0, which corresponds to an uncertainty in LST lower than 1 K. The Sentinel-3 LST QC does not include other criteria of data quality (Ghent, 2017). Note that in this study, only the valid SMAP pixels (with valid SMAP SM retrievals) were considered in the computation of gap percentages within the disaggregated images so that the computed data gaps correspond to the actual cloud cover on optical images, plus the SMAP pixels with a cloud cover larger than a threshold value of 50% over which disaggregation is not applied.

Figure 5 shows a qualitative analysis between MODIS-based (left) and Sentinel-3-based (right) DISPATCH_{veg-ext} disaggregated SM images on DOY 204 for 2018 over the MODIS tile H18V04. A large data gap can be seen in the MODIS-based disaggregated SM image due to cloud cover. Most of these voids are filled by using Sentinel-3 LST in the disaggregation of SM products, thereby significantly increasing the spatial coverage of disaggregated SM. In our study, the cloud cover percentage is analyzed by calculating the valid pixels in the 1 km resolution disaggregated SM images using Sentinel-3 LST and MODIS LST as an input. Such an analysis is undertaken for data in 2018 over two distinct extents: the MODIS tile H18V04 and ICOS study area. It is observed that there is an increase in the number of valid pixels from 21% in MODIS LST disaggregated SM to 65% in Sentinel-3 LST disaggregated SM for MODIS tile H18V04 for 2018. Similarly, there is an increase in the number of valid pixels from 40% in MODIS LST disaggregated SM to 92% in Sentinel-3 LST disaggregated SM for ICOS study areas for 2018. We assume that the reason for the increase in spatial coverage is the overpass time of Sentinel-3 (9:30 am), which is earlier than MODIS Terra (10:30 am).

Further quantitative analysis is done in order to analyze the performance of disaggregated SM using Sentinel-3 instead of MODIS LST. Figure 6 shows a scatterplot between disaggregated SM products using Sentinel-3 LST and MODIS LST as an input for Auradé (ICOS), BA (dryland) and L03 (REMEDHUS) sites separately. Both datasets are significantly correlated with an average overall correlation coefficient of about 0.7. The mean bias (MB) is very small ($0.01 \text{ m}^3/\text{m}^3$) between both products, given that they both rely on the same LR SMAP observations. It is observed that the range of SM values is similar in both products so that the main difference remains the spatial coverage, which is significantly larger for Sentinel-3 LST data.

3.4 Accuracy of DISPATCH Relative to Copernicus Sentinel-1 and SMAP/S1 SM Data

Sentinel-1 radar data are not affected by clouds. The objective here is to compare the DISPATCH_{veg-ext} and Copernicus Sentinel-1 and SMAP/S1 1 km resolution SM data sets in terms of 1) the number of valid pixels and 2) their accuracy at all the validation sites of the three study areas.

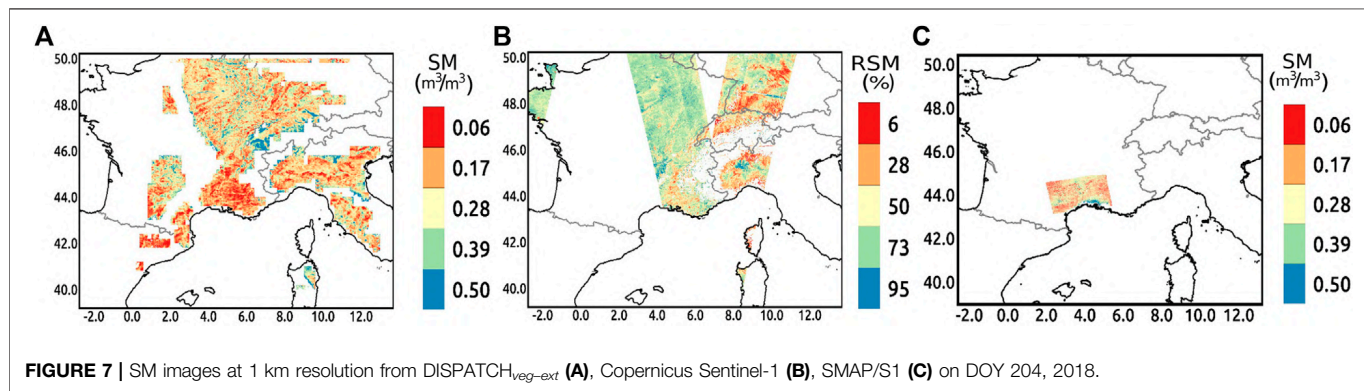


FIGURE 7 | SM images at 1 km resolution from DISPATCH_{veg-ext} (A), Copernicus Sentinel-1 (B), SMAP/S1 (C) on DOY 204, 2018.

TABLE 4 | Statistical results in terms of correlation (R), slope of the linear regression (Slope), mean bias (MB) and RMSD between Copernicus Sentinel-1 1 km resolution satellite product and *in situ* SM.

Network	Site	Year	Copernicus Sentinel-1				
			NR	R (-)	Slope (-)	MB (m³/m³)	RMSD (m³/m³)
ICOS	Auradé	2017	155	0.28	0.60	0.04	0.11
		2018	134	0.27	0.45	0	0.11
	Lamasquère	2017	108	0.35	0.86	0.02	0.10
		2018	79	0.31	0.44	-0.01	0.09
		All	119	0.30	0.59	0.01	0.10
Dryland	BA	2019	40	0.54	0.48	-0.08	0.11
		GA	40	0.32	0.33	-0.04	0.09
		HA1	40	-0.03	-0.02	-0.10	0.13
		HA2	40	0.18	0.16	0.06	0.08
		PM	39	0.50	0.43	-0.04	0.06
		All	40	0.30	0.28	-0.04	0.09
RHEMEDUS	K13	2017	117	0.23	0.31	0.04	0.10
		K10	115	0.40	1.37	-0.09	0.12
		M05	114	0.34	0.57	-0.05	0.09
		N09	115	0.51	0.69	0.01	0.07
		I06	61	0.14	0.80	-0.11	0.13
		M09	115	0.30	0.52	-0.04	0.09
		F06	61	0.32	0.33	-0.01	0.09
		H13	61	0.69	1.43	-0.02	0.07
		L03	113	0.33	0.96	-0.07	0.10
		O07	114	0.46	1.04	-0.10	0.12
		K04	115	0.37	1.86	-0.13	0.15
		L07	115	0.25	0.37	-0.03	0.09
		F11	61	0.65	1.42	-0.09	0.12
All	98	0.38	0.90	-0.05	0.10		

NR, Number of retrieval.

TABLE 5 | Statistical results in terms of correlation (R), slope of the linear regression (Slope), mean bias (MB) and RMSD between SMAP/S1 1 km resolution satellite product and *in situ* SM.

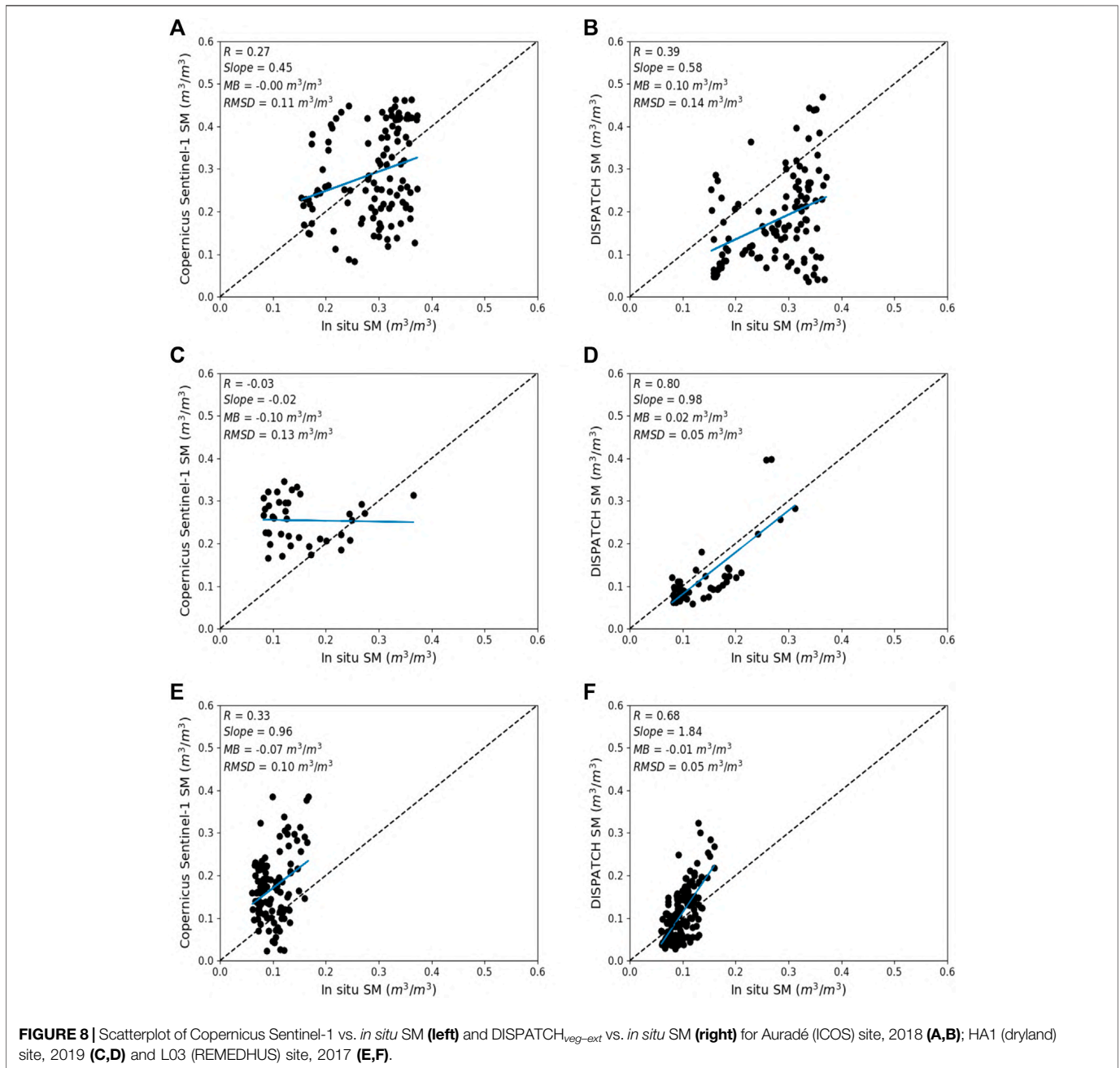
Network	Site	Year	SMAP/S1				
			NR	R (-)	Slope (-)	MB (m³/m³)	RMSD (m³/m³)
ICOS	Auradé	2017	104	0.22	0.21	0.05	0.08
		2018	101	0.37	0.54	0.02	0.09
	Lamasquère	2017	89	0.37	0.47	0.05	0.07
		2018	86	0.51	0.63	0.07	0.10
		All	95	0.37	0.47	0.05	0.09
Dryland	BA	2019	32	0.82	0.77	-0.01	0.04
		GA	32	0.69	0.68	-0.03	0.06
		HA1	32	0.76	0.81	-0.07	0.09
		HA2	32	0.75	0.61	-0.04	0.05
		PM	31	0.70	0.72	-0.04	0.06
		All	32	0.74	0.72	-0.04	0.06
RHEMEDUS	K13	2017	107	0.53	0.42	0.09	0.11
		K10	106	0.51	1.01	-0.05	0.07
		M05	109	0.64	0.74	0	0.04
		N09	105	0.47	0.34	0.09	0.11
		I06	109	0.54	2.25	-0.08	0.09
		M09	73	0.57	0.62	0.04	0.06
		F06	74	0.70	0.46	0.06	0.08
		H13	72	0.74	0.90	0.03	0.05
		L03	108	0.67	1.48	-0.01	0.05
		O07	99	0.63	0.75	-0.02	0.04
		K04	109	0.51	1.83	-0.09	0.11
		L07	107	0.63	0.67	0.06	0.08
		F11	75	0.76	1.47	-0.06	0.08
All	96	0.61	0.99	0.01	0.08		

NR, Number of retrieval.

Figure 7 compares DISPATCH_{veg-ext} disaggregated SM, Copernicus SM, and SMAP/S1 SM data on DOY 202, 2018 over the MODIS tile H18V04. It is clear from the visual comparison that, on one hand DISPATCH and Copernicus data have their spatial coverage limited due to cloud cover and Sentinel-1 field of view, respectively. On the other hand, the spatial coverage of SMAP/Sentinel-1 L2 product, which combines both SMAP and Sentinel-1 data, is determined by the field of view overlap at the concurrent overpass time of Sentinel-1 and SMAP. Tables 3–5 report the number of DISPATCH, Copernicus and SMAP/S1 observations concurrent with the *in situ* SM

measurements collected at each monitoring station. The number of valid retrievals for DISPATCH_{veg-ext} is 22% (50%) larger for the temperate study area and 57% (72%) larger for both semi-arid study areas as compared to Copernicus (and SMAP/S1) products, respectively.

Table 4 presents the correlation (R), slope of the linear regression (Slope), mean bias (MB) and RMSD between Copernicus Sentinel-1-based SM and *in situ* SM. It is reminded that for statistical comparison, Copernicus Sentinel-1 SM (%) is converted into volumetric SM (m³/m³) from Eq. 5. Statistical results in Tables 3 and 4 used to quantitatively assess



the performance of DISPATCH_{veg-ext} relative to the Copernicus SM retrieval approach. The correlation between satellite and *in situ* measurement is generally closer to 1 for DISPATCH than for Copernicus product ranging from 0.39 to 0.80 and from -0.03 to 0.69, respectively. The poorer statistics for the Copernicus Sentinel-1-based SM can be attributed to two factors. In temperate regions, the vegetation cover with a leaf area index larger than 0.6 is likely to drastically reduce the sensitivity of C-band backscatter to SM. In semi-arid regions, the effective soil roughness seen by active sensors has been shown to increase in dry conditions due to volume scattering (Escorihuela and Quintana-Seguí, 2016; Ojha et al., 2020), thus artificially increasing the Sentinel-1-retrieved SM. As an illustration of

both possible effects, **Figure 8** presents a scatterplot of DISPATCH_{veg-ext} vs. *in situ* SM and of Copernicus vs. *in situ* SM for Auradé (ICOS), HA1 (dryland) and L03 (REMEDHUS) sites separately. In particular, the bi-modal behavior of the Sentinel-1-retrieved SM can be attributed to volume scattering in very dry conditions. It can be the reason for the negative correlation and slope of Copernicus Sentinel-1 based SM for HA1 site. The limitation of the bi-modal behavior of Copernicus Sentinel-1 based SM for dryland areas is overcome by DISPATCH_{veg-ext} algorithm and exhibits a better representation of SM at 1 km resolution.

The performance of optical-based (DISPATCH) and radar-based (SMAP/S1) SMAP disaggregated SM products is assessed

by the statistical comparison presented in **Tables 3** and **5**. The correlation between satellite and *in situ* measurements is in the range of 0.39–0.80 and 0.22–0.82 for DISPATCH and SMAP-S1 product, respectively. The overall statistical difference between SMAP/S1 and DISPATCH 1 km disaggregated products is relatively small for all three study areas. DISPATCH and SMAP/S1 perform well over the dryland semi-arid sites with a mean correlation larger than 0.7 with however, a significant negative bias ($-0.04 \text{ m}^3/\text{m}^3$) on SMAP/S1. The statistical metrics for SMAP/S1 are slightly poorer as compared to DISPATCH in the temperate study area. This could be explained by a lower sensitivity to SM of SMAP/S1 product over vegetated areas where the vegetation water content is greater than $3 \text{ kg}/\text{m}^2$ (Das et al., 2019). Nonetheless, the performance of both disaggregated products over all three study areas remains rather similar and the main advantage of DISPATCH compared to the official SMAP product is the larger spatio-temporal coverage. SMAP/S1 1 km product is limited by the temporal frequency of Sentinel-1 with an interval of 6 days in Europe.

4 CONCLUSION

DISPATCH is a well-known optical/thermal-based disaggregation method of passive microwave-derived SM data. It is usually implemented using MODIS LST/NDVI and SMOS/SMAP SM data to provide 1 km resolution disaggregated SM images. The application of DISPATCH to large areas at high frequency is however limited by 1) the loss of sensitivity of LST to the surface SM over densely vegetated areas and 2) the unavailability of optical data under cloud cover. To improve the spatio-temporal coverage of 1 km resolution DISPATCH SM data, a new algorithm named DISPATCH_{veg-ext} algorithm is proposed. DISPATCH_{veg-ext} differs from DISPATCH_{classic} in mainly one aspect: the use of TVDI in the DISPATCH downscaling relationship to apply the disaggregation to densely vegetated areas. Moreover, DISPATCH_{veg-ext} is tested using Sentinel-3 LST instead of MODIS LST as input, in order to assess the impact of the thermal observation time on the output data gaps due to cloud cover. This approach is evaluated by comparing the disaggregated SM with *in situ* measurements over a temperate and two semi-arid regions.

First, the comparison is done between DISPATCH_{classic} and DISPATCH_{veg-ext} disaggregated SM at 1 km resolution. Visual analysis indicates a significant increase in the spatial coverage of DISPATCH_{veg-ext} disaggregated SM images due to the inclusion of densely vegetated areas. In addition, the temporal correlation between satellite and *in situ* SM is increased by 9% and the RMSD is decreased by 6% in the temperate region. Similarly, for the semi-arid regions, the temporal correlation is increased by 7–8% and the RMSD is decreased by 6–18%. Furthermore, the use of EVI instead of NDVI improves the robustness of the disaggregated SM over vegetated areas by increasing the correlation by 7% over the temperate region and by up to 4% over the semi-arid regions.

Second, the use of Sentinel-3 LST (09:30 am overpass) in place of MODIS LST (10:30 am and 1:30 pm overpass) to disaggregate SM at 1 km resolution very significantly increases the spatial coverage of

disaggregated SM at 1 km resolution. Both MODIS- and Sentinel-3-based disaggregated SM data sets are found to be significantly correlated. However, as a caveat, one should keep in mind that the overpass time of thermal data is a compromise between 1) the overall cloud cover, which may be less early in the morning but also 2) the coupling between LST and SM, which is stronger at solar noon. Instead of polar orbit satellites, geostationary satellites have been also used to downscale SMOS SM data (Piles et al., 2016; Tagesson et al., 2018). The point is that the currently available geostationary thermal sensors have a spatial resolution of about 2–3 km at nadir, corresponding to a resolution of 4–5 km at the latitudes of our study areas. In the future, the possible advent of high-resolution geostationary thermal infrared satellites will be very useful in DISPATCH to significantly reduce the gaps in disaggregated SM images due to cloud cover.

Third, the accuracy of DISPATCH_{veg-ext} is evaluated by comparison with Copernicus Sentinel-1 SM and SMAP/S1 SM products separately, which both have the same (1 km) spatial resolution. DISPATCH_{veg-ext} is generally more accurate than the Copernicus product and its spatio-temporal coverage is significantly larger than that of SMAP/S1 product. Such a comparison opens up a new research towards the development of synergies between thermal-based (DISPATCH) and Sentinel-1-based SM (Amazirh et al., 2019). The high spatio-temporal resolution together with the all-weather capability of Sentinel-1 data are essential assets for that purpose. In particular, the SMOS/SMAP SM can be disaggregated at 100 m resolution using DISPATCH and Landsat thermal data (Ojha et al., 2019). At such high spatial resolution however, the revisit time of current thermal sensors is relatively long (16 days for Landsat). Therefore, the synergy between DISPATCH and Sentinel-1 data is expected to be very useful at high spatial resolution, especially before the advent of future thermal missions like TRISHNA (Lagouarde et al., 2019) and LSTM (Koetz et al., 2018).

DATA AVAILABILITY STATEMENT

The original contributions presented in the study are included in the article/Supplementary Material, further inquiries can be directed to the corresponding author.

AUTHOR CONTRIBUTIONS

NO: implementation, validation, investigation, data curation and writing original draft of the paper; OM: supervision, reviewing and editing; CS and ME: reviewing and editing.

FUNDING

This study was supported by the European Commission Horizon 2020 Program for Research and Innovation (H2020) in the context of the Marie Skłodowska-Curie Research and Innovation Staff Exchange 445 (RISE) action (ACCWA

project, Grant Agreement No.: 823965), and by the Partnership for Research and 446 Innovation in the Mediterranean Area (PRIMA) IDEWA project.

ACKNOWLEDGMENTS

Soil Moisture measurements at Lamasquère (FR-Lam) and Auradé (FR-Aur) were mainly funded by ICOS ERIC. These

experimental sites also benefited from the support and facilities of the Regional Spatial Observatory (OSR), CNRS (Centre National de la Recherche Scientifique), CNES (Centre National d'Etudes Spatiales), University of Toulouse. The author also thank International soil moisture network (ISMN) for providing *in situ* soil moisture measurements for REMEDHUS network and Pere Quintana Seguí (Observatori de l'Ebre, URL-CSIC) for providing *in situ* soil moisture measurements for dryland areas of Spain.

REFERENCES

- Albergel, C., Rüdiger, C., Pellarin, T., Calvet, J.-C., Fritz, N., Froissard, F., et al. (2008). From near-surface to root-zone soil moisture using an exponential filter: an assessment of the method based on *in-situ* observations and model simulations. *Hydrol. Earth Syst. Sci.* 12, 1323–1337. doi:10.5194/hess-12-1323-2008
- Amazirh, A., Merlin, O., and Er-Raki, S. (2019). Including sentinel-1 radar data to improve the disaggregation of modis land surface temperature data. *ISPRS J. Photogramm. Remote Sens.* 150, 11–26. doi:10.1016/j.isprsjprs.2019.02.004
- Atwood, D. K., Andersen, H.-E., Matthijs, B., and Holecz, F. (2014). Impact of topographic correction on estimation of aboveground boreal biomass using multi-temporal, l-band backscatter. *IEEE J. Sel. Top. Appl. Earth Obs. Remote Sens.* 7, 3262–3273. doi:10.1109/jstars.2013.2289936
- Bauer-Marschallinger, B., Freeman, V., Cao, S., Paulik, C., Schaufler, S., Stachl, T., et al. (2018). Toward global soil moisture monitoring with sentinel-1: harnessing assets and overcoming obstacles. *IEEE Trans. Geosci. Remote Sens.* 57, 520–539. doi:10.1109/TGRS.2018.2858004
- Béziat, P., Ceschia, E., and Dedieu, G. (2009). Carbon balance of a three crop succession over two cropland sites in south west France. *Agric. For. Meteorol.* 149, 1628–1645. doi:10.1016/j.agrformet.2009.05.004
- Brisson, N., and Perrier, A. (1991). A semiempirical model of bare soil evaporation for crop simulation models. *Water Resour. Res.* 27, 719–727. doi:10.1029/91wr00075
- Carlson, T. (2007). An overview of the “triangle method” for estimating surface evapotranspiration and soil moisture from satellite imagery. *Sensors* 7, 1612–1629. doi:10.3390/s7081612
- Chen, F., Crow, W. T., Starks, P. J., and Moriasi, D. N. (2011). Improving hydrologic predictions of a catchment model via assimilation of surface soil moisture. *Adv. Water Resour.* 34, 526–536. doi:10.1016/j.advwatres.2011.01.011
- Cleugh, H. A., Leuning, R., Mu, Q., and Running, S. W. (2007). Regional evaporation estimates from flux tower and modis satellite data. *Remote Sens. Environ.* 106, 285–304. doi:10.1016/j.rse.2006.07.007
- Colliander, A., Fisher, J. B., Halverson, G., Merlin, O., Misra, S., Bindlish, R., et al. (2017). Spatial downscaling of smap soil moisture using modis land surface temperature and ndvi during smapvex15. *IEEE Geosci. Remote Sens. Lett.* 14, 2107–2111. doi:10.1109/lgrs.2017.2753203
- Cosby, B., Hornberger, G. M., Clapp, R. B., and Ginn, T. R. (1984). A statistical exploration of the relationships of soil moisture characteristics to the physical properties of soils. *Water Resour. Res.* 20, 682–690. doi:10.1029/wr020i006p00682
- Das, N. N., Entekhabi, D., Dunbar, R. S., Colliander, A., Chen, F., Crow, W., et al. (2018). The smap mission combined active-passive soil moisture product at 9 km and 3 km spatial resolutions. *Remote Sens. Environ.* 211, 204–217. doi:10.1016/j.rse.2018.04.011
- Das, N. N., Entekhabi, D., Dunbar, S., Chaubell, M., Jagdhuber, T., Colliander, A., et al. (2019). The SMAP and copernicus sentinel 1A/B microwave active-passive high resolution surface soil moisture product and its applications.
- Das, N. N., Entekhabi, D., and Njoku, E. G. (2010). An algorithm for merging smap radiometer and radar data for high-resolution soil-moisture retrieval. *IEEE Trans. Geosci. Remote Sens.* 49 (5), 1504–1512. doi:10.1109/TGRS.2010.2089526
- Dirmeyer, P. A. (2000). Using a global soil wetness dataset to improve seasonal climate simulation. *J. Clim.* 13, 2900–2922. doi:10.1175/1520-0442(2000)013<2900:uagswd>2.0.co;2
- Dorigo, W., Wagner, W., Hohensinn, R., Hahn, S., Paulik, C., Xaver, A., et al. (2011). International soil moisture network: a data hosting facility for global *in situ* soil moisture measurements. *Hydrol. Earth Syst. Sci.* 15, 1675–1698. doi:10.5194/hess-15-1675-2011
- Douville, H. (2004). Relevance of soil moisture for seasonal atmospheric predictions: is it an initial value problem?. *Clim. Dyn.* 22, 429–446. doi:10.1007/s00382-003-0386-5
- Entekhabi, D., Njoku, E. G., O'Neill, P. E., Kellogg, K. H., Crow, W. T., Edelstein, W. N., et al. (2010). The soil moisture active passive (SMAP) mission. *Proc. IEEE* 98, 704–716. doi:10.1109/jproc.2010.2043918
- Escorihuela, M. J., and Quintana-Seguí, P. (2016). Comparison of remote sensing and simulated soil moisture datasets in mediterranean landscapes. *Remote Sens. Environ.* 180, 99–114. doi:10.1016/j.rse.2016.02.046
- Ford, T., Harris, E., and Quiring, S. (2013). Estimating root zone soil moisture using near-surface observations from SMOS. *Hydrol. Earth Syst. Sci. Discuss.* 10, 8325–8364. doi:10.5194/hessd-10-8325-2013
- Gao, B.-C. (1996). NDWI—a normalized difference water index for remote sensing of vegetation liquid water from space. *Remote Sens. Environ.* 58, 257–266. doi:10.1016/s0034-4257(96)00067-3
- Georgiana Stefan, V., Escorihuela, M. J., Merlin, O., Chihrane, J., Ghaout, S., and Piou, C. (2018). “Using Sentinel-3 land surface temperature to derive high resolution soil moisture estimates for desert locust management,” in EGU general assembly conference abstracts, Vienna, Austria, April 8–13, 2018 (Vienna, Austria: AGU), Vol. 20, 13752.
- Ghent, D. (2017). S3 validation report—slstr, s3mpc.uol.vr.029-i1r0-slstr l2 land validation report.docx. Available at: <https://sentinel.esa.int/web/sentinel/technical-guides/sentinel-3-slstr/cal-val-activities/validation>.
- Gitelson, A. A. (2004). Wide dynamic range vegetation index for remote quantification of biophysical characteristics of vegetation. *J. Plant Physiol.* 161, 165–173. doi:10.1078/0176-1617-01176
- Guérif, M., and Duke, C. L. (2000). Adjustment procedures of a crop model to the site specific characteristics of soil and crop using remote sensing data assimilation. *Agric. Ecosyst. Environ.* 81, 57–69. doi:10.1016/s0167-8809(00)00168-7
- Gutman, G., and Ignatov, A. (1998). The derivation of the green vegetation fraction from NOAA/AVHRR data for use in numerical weather prediction models. *Int. J. Remote Sens.* 19, 1533–1543. doi:10.1080/014311698215333
- Hamlet, A. F., Mote, P. W., Clark, M. P., and Lettenmaier, D. P. (2007). Twentieth-century trends in runoff, evapotranspiration, and soil moisture in the western United States. *J. Clim.* 20, 1468–1486. doi:10.1175/jcli4051.1
- Huete, A., Didan, K., Miura, T., Rodriguez, E. P., Gao, X., and Ferreira, L. G. (2002). Overview of the radiometric and biophysical performance of the modis vegetation indices. *Remote Sens. Environ.* 83, 195–213. doi:10.1016/s0034-4257(02)00096-2
- Jagdhuber, T., Entekhabi, D., Das, N. N., Link, M., Montzka, C., Kim, S., et al. (2017). “Microwave covariation modeling and retrieval for the dual-frequency active-passive combination of sentinel-1 and SMAP,” in 2017 IEEE international geoscience and remote sensing symposium (IGARSS), Fort Worth, TX, July 23–28, 2017 (IEEE), 3996–3999. doi:10.1109/IGARSS.2017.8127876

- Jiang, Z., Huete, A. R., Li, J., and Chen, Y. (2006). An analysis of angle-based with ratio-based vegetation indices. *IEEE Trans. Geosci. Remote Sens.* 44, 2506–2513. doi:10.1109/tgrs.2006.873205
- Kerr, Y. H., Waldteufel, P., Richaume, P., Wigneron, J. P., Ferrazzoli, P., Mahmoodi, A., et al. (2012). The SMOS soil moisture retrieval algorithm. *IEEE Trans. Geosci. Remote Sens.* 50, 1384–1403. doi:10.1109/tgrs.2012.2184548
- Kim, J., and Hogue, T. S. (2012). Evaluation and sensitivity testing of a coupled landsat-modis downscaling method for land surface temperature and vegetation indices in semi-arid regions. *J. Appl. Remote Sens.* 6, 063569. doi:10.1117/1.jrs.6.063569
- Koetz, B., Bastiaanssen, W., Berger, M., Defournay, P., Del Bello, U., Drusch, M., et al. (2018). “High spatio-temporal resolution land surface temperature mission—a copernicus candidate mission in support of agricultural monitoring,” in IGARSS 2018-2018 IEEE international geoscience and remote sensing symposium, Valencia, Spain, July 22–27, 2018 (IEEE), 8160–8162. doi:10.1109/IGARSS.2018.8517433
- Kogan, F. N. (1995). Application of vegetation index and brightness temperature for drought detection. *Adv. Space Res.* 15, 91–100. doi:10.1016/0273-1177(95)00079-t
- Kumar, S. V., Reichle, R. H., Koster, R. D., Crow, W. T., and Peters-Lidard, C. D. (2009). Role of subsurface physics in the assimilation of surface soil moisture observations. *J. Hydrometeorol.* 10, 1534–1547. doi:10.1175/2009jhm1134.1
- Lagouarde, J.-P., Bhattacharya, B., Crébassol, P., Gamet, P., Adlakha, D., Murthy, C., et al. (2019). “Indo-French high-resolution thermal infrared space mission for earth natural resources assessment and monitoring—concept and definition of trishna,” in ISPRS-GEOGLAM-ISRS joint international workshop on “earth observations for agricultural monitoring” New Delhi, India, Vol. 42, 403.
- Lievens, H., Reichle, R. H., Liu, Q., De Lannoy, G. J. M., Dunbar, R. S., Kim, S. B., et al. (2017). Joint sentinel-1 and SMAP data assimilation to improve soil moisture estimates. *Geophys. Res. Lett.* 44, 6145–6153. doi:10.1002/2017gl073904
- Lievens, H., Tomer, S. K., Al Bitar, A., De Lannoy, G. J. M., Drusch, M., Dumedah, G., et al. (2015). SMOS soil moisture assimilation for improved hydrologic simulation in the murray darling basin, Australia. *Remote Sens. Environ.* 168, 146–162. doi:10.1016/j.rse.2015.06.025
- Liu, H. Q., and Huete, A. (1995). A feedback based modification of the NDVI to minimize canopy background and atmospheric noise. *IEEE Trans. Geosci. Remote Sens.* 33, 457–465. doi:10.1109/tgrs.1995.8746027
- Malbêteau, Y., Merlin, O., Molero, B., Rüdiger, C., and Bacon, S. (2016). Dispatch as a tool to evaluate coarse-scale remotely sensed soil moisture using localized *in situ* measurements: application to SMOS and AMSR-E data in southeastern Australia. *Int. J. Appl. Earth Obs. Geoinf.* 45, 221–234. doi:10.1016/j.jag.2015.10.002
- Matsushita, B., Yang, W., Chen, J., Onda, Y., and Qiu, G. (2007). Sensitivity of the enhanced vegetation index (EVI) and normalized difference vegetation index (NDVI) to topographic effects: a case study in high-density cypress forest. *Sensors* 7, 2636–2651. doi:10.3390/s7112636
- Merlin, O., Chehbouni, A. G., Kerr, Y. H., Njoku, E. G., and Entekhabi, D. (2005). A combined modeling and multispectral/multiresolution remote sensing approach for disaggregation of surface soil moisture: application to SMOS configuration. *IEEE Trans. Geosci. Remote Sens.* 43, 2036–2050. doi:10.1109/tgrs.2005.853192
- Merlin, O., Escorihuela, M. J., Mayoral, M. A., Hagolle, O., Al Bitar, A., and Kerr, Y. (2013). Self-calibrated evaporation-based disaggregation of SMOS soil moisture: an evaluation study at 3km and 100m resolution in Catalunya, Spain. *Remote Sens. Environ.* 130, 25–38. doi:10.1016/j.rse.2012.11.008
- Merlin, O., Rüdiger, C., Al Bitar, A., Richaume, P., Walker, J. P., and Kerr, Y. H. (2012). Disaggregation of SMOS soil moisture in southeastern Australia. *IEEE Trans. Geosci. Remote Sens.* 50, 1556–1571. doi:10.1109/tgrs.2011.2175000
- Merlin, O., Stefan, V. G., Amazirh, A., Chanzy, A., Ceschia, E., Er-Raki, S., et al. (2016). Modeling soil evaporation efficiency in a range of soil and atmospheric conditions using a meta-analysis approach. *Water Resour. Res.* 52, 3663–3684. doi:10.1002/2015wr018233
- Mishra, V., Ellenburg, W. L., Griffin, R. E., Mecikalski, J. R., Cruise, J. F., Hain, C. R., et al. (2018). An initial assessment of a smap soil moisture disaggregation scheme using tir surface evaporation data over the continental United States. *Int. J. Appl. Earth Obs. Geoinform.* 68, 92–104. doi:10.1016/j.jag.2018.02.005
- Molero, B., Merlin, O., Malbêteau, Y., Al Bitar, A., Cabot, F., Stefan, V., et al. (2016). SMOS disaggregated soil moisture product at 1 km resolution: processor overview and first validation results. *Remote Sens. Environ.* 180, 361–376. doi:10.1016/j.rse.2016.02.045
- Moran, M., Clarke, T., Inoue, Y., and Vidal, A. (1994). Estimating crop water deficit using the relation between surface-air temperature and spectral vegetation index. *Remote Sens. Environ.* 49, 246–263. doi:10.1016/0034-4257(94)90020-5
- Mu, Q., Heinsch, F. A., Zhao, M., and Running, S. W. (2007). Development of a global evapotranspiration algorithm based on MODIS and global meteorology data. *Remote Sens. Environ.* 111, 519–536. doi:10.1016/j.rse.2007.04.015
- Narayan, U., Lakshmi, V., and Jackson, T. J. (2006). High-resolution change estimation of soil moisture using l-band radiometer and radar observations made during the smex02 experiments. *IEEE Trans. Geosci. Remote Sens.* 44, 1545–1554. doi:10.1109/tgrs.2006.871199
- Ojha, N., Merlin, O., and Escorihuela, M. J. (2020). “Towards synergies between thermal-disaggregated and Sentinel1-based soil moisture data sets,” in 2020 Mediterranean and Middle-East geoscience and remote sensing symposium (M2GARSS), Tunis, Tunisia, March 9–11, 2020 (IEEE).
- Ojha, N., Merlin, O., Molero, B., Suere, C., Olivera-Guerra, L., Ait Hssaine, B., et al. (2019). Stepwise disaggregation of SMAP soil moisture at 100 m resolution using landsat-7/8 data and a varying intermediate resolution. *Remote Sens.* 11, 1863. doi:10.3390/rs11161863
- O’Neill, P., Chan, S., Njoku, E., Jackson, T., and Bindlish, R. (2018). *Algorithm theoretical basis document level 2 & 3 soil moisture (passive) data products; revision b*. Pasadena, CA: Jet Propulsion Lab., California Institute of Technology.
- Peng, J., Loew, A., Zhang, S., Wang, J., and Niesel, J. (2015a). Spatial downscaling of satellite soil moisture data using a vegetation temperature condition index. *IEEE Trans. Geosci. Remote Sens.* 54, 558–566. doi:10.1109/TGRS.2015.2462074
- Peng, J., Niesel, J., and Loew, A. (2015b). Evaluation of soil moisture downscaling using a simple thermal-based proxy—the REMEDHUS network (Spain) example. *Hydrol. Earth Syst. Sci.* 19, 4765–4782. doi:10.5194/hess-19-4765-2015
- Piles, M., Entekhabi, D., and Camps, A. (2009). A change detection algorithm for retrieving high-resolution soil moisture from SMAP radar and radiometer observations. *IEEE Trans. Geosci. Remote Sens.* 47, 4125–4131. doi:10.1109/tgrs.2009.2022088
- Piles, M., Petropoulos, G. P., Sánchez, N., González-Zamora, Á., and Ireland, G. (2016). Towards improved spatio-temporal resolution soil moisture retrievals from the synergy of SMOS and MSG SEVIRI spaceborne observations. *Remote Sens. Environ.* 180, 403–417. doi:10.1016/j.rse.2016.02.048
- Sandholt, I., Rasmussen, K., and Andersen, J. (2002). A simple interpretation of the surface temperature/vegetation index space for assessment of surface moisture status. *Remote Sens. Environ.* 79, 213–224. doi:10.1016/s0034-4257(01)00274-7
- Sobrino, J. A., Jimenez-Munoz, J. C., Soria, G., Brockmann, C., Ruescas, A., Danne, O., et al. (2015). “A prototype algorithm for land surface temperature retrieval from Sentinel-3 mission,” in Sentinel-3 for science workshop Venice, Italy, Vol. 734, 38.
- Stefan, V. G., Merlin, O., Er-Raki, S., Escorihuela, M. J., and Khabba, S. (2015). Consistency between *in situ*, model-derived and high-resolution-image-based soil temperature endmembers: towards a robust data-based model for multi-resolution monitoring of crop evapotranspiration. *Remote Sens.* 7, 10444–10479. doi:10.3390/rs70810444
- Tagesson, T., Horion, S., Nieto, H., Zaldo Fornies, V., Mendiguren González, G., Bulgin, C. E., et al. (2018). Disaggregation of SMOS soil moisture over West Africa using the temperature and vegetation dryness index based on SEVIRI land surface parameters. *Remote Sens. Environ.* 206, 424–441. doi:10.1016/j.rse.2017.12.036
- Talleg, T., Béziat, P., Jarosz, N., Rivalland, V., and Ceschia, E. (2013). Crops’ water use efficiencies in temperate climate: comparison of stand, ecosystem and agronomical approaches. *Agric. For. Meteorol.* 168, 69–81. doi:10.1016/j.agrformet.2012.07.008
- Verhoest, N. E., Lievens, H., Wagner, W., Álvarez-Mozos, J., Moran, M., and Mattia, F. (2008). On the soil roughness parameterization problem in soil moisture retrieval of bare surfaces from synthetic aperture radar. *Sensors* 8, 4213–4248. doi:10.3390/s8074213
- Waite, W. P., and MacDonald, H. C. (1971). “Vegetation penetration” with K-band imaging radars. *IEEE Trans. Geosci. Electron.* 9, 147–155. doi:10.1109/tge.1971.271487

- Wanders, N., Bierkens, M. F., de Jong, S. M., de Roo, A., and Karssenber, D. (2014). The benefits of using remotely sensed soil moisture in parameter identification of large-scale hydrological models. *Water Resour. Res.* 50, 6874–6891. doi:10.1002/2013wr014639
- Wegmuller, U., and Werner, C. (1997). Retrieval of vegetation parameters with SAR interferometry. *IEEE Trans. Geosci. Remote Sens.* 35, 18–24. doi:10.1109/36.551930
- Wigneron, J.-P., Jackson, T., O'Neill, P., De Lannoy, G., De Rosnay, P., Walker, J., et al. (2017). Modelling the passive microwave signature from land surfaces: a review of recent results and application to the L-band SMOS & SMAP soil moisture retrieval algorithms. *Remote Sens. Environ.* 192, 238–262. doi:10.1016/j.rse.2017.01.024
- Yang, Y., Guan, H., Long, D., Liu, B., Qin, G., Qin, J., et al. (2015). Estimation of surface soil moisture from thermal infrared remote sensing using an improved trapezoid method. *Remote Sens.* 7, 8250–8270. doi:10.3390/rs70708250
- Zhang, D., and Zhou, G. (2016). Estimation of soil moisture from optical and thermal remote sensing: a review. *Sensors* 16, 1308. doi:10.3390/s16081308

Conflict of Interest: Author ME is employed by the company isardSAT.

The remaining authors declare that the research was conducted in the absence of any commercial or financial relationships that could be construed as a potential conflict of interest.

Copyright © 2021 Ojha, Merlin, Suere and Escorihuela. This is an open-access article distributed under the terms of the Creative Commons Attribution License (CC BY). The use, distribution or reproduction in other forums is permitted, provided the original author(s) and the copyright owner(s) are credited and that the original publication in this journal is cited, in accordance with accepted academic practice. No use, distribution or reproduction is permitted which does not comply with these terms.

Chapter 5

How to further enhance the downscaling resolution

Contents

5.1	Introduction	86
5.2	Implementing a new DISPATCH algorithm at 100 m resolution	87
5.3	Practical algorithm to bridge the gap between SMAP and Landsat resolution .	90
5.4	Selecting an optimal intermediate spatial resolution and evaluating DISPATCH at 100 m resolution	92
5.5	Conclusion	95
5.6	Article : Stepwise disaggregation of SMAP soil moisture at 100 m resolution using Landsat-7/8 data and a varying intermediate resolution	95

5.1 Introduction

The $DISPATCH_{veg-ext}$ algorithm developed in the previous chapter is originally applied to SMOS or SMAP soil moisture (SM) data using the 1 km resolution MODIS optical/thermal data as ancillary information. In this configuration, DISPATCH thus provides SM data at 1 km resolution on a daily temporal scale. SM data sets at 1 km resolution can be used for different applications such as evapotranspiration monitoring, retrieving soil properties, root-zone SM estimation, and other hydrological purposes. But a 1 km SM resolution product is not sufficient for many agricultural applications such as early crop detection, yield estimation, water stress detection, irrigation scheduling, and fine scale hydrological purposes such as flood forecasting, drought monitoring, groundwater level assessment. Therefore, SM data are required at a higher resolution to be useful for a wider variety of applications.

Currently, there exist few thermal sensors that collect land surface temperature (LST) data at high – typically 100 m – resolution, especially Landsat and Advanced Spaceborne Thermal Emission and Reflection Radiometer (ASTER). Still, the DISPATCH algorithm is commonly applied to daily global coverage MODIS thermal data, but there is no routine application that can directly apply the DISPATCH algorithm to the Landsat data to provide SM at 100 m resolution (Merlin et al., 2009, 2013). In particular, a few challenges need to be addressed before extending the DISPATCH algorithm to 100 m resolution: 1) Landsat does not provide daily global coverage like MODIS data, so a stepwise approach is required to define each Landsat scene separately over the 1 km disaggregated SMOS/SMAP data, and 2) the contextual nature of DISPATCH depends on the extreme wet and dry edges within the SMOS/SMAP pixel, and the accuracy of temperature endmembers is expected to vary with the spatial extent over which the DISPATCH algorithm is applied and 3) the presence of boxy artifacts that occur due to the combination of multi-resolution datasets.

The 100 m SM resolution product is evaluated over the R3 irrigated agricultural region for 22 irrigated crop fields. The output product is analyzed on 5cm surface SM during the season of 2016.

Chapter splits into three sections: 1) describing the overall methodology to overcome the issues mentioned above 2) presenting the practical algorithm to achieve the 100 m resolution from SMAP, MODIS, and Landsat data introducing an optimal intermediate spatial resolution (ISR) 3) validating the 100 m resolution SM product with available in situ SM measurements.

The 100 m resolution SM data set is evaluated over the R3 irrigated district near Marrakech (Morocco) for 22 irrigated crop fields.

5.2 Implementing a new DISPATCH algorithm at 100 m resolution

The methodology applied for the DISPATCH algorithm at 1 km resolution is not fully applicable at 100 m resolution. The main difference encountered while increasing the spatial resolution to 100 m is : 1) the LST value range increases with spatial resolution as the heterogeneity of the land surfaces increases, and the temperature endmembers estimation should be adapted to such conditions, 2) a robust representation of the SEE model is needed to cover at such high resolution the full range of SM values from residual to saturation. Hereafter, the new algorithm developed at 100 m resolution will be named *DISPATCH*_{100m}.

To better estimate wet and dry edges, the algorithm described in [Tang et al. \(2010\)](#) is used to remove outliers from the LST-fvg graph. First, the algorithm iteratively processes each pixel and finds the maximum temperature for each fvg interval. Then, the highest temperature of each fvg interval is linearly approximated to estimate the dry edge. The wet edge is calculated similarly to the dry edge by removing outliers on the lower end. This method removes the isolated points with abnormally high/low LST and provides a more robust representation of wet edge and dry edge.

A visual representation of the calculation of temperature endmembers for the *DISPATCH*_{veg-ext} and for the *DISPATCH*_{100m} algorithm, both applied at 100 m resolution, is shown in Figure 5.1. For *DISPATCH*_{veg-ext}, the temperature endmembers are calculated from the maximum and minimum temperatures within a given SMAP pixel. Note that wet edge and dry edges are computed for each SMOS or SMAP pixel individually. On the one hand, if the *DISPATCH*_{veg-ext} algorithm was used to calculate temperature endmembers at 100 m resolution, it is evident from Figure 5.1 that the dry edge would be overestimated, and wet edge would be underestimated. On the other hand, the *DISPATCH*_{100m} algorithm calculates the temperature endmembers by removing the outliers, and hence the computed temperature endmembers look more accurate for estimating the wet and dry edges to be used by DISPATCH.

The linear SEE(SM) model was a suitable approximation for *DISPATCH*_{classic} when applied at the 1 km resolution. As we increase the spatial resolution to 100 m, the spatial heterogeneity will increase, and the linear relationship of SEE with SM will not cover such a large spatial heterogeneity. So, a non-linear, more physically-based model of SEE is proposed ([Komatsu, 2003](#); [Merlin et al., 2016](#)). When replacing the SEE model in DISPATCH, it is crucial to check the new model's performance compared to the old model. For this, the correlation coefficient and slope between high-resolution Landsat-derived SEE and in situ SM are estimated for both models separately (shown in Figure 5.2). The correlation coefficient and slope of the linear SEE model are 0.87 and 0.17, and for the non-linear SEE model, it is 0.87 and 0.41, respectively. It is observed that correlation coefficient is similar in both cases, but the slope significantly decreases for the linear case. The results are entirely compatible with using a non-linear model for SEE at 100 m resolution.

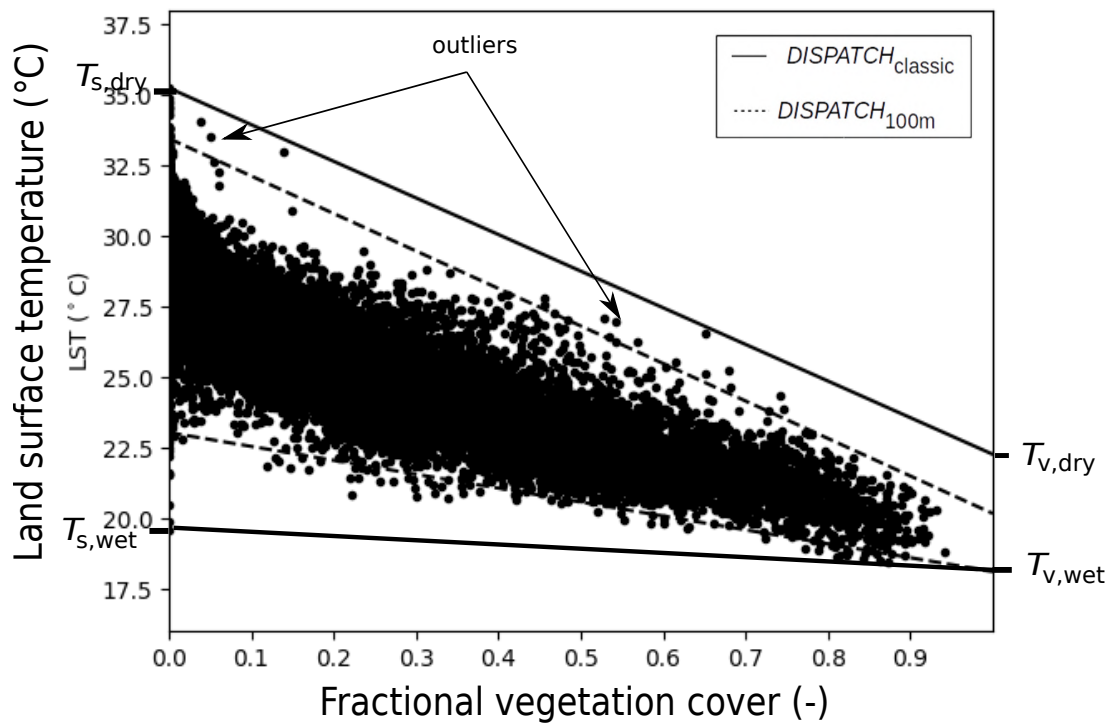


Figure 5.1: $DISPATCH_{veg-ext}$ and $DISPATCH_{100m}$ algorithms calculate the wet and dry edges in Land surface temperature-fractional vegetation feature space for 100 m resolution Landsat data.

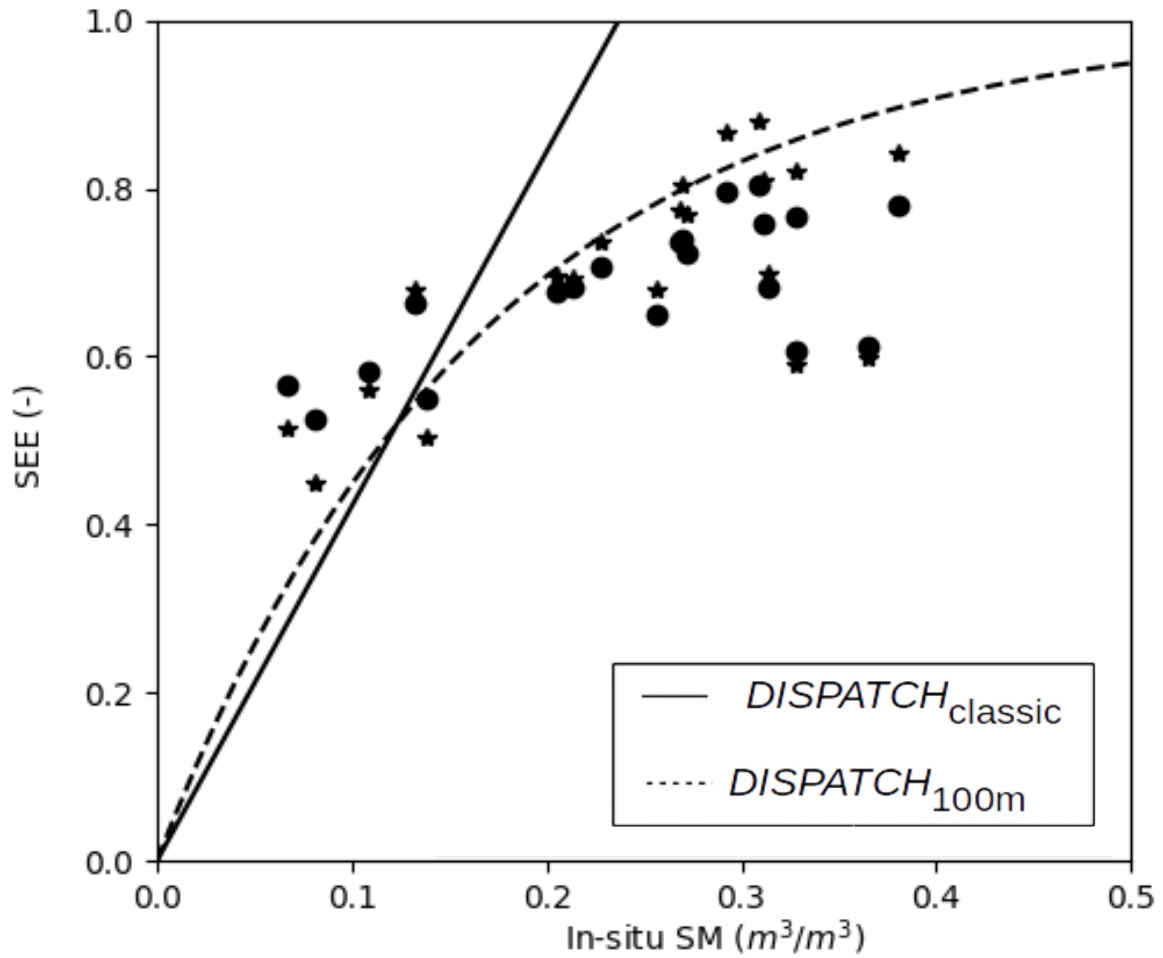


Figure 5.2: Landsat-derived SEE as a function of in situ SM superimposed with the SEE(SM) and SEE(LST) models for both linear and non-linear SEE models derived from $DISPATCH_{classic}$ and $DISPATCH_{100m}$ algorithms separately.

5.3 Practical algorithm to bridge the gap between SMAP and Landsat resolution

Once the above modifications for the DISPATCH algorithm are in place, may run the new algorithm to disaggregate the low (40 km) resolution SM to high (100 m) resolution SM. However, the gap between the low and high resolutions becomes enormous, which is expected to deteriorate the disaggregation output. This is especially true because of the non-linear relationship between SEE and SM. So to overcome this limitation, a new methodology is introduced based on a two-step downscaling algorithm (shown in Figure 6.1). The two steps downscaling algorithm are carried out in different phases. At first, SMOS/SMAP SM at 40 km resolution is disaggregated to 1 km resolution using MODIS LST/NDVI at 1 km resolution. Then, the 1 km disaggregated SM product is further aggregated at different intermediate spatial resolutions (ISR) (from 1 km to 40 km). *DISPATCH*_{100m} algorithm is next applied to the ISR SM pixel to provide a SM image disaggregated at 100 m resolution. An intermediate step is added after the aggregation step to derive several (number N) ISR pixels that partially overlap to reduce the boxy artifact effects in the 100 m resolution disaggregated image. Various ISR grids are made from the 1 km resolution data by displacing the ISR grid in different directions, where N is decided by the number of displacements. The DISPATCH algorithm is finally applied using Landsat LST and NDVI data to each N number ISR SM image separately to provide SM at 100 m resolution. All the N disaggregated images are averaged and composited to the single image, which is the final output of the *DISPATCH*_{100m} process.

It is worth mentioning that the ISR is also useful due to the contextual nature of the LST-fvg graph. Based on the contextual approach, the DISPATCH algorithm calculates the temperature endmembers from the LST-fvg graph. Thus, the temperature endmembers depend on surface heterogeneity present within the corresponding area, which varies with the spatial extent of that area. Since the spatial extent of the second phase of the disaggregation step is dependent on the ISR resolution, selecting an optimal ISR is necessary for the accuracy of the disaggregated SM. To be specific, if we increase the ISR, the heterogeneity of the land surface will increase. Hence, the calculation of the temperature endmembers will be more accurate when considering the heterogeneity issue. However, the ISR value is also a compromise with the spatial heterogeneity of the meteorological forcing, given that contextual methods assume uniform atmospheric conditions within the study extent.

To better understand how the LST-fvg graph behaves for different ISR values, Figure 5.4 illustrates the results for different ISR values: 1 km, 3 km, 5 km, 10 km, and 30 km. It is seen from the graph that the range of LST and fvg values increase with the increase in ISR (spatial extent) because of the increase in spatial variability. The mean LST values for smaller ISR values are likely to be biased, which would induce biases in SEE/TDVI estimates and subsequently in disaggregated SM values. More uncertainty will be observed in the wet and dry edges if we decrease the spatial extent. Nevertheless, if we increase the spatial extent too much, the spatial variability of meteorological conditions may reach the critical level and invalidate the contextual nature of DISPATCH. The constraints (accuracy of temperature endmembers and the gap between low and high resolutions) represent an essential rationale for selecting a sequential method between 40 km and 100 m resolutions.

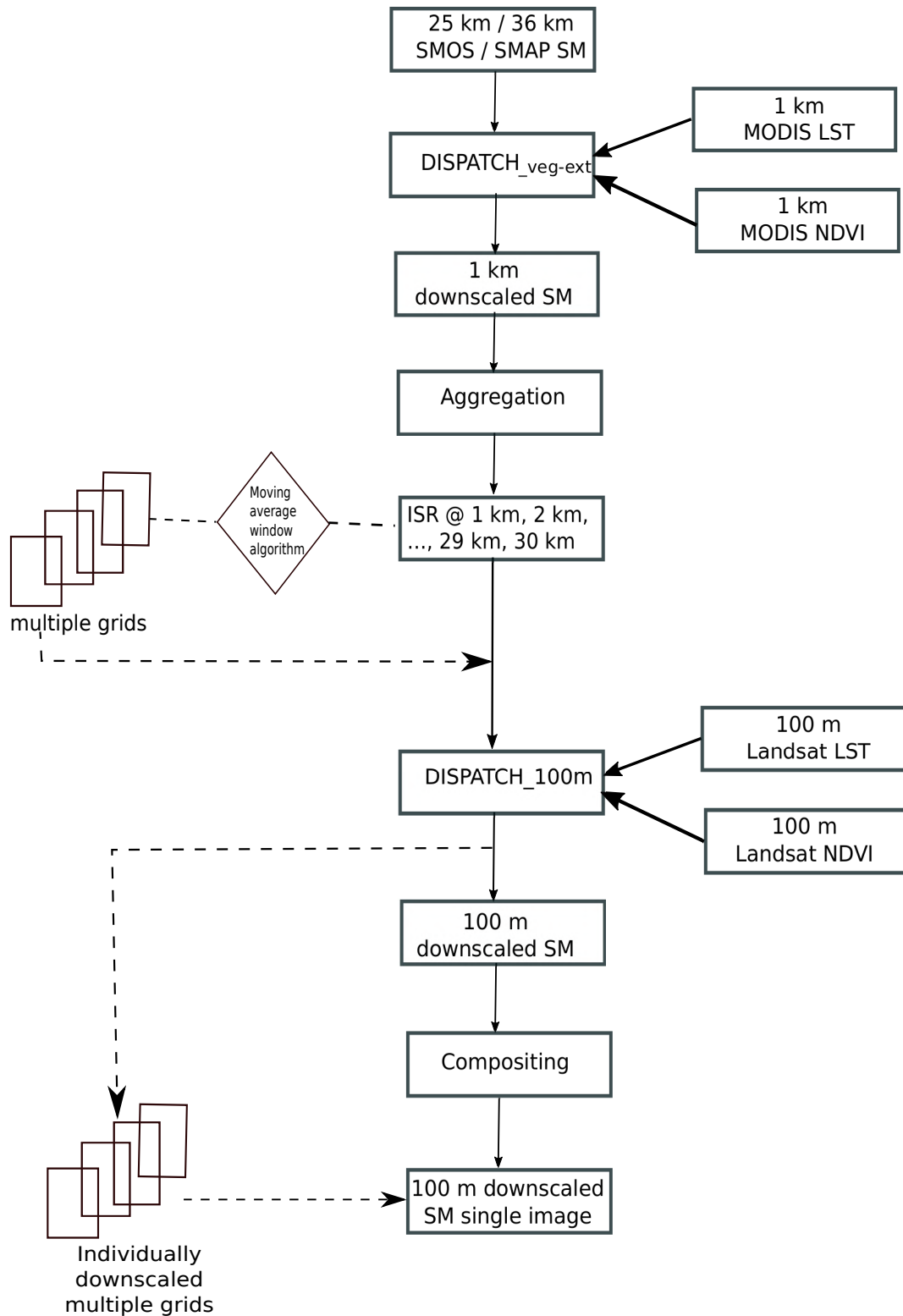


Figure 5.3: Flowchart of the two-step downscaling approach from 40 km resolution to 1 km ($DISPATCH_{veg-ext}$), from 1 km to ISR (aggregation to variable ISR), and from ISR to 100 m ($DISPATCH_{100m}$)

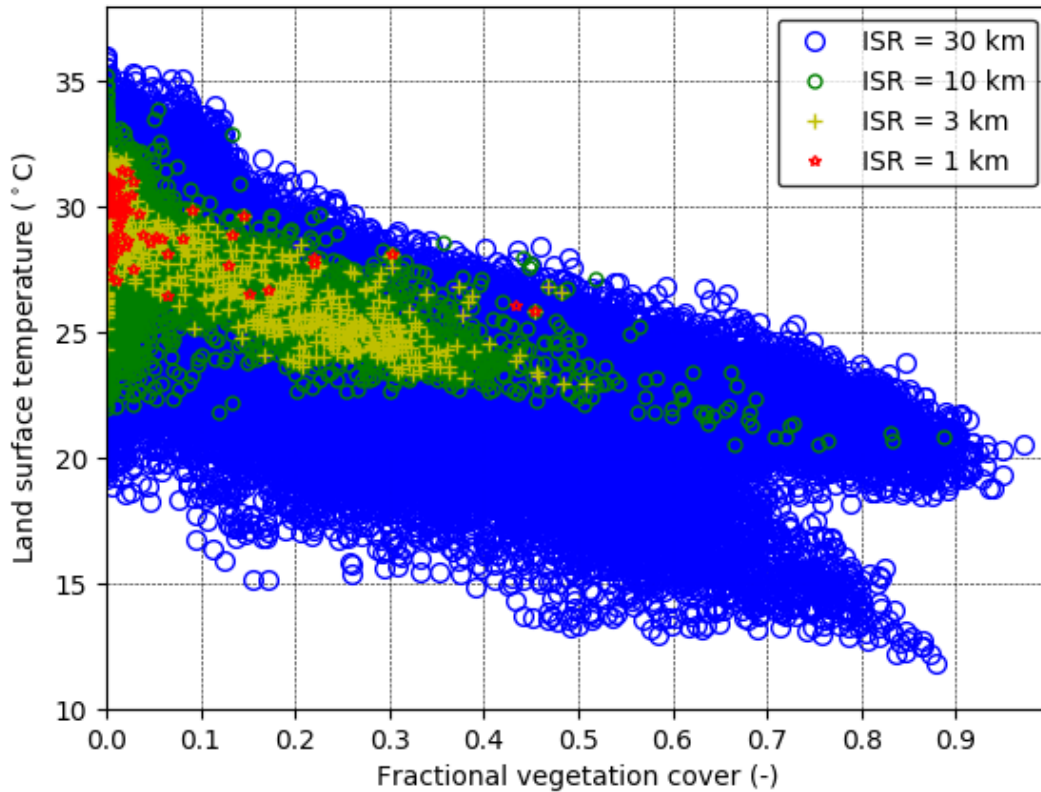


Figure 5.4: The LST-fvg feature space graph is represented for an ISR pixel of 30 km, 10 km, 3 km and 1 km for Landsat LST and fvg data at 100 m resolution.

5.4 Selecting an optimal intermediate spatial resolution and evaluating DISPATCH at 100 m resolution

A sensitivity analysis is done for different ISR values to understand the importance of ISR in the DISPATCH algorithm and to assist in selecting an optimal ISR in terms of disaggregation accuracy at 100 m resolution. Different ISR ranging from 1 km to 30 km (obtained from the 1 km SM product) are separately used as input, and the $DISPATCH_{100m}$ output results are evaluated to find the optimal ISR. The sensitivity is evaluated with in situ SM of R3 irrigated areas for 22 parcels on day of year (DOY) 6, 14, 30, 38, 62, and 78 of 2016. The DOY is selected based on the availability of the in situ SM data and the overpass dates of Landsat. Statistical analysis is performed (illustrated in Figure 5.5) by considering correlation coefficient (R), the slope of the linear regression (slope) root mean square difference (RMSD), and absolute mean bias (Absolute MB) between disaggregated and in situ SM. It is observed that the temporal variability of R and slope is more prominent for lower ISR, a negative slope is observed for ISR lower than 5 km, and a positive slope is observed for ISR greater than 10 km. From day-to-day spatial variability, it is observed that R increases from ISR 1 km to 5 km, and then it becomes constant until 30 km while the slope decreases with the increase in ISR from 10 to 30 km.

The slope of linear regression is a good indicator of disaggregation efficiency. The reduction in

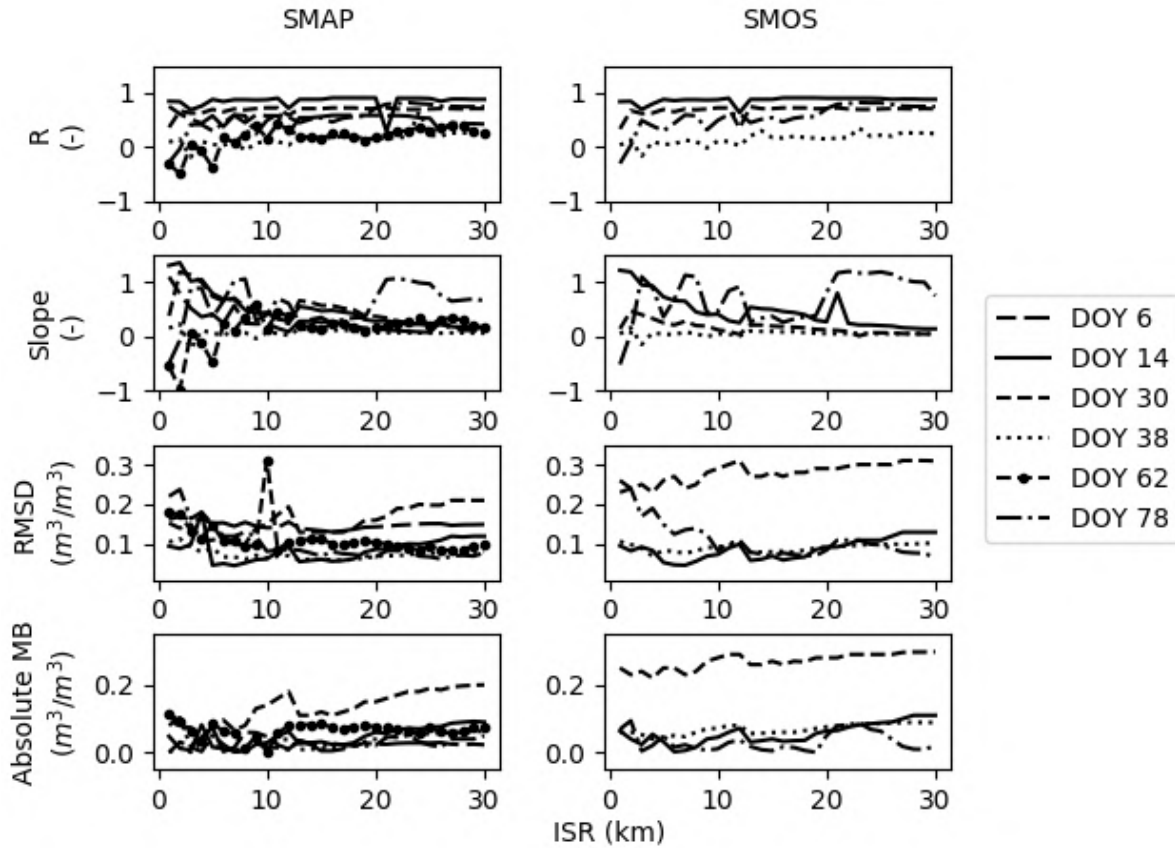


Figure 5.5: Correlation coefficient (R), slope of the linear regression (slope), absolute mean bias (Absolute MB) and root mean square difference (RMSD) between 100 m resolution disaggregated and in situ SM for a range of ISR values (from 1 km to 30 km) for SMAP (left) and SMOS (right) data and for each sampling date separately.

the linear regression slope can be explained by the gap between high and low resolutions. As the gap increases, the disaggregation efficiency decreases. Another key observation from the Figure 5.5 is that MB increases with the increase in ISR, representing the worsening of the disaggregation performance. These factors prohibit the use of high and low values of ISR in DISPATCH algorithms. Hence based on this statistical analysis ISR, 10 km shows an optimal ISR for the downscaling algorithm.

ISR is thus set to 10 km, and the two-step downscaling is performed to disaggregate the 40 km resolution SMOS/SMAP pixel to 100 m resolution using Landsat optical/thermal data for each sampling date. The statistical comparison between 100 m resolution disaggregated and in situ SM is reported in Table 5.1.

The statistical comparison between 100 m disaggregated SM products and in situ SM measurements shows that the $DISPATCH_{100m}$ SM output product is able to capture the spatial heterogeneity that occurs in agricultural areas, illustrated by the significant spatial correlation coefficient (0.57 to .87). Statistical analysis in general shows that the DISPATCH-100m algorithm performs better when the sub-pixel variability is larger than $0.06 \text{ m}^3/\text{m}^3$.

Day of year (DOY)	SMAP				SMOS			
	R (-)	Slope (-)	Absolute MB (m^3/m^3)	RMSD (m^3/m^3)	R (-)	Slope (-)	Absolute MB (m^3/m^3)	RMSD (m^3/m^3)
6	0.57	0.24	0.05	0.14	-	-	-	-
14	0.87	0.44	0.03	0.06	0.87	0.41	0.05	0.07
30	0.72	0.44	0.14	0.15	0.72	0.12	0.28	0.29
38	0.11	0.07	0.02	0.07	0.11	0.05	0.07	0.09
62	0.16	0.14	0.002	0.31	-	-	-	-
78	0.49	0.40	0.02	0.08	0.49	0.46	0.01	0.08
All	0.55	0.34	0.05	0.09	0.55	0.26	0.10	0.13

Table 5.1: Statistical results in terms of correlation coefficient (R), slope of the linear regression, absolute mean bias (MB) and root mean square difference (RMSD) between 100 m resolution disaggregated and in situ SM using an ISR set to 10 km (single grid) and SMAP and SMOS data as input separately.

5.5 Conclusion

A stepwise sequential downscaling approach is developed to disaggregate 40 km resolution SMAP/SMOS SM to 100 m resolution using the DISPATCH algorithm and Landsat LST/NDVI data. At first, the 40 km resolution SM is disaggregated to 1 km resolution using MODIS LST/NDVI and $DISPATCH_{veg-ext}$. Then the 1 km downscaled SM product is aggregated to an ISR. Further, the aggregated ISR SM is disaggregated to 100 m resolution using Landsat LST/NDVI, and a new algorithm ($DISPATCH_{100m}$) adapted to the high variability encountered at 100 m resolution. Especially, the $DISPATCH_{100m}$ algorithm suggests two enhancements to the existing algorithms so that it can be applicable at high resolution: 1) by using a non-linear SEE as a function of SM to cover the full range of SM values 2) by improving the estimation of temperature endmembers for the calculation of wet edge and dry edges by removing outliers in LST data.

By using the distributed in situ SM measurements collected over the R3 perimeter, it was possible to identify an optimal ISR value, which maximizes the statistical disaggregation results. The better results are obtained for an ISR set to 10 km and when the spatial variability is larger significant than $0.06 m^3/m^3$. Since the improved algorithm uses Landsat optical/thermal data as one of its inputs, the algorithm is prone to loss in spatial extent due to cloud cover and the long repeat cycle (16 days) of Landsat. Two different and complementary strategies are proposed to overcome this limitation by building a synergy with radar data (**Chapter 6**) and developing a coupled disaggregation-assimilation scheme in a dynamical SM model (**Chapter 7**).

5.6 Article : Stepwise disaggregation of SMAP soil moisture at 100 m resolution using Landsat-7/8 data and a varying intermediate resolution

1. Ojha, N., Merlin, O., Molero, B., Suere, C., Olivera-Guerra, L., Ait Hssaine, B., Amazirh, A., Al Bitar, A., Escorihuela, M.J. and Er-Raki, S., 2019. Stepwise disaggregation of SMAP soil moisture at 100 m resolution using Landsat-7/8 data and a varying intermediate resolution. Remote Sensing, 11(16), p.1863.



Article

Stepwise Disaggregation of SMAP Soil Moisture at 100 m Resolution Using Landsat-7/8 Data and a Varying Intermediate Resolution

Nitu Ojha ^{1,*}, Olivier Merlin ¹, Beatriz Molero ¹, Christophe Suere ¹, Luis Olivera-Guerra ¹,
Bouchra Ait Hssaine ^{2,3}, Abdelhakim Amazirh ^{2,3}, Ahmad Al Bitar ¹ and
Maria Jose Escorihuela ⁴ and Salah Er-Raki ^{2,3}

¹ Centre d'Etudes Spatiales de la Biosphère (CESBIO, Université de Toulouse (CNES/CNRS/INRA,IRD/UPS), 31013 Toulouse, France

² Faculty of Sciences and Techniques, Cadi Ayyad University, Marrakech 40000, Morocco

³ Center for Remote Sensing Application (CRSA), University Mohammed VI Polytechnic (UM6P), Benguerir 43150, Morocco

⁴ isardSAT S.L, Parc Tecnologic Barcelona Activa, 08042 Barcelona, Spain

* Correspondence: ojhan@cesbio.cnes.fr or nituojha11@gmail.com

Received: 25 June 2019; Accepted: 4 August 2019; Published: 9 August 2019



Abstract: Global soil moisture (SM) products are currently available from passive microwave sensors at typically 40 km spatial resolution. Although recent efforts have been made to produce 1 km resolution data from the disaggregation of coarse scale observations, the targeted resolution of available SM data is still far from the requirements of fine-scale hydrological and agricultural studies. To fill the gap, a new disaggregation scheme of Soil Moisture Active and Passive (SMAP) data is proposed at 100 m resolution by using the disaggregation based on physical and theoretical scale change (DISPATCH) algorithm. The main objectives of this paper is (i) to implement DISPATCH algorithm at 100 m resolution using SMAP SM and Landsat land surface temperature and vegetation index data and (ii) to investigate the usefulness of an intermediate spatial resolution (ISR) between the SMAP 36 km resolution and the targeted 100 m resolution. The sequential disaggregation approach from 36 km to ISR (ranging from 1 km to 30 km) and from ISR to 100 m resolution is evaluated over 22 irrigated field crops in central Morocco using in-situ SM measurements collected from January to May 2016. The lowest root mean square difference (RMSD) between the 100 m resolution disaggregated and in-situ SM is obtained when the ISR is around 10 km. Therefore, the two-step disaggregation is more efficient than the direct disaggregation from SMAP to 100 m resolution. Moreover, we propose a moving average window algorithm to increase the accuracy in the 100 m resolution SM as well as to reduce the low-resolution boxy artifacts on disaggregated images. The correlation coefficient between 100 m resolution disaggregated and in situ SM ranges between 0.5–0.9 for four out of the six extensive sampling dates. This methodology relies solely on remote sensing data and can be easily implemented to monitor SM at a high spatial resolution over irrigated regions.

Keywords: disaggregation; soil moisture; DISPATCH; Intermediate spatial resolution; SMAP

1. Introduction

Knowledge of soil moisture provides key information about the coupling between the land surface and atmosphere. By controlling the partitioning of water inputs (precipitation, irrigation) into evaporation, infiltration, and runoff, the soil water content is related to the crop water consumption [1], hydrological fluxes [2], weather predictions [3] and climate projections [4].

L-band (1.4 GHz) microwave radiometry is currently the most adapted remote sensing technique for the estimation of near-surface soil moisture (SM) from space [5–10]. Microwave observations at L-band, as compared to higher microwave frequencies, are more sensitive to SM and less sensitive to the soil surface roughness and vegetation optical depth [11]. In this context, European Space Agency (ESA) and National Aeronautics and Space Administration (NASA) have launched the SMOS [6,12] and SMAP [5] satellites in 2009 and 2014, respectively. Both satellites embark an L-band radiometer to retrieve the 3–5 cm SM with a repeat cycle of less than 3 days globally. The spatial resolution of both radiometers is approximately 40 km [5,6].

Despite the high radiometric accuracy achieved by L-band radiometers, the data provided globally have a low spatial resolution, which makes the validation of remote sensing products difficult and limits their application to large scale studies only [13]. For hydro-agriculture purposes, there is a crucial need for SM data at a higher spatial resolution [14,15]. Consequently, disaggregation techniques have been proposed to improve the spatial resolution of the SM data available at a high temporal frequency [16–22]. Existing downscaling methods for SM can be classified into three major groups (1) satellite-based methods; (2) methods using Geo-information data and (3) model-based methods [23,24]. The satellite methods combine the use of radar and optical data to coarse scale microwave radiometry [24]. Among optical-based methods, many studies have used as fine-scale information the fractional vegetation cover and land surface temperature (LST) derived from high-resolution (1 km to 100 m) optical/thermal sensors. The general idea of these methods is to relate LST to SM via the evapotranspiration process [20,25].

Relying on this principle, the disaggregation based on physical and theoretical scale change (DISPATCH) method [26,27] estimates the soil evaporative efficiency (SEE defined as the ratio of actual to potential soil evaporation), and implements a downscaling relationship that links the disaggregated SM to the low-resolution (LR) observation and the high-resolution (HR) SEE. The optical-derived SEE is expressed as a linear function of the retrieved soil temperature [28] and the minimum and maximum soil temperatures observed at HR within the LR pixel [26], according to the so-called contextual approach [29]. Based on the DISPATCH algorithm, the CATDS Level-4 Disaggregation (C4DIS) processor [30] was implemented at the Centre Aval de Traitement des Données SMOS (CATDS) as a level 4 product. C4DIS produces 1 km resolution SM data at the quasi-global scale from SMOS level 3 and Moderate resolution Imaging Spectroradiometer (MODIS) data.

The 1 km resolution SM disaggregated from SMOS products are currently used in a range of disciplines including root-zone soil moisture monitoring [31], detecting irrigated areas at the perimeter scale [32,33], retrieving soil properties from space [34], preventing the spread of desert locust swarms [35], evapotranspiration monitoring over rainfed areas [36], flood forecasting over large basins [37], estimating crop yield [38], and the methods to produce them are continuously evolving and maturing (Merlin et al. 2017). Note that few studies have applied the DISPATCH method to SMAP SM using MODIS data [39]. However, the 1 km resolution is often insufficient for many other fine-scale applications and areas where the surface is highly heterogeneous (e.g., [1]). SM data at the sub-kilometric (typically hectometric) resolution are especially required in agriculture for early crop detection, irrigation scheduling, water stress and yield monitoring [40] and in fine-scale hydrological studies for flood risk prevention, drought monitoring and groundwater level assessment [41], among other potential applications.

In fact, there is still no routine application of DISPATCH to Landsat data, which yet would be useful to increase the spatial resolution of available SM products up to 100 m [27,42]. One difficulty is that Landsat data do not provide global coverage at the daily scale (like MODIS data) so that a sequential approach is needed to “delineate” the 1 km resolution disaggregated SMAP data over each Landsat scene separately before DISPATCH can be implemented at 100 m resolution. Another difficulty is the contextual nature of DISPATCH, which relies on the extreme wet and dry conditions present within the LR pixel to calibrate the SEE model. Especially, the accuracy in temperature endmembers is expected to vary with the spatial extent over which DISPATCH is applied. A third difficulty is the

presence of boxy artifacts visible at LR when combining multi-source/multi-resolution remote sensing data within a disaggregation methodology. Boxy artifacts are common problems with downscaling methods [26,27,43].

In this context, this paper presents a new methodology to disaggregate optimally the 36 km resolution SMAP SM to 100 m resolution using Landsat data. The main objective is to assess the usefulness of an optimal intermediate spatial resolution (ISR) between the SMAP and Landsat resolutions. In practice, the 1 km resolution SM disaggregated from SMAP data using MODIS data (similar to C4DIS product for SMAP) is aggregated at ISR ranging from 1 km to 30 km, and DISPATCH is applied to ISR SM. The novelty of this paper thus lies in: (1) the application of DISPATCH to SMAP data at 100 m resolution, (2) the use of an ISR between SMAP and Landsat resolutions and (3) the removal of boxy artifacts on the 100 m resolution disaggregated images using a new technique.

Herein, the stepwise disaggregation approach is tested over an experimental area in central Morocco, comprised of 22 irrigated field crops over which the 0–5 cm SM has been monitored during the 2015–2016 season.

2. Materials and Methods

2.1. Study Area

The study focuses on a 30 km by 30 km area of the R3 irrigated zone (31.70N, 7.35W) located 40 km east of Marrakesh city in the Haouz plain, central Morocco (see Figure 1). To assess the performance of DISPATCH at the 100 m resolution, a set of 22 irrigated wheat fields, covering 3–4 ha each (Figure 1), were selected within a 1 km resolution MODIS pixel. SM sampling was undertaken on clear sky dates with almost simultaneous SMAP/MODIS/Landsat data over the 22 crop fields and repeated measurements were made along the agricultural season to cover all the phenological stages of wheat. Climate of the study area is mainly semi-arid with an annual average precipitation of 250 mm [44,45]. The soil texture in the R3 perimeter is mainly clayey. Flood irrigation is the most widely used method in this district. Wheat is generally sown in November–December and a mean total of 6 irrigations is applied to wheat crops from February till April, typically every 3 weeks. Harvesting is done in late May or early June [46,47].

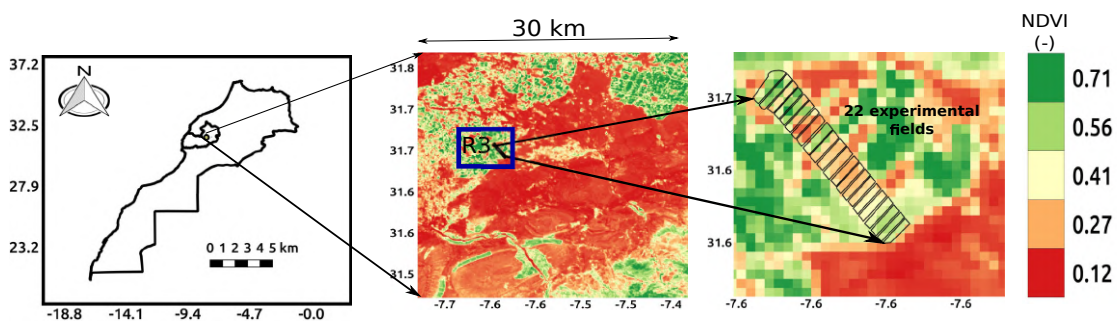


Figure 1. Location of Marrakesh, the Haouz plain in central Morocco and the 22 experimental crop fields in the R3 perimeter.

2.2. In-Situ Data

The 0–5 cm SM was measured manually from January to May months during the 2015–2016 agricultural season. The sampling strategy was to use theta probes to collect 10 distinct measurements for each of the 22 crop fields [48]. In practice, as the 22 parcels were chosen to be aligned and contiguous, two transects along both sides of the crop fields were walked and 5 theta probes measurements were taken on each crop side, at least 5 m from the field border. Theta probe measurements were calibrated using the gravimetric method, based on soil samples collected on each sampling date. In this study, the field-scale SM corresponds to the mean 0–5 cm calibrated theta probe measurements as in Amazirh et al. [49]. Among the 7 available sampling dates, only 6 are used herein in order to satisfy the

following criteria: SM measurements are available on a clear-sky Landsat overpass date, and the time difference between SMAP and Landsat overpasses is one day at maximum. The clear-sky dates with quasi-concurrent in-situ sampling and the satellite overpasses of SMAP, SMOS, MODIS and Landsat were on DOY 6, 14, 30, 38, 62 and 78. The remaining sampling dates are suitable for our study and help us identify the variability in SM along the growth of crops.

2.3. Remote Sensing Data

2.3.1. SMAP

SMAP was launched by NASA on 31 January 2015. SMAP is the first L-band mission combining both radar (active) and radiometer (passive) data to provide SM at a range of resolutions from 3 km (active) to 36 km (passive) with a revisit cycle of 2–3 days. But due to the failure of the SMAP radar, the SM produced from SMAP is currently provided on a ~36 km and ~9 km (by using a re-sampling technique) resolution grid. Note that a product combining SMAP and C-Band Sentinel-1 data has been recently provided by the mission [50]. SMAP has a near-polar sun-synchronous orbit at an altitude of 658 km with 6:00 a.m./p.m. local time descending/ascending overpass. SMAP works on multi-polarization with a fixed incidence angle at 40 degrees and a swath of ~1000 km [5]. In this paper, the SMAP level-3 (product name SPL3SMP A/D, version 005, Colliander et al. [51]) is used. The product is provided in HDF format on the version 2 cylindrical EASE grid at 36 km resolution. Data can be downloaded from <https://nsidc.org/data/SPL3SMP/versions/5>.

2.3.2. MODIS

MODIS LST and NDVI data are used by the C4DIS processor [30] to provide the 1 km resolution SM from the disaggregation of SMAP level-3 SM data. LST is extracted from version 5 MOD11A1, Terra overpass (10:30 a.m.) on ascending node and MYD11A, Aqua overpass (1 p.m.) on descending node. For each (ascending or descending) SMAP overpass, there are 6 MODIS LST products taken as input to C4DIS (one day before, same day and one day after SMAP overpass for both Aqua and Terra platforms). NDVI is extracted from version 5 MOD13, only for Terra overpass with an interval of 16 days [19,52].

2.3.3. Landsat

Landsat-7 and Landsat-8 were launched by NASA in April 1999 and February 2013, respectively. The images were downloaded from the USGS website, which provides surface reflectance and thermal radiances data in different spectral bands. The revisit time of each sensor is 16 days and there is an 8-day lag between Landsat-7 and Landsat-8 so that the Landsat constellation potentially provides (in cloud-free conditions) optical/thermal data every 8 days globally. The Landsat-7/8 30 m resolution reflectance data are aggregated at 100 m resolution and used to derive the fractional vegetation cover. The Landsat NDVI is calculated as the ratio of the re-sampled near-infrared reflectance to re-sampled red reflectance difference divided by their sum, and the fractional vegetation (f_v) is estimated as:

$$f_v = \frac{NDVI_{HR} - NDVI_s}{NDVI_v - NDVI_s} \quad (1)$$

where, $NDVI_{HR}$ represents the NDVI at high (100 m) resolution, $NDVI_s$ the NDVI at bare soil and $NDVI_v$ the NDVI at full cover vegetation. For this study, $NDVI_s$ and $NDVI_v$ are set to 0.1 and 0.9, respectively. Landsat-7 and Landsat-8 provide thermal infrared (TIR) data with a spatial resolution of 60 m and 100 m, respectively. LST is derived by using the single channel (SC) algorithm [53] from Landsat-7 band-6 and Landsat-8 band-7 as:

$$LST = \gamma \left[\frac{1}{\varepsilon} \left(\varphi_1 \cdot L_{sen} + \varphi_2 \right) + \varphi_3 \right] + \delta \quad (2)$$

where, ε is the surface emissivity, (γ, δ) are parameters depending on the radiance and brightness temperature of the Landsat thermal band and $\varphi_1, \varphi_2, \varphi_3$ are atmospheric variables function of the atmospheric water vapor content (ω) and derived from radiative transfer simulations using the GAPRI database [54]. The ω variable is obtained from the MODIS product MOD05.

2.3.4. SRTM

SRTM (Shuttle Radar Topography Mission) 1 arc second global data are used to correct Landsat LST for topographic effects [27]. Although the study area is rather flat, the topographic correction is applied by default in DISPATCH. The 30 m resolution SRTM data are aggregated to 100 m resolution, consistent with the Landsat LST resolution.

2.4. DISPATCH

2.4.1. General Equations

The main equations of the DISPATCH method implemented at both 1 km and 100 m resolutions are reminded in this subsection. The SM downscaled at HR (refers to either 1 km or 100 m resolution) is written as:

$$SM_{HR} = SM_{LR} + \left(\frac{\delta SEE}{\delta SM} \right)_{LR}^{-1} * (SEE_{HR} - SEE_{LR}) \quad (3)$$

where, SM_{HR} represents the disaggregated SM at HR, SM_{LR} the SM at LR (refers to either SMAP or ISR resolution) derived from SMAP data or from their disaggregation to 1 km resolution, SEE_{HR} the SEE at HR derived from MODIS or Landsat, SEE_{LR} the HR SEE aggregated at LR, and $\left(\frac{\delta SEE}{\delta SM} \right)_{LR}^{-1}$ the inverse of the partial derivative of the SEE(SM) model evaluated at LR. SEE is assumed to follow a linear relationship with the soil temperature [28] and is thus expressed as:

$$SEE_{HR} = \frac{T_{s,dry} - T_{s,HR}}{T_{s,dry} - T_{s,wet}} \quad (4)$$

where T_s is the soil surface temperature, $T_{s,dry}$ and $T_{s,wet}$ the soil temperature in fully dry ($SEE = 0$) and water-saturated ($SEE = 1$) conditions, respectively. Temperature endmembers $T_{s,dry}$ and $T_{s,wet}$ are calculated from a graph between LST and f_v derived at HR from MODIS or Landsat data. The soil temperature is derived from a linear decomposition of LST into soil and vegetation temperature. The trapezoidal method [26,55] is used to estimate the vegetation temperature, and the soil temperature is expressed as the residual term:

$$T_{s,HR} = \frac{T_{HR} - f_{v,HR} * T_{v,HR}}{1 - f_{v,HR}} \quad (5)$$

where T_{HR} represents the LST at HR, $T_{v,HR}$ the vegetation temperature at HR and $f_{v,HR}$ the fractional vegetation cover at HR.

The downscaling relationship of Equation (3) is hence based on two SEE models: SEE as a function of SM to estimate the first derivative at LR, and SEE as a function of LST (expressed in Equations (4) and (5)) to estimate the spatial variability of SM at HR.

2.4.2. DISPATCH at 1 km Resolution

Note that C4DIS is labeled as DISPATCH_{Lin} (for linear SEE model) in this study to distinguish the methodologies applied at 1 km and 100 m resolution. The current version of C4DIS/DISPATCH_{Lin}

is based on the various studies that have been done in the past using 1 km resolution MODIS data (Merlin et al. 2013, 2012b, 2010, 2009, 2008). In DISPATCH_{Lin} algorithm, the SEE(SM) model is linear:

$$SEE = \frac{SM}{SM_p} \quad (6)$$

where, SM_p is a soil moisture parameter (in soil moisture unit), which depends on soil properties and atmospheric conditions. It is calibrated at the SMAP pixel scale at the satellite overpass time using LR SEE and SM estimates ($SM_p = \frac{SM_{LR}}{SEE_{LR}}$). In this case, the derivative in Equation (3) is simply SM_p . The SEE(LST) model implemented in DISPATCH_{Lin} is based on Equation (4) using the temperature endmembers calculated by the simplest extrapolation method within the LST- f_v feature space: $T_{s,dry}$ and $T_{s,wet}$ are set to the maximum and minimum soil temperature within a given LR pixel.

This approach is implemented for C4DIS/DISPATCH_{Lin} and has provided favorable results at 1 km resolution for arid and semi-arid areas [26,30].

2.4.3. DISPATCH at 100 m Resolution

When applying the DISPATCH methodology at 100 m resolution over extremely heterogeneous areas like irrigated perimeters, one expects two main differences with the 1 km case. First, the range of LST values should increase at 100 m resolution, thereby enabling a more accurate definition of temperature endmembers, if the effect of outliers can be removed [56]. The second difference is that the full SM range (from the residual SM to the SM at saturation) is likely to be present within each LR pixel. Such extreme heterogeneity requires a robust representation of the SEE(SM) relationship over the full SM range. Especially, given that the SEE(SM) is known to be nonlinear [28,57,58], the linear approximation made in the 1 km case (Equation (6) is no more valid. Both differences between the 100 m and 1 km case involve two changes in the disaggregation algorithm: (i) the SEE model in Komatsu [57] replaces the linear SEE model, and (ii) the method in Tang et al. [56] is used to robustly determine the wet and dry edges. For clarity, the implementation of DISPATCH at 100 m resolution is labeled DISPATCH_{Exp} (for nonlinear SEE model).

In DISPATCH_{Exp}, the SEE(SM) model is expressed as [57]:

$$SEE = 1 - \exp\left(-\frac{SM}{SM_p}\right) \quad (7)$$

where SM_p is calculated from LR SM (the 1 km resolution disaggregated SM aggregated at ISR) and HR (Landsat-derived) SEE aggregated at ISR:

$$SM_p = \frac{SM_{LR}}{-\ln(1 - SEE_{LR})} \quad (8)$$

Note that the derivative in Equation (3) of the SEE(SM) model of Equation (7) can be computed in two different ways, as a function of LR SM:

$$\left(\frac{\delta SEE}{\delta SM}\right)_{LR}^{-1} = SM_p * \exp\left(-\frac{SM_{LR}}{SM_p}\right) \quad (9)$$

or as a function of LR SEE:

$$\left(\frac{\delta SEE}{\delta SM}\right)_{LR}^{-1} = \frac{SM_p}{1 - SEE_{LR}} \quad (10)$$

As both expressions of the derivative are valid, the average of both estimates is implemented in DISPATCH_{Exp} in order to stabilize the slope estimation with respect to uncertainties in both LR SM and SEE.

Regarding the SEE(LST) model, the algorithm in Tang et al. [56] automatically calculates the temperature endmembers by removing outliers. It processes pixels in an iterative manner to calculate the highest temperature for each f_v interval. A linear approximation of highest temperatures is used to estimate the dry edge. In Tang et al. [56], the wet edge is assumed to be parallel to x -axis with constant surface temperature. Herein, a slight modification is done to estimate the wet edge similar to the dry edge (in that case, the wet edge temperature is not kept as a constant) by removing outliers. This process thus removes specious dry and wet points before determining the dry and wet edges and their corresponding temperature endmembers.

Figure 2 gives an illustration of the calculation of wet and dry edges from LST- f_v graph by using two different algorithms. For DISPATCH_{Lin}, the temperature endmembers ($T_{s,dry}$ and $T_{s,wet}$) are the minimum and maximum temperature within a given SMAP pixel. Dry and wet edges are calculated independently for every SMAP pixel in the image. It can be seen that if we apply the same algorithm for the calculation of temperature endmembers at 100 m resolution, the temperature endmember calculation may overestimate the dry edge and underestimate the wet edge. When removing the outliers from the temperature endmember calculation [56], the dry and wet edges follow more closely the contour of data points, and the estimated temperature endmembers are supposedly more accurate.

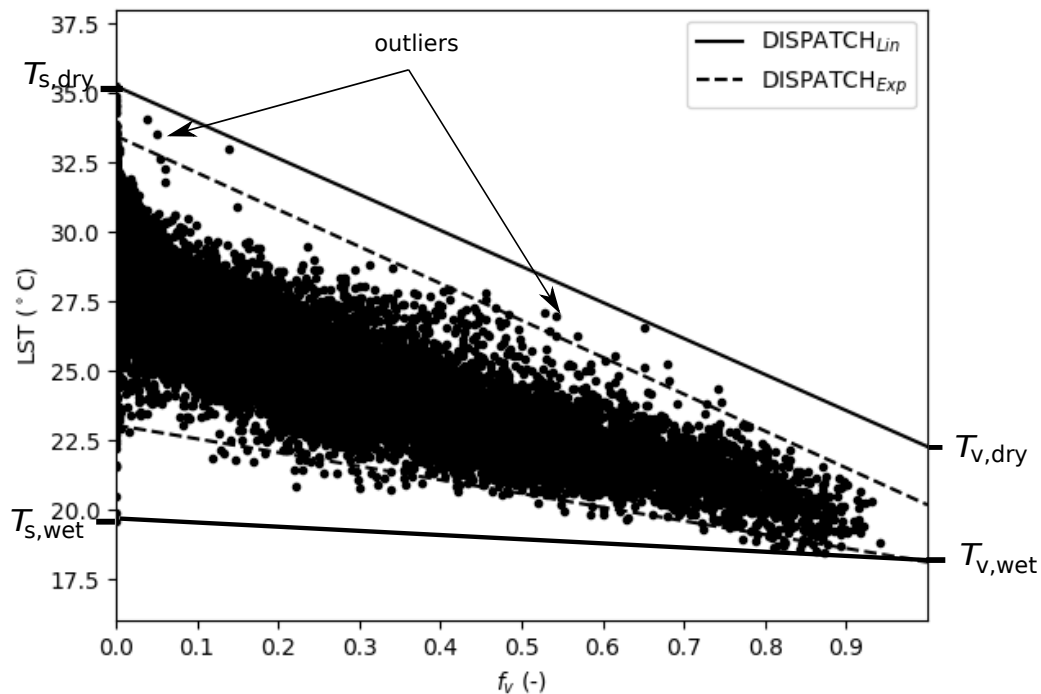


Figure 2. Two different algorithms to calculate the wet and dry edges of the LST- f_v feature space for 100 m resolution Landsat data on DOY 38.

2.5. Sequential Downscaling

Figure 3 presents a flow chart of the sequential disaggregation in 3 successive steps. SMAP SM is first disaggregated from 36 km to 1 km resolution using MODIS data and DISPATCH_{Lin} algorithm. Then the 1 km resolution SM is aggregated at ISR. Next, the ISR SM is further disaggregated at 100 m resolution using Landsat data and DISPATCH_{Exp} algorithm.

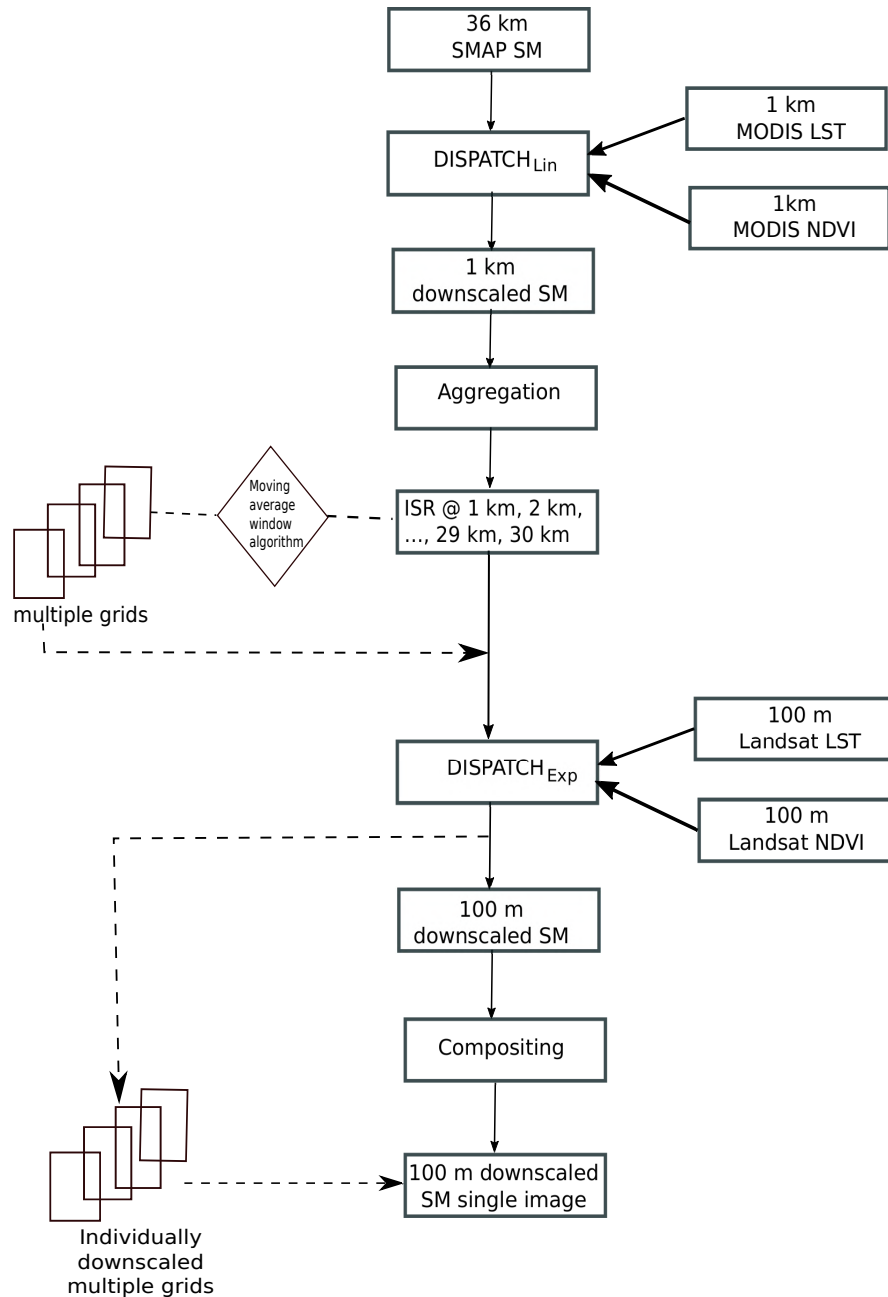


Figure 3. Flowchart of the stepwise sequential downscaling approach from 36 km resolution to 1 km (DISPATCH_{Lin}), from 1 km to ISR (aggregation to variable ISR), and from ISR to 100 m (DISPATCH_{Exp}).

The reason for the selection of a range of ISRs is associated with the contextual nature of DISPATCH, which makes the determination of temperature endmembers i.e., $T_{s,dry}$ and $T_{s,wet}$, and hence the 100 m resolution Landsat-derived SEE, dependent on the spatial extent [59]. In particular, the larger the spatial extent, the more heterogeneous the surface becomes. Therefore, the accuracy in temperature endmembers should increase with the spatial extent, as long as the meteorological forcing data remain relatively uniform (underlying assumption of the contextual analysis). Therefore, an optimal ISR in terms of SM accuracy at the 100 m resolution appears to be a compromise between (i) the accuracy in temperature endmembers and (ii) the gap between LR and HR. One major

objective of this paper is to check the sensitivity of the sequential approach to ISR and to propose an optimal ISR for routine application.

Figure 4 plots the LST- f_v feature space obtained for 100 m resolution Landsat data collected on DOY 38 and for 4 distinct spatial extents within the study area: 1 km, 3 km, 10 km, and 30 km. It can be seen that the range of LST and f_v values increases with the spatial extent over which the temperature endmembers are estimated. The mean LST is also larger for the smaller ISR values; which may induce bias in the disaggregation. If we consider that the temperature endmembers retrieved from the 10 km pixel resemble the real dry and wet soil temperatures, then more uncertainty can be seen while decreasing the spatial extent. An inaccurate representation of the wet/dry and bare/vegetated soil conditions within the spatial extent (ISR pixel) will directly affect the calculation of temperature endmembers and hence the thermal-derived SEE, and finally downscaling. Conversely, when extending (too much) the spatial extent, the spatial variability of air temperature (and wind speed notably) may reach a critical level that invalidates the contextual approach's assumption regarding the uniformity of meteorological forcing. In this respect, the LST- f_v feature space plotted in Figure 4 for a spatial extent of 30 km indicates that two trapezoidal shapes appear separately, which may be a signature of sub-areas having different meteorological forcing. Both constraints (heterogeneity of surface conditions and homogeneity of meteorological conditions) actually represent an important rationale for implementing a sequential method with an ISR between the 1 km and SMAP resolution.

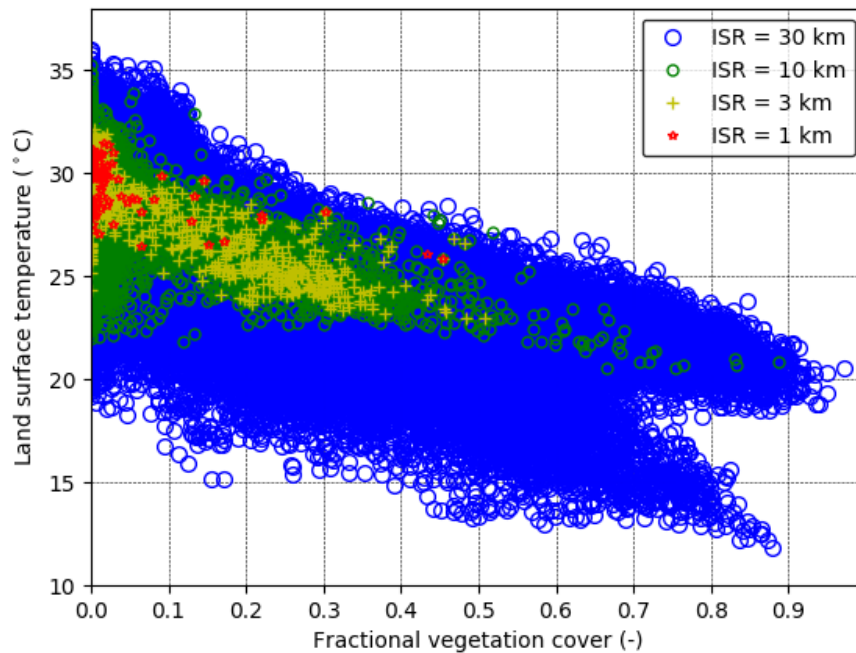


Figure 4. The LST- f_v feature space is plotted for 100 m resolution pixels within a 30 km, 10 km, 3 km and 1 km ISR pixel.

Once the spatial extent of the LST- f_v feature space and the algorithm for estimating temperature endmembers have been defined, one can check the linearity or non-linearity of the SEE(SM) model and its consistency with the SEE(LST) model. Figure 5 plots Landsat-derived SEE as a function of in-situ SM for DOY 14. The predictions of the SEE(SM) model of Equation (7) is also plotted, with SM_p estimated by setting in Equation (8) LR SM and LR SEE to the mean in situ SM and the mean Landsat-derived SEE, respectively. The correlation coefficient and slope between SEE(SM) and SEE(LST) estimates are 0.87 and 0.41 for DISPATCH $_{Exp}$ algorithm. For comparison purposes, Figure 5 also plots SEE(SM)

and SEE(LST) predictions for the DISPATCH_{Lin} algorithm. The correlation coefficient and slope between both models are 0.87 and 0.17 respectively. Even though the correlation coefficient shows similar values for both DISPATCH_{Lin} and DISPATCH_{Exp}, the slope is significantly lower than that for DISPATCH_{Exp}. Those results are fully consistent with our approach to make the SEE(SM) non-linear (using the exponential form of [57]) and to improve the temperature endmembers algorithm [56] of the SEE(LST) model within the new DISPATCH_{Exp} downscaling algorithm.

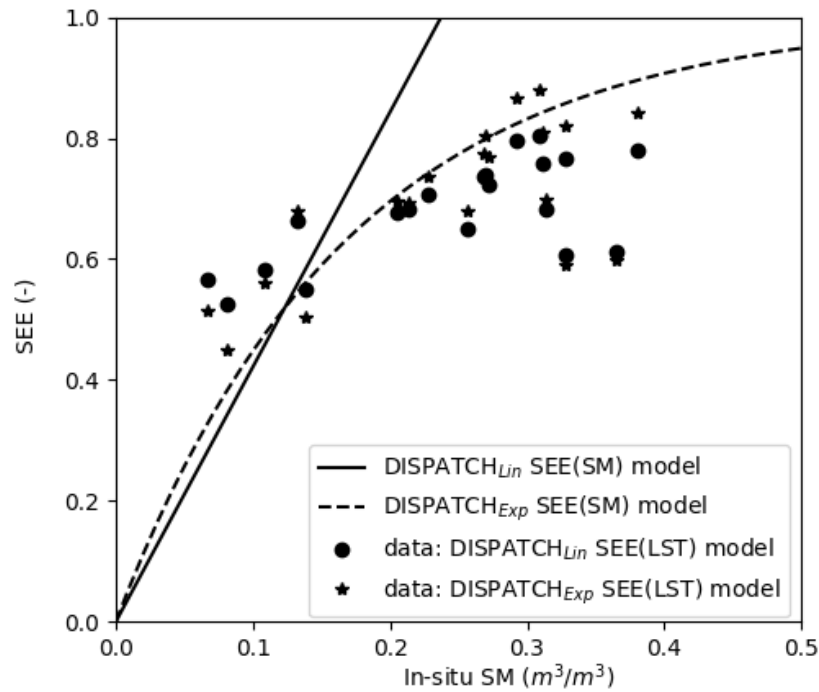


Figure 5. Landsat-derived SEE as a function of in situ SM superimposed with the SEE(SM) model for both DISPATCH_{Lin} and DISPATCH_{Exp} algorithms, for data on DOY 14.

2.6. Inclusion of Multiple ISR Grids

The use of multiple LR grids as input to disaggregation approaches has been proposed in Hoehn et al. [60] and Merlin et al. [26]. Hoehn et al. [60] compared downscaling results obtained from single coarse resolution grid (using fixed window) and using multiple overlapping coarse resolution grids (by shifting windows). Shifting windows using multiple grids showed better performance as compared to the fixed window case with respect to error and smoothness.

In this paper, we propose to define multiple ISR grids as an input to DISPATCH_{Exp} as in Merlin et al. [26] and Hoehn et al. [60]. However, one difference herein is that the multiple ISR grids are built from actual observations at the (higher) 1 km resolution and consequently, they are derived neither from the LR overlapped observations [26], nor from the oversampling of LR (SMAP) observations [60].

Figure 6 gives an illustration of the moving average window algorithm, over the 1 km resolution grid of the DISPATCH_{Lin} output data. The algorithm successively shifts an ISR grid in both directions (east-west and north-south) of a predefined constant distance. In the diagram of Figure 6, ISR is set to 10 km and the distance separating the so generated ISR grids is set to 2 km. Once the multiple grids have been generated, they are independently used as input to DISPATCH_{Exp}. As a first step, multiple ISR SM grids are thus overlapped with 100 m resolution Landsat data and disaggregated separately to get multiple 100 m resolution disaggregated SM images. As a second step, the separate

100 m resolution downsampled SM images are composited (simple average) to produce a single 100 m resolution SM disaggregated image.

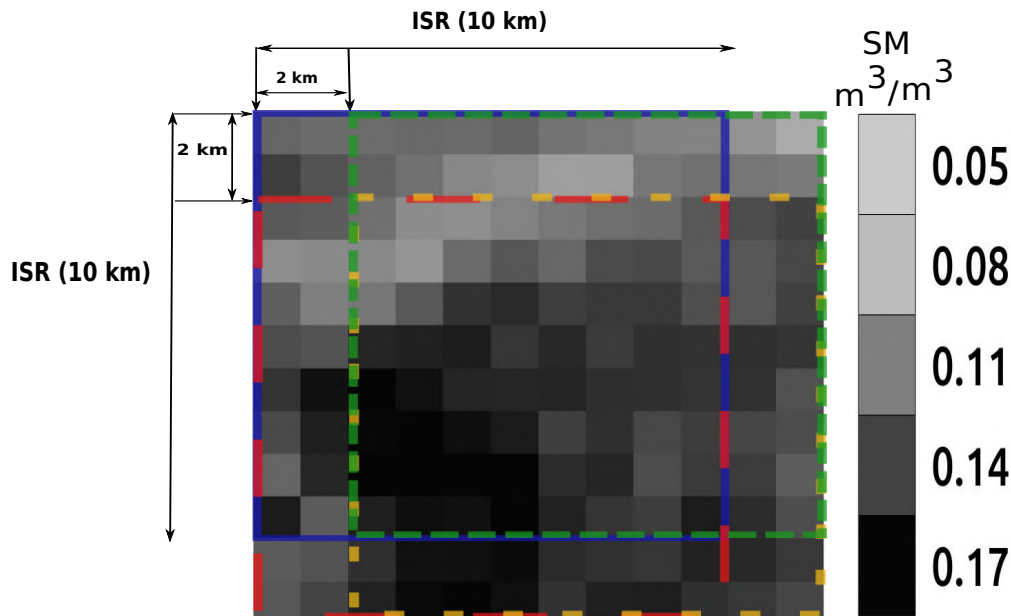


Figure 6. Illustration of the moving average window algorithm applied to the 1 km resolution DISPATCH_{Lin} SM with a shift of ISR (set to 10 km in this case) grids in both directions (east-west and north-south) with a constant spacing of 2 km between ISR grids.

3. Results

This section analyzes the potential of the sequential downscaling approach by investigating (1) the method calibration (2) the method accuracy for a range of ISR values using the single grid algorithm, and (3) the usefulness of the multiple grid (compared to the single grid) algorithm.

3.1. Calibration

The calibration of SM_p parameter in Equation (8) is undertaken using the DISPATCH_{Lin} data sets derived from SMAP, on each date when Landsat data are available. Figure 7 plots SM_p as a function of ISR for each Landsat overpass date. The mean and standard deviation of retrieved SM_p are computed within the 30 km by 30 km study domain. It can be seen that for all dates, the retrieved SM_p behaves quite similarly with respect to ISR. It sharply increases for an ISR increasing from 1 km to 3–4 km and then keeps a relatively stable value for ISR values ranging between 3–4 km and 30 km. Note that significant fluctuations of SM_p are observed for ISR values larger than 15 km, due to the bounded extent of the study area i.e., the mean SM_p is computed using a single retrieved value. However, the SM_p value after convergence is not fully consistent for different dates. In fact, the estimation of SM_p in Equation (8) mainly depends on LR SM and SEE data, so that any error in SMAP SM and Landsat-derived SEE estimates leads to temporal variabilities in retrieved SM_p .

The standard deviation of the retrieved SM_p values within the 30 km by 30 km area is also plotted as a function of ISR ranging from 1 km to 30 km. It can be seen that the spatial variability in retrieved SM_p significantly decreases in the higher ISR range to reach a minimum for ISR values larger than 10 km. Note that the standard deviation becomes zero for ISR equal or larger than 15 km (not shown in the graph) because in such cases, a single ISR pixel is obtained within the whole extent of the (30 km wide) study area. Figure 8 presents the images of SM_p retrieved for ISR equal to 1 km, 3 km, 10 km, and 30 km. The spatial variability of SM_p strongly increases when ISR decreases and tends to 1 km and the average of 1 km resolution SM_p is significantly different from the SM_p

retrieved over 10 km ISR pixels. Such behavior is explained by the non-linear impact of LR SEE on SM_p (see Equation (8)), and by the non-representativeness of temperature endmembers for ISR lower than 5 km.

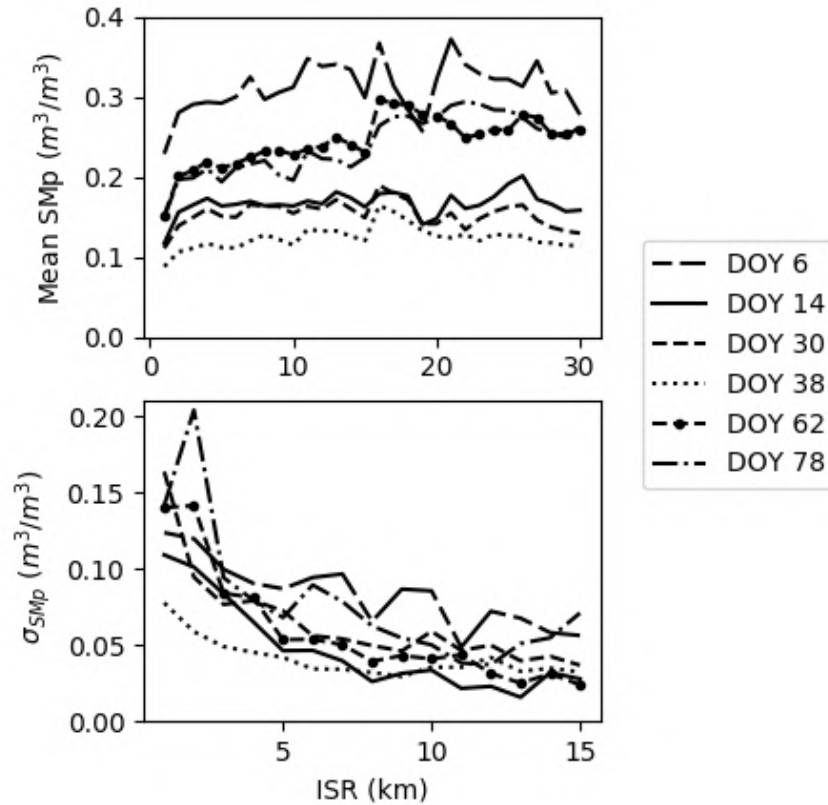


Figure 7. Mean (top) and standard deviation (bottom) of the parameter SM_p (Equation (8)) plotted as function of ISR ranging from 1 to 30 km for each Landsat overpass date separately.

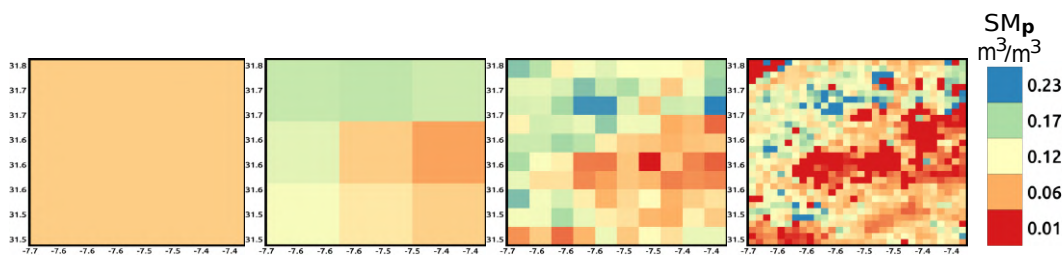


Figure 8. SM_p parameter images derived from SMAP data on DOY 38 for ISR equal to 30 km, 10 km, 3 km and 1 km from left to right, respectively

From the results presented in Figures 7 and 8, it can be concluded that (1) the retrieved SM_p is spatially and temporally representative for ISR equal to or larger than 10 km, and (2) significant spatial/temporal variabilities of SM_p (associated with uncertainties in temperature endmembers) and non linear effects (associated with the non linear SEE(SM) relationship) are obtained for ISR lower than 5 km.

3.2. Evaluation of 100 m Disaggregated SM

The SM_p retrieved from Equation (8) is first used to calculate the derivative from the average of Equations (9) and (10). A range of different ISR values is then chosen to evaluate the sensitivity of

100 m resolution disaggregated SM to ISR. To do so, the 1 km resolution disaggregated SM (the output of $DISPATCH_{Lin}$) is aggregated to 1, 2, 3,, and 30 km and in each case, the aggregated ISR SM together with its associated spatial extent is used as an input to $DISPATCH_{Exp}$. Such a sensitivity analysis is undertaken for each SMAP overpass date, separately.

The statistical comparison in terms of correlation coefficient (R), slope of the linear regression (slope), root mean square deviation (RMSD) and absolute mean bias (MB) between $DISPATCH_{Exp}$ disaggregated SM and in-situ SM is illustrated in Figure 9 for ISR ranging from 1 to 30 km for each sampling date. The temporal variability (standard deviation) of R and of the slope of the linear regression is relatively large in the lower range of ISR values. The slope gets even negative values for ISR lower than 5 km on several dates, while the slope is always positive for ISR larger than 10 km. This result is consistent with the stability of SM_p retrievals observed previously for ISR larger than 5 km.

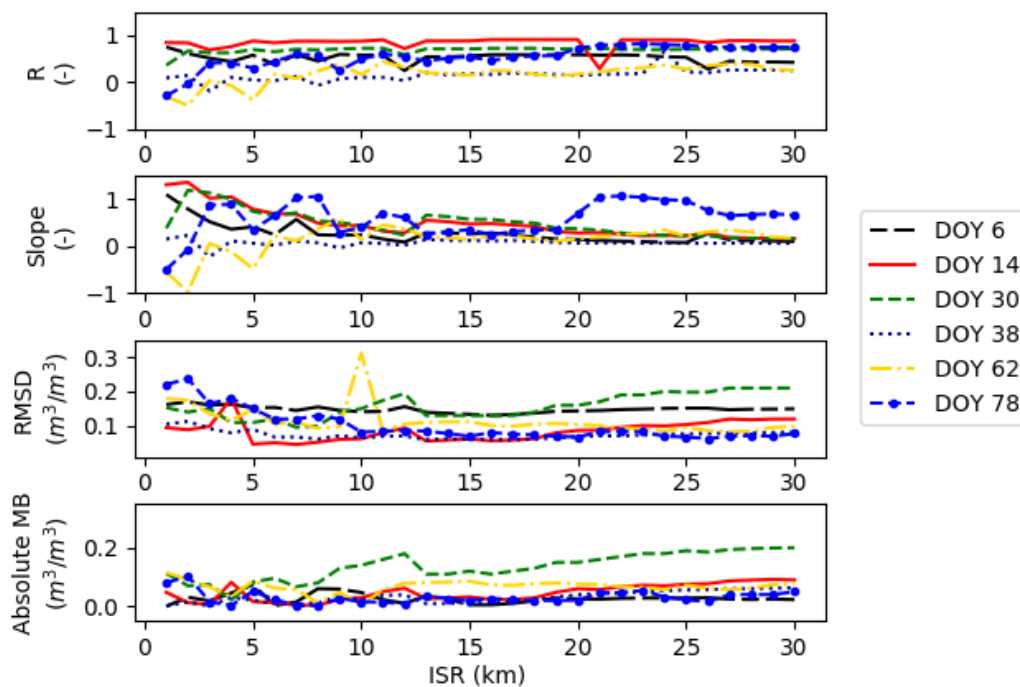


Figure 9. Correlation coefficient (R), slope of the linear regression, absolute mean bias (MB) and root mean square difference (RMSD) between 100 m resolution disaggregated and in situ SM for a range of ISR values (from 1 km to 30 km) for each sampling date separately.

When considering the full ISR range (1–30 km), and despite the date-to-date variability, a slight general increase of R is obtained in the 1–10 km range, whereas it keeps an approximately constant value for larger ISRs. Regarding the slope of the linear regression, an opposite finding is obtained. For ISR values larger than 5 km, the slope keeps decreasing with a value at $ISR = 30$ km mostly very close to zero. Note that the sudden increase of the slope for $ISR = 20$ km on DOY 78 is due to the fact that statistical results are obtained from a single (unrepresentative) ISR pixel that fits into the 30 km by 30 km study area. The decrease of the slope is attributed to the gap between the LR and the HR, which increases with ISR. In fact, the disaggregation efficiency (as defined in [61]) is expected to decrease with the LR to HR ratio, due to the decrease of the spatial variability represented at HR by the LR observation. The slope of the linear regression was actually found to be a good indicator of the disaggregation efficiency [61], consistent with the results presented in Figure 9. A second important impact of ISR is the increase of the absolute MB between the 100 m resolution disaggregated and in situ SM, especially in the 10–30 km range. The worsening of downscaling performances (in terms of the

slope of the linear regression and MB) in the 10–30 km range is due to the linear approximation of the downscaling relationship (Equation (3)). An optimal ISR is thus found at around 10 km. Optimal results in terms of RMSD between 100 m resolution and in-situ SM is actually obtained for ISR close to 10 km. Therefore, ISR set to 10 km throughout the rest of the paper.

For illustration purposes, Figure 10 represents the sequential downscaling of SM from SMAP data collected on DOY 38: the disaggregation of SMAP SM to 1 km resolution, the aggregation of the 1 km resolution disaggregated SM to ISR (10 km), and the disaggregation of ISR SM to 100 m resolution. It is reminded that the extra aggregation step is undertaken (i) to increase the representativeness/accuracy of the temperature endmembers extrapolated from the LST- f_v feature space, (ii) to increase the stability of the disaggregation calibration (via the SM_p retrieval) and (iii) to reduce random uncertainties in the ISR SM used as input to $DISPATCH_{Exp}$.

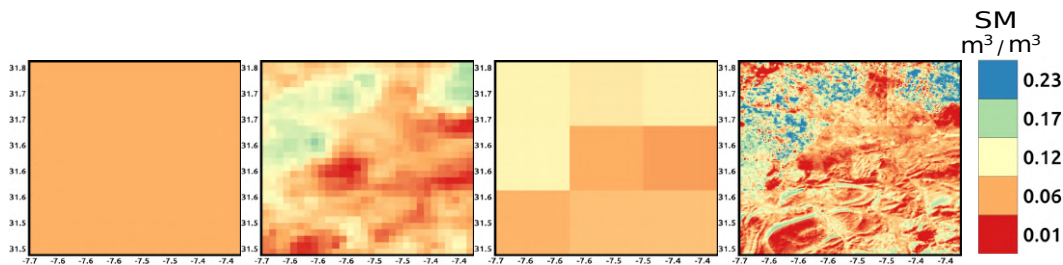


Figure 10. From left to right: images of 36 km resolution SMAP SM, 1 km resolution $DISPATCH_{Exp}$ SM, 10 km resolution aggregated $DISPATCH_{Exp}$ SM and 100 m resolution disaggregated SM on DOY 38.

As a first evaluation of the disaggregation at 100 m resolution independently from the uncertainty in SMAP data, $DISPATCH_{Exp}$ is run for all sampling dates (DOY 6, 14, 30, 38, 62 and 78) by setting the ISR observation to a fraction of the mean (daily areal average of) in-situ SM. By considering that the average of all in-situ SM measurements is representative of the SM over the irrigated area and that the SM over dry land is about 0, a rough estimate of the LR SM is derived as half the mean in situ measurements (the fraction of dry land in the 10 km ISR pixel covering the experimental fields is about 50%). Figure 11 plots the 100 m resolution disaggregated SM versus in situ measurements. Statistical results in terms of R, slope of the linear regression, absolute MB and RMSD are reported in Table 1 for synthetic LR. R is in the range 0.6–0.9 for four dates (DOY 6, 14, 30 and 78), while it is in the range 0.1–0.2 on two dates (DOY 38 and 62). In terms of correlation, better results are obtained on the sampling dates with a larger spatial variability in SM measurements, and reciprocally, poorer results are obtained when SM is relatively uniform at the sub-pixel scale. In terms of bias, however, relatively low absolute MB (lower than $0.03 \text{ m}^3/\text{m}^3$) is obtained except for DOY 6, 62 and 78 with an absolute MB of 0.07, 0.08 and $0.11 \text{ m}^3/\text{m}^3$, respectively. The reason is that the mean in situ measurements (weighted by the fraction of irrigated land) may not be fully representative of the real SM at the ISR (10 km) scale, as irrigation is not applied uniformly within the irrigated perimeter. Nevertheless, the application of $DISPATCH_{Exp}$ to synthetic LR (ISR) SM data allows for assessing the performance of the downscaling methodology independently of SMAP data and $DISPATCH_{Lin}$ algorithm. We conclude that $DISPATCH_{Exp}$ is relatively efficient when the sub-pixel variability is larger than $0.06 \text{ m}^3/\text{m}^3$.

Next, $DISPATCH_{Exp}$ is tested using SMAP data (ISR is still set to 10 km in the sequential downscaling). Figure 12 represents the comparison between $DISPATCH_{Exp}$ and in situ SM and Table 1 for SMAP single grid reports the associated statistical results. It can be seen that results are not significantly degraded in terms of R compared to the case when using synthetic LR observation as input to $DISPATCH_{Exp}$ (see Table 1). In fact, the sub-pixel variability of SM is represented by the Landsat-derived SEE in both real and synthetic cases, which explains similar R results. However, the $DISPATCH_{Lin}$ data derived from SMAP data may involve LR differences in terms of MB and RMSD at 100 m resolution.

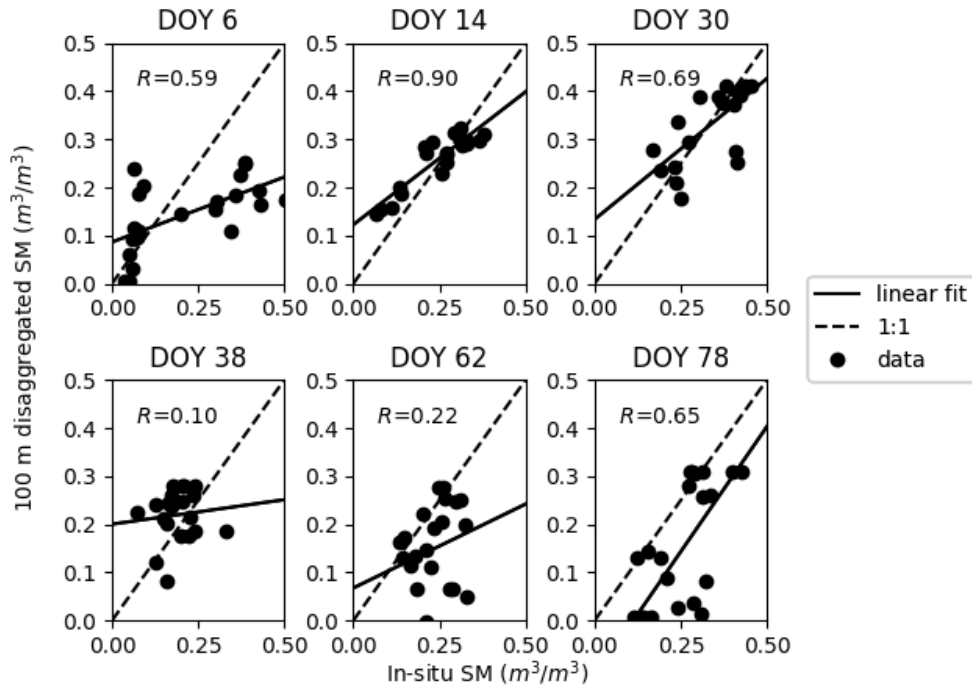


Figure 11. Graph plotting 100 m resolution disaggregated versus in-situ SM with the LR SM set to a fraction of the mean in-situ SM.

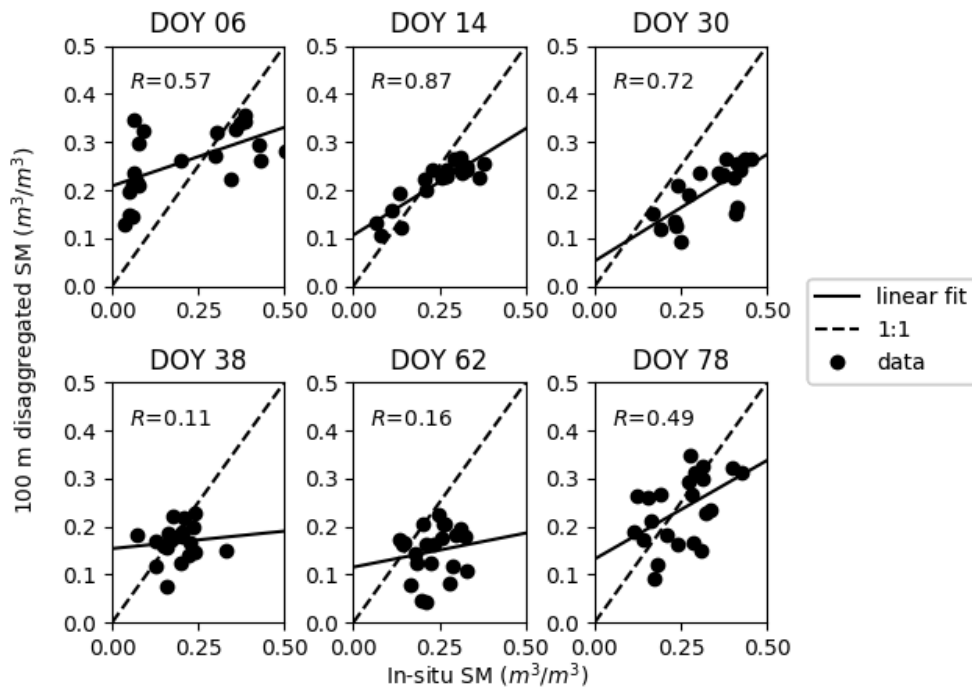


Figure 12. Same as Figure 11 but with LR SM set to the DISPATCH_{Lin} SM obtained from SMAP and aggregated at 10 km resolution (single grid).

Table 1. Statistical results in terms of correlation coefficient (R), slope of the linear regression, absolute mean bias (MB) and root mean square difference (RMSD) between 100 m resolution disaggregated and in-situ SM for Synthetic, SMAP single grid and SMAP multiple grid LR SM cases separately (ISR is set to 10 km).

Day of Year (DOY)	Synthetic				SMAP Single Grid				SMAP Multiple Grid			
	R (-)	Slope (-)	Absolute MB (m ³ /m ³)	RMSD (m ³ /m ³)	R (-)	Slope (-)	Absolute MB (m ³ /m ³)	RMSD (m ³ /m ³)	R (-)	Slope (-)	Absolute MB (m ³ /m ³)	RMSD (m ³ /m ³)
6	0.59	0.27	0.069	0.15	0.57	0.24	0.05	0.14	0.54	0.23	0.01	0.14
14	0.90	0.55	0.014	0.049	0.87	0.44	0.03	0.06	0.90	0.47	0.03	0.06
30	0.69	0.59	0.006	0.066	0.72	0.44	0.14	0.15	0.70	0.52	0.12	0.14
38	0.10	0.10	0.03	0.08	0.11	0.07	0.02	0.07	0.12	0.08	0.03	0.07
62	0.22	0.35	0.08	0.13	0.16	0.14	0.002	0.31	0.20	0.21	0.07	0.10
78	0.65	1.04	0.11	0.15	0.49	0.40	0.02	0.08	0.54	0.31	0.12	0.14
All	0.53	0.48	0.052	0.104	0.55	0.34	0.05	0.09	0.57	0.35	0.08	0.10

3.3. Reducing Boxy Artifact

As demonstrated and discussed above, setting an ISR between the SMAP and Landsat resolutions has many advantages in terms of accuracy and robustness of DISPATCH_{Exp}. However, one drawback with an ISR equal to 10 km, is that the ISR grid may be still apparent in the 100 m resolution disaggregated image. Such effects are called boxy artifacts [62]. To reduce these boxy artifacts and to potentially increase the accuracy in 100 m disaggregated SM, a Monte-Carlo sampling method is proposed as an extra step in the pre and post-processing of input/output data of DISPATCH_{Exp}.

The preprocessing steps include: (i) selecting 10 km resolution SM pixels such that an equal number of HR (Landsat) pixels falls within each ISR pixel (ii) shifting the 10 km ISR pixels with a distance of 2 km in east-west and north-south directions, so as to generate a set of 25 ISR SM images, (iii) overlapping each image with HR Landsat optical/thermal data, and (iv) disaggregating individually each ISR image to 100 m resolution. Therefore, a set of 25 possible disaggregated 100 m SM images is obtained. The post-processing step consists in combining the 25 disaggregated SM images. The simple averaging is used to produce a single 100 m disaggregated image.

The multiple-grid procedure illustrated in Figure 6 is applied over our 30 km by 30 km study area for SMAP data and for each date separately. Figure 13 presents the 100 m resolution SM disaggregated images by applying the single grid and multiple grid algorithms for each date separately. It can be seen on DOY 6, 38 and 78 that the boxy artifacts at 10 km resolution present on the image obtained using the single grid algorithm have completely disappeared in the multiple grids application. Note that the boxy artifacts are not visible for the other dates due to strips (data gaps) present in the Landsat 7 images. The moving window algorithm also smoothens the disaggregated image at the image borders. Especially, the errors that generally occur at the corners of the image due to sudden changes in temperature endmembers and coarse scale SM are reduced. The composited image is of better quality by reducing the random errors associated with the uncertainty in LR observations and the disaggregation methodology (involving non-linear relationships between SEE and SM), which make the disaggregated image more realistic than using the single grid algorithm.

Table 2 reports the standard deviation of 100 m resolution disaggregated SM within each image for the single and multiple grid algorithms, separately. The standard deviation is systematically lower when applying multiple grids for all the dates. It means that the multiple grid application significantly reduces the variabilities attributed to random uncertainties in DISPATCH_{Exp} input data. A quantitative comparison between 100 m disaggregated SM and in situ measurements is also proposed in Table 1 for SMAP multiple grid. By comparing the statistical results from the single grid and multiple grid (Table 1) algorithm, it can be seen that both the R and slope of the linear regression between 100 m resolution disaggregated and in situ SM are generally increased by applying multiple grids. Therefore, the proposed moving window method not only provides continuous SM images but also increases the efficiency of the disaggregation approach at 100 m resolution.

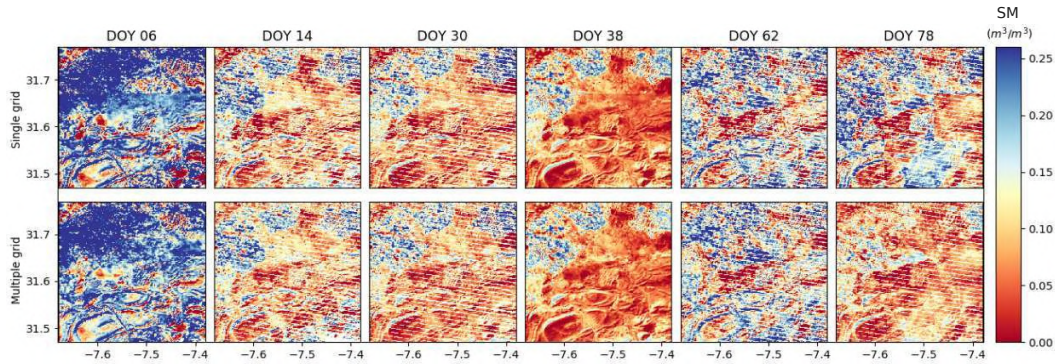


Figure 13. 100 m resolution disaggregated SMAP SM images when using an ISR set to 10 km for single grid (**top**) and moving average window (**bottom**) algorithm for each Landsat overpass date separately.

Table 2. Standard deviation of 100 m resolution disaggregated SM within each DISPATCH_{Exp} image for the single grid and multiple grid algorithm.

Day of Year (DOY)	Single Grid (m^3/m^3)	Multiple Grid (m^3/m^3)
6	0.135	0.115
14	0.075	0.069
30	0.075	0.068
38	0.058	0.055
62	0.096	0.092
78	0.094	0.052
All	0.089	0.075

4. Discussion

High spatial resolution soil moisture data are fundamental for hydro-agricultural purposes as well as for other kind of applications. The DISPATCH method sequentially applied to SMAP data at 1 km resolution (using MODIS) and at 100 m resolution (using Landsat) has potential for providing such data. However, the performance of the approach may depend on the surface and atmospheric conditions. In addition, the temporal resolution of 100 m resolution DISPATCH data is currently limited by (i) the repeat cycle (16 days) of Landsat and (ii) the cloud free conditions required to use optical/thermal data. This section thus discusses the applicability and expected performance of DISPATCH in a context wider than our semi-arid irrigated study area.

The disaggregation of coarse scale soil moisture data is still a relatively recent research avenue [24], and consequently, few studies have compared the performance of existing methods. Sabaghy et al. [23] undertook the first comprehensive and systematic comparison study of several radar-based and optical/thermal-based SM downscaling methods. The SM downscaled from SMOS and SMAP data were evaluated against in situ as well as airborne SM estimates using the AACES data set in Southeastern Australia. DISPATCH was among the most efficient downscaling methods, especially when evaluating the spatial representation at 1 km resolution. The results presented in this paper are consistent with Sabaghy et al. [23] and previous validation exercises of DISPATCH. However, several intrinsic limitations common to optical/thermal-based downscaling approaches needs to be acknowledged, while several weaknesses specific to DISPATCH could be addressed in the future.

In this study, the mean RMSD (about $0.10 \text{ m}^3/\text{m}^3$) between disaggregated SMAP and in situ SM is relatively large and need to be interpreted in terms of bias and precision and to be compared with the spatio-temporal variability of SM existing within the study area. First, the mean RMSD is mostly explained by daily biases (mean bias of about $0.08 \text{ m}^3/\text{m}^3$) while the slope of the linear regression between disaggregated and in-situ SM is systematically and significantly positive. Second, the spatial variability of SM at 100 m resolution is extreme over the irrigated area with surface conditions ranging

from bone dry to soil fully saturated. Over the sampled area, the minimum and maximum measured SM value was 0.03 to $0.45 \text{ m}^3/\text{m}^3$, respectively. In such highly heterogeneous areas, relatively large errors in SM estimates are thus expected. It is however reminded that the disaggregation error should be smaller than the actual SM variability, as an indicator of the relevance of such disaggregated SM data [63].

It is reminded that the DISPATCH methodology relies on the relationship between moisture and the LST. LST is in fact a signature of the surface energy balance, which is highly linked to the evaporation flux and the associated soil water availability. NDVI data are used in DISPATCH to partition the LST into its soil and vegetation components, given that the soil temperature is more directly linked to the top SM while the vegetation temperature is related to the deeper root zone SM [26]. Therefore, the application of the DISPATCH method over irrigated regions is fully relevant. In our study area, flood irrigation consists in applying about 60 mm in several (typically 4) hours so as to flood the entire field. However, the irrigation water rapidly infiltrates into the soil so that there is little chance that the Landsat satellite actually “sees” any inundated field (although it may potentially happen), all the more as the typical frequency of flood irrigations is one every 3 weeks. The flood irrigation technique is still widely applied in Morocco and in many developing countries where traditional practices persist. Note that the application of DISPATCH over drip irrigated crops would require thermal data with a high repeat cycle, consistent with the irrigation frequency for the drop-by-drop technique.

One major limitation of DISPATCH is the availability of optical/thermal data. DISPATCH has been tested mostly under arid or semi-arid regions where the cloud cover is rather small. In particular, the cloud cover of the Haouz plain is about 40% from January to May while its overall yearly percentage is 30% [64]. The 100 m resolution downscaled SM time series is thus expected to be much less dense over other regions having a larger cloud cover. In addition, as DISPATCH relies on the LST-moisture relationship, the performance of downscaling depends on the atmospheric evaporative demand. Therefore, testing its applicability to different climatic conditions will be needed in the future, notably by identifying moisture-limited and energy-limited regions.

Other limitations specific to DISPATCH includes the non-linear behavior of the SEE(SM) relationship and the so-called “boxiness” within the downscaled image. From Figures 11 and 12, relationships between disaggregated and in-situ SM appear to be non-linear on several dates (DOY 6 notably). This is explained by (i) the non-linear behavior of SEE for a range of SM values and (ii) the linear approximation of DISPATCH around the LR SM (Equation (3)). It seems that using a non-linear SEE(SM) model in Equation (3) is not sufficient to represent the nonlinear SEE(SM) relationship when the SM variability is extreme. Future studies will address this issue by, for instance, correcting the SEE(SM) relationship when the sub-pixel SM variability is larger than a given threshold. Regarding the “boxiness” within the image, it is a relatively small effect compared to the spatial variability of SM represented by the DISPATCH method. Quantitatively, the RMSD between the SM produced from single grid and multiple grid applications is $0.019 \text{ m}^3/\text{m}^3$, while the standard deviation of disaggregated SM within the study area is 0.089 and $0.075 \text{ m}^3/\text{m}^3$ for the single and multiple grid case, respectively. In fact, as shown in Figure 13 the single grid application (without removing the boxiness within the image) already provides 100 m resolution SM images with borders between ISR pixels very consistent from one ISR pixel to another adjacent ISR pixel. Therefore, the stepwise method proposed in this paper does transfer in a satisfying manner the SM information from the 36 km SMAP resolution to the targeted 100 m resolution.

5. Conclusions

A stepwise disaggregation approach of SMAP SM is developed at 100 m resolution using the DISPATCH methodology and Landsat data. SMAP SM is first disaggregated from 36 km to 1 km resolution using MODIS data and DISPATCH_{Lin} algorithm. Then the 1 km resolution SM is aggregated as ISR. Next, the ISR SM is further disaggregated at 100 m resolution using Landsat data and DISPATCH_{Exp} algorithm. In order to take into account the increase of resolution, the new

DISPATCH_{Exp} algorithm brings several innovations compared to the DISPATCH version currently implemented at CATDS (DISPATCH_{Lin}) in two aspects: (i) the SEE is a non-linear function of SM, and (ii) the SEE(LST) model is improved by better constraining the determination of temperature endmembers. The approach is evaluated using in situ measurements collected on the dates with concurrent SMAP, MODIS, and Landsat overpasses.

ISR is varied between 1 km and 30 km with a 1 km step, and sensitivity of the calibration parameter (SM_p) of DISPATCH_{Exp} to ISR is analyzed. The retrieved SM_p is spatially and temporally representative for ISR equal or larger than 10 km, while significant spatial variabilities of SM_p (associated with uncertainties in temperature endmembers) and non-linear effects (associated with the non-linear SEE(SM) relationship) are obtained for ISR lower than 5 km. Optimal results in terms of RMSD between 100 m resolution and in situ SM are obtained for ISR close to 10 km. Therefore, the two-step disaggregation is more efficient than the direct disaggregation from SMAP to 100 m resolution. This is due to the trade-off existing between the performance (increasing with the ISR and its sub-pixel variability) of the contextual-based DISPATCH method and the statistical match (decreasing with ISR) between ISR remotely sensed and field-scale SM estimates. The correlation coefficient between 100 m resolution disaggregated and in situ SM ranges between 0.5–0.9 for four out of the six sampling dates. Better results are obtained on the sampling dates with a larger spatial variability in SM measurements, and reciprocally, poorer results are obtained when SM is relatively uniform at the sub-pixel scale.

Finally, a new method is proposed to reduce boxy artifacts at 10 km resolution in 100 m resolution disaggregated SM images. The multiple grid application perfectly smoothens the composited 100 m resolution disaggregated SM image and, in addition, quantitatively improves the efficiency of the downscaling approach by increasing the correlation coefficient and slope of the linear regression between 100 m resolution disaggregated and in situ SM.

The DISPATCH-based sequential disaggregation scheme has the advantage of being independent on ground-based measurements, as all input parameters (i.e., temperature endmembers and SM_p) are calibrated using remote sensing data. However, the unavailability of optical/thermal (MODIS/Landsat) data in cloudy conditions is still a severe limitation for operational applications. One key avenue for producing SM data sets at high spatial-temporal resolution could be the synergy with radar-based approaches [18,24]. Recently, Amazirh et al. [49] calibrated the main parameters of a radar-based SM retrieval method using a thermal-derived SM proxy. In the same vein, the 100 m resolution DISPATCH_{Exp} SM data sets obtained from SMAP data on MODIS/Landsat clear sky days could represent a cornerstone in the construction of synergies between passive/active microwave and optical/thermal data.

Author Contributions: Conceptualization, N.O. and O.M.; methodology, N.O. and O.M.; validation N.O. and O.M.; supervision O.M.; investigation, N.O.; data curation, N.O., L.O.-G., B.A.H. and A.A.; writing—original draft preparation, N.O., O.M.; writing—review and editing, N.O., O.M., B.M., C.S., A.A.B., M.J.E. and S.E.-R.

Funding: This study was supported by the European Commission Horizon 2020 Programme for Research and Innovation (H2020) in the context of the Marie Skłodowska-Curie Research and Innovation Staff Exchange (RISE) action (REC project, grant agreement no: 645642 followed by ACCWA project, grant agreement no.: 823965).

Acknowledgments: We would like to thank the National Aeronautics and Space Administration (NASA) for freely providing the data. We would also like to thank the reviewers for their valuable comments.

Conflicts of Interest: The authors declare no conflict of interest.

References

1. Bisquert, M.; Sánchez, J.; López-Urrea, R.; Caselles, V. Estimating high resolution evapotranspiration from disaggregated thermal images. *Remote Sens. Environ.* **2016**, *187*, 423–433. [[CrossRef](#)]
2. Maurer, E.P.; Wood, A.; Adam, J.; Lettenmaier, D.P.; Nijssen, B. A long-term hydrologically based dataset of land surface fluxes and states for the conterminous United States. *J. Clim.* **2002**, *15*, 3237–3251. [[CrossRef](#)]

3. Koster, R.D.; Dirmeyer, P.A.; Guo, Z.; Bonan, G.; Chan, E.; Cox, P.; Gordon, C.; Kanae, S.; Kowalczyk, E.; Lawrence, D.; et al. Regions of strong coupling between soil moisture and precipitation. *Science* **2004**, *305*, 1138–1140. [[CrossRef](#)] [[PubMed](#)]
4. Wang, K.; Dickinson, R.E. A review of global terrestrial evapotranspiration: Observation, modeling, climatology, and climatic variability. *Rev. Geophys.* **2012**, *50*. [[CrossRef](#)]
5. Entekhabi, D.; Njoku, E.G.; O'Neill, P.E.; Kellogg, K.H.; Crow, W.T.; Edelstein, W.N.; Entin, J.K.; Goodman, S.D.; Jackson, T.J.; Johnson, J.; et al. The soil moisture active passive (SMAP) mission. *Proc. IEEE* **2010**, *98*, 704–716. [[CrossRef](#)]
6. Kerr, Y.H.; Waldteufel, P.; Wigneron, J.P.; Delwart, S.; Cabot, F.; Boutin, J.; Escorihuela, M.J.; Font, J.; Reul, N.; Gruhier, C.; et al. The SMOS mission: New tool for monitoring key elements of the global water cycle. *Proc. IEEE* **2010**, *98*, 666–687. [[CrossRef](#)]
7. Wagner, W. Operational Readiness of Microwave Remote Sensing of Soil Moisture: An Update. In Proceedings of the EGU General Assembly 2010, Vienna, Austria, 2–7 May 2010; Volume 12, p. 2636.
8. Kerr, Y.H.; Waldteufel, P.; Wigneron, J.P.; Martinuzzi, J.; Font, J.; Berger, M. Soil moisture retrieval from space: The Soil Moisture and Ocean Salinity (SMOS) mission. *IEEE Trans. Geosci. Remote Sens.* **2001**, *39*, 1729–1735. [[CrossRef](#)]
9. Schmugge, T. Applications of passive microwave observations of surface soil moisture. *J. Hydrol.* **1998**, *212*, 188–197. [[CrossRef](#)]
10. Schmugge, T.; Jackson, T. Mapping surface soil moisture with microwave radiometers. *Meteorol. Atmos. Phys.* **1994**, *54*, 213–223. [[CrossRef](#)]
11. Bindlish, R.; Crow, W.T.; Jackson, T.J. Role of passive microwave remote sensing in improving flood forecasts. *IEEE Geosci. Remote Sens. Lett.* **2009**, *6*, 112–116. [[CrossRef](#)]
12. Kerr, Y.H.; Waldteufel, P.; Richaume, P.; Wigneron, J.P.; Ferrazzoli, P.; Mahmoodi, A.; Al Bitar, A.; Cabot, F.; Gruhier, C.; Juglea, S.E.; et al. The SMOS soil moisture retrieval algorithm. *IEEE Trans. Geosci. Remote Sens.* **2012**, *50*, 1384–1403. [[CrossRef](#)]
13. Malbêteau, Y.; Merlin, O.; Molero, B.; Rüdiger, C.; Bacon, S. DisPATCH as a tool to evaluate coarse-scale remotely sensed soil moisture using localized in situ measurements: Application to SMOS and AMSR-E data in Southeastern Australia. *Int. J. Appl. Earth Obs. Geoinf.* **2016**, *45*, 221–234. [[CrossRef](#)]
14. Walker, J.P.; Houser, P.R. Requirements of a global near-surface soil moisture satellite mission: Accuracy, repeat time, and spatial resolution. *Adv. Water Resour.* **2004**, *27*, 785–801. [[CrossRef](#)]
15. Hawley, M.E.; Jackson, T.J.; McCuen, R.H. Surface soil moisture variation on small agricultural watersheds. *J. Hydrol.* **1983**, *62*, 179–200. [[CrossRef](#)]
16. Fang, B.; Lakshmi, V.; Bindlish, R.; Jackson, T.J. Downscaling of SMAP soil moisture using land surface temperature and vegetation data. *Vadose Zone J.* **2018**, *17*, 1. [[CrossRef](#)]
17. Chen, N.; He, Y.; Zhang, X. NIR-Red Spectra-Based Disaggregation of SMAP Soil Moisture to 250 m Resolution Based on OzNet in Southeastern Australia. *Remote Sens.* **2017**, *9*, 51. [[CrossRef](#)]
18. Tomer, S.K.; Al Bitar, A.; Sekhar, M.; Zribi, M.; Bandyopadhyay, S.; Kerr, Y. MAPSM: A spatio-temporal algorithm for merging soil moisture from active and passive microwave remote sensing. *Remote Sens.* **2016**, *8*, 990. [[CrossRef](#)]
19. Piles, M.; Camps, A.; Vall-Llossera, M.; Corbella, I.; Panciera, R.; Rudiger, C.; Kerr, Y.H.; Walker, J. Downscaling SMOS-derived soil moisture using MODIS visible/infrared data. *IEEE Trans. Geosci. Remote Sens.* **2011**, *49*, 3156–3166. [[CrossRef](#)]
20. Merlin, O.; Chehbouni, A.; Walker, J.P.; Panciera, R.; Kerr, Y.H. A simple method to disaggregate passive microwave-based soil moisture. *IEEE Trans. Geosci. Remote Sens.* **2008**, *46*, 786–796. [[CrossRef](#)]
21. Panciera, R.; Walker, J.P.; Kalma, J.D.; Kim, E.J.; Hacker, J.M.; Merlin, O.; Berger, M.; Skou, N. The NAFE'05/CoSMOS data set: Toward SMOS soil moisture retrieval, downscaling, and assimilation. *IEEE Trans. Geosci. Remote Sens.* **2008**, *46*, 736–745. [[CrossRef](#)]
22. Kim, G.; Barros, A.P. Downscaling of remotely sensed soil moisture with a modified fractal interpolation method using contraction mapping and ancillary data. *Remote Sens. Environ.* **2002**, *83*, 400–413. [[CrossRef](#)]
23. Sabaghy, S.; Walker, J.P.; Renzullo, L.J.; Jackson, T.J. Spatially enhanced passive microwave derived soil moisture: Capabilities and opportunities. *Remote Sens. Environ.* **2018**, *209*, 551–580. [[CrossRef](#)]
24. Peng, J.; Loew, A.; Merlin, O.; Verhoest, N.E. A review of spatial downscaling of satellite remotely sensed soil moisture. *Rev. Geophys.* **2017**, *55*, 341–366. [[CrossRef](#)]

25. Taconet, O.; Bernard, R.; Vidal-Madjar, D. Evapotranspiration over an agricultural region using a surface flux/temperature model based on NOAA-AVHRR data. *J. Clim. Appl. Meteorol.* **1986**, *25*, 284–307. [[CrossRef](#)]
26. Merlin, O.; Rudiger, C.; Al Bitar, A.; Richaume, P.; Walker, J.P.; Kerr, Y.H. Disaggregation of SMOS soil moisture in Southeastern Australia. *IEEE Trans. Geosci. Remote Sens.* **2012**, *50*, 1556–1571. [[CrossRef](#)]
27. Merlin, O.; Escorihuela, M.J.; Mayoral, M.A.; Hagolle, O.; Al Bitar, A.; Kerr, Y. Self-calibrated evaporation-based disaggregation of SMOS soil moisture: An evaluation study at 3 km and 100 m resolution in Catalunya, Spain. *Remote Sens. Environ.* **2013**, *130*, 25–38. [[CrossRef](#)]
28. Merlin, O.; Stefan, V.G.; Amazirh, A.; Chanzy, A.; Ceschia, E.; Er-Raki, S.; Gentine, P.; Tallec, T.; Ezzahar, J.; Bircher, S.; et al. Modeling soil evaporation efficiency in a range of soil and atmospheric conditions using a meta-analysis approach. *Water Resour. Res.* **2016**, *52*, 3663–3684. [[CrossRef](#)]
29. Sandholt, I.; Rasmussen, K.; Andersen, J. A simple interpretation of the surface temperature/vegetation index space for assessment of surface moisture status. *Remote Sens. Environ.* **2002**, *79*, 213–224. [[CrossRef](#)]
30. Molero, B.; Merlin, O.; Malbêteau, Y.; Al Bitar, A.; Cabot, F.; Stefan, V.; Kerr, Y.; Bacon, S.; Cosh, M.; Bindlish, R.; et al. SMOS disaggregated soil moisture product at 1km resolution: Processor overview and first validation results. *Remote Sens. Environ.* **2016**, *180*, 361–376. [[CrossRef](#)]
31. Dumedah, G.; Walker, J.P.; Merlin, O. Root-zone soil moisture estimation from assimilation of downscaled Soil Moisture and Ocean Salinity data. *Adv. Water Resour.* **2015**, *84*, 14–22. [[CrossRef](#)]
32. Escorihuela, M.J.; Quintana-Seguí, P. Comparison of remote sensing and simulated soil moisture datasets in Mediterranean landscapes. *Remote Sens. Environ.* **2016**, *180*, 99–114. [[CrossRef](#)]
33. Malbeteau, Y.; Merlin, O.; Balsamo, G.; Er-Raki, S.; Khabba, S.; Walker, J.; Jarlan, L. Toward a Surface Soil Moisture Product at High Spatiotemporal Resolution: Temporally Interpolated, Spatially Disaggregated SMOS Data. *J. Hydrometeorol.* **2018**, *19*, 183–200. [[CrossRef](#)]
34. Bandara, R.; Walker, J.P.; Rüdiger, C.; Merlin, O. Towards soil property retrieval from space: An application with disaggregated satellite observations. *J. Hydrol.* **2015**, *522*, 582–593. [[CrossRef](#)]
35. Escorihuela, M.J.; Merlin, O.; Stefan, V.; Moyano, G.; Eweys, O.A.; Zribi, M.; Kamara, S.; Benahi, A.S.; Ebbe, M.A.B.; Chihrane, J.; et al. SMOS based high resolution soil moisture estimates for Desert locust preventive management. *Remote Sens. Appl. Soc. Environ.* **2018**, *11*, 140–150.
36. Hssaine, B.A.; Merlin, O.; Ezzahar, J.; Ojha, N.; Er-raki, S.; Khabba, S. An evapotranspiration model self-calibrated from remotely sensed surface soil moisture, land surface temperature and vegetation cover fraction: Application to disaggregated SMOS and MODIS data. *Hydrol. Earth Syst. Sci.* **2019**, under review. [[CrossRef](#)]
37. Lievens, H.; Tomer, S.K.; Al Bitar, A.; De Lannoy, G.J.; Drusch, M.; Dumedah, G.; Franssen, H.J.H.; Kerr, Y.; Martens, B.; Pan, M.; et al. SMOS soil moisture assimilation for improved hydrologic simulation in the Murray Darling Basin, Australia. *Remote Sens. Environ.* **2015**, *168*, 146–162. [[CrossRef](#)]
38. Leroux, L.; Baron, C.; Castets, M.; Escorihuela, M.J.; Diouf, A.; Bégué, A.; Lo Seen, D. Estimating maize grain yield in scarce field-data environment: An approach combining remote sensing and crop modeling in Burkina Faso. In Proceedings of the ABSTRACT AFRICAGIS 2017, Addis Ababa, Ethiopia, 20–24 November 2017.
39. Colliander, A.; Fisher, J.B.; Halverson, G.; Merlin, O.; Misra, S.; Bindlish, R.; Jackson, T.J.; Yueh, S. Spatial downscaling of SMAP soil moisture using MODIS land surface temperature and NDVI during SMAPVEX15. *IEEE Geosci. Remote Sens. Lett.* **2017**, *14*, 2107–2111. [[CrossRef](#)]
40. French, A.N.; Hunsaker, D.J.; Thorp, K.R. Remote sensing of evapotranspiration over cotton using the TSEB and METRIC energy balance models. *Remote Sens. Environ.* **2015**, *158*, 281–294. [[CrossRef](#)]
41. Loheide, S.P., II; Gorelick, S.M. A local-scale, high-resolution evapotranspiration mapping algorithm (ETMA) with hydroecological applications at riparian meadow restoration sites. *Remote Sens. Environ.* **2005**, *98*, 182–200. [[CrossRef](#)]
42. Merlin, O.; Al Bitar, A.; Walker, J.P.; Kerr, Y. A sequential model for disaggregating near-surface soil moisture observations using multi-resolution thermal sensors. *Remote Sens. Environ.* **2009**, *113*, 2275–2284. [[CrossRef](#)]
43. Fang, B.; Lakshmi, V. Soil moisture at watershed scale: Remote sensing techniques. *J. Hydrol.* **2014**, *516*, 258–272. [[CrossRef](#)]
44. Jarlan, L.; Khabba, S.; Er-Raki, S.; Le Page, M.; Hanich, L.; Fakir, Y.; Merlin, O.; Mangiarotti, S.; Gascoin, S.; Ezzahar, J.; et al. Remote sensing of water resources in semi-arid mediterranean areas: The joint international laboratory TREMA. *Int. J. Remote Sens.* **2015**, *36*, 4879–4917. [[CrossRef](#)]

45. Er-Raki, S.; Chehbouni, A.; Guemouria, N.; Duchemin, B.; Ezzahar, J.; Hadria, R. Combining FAO-56 model and ground-based remote sensing to estimate water consumptions of wheat crops in a semi-arid region. *Agric. Water Manag.* **2007**, *87*, 41–54. [[CrossRef](#)]
46. Duchemin, B.; Hagolle, O.; Mougénot, B.; Benhadj, I.; Hadria, R.; Simonneaux, V.; Ezzahar, J.; Hoedjes, J.; Khabba, S.; Kharrou, M.; et al. Agrometeorological study of semi-arid areas: An experiment for analysing the potential of time series of FORMOSAT-2 images (Tensift-Marrakech plain). *Int. J. Remote Sens.* **2008**, *29*, 5291–5299. [[CrossRef](#)]
47. Duchemin, B.; Hadria, R.; Erraki, S.; Boulet, G.; Maisongrande, P.; Chehbouni, A.; Escadafal, R.; Ezzahar, J.; Hoedjes, J.; Kharrou, M.; et al. Monitoring wheat phenology and irrigation in Central Morocco: On the use of relationships between evapotranspiration, crops coefficients, leaf area index and remotely-sensed vegetation indices. *Agric. Water Manag.* **2006**, *79*, 1–27. [[CrossRef](#)]
48. Miller, J.; Gaskin, G. ThetaProbe ML2x. In *Principles of Operation and Applications*; MLURI Technical Note; The Macaulay Land Use Research Institute: Aberdeen, UK, 1999.
49. Amazirh, A.; Merlin, O.; Er-Raki, S.; Gao, Q.; Rivalland, V.; Malbeteau, Y.; Khabba, S.; Escorihuela, M.J. Retrieving surface soil moisture at high spatio-temporal resolution from a synergy between Sentinel-1 radar and Landsat thermal data: A study case over bare soil. *Remote Sens. Environ.* **2018**, *211*, 321–337. [[CrossRef](#)]
50. Das, N.N.; Entekhabi, D.; Kim, S.; Jagdhuber, T.; Dunbar, S.; Yueh, S.; Colliander, A. High-resolution enhanced product based on SMAP active-passive approach using Sentinel 1 data and its applications. In Proceedings of the 2017 IEEE International Geoscience and Remote Sensing Symposium (IGARSS) 2017, Fort Worth, TX, USA, 23–28 July 2017; pp. 2493–2494.
51. Colliander, A.; Jackson, T.J.; Bindlish, R.; Chan, S.; Das, N.; Kim, S.; Cosh, M.; Dunbar, R.; Dang, L.; Pashaian, L.; et al. Validation of SMAP surface soil moisture products with core validation sites. *Remote Sens. Environ.* **2017**, *191*, 215–231. [[CrossRef](#)]
52. Chen, D.; Huang, J.; Jackson, T.J. Vegetation water content estimation for corn and soybeans using spectral indices derived from MODIS near-and short-wave infrared bands. *Remote Sens. Environ.* **2005**, *98*, 225–236. [[CrossRef](#)]
53. Jiménez-Muñoz, J.C.; Sobrino, J.A.; Skoković, D.; Mattar, C.; Cristóbal, J. Land surface temperature retrieval methods from Landsat-8 thermal infrared sensor data. *IEEE Geosci. Remote Sens. Lett.* **2014**, *11*, 1840–1843. [[CrossRef](#)]
54. Mattar, C.; Durán-Alarcón, C.; Jiménez-Muñoz, J.C.; Santamaría-Artigas, A.; Olivera-Guerra, L.; Sobrino, J.A. Global atmospheric profiles from reanalysis information (GAPRI): A new database for earth surface temperature retrieval. *Int. J. Remote Sens.* **2015**, *36*, 5045–5060. [[CrossRef](#)]
55. Moran, M.; Clarke, T.; Inoue, Y.; Vidal, A. Estimating crop water deficit using the relation between surface-air temperature and spectral vegetation index. *Remote Sens. Environ.* **1994**, *49*, 246–263. [[CrossRef](#)]
56. Tang, R.; Li, Z.L.; Tang, B. An application of the Ts–VI triangle method with enhanced edges determination for evapotranspiration estimation from MODIS data in arid and semi-arid regions: Implementation and validation. *Remote Sens. Environ.* **2010**, *114*, 540–551. [[CrossRef](#)]
57. Komatsu, T.S. Toward a robust phenomenological expression of evaporation efficiency for unsaturated soil surfaces. *J. Appl. Meteorol.* **2003**, *42*, 1330–1334. [[CrossRef](#)]
58. Chanzy, A.; Bruckler, L. Significance of soil surface moisture with respect to daily bare soil evaporation. *Water Resour. Res.* **1993**, *29*, 1113–1125. [[CrossRef](#)]
59. Wang, J. Scale Effects on the Remote Estimation of Evapotranspiration. Ph.D. Thesis, Texas State University, San Marcos, TX, USA, 2012.
60. Hoehn, D.C.; Niemann, J.D.; Green, T.R.; Jones, A.S.; Grazaitis, P.J. Downscaling soil moisture over regions that include multiple coarse-resolution grid cells. *Remote Sens. Environ.* **2017**, *199*, 187–200. [[CrossRef](#)]
61. Merlin, O.; Chehbouni, A.G.; Kerr, Y.H.; Njoku, E.G.; Entekhabi, D. A combined modeling and multispectral/multiresolution remote sensing approach for disaggregation of surface soil moisture: Application to SMOS configuration. *IEEE Trans. Geosci. Remote Sens.* **2005**, *43*, 2036–2050. [[CrossRef](#)]
62. Agam, N.; Kustas, W.P.; Anderson, M.C.; Li, F.; Colaizzi, P.D. Utility of thermal sharpening over Texas high plains irrigated agricultural fields. *J. Geophys. Res. Atmos.* **2007**, *112*, D19. [[CrossRef](#)]

63. Merlin, O.; Malbêteau, Y.; Notfi, Y.; Bacon, S.; Khabba, S.; Jarlan, L. Performance metrics for soil moisture downscaling methods: Application to DISPATCH data in central Morocco. *Remote Sens.* **2015**, *7*, 3783–3807. [[CrossRef](#)]
64. Wilson, A.M.; Jetz, W. Remotely sensed high-resolution global cloud dynamics for predicting ecosystem and biodiversity distributions. *PLoS Biol.* **2016**, *14*, e1002415. [[CrossRef](#)]



© 2019 by the authors. Licensee MDPI, Basel, Switzerland. This article is an open access article distributed under the terms and conditions of the Creative Commons Attribution (CC BY) license (<http://creativecommons.org/licenses/by/4.0/>).

Chapter 6

Building a synergy of disaggregated passive microwave soil moisture approach with radar-based retrieval approach

Contents

6.1	Introduction	120
6.2	A new radar-DISPATCH coupling method	120
6.3	Validation	123
6.4	Conclusion	125
6.5	Article : A calibration/disaggregation coupling scheme for retrieving soil moisture at high spatio-temporal resolution: synergy between SMAP passive microwave, MODIS/Landsat optical/thermal and Sentinel-1 radar data	126

6.1 Introduction

Active microwave sensors or radars are sensitive to soil moisture (SM) (Ulaby et al., 1983; Kornelsen and Coulibaly, 2013). With the recent advent of Sentinel-1 missions, C-band radar data can be used to invert SM at fine resolution with a potential repeat cycle of 6 days (Zribi and Dechambre, 2003; Baghdadi et al., 2012; Ouaadi et al., 2020). An essential asset of radar is that it can provide SM information in all weather conditions. The downside is that the radar data are influenced by vegetation biomass and structure (Wagner et al., 1999), surface roughness (Mattia et al., 1997), and topography (van Zyl et al., 1993), making the direct estimation of SM from the backscattering coefficient a complex process.

Several models have been proposed in the last 30 years to retrieve SM from the backscattering coefficient. They can be categorized into theoretical (Fung et al., 1992), semi-empirical and empirical models (Dubois et al., 1995; Oh, 2004; Baghdadi et al., 2016). These models cannot provide SM over large extents because the water content in soil and vegetation components makes SM estimation from backscattering coefficients an infeasible process. So this model requires prior information about the vegetation component and the soil roughness, and hence SM estimation is limited to specific, well-monitored regions.

An avenue to overcome radar's limitations related to the uncertainty in model parameters is to develop a synergy with passive microwave or optical/thermal data. A common synergy between radar and passive microwave data determines the sub-pixel variability of a passive microwave pixel at finer resolution using radar pixels. But this method provides SM at low temporal resolution because of the need for quasi-simultaneous overpasses of both (i.e., SMAP and Sentinel-1) satellites. Another suggested method is to combine the active microwave with optical/thermal data. To my knowledge, the first study on this subject was published recently by Amazirh et al. (2018). Despite the limited literature, optical/thermal data have been extensively used to monitor the evapotranspiration, and the evaporative fraction, which can be more or less directly related to SM for a large range of land covers.

All the methods mentioned above about the synergy of radar with passive microwave and/or optical/thermal data have great potential to improve the retrieval of SM in terms of spatial resolution, temporal resolution, and accuracy in various conditions. In this context, a novel method is devised by generating synergy between passive microwave, active microwave, and optical/thermal data to deliver SM data at high spatio-temporal resolution with improved accuracy. There is currently no such multi-satellite synergistic technique available.

To achieve the proposed synergy the radar parameter is calibrated from disaggregated SM at 100 m resolution using the active radiative transfer model. Then the calibrated radar parameter is then used in the inverse mode of the active radiative transfer model to estimate the SM. The models, with different vegetation indices, are evaluated over the irrigated and rainfed areas of Morocco.

6.2 A new radar-DISPATCH coupling method

We propose the synergy based on the calibration at high-resolution of the radar retrieval approach using the SM images obtained from the disaggregation of SMOS or SMAP SM using DISPATCH. The advantage of such an approach is that it does not require in situ SM measurements for cal-

ibrating radar parameters that are difficult to estimate directly (e.g., soil roughness, vegetation structural characteristics). However, it requires a quasi-simultaneous overpass of SMOS/SMAP, Landsat, and Sentinel-1 satellites. Once calibrated, the radar model parameter is used in the inverse mode to estimate the SM on every Sentinel-1 overpass.

For clarity, the coupling of disaggregated SM and radar backscatter coefficient from Sentinel-1 is described in the successive steps shown in Figure 6.1. At first, the SMAP/SMOS SM at 40 km resolution is disaggregated to 1 km resolution using optical/thermal data from MODIS. Then, the 1 km disaggregated SM is aggregated to 10 km. Further, the 10 km resolution SM pixel is disaggregated to 100 m resolution using Landsat optical/thermal data. The downscaled SM product at 100 m resolution is next used as a reference dataset for calibrating the radar parameters. Finally, the radar model is used in inverse mode to predict SM on each Sentinel-1 overpass date. Thus, the estimated SM is at last evaluated with in situ SM on the Sentinel-1 overpass dates.

In this thesis, the proposed synergy coupling DISPATCH and radar data is investigated using two different types of active microwave radiative transfer model (RTM): 1) a fully empirical model (with linear assumption) 2) a semi-empirical model (with non-linear assumption). The models are expressed for a given polarization pol (pol=VV, HH or VH).

The empirical RTM is expressed as:

$$\sigma_{pol,empirical} = a * SM + b * V + c \quad (6.1)$$

where a, b, and c are three coefficients for the empirical RTM to be calibrated and V is the vegetation descriptors. Three vegetation descriptors are considered: NDVI, polarization ratio (PR) and coherence (CO).

The semi-empirical RTM is based on Water Cloud model (WCM) of [Attema and Ulaby \(1978\)](#). The model is expressed as the sum of the contribution from the vegetation and the soil attenuated by the vegetation effect. The contribution from vegetation can be written as:

$$\sigma_{pol,veg} = A_{pol} * V_1 \cos\theta * (1 - T_{pol}^2) \quad (6.2)$$

$$T_{pol}^2 = e^{2B_{pol}V_2 \sec\theta} \quad (6.3)$$

where θ is the incidence angle, T_{pol}^2 is the two-way attenuation, V_1 and V_2 are the vegetation parameters and A_{pol} and B_{pol} are the coefficient parameters which depend on vegetation characteristics. Here, $V_1=V_2=V$ where V can be values from either NDVI, PR or CO. The contribution from soil can be written as:

$$\sigma_{pol,soil} = a_{WCM} * SM + c_{WCM} \quad (6.4)$$

where a_{WCM} and c_{WCM} are the calibration coefficients.

Semi-empirical RTM is constructed by combining vegetation contribution and soil contributions, and hence written as:

$$\sigma_{pol,semi-empirical} = \sigma_{pol,veg} + T_{pol}^2 \sigma_{pol,soil} \quad (6.5)$$

$$\sigma_{pol,semi-empirical} = A_{pol} V \cos\theta [(1 - e^{-2B_{pol}V \sec\theta}) + (e^{-2B_{pol}V \sec\theta})(a_{WCM} * SM + c_{WCM})] \quad (6.6)$$

where, $A_{pol} \cos \theta$ and $B_{pol} \cos \theta$ are calibration coefficients and assumed to be constant over each experimental site. For consistency with the linear RTM parameterization, the parameter $A_{pol} \cos \theta$ and $B_{pol} \cos \theta$ are renamed as b_{WCM} and d_{WCM} respectively. So, the semi-empirical model consists of 4 constant parameters (a_{WCM} , b_{WCM} , c_{WCM} and d_{WCM}) to be evaluated and the equation can be rewritten as:

$$\sigma_{pol,semi-empirical} = b_{WCM} V [(1 - e^{-d_{WCM} V})] + (e^{-d_{WCM} V})(a_{WCM} * SM + c_{WCM}) \quad (6.7)$$

Both empirical and semi-empirical models are calibrated using the disaggregated SM time series at 100 m resolution. The calibration parameters for the empirical (linear) RTM model is estimated from the multi-linear regression by using the ordinary least squares method. For the semi-empirical RTM, the calibration parameters are estimated from the non-linear least square model based on the Levenberg-Marquardt algorithm. The algorithm attempts to minimize the square of error difference between the estimated and the observed. The standard error is also calculated from the covariance metrics to estimate the uncertainties in the retrieved calibration parameters.

To derive SM, both RTM models are used in inverse mode, which gives for the empirical RTM:

$$SM_{empirical} = \frac{(\sigma_{pol} - b * V - c)}{a} \quad (6.8)$$

and for the semi-empirical RTM:

$$SM_{semi-empirical} = \frac{(\sigma_{pol} - b_{WCM} * V) * e^{d_{WCM} V} + b_{WCM} * V - c_{WCM}}{a_{WCM}} \quad (6.9)$$

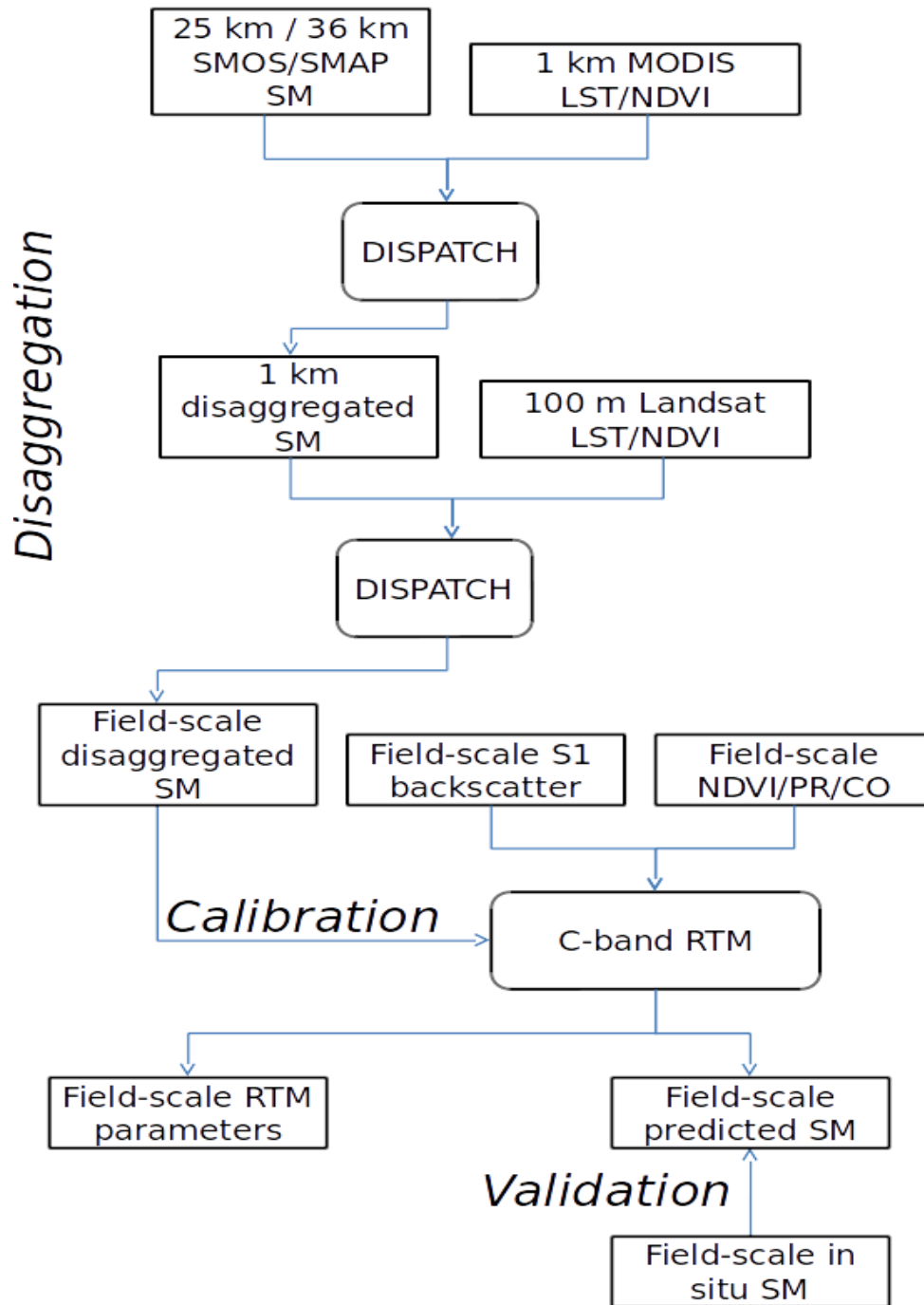


Figure 6.1: The schematic diagram for developing a relationship between disaggregation and calibration scheme combines SMAP/SMOS SM, MODIS/Landsat optical/thermal, and Sentinel-1 radar data at various spatial resolutions to produce an SM product at the field scale at the temporal frequency of Sentinel-1.

6.3 Validation

The two (empirical and semi-empirical) radar models, together with the three different vegetation descriptors used as input (NDVI, PR, and CO), are evaluated in terms of SM estimates over the irrigated and rainfed experimental sites of Morocco. The radar parameters are estimated

from in situ and *DISPATCH*_{100m} SM datasets to assess the calibration strategy separately.

Temporal analysis is first carried out for the six configurations using in situ and DISPATCH 100 m SM datasets as calibration references separately. When in situ SM is used for the calibration, the PR vegetation descriptor shows better results, with correlation coefficient (R) in the range 0.72-0.82 (empirical) and 0.74-0.80 (semi-empirical). When DISPATCH is used for calculating calibration parameters, the NDVI vegetation descriptor performs better for both models with R in the range of 0.76-0.79 (empirical) and 0.77-0.80 (semi-empirical). Hence, parameters calculated using DISPATCH datasets can be used as reference calibration parameters.

A spatio-temporal analysis is also performed for six configurations using in situ SM and DISPATCH 100 m SM reference datasets over the R3 irrigated area for DOY 14, 30, 38, 62, and 78 of 2016. The estimated SM is evaluated with in situ SM for all given dates separately. The results reveal that NDVI vegetation descriptor shows an R for DOY 14, 30, and 38 in the range 0.53-0.74 for both models. But the PR vegetation descriptor shows a better performance for DOY 62 and 78 with an R in the range of 0.15-0.41 (empirical) and 0.09-0.37 (semi-empirical). The time series of R and slope of linear regression (slope) between the predicted SM and in situ SM for both empirical and semi-empirical models for both NDVI and PR vegetation descriptors separately are shown in Figure 6.2. It is observed that R and S behave similarly for both the vegetation descriptors. R and S increase during the early stage of vegetation growth, and then both R and S start decreasing when the vegetation is fully developed. When the vegetation index is above 0.6, then the R decreases for both models. The graph also shows that NDVI performs better during an early stage of vegetation growth and PR performs better when vegetation is fully grown. The NDVI is more sensitive than the PR due to the small variabilities of vegetation cover during the early stage of crops. At the same time, NDVI gets saturated within a given threshold value. Therefore, the choice of NDVI and PR as vegetation descriptors in the model compromise precision and accuracy and depends on the crop covers.

Overall, based on the analysis of our datasets, it is observed that a empirical model using PR as a vegetation descriptor shows a good compromise in terms of robustness all along the season and has only three parameters to estimate.

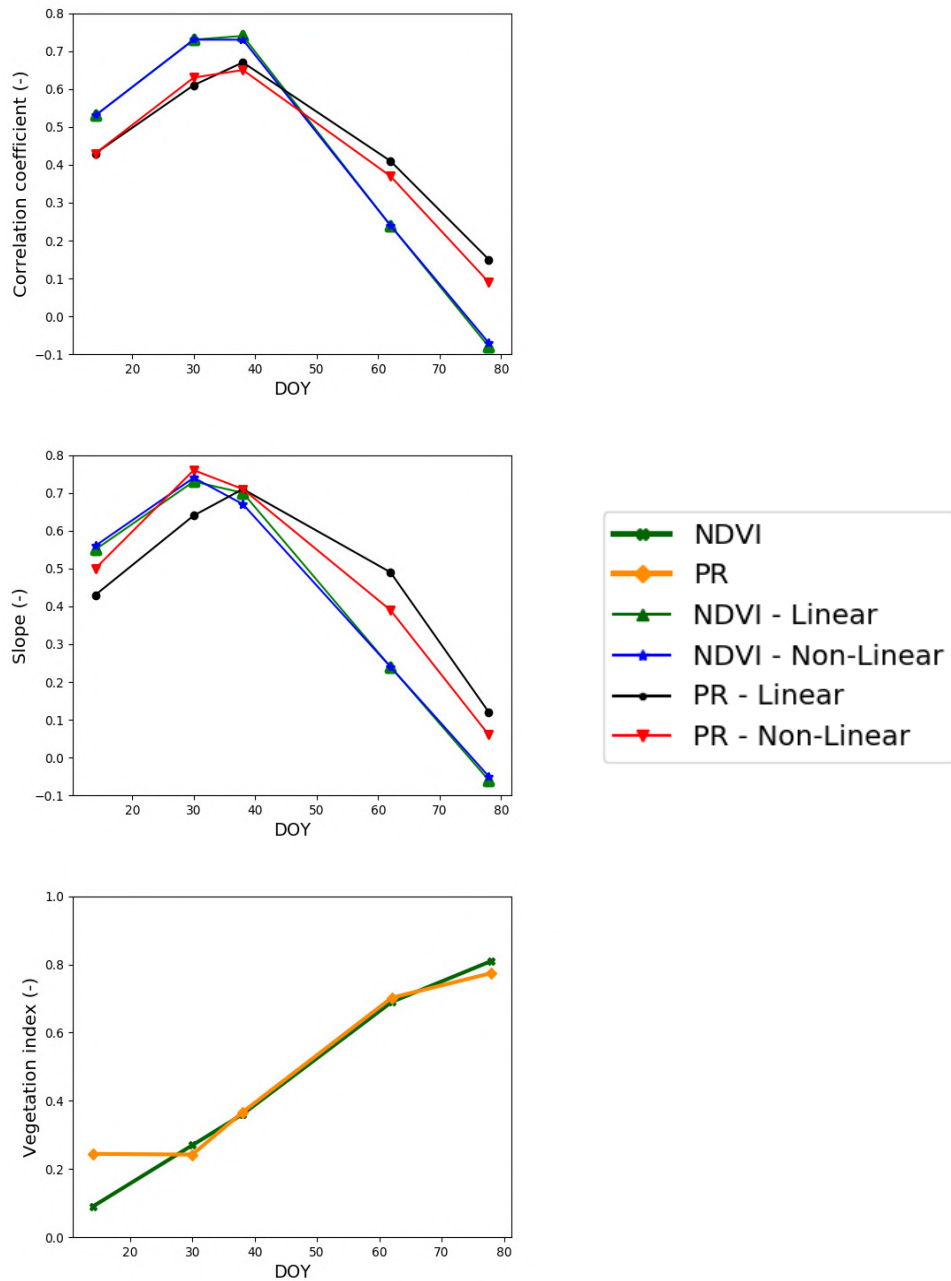


Figure 6.2: Time series of the correlation coefficient and slope of the linear regression between estimated and in situ SM for both (empirical and semi-empirical) active radiative transfer model and two vegetation descriptors (NDVI and PR) separately where in situ SM datasets are used for the calibration.

6.4 Conclusion

This chapter introduces a new method for combining high spatial resolution, multi-resolution passive microwave, optical/thermal data, and active microwave images. The technique uses disaggregated 100 m resolution SM products (obtained from the synergy of passive microwave and optical/thermal data) to develop a synergy with C-band radar. A methodology containing three

steps is proposed to obtain the synergy: 1) SMAP SM at 36 km resolution is disaggregated to 100m resolution with the use of the sequential downscaling algorithm presented in **Chapter 5**, 2) the 100 m resolution disaggregated SM is used to calibrate the parameter of a radar model, and 3) the calibrated parameters are used as input to the radar model in the inverse model, to retrieve SM at the field scale on each Sentinel-1 overpass. The two linear empirical and non-linear semi-empirical models are used to develop a synergy between the backscattering coefficient of radar and disaggregated SM at the field scale. Both models are analyzed with three different vegetation descriptors NDVI, polarization ratio (PR), and coherence (CO) that can better represent the spatial variability of vegetation. Both in situ SM and *DISPATCH*_{100m} SM datasets are used as a reference to calibrate the radar parameters.

Results show better performance for the PR vegetation descriptor when in situ SM is used for calibration. In contrast, NDVI shows better performance when DISPATCH SM datasets are used for calibration. It is also found that the NDVI vegetation descriptor performs better during the early stages of vegetation growth, but the PR vegetation descriptor shows consistent results all over the agricultural season. In our case, both linear and non-linear models show similar behaviors, and the complexity of the non-linearity of the RTM model is not justified.


Both models are quite generic and require few parameters to be calibrated for large-scale applications. One strength and originality of the algorithm is that it does not need ground measurements for calibration. Moreover, it has a solid potential to provide SM data frequently on the Sentinel-1 overpass dates. However, the algorithm was tested by assuming that the incidence angle and other parameters are constant. In the future, this approach will be tested for different incidence angles of Sentinel-1 and various crop types and surface conditions. Further investigation is also required for the dynamic analysis of calibration parameters using DISPATCH 100m datasets to be useful for estimating SM over highly anthropized (like agricultural) environments.

6.5 Article : A calibration/disaggregation coupling scheme for retrieving soil moisture at high spatio-temporal resolution: synergy between SMAP passive microwave, MODIS/Landsat optical/thermal and Sentinel-1 radar data

1. Ojha, N., Merlin, O., Amazirh, A., Ouadi, N., Rivalland, V., Jarlan, L., Er-Raki, S. and Escorihuela, M.J., 2021. A Calibration/Disaggregation Coupling Scheme for Retrieving Soil Moisture at High Spatio-Temporal Resolution: Synergy between SMAP Passive Microwave, MODIS/Landsat Optical/Thermal and Sentinel-1 Radar Data. *Sensors*, 21(21), p.7406

Article

A Calibration/Disaggregation Coupling Scheme for Retrieving Soil Moisture at High Spatio-Temporal Resolution: Synergy between SMAP Passive Microwave, MODIS/Landsat Optical/Thermal and Sentinel-1 Radar Data

Nitu Ojha ¹, Olivier Merlin ^{1,*}, Abdelhakim Amazirh ², Nadia Ouaadi ^{1,3}, Vincent Rivalland ¹, Lionel Jarlan ¹, Salah Er-Raki ⁴ and Maria Jose Escorihuela ⁵

- ¹ CESBIO, Université de Toulouse, CNES/CNRS/INRA, IRD/UPS, 31400 Toulouse, France; ojhan@cesbio.cnes.fr (N.O.); nadia.ouaadi@gmail.com (N.O.); vincent.rivalland@cesbio.cnes.fr (V.R.); lionel.jarlan@ird.fr (L.J.)
 - ² Center for Remote Sensing Applications (CRSA), Mohammed VI Polytechnic University (UM6P), Ben Guerir 43150, Morocco; abdelhakim.amazirh@gmail.com
 - ³ LMFE, Department of Physics, Faculty of Sciences Semlalia, Cadi Ayyad University, Marrakech 40000, Morocco
 - ⁴ ProcEDE, Département de Physique Appliquée, Faculté des Sciences et Techniques, Université Cadi Ayyad, Marrakech 40000, Morocco; s.erraki@uca.ma
 - ⁵ isardSAT S.L., Parc Tecnologic Barcelona Activa, 08042 Barcelona, Spain; mj.escorihuela@isardsat.cat
- * Correspondence: olivier.merlin@cesbio.cnes.fr



Citation: Ojha, N.; Merlin, O.; Amazirh, A.; Ouaadi, N.; Rivalland, V.; Jarlan, L.; Er-Raki, S.; Escorihuela, M.J. A Calibration/Disaggregation Coupling Scheme for Retrieving Soil Moisture at High Spatio-Temporal Resolution: Synergy between SMAP Passive Microwave, MODIS/Landsat Optical/Thermal and Sentinel-1 Radar Data. *Sensors* **2021**, *21*, 7406. <https://doi.org/10.3390/s21217406>

Academic Editor: José Darrozes

Received: 13 October 2021

Accepted: 4 November 2021

Published: 8 November 2021

Publisher's Note: MDPI stays neutral with regard to jurisdictional claims in published maps and institutional affiliations.



Copyright: © 2021 by the authors. Licensee MDPI, Basel, Switzerland. This article is an open access article distributed under the terms and conditions of the Creative Commons Attribution (CC BY) license (<https://creativecommons.org/licenses/by/4.0/>).

Abstract: Soil moisture (SM) data are required at high spatio-temporal resolution—typically the crop field scale every 3–6 days—for agricultural and hydrological purposes. To provide such high-resolution SM data, many remote sensing methods have been developed from passive microwave, active microwave and thermal data. Despite the pros and cons of each technique in terms of spatio-temporal resolution and their sensitivity to perturbing factors such as vegetation cover, soil roughness and meteorological conditions, there is currently no synergistic approach that takes advantage of all relevant (passive, active microwave and thermal) remote sensing data. In this context, the objective of the paper is to develop a new algorithm that combines SMAP L-band passive microwave, MODIS/Landsat optical/thermal and Sentinel-1 C-band radar data to provide SM data at the field scale at the observation frequency of Sentinel-1. In practice, it is a three-step procedure in which: (1) the 36 km resolution SMAP SM data are disaggregated at 100 m resolution using MODIS/Landsat optical/thermal data on clear sky days, (2) the 100 m resolution disaggregated SM data set is used to calibrate a radar-based SM retrieval model and (3) the so-calibrated radar model is run at field scale on each Sentinel-1 overpass. The calibration approach also uses a vegetation descriptor as ancillary data that is derived either from optical (Sentinel-2) or radar (Sentinel-1) data. Two radar models (an empirical linear regression model and a non-linear semi-empirical formulation derived from the water cloud model) are tested using three vegetation descriptors (NDVI, polarization ratio (PR) and radar coherence (CO)) separately. Both models are applied over three experimental irrigated and rainfed wheat crop sites in central Morocco. The field-scale temporal correlation between predicted and in situ SM is in the range of 0.66–0.81 depending on the retrieval configuration. Based on this data set, the linear radar model using PR as a vegetation descriptor offers a relatively good compromise between precision and robustness all throughout the agricultural season with only three parameters to set. The proposed synergistic approach combining multi-resolution/multi-sensor SM-relevant data offers the advantage of not requiring in situ measurements for calibration.

Keywords: disaggregation; soil moisture; synergy; Sentinel-1; DISPATCH; SMAP; Landsat

1. Introduction

Soil moisture (SM) controls the energy exchange between the land surface and the atmosphere, as well as the terrestrial hydrological cycle and ecological environments [1]. Hence, SM information at a fine space-time scale is beneficial for agricultural [2] and other hydrological applications [3]. In situ measurements can provide SM estimates at a field scale, but they cannot capture all the spatial variability. The spatial variability of SM especially occurs due to vegetation, soil roughness, soil texture, terrain, and atmospheric and anthropogenic (e.g., irrigation) effects, which significantly impact SM [4]. One major motive for monitoring SM at a fine scale is the management of water resources over irrigated areas, i.e., the optimization of irrigation in terms of scheduling and dispatching [5,6]. Collecting time and cost are also the main constraints that make in situ SM measurements impractical for global SM monitoring. Instead, remote sensing offers a good compromise in the global tracking of SM over an enormous range of spatial and temporal scales.

Nowadays, L-band microwave radiometers are routinely used to provide SM data on a global basis. Based on L-band radiometry, two satellites are currently in operation: (1) Soil Moisture and Ocean Salinity (SMOS), launched by ESA in November 2010 [7], and (2) Soil Moisture Active Passive (SMAP), launched by NASA in January 2015 [8]. Both satellites provide SM retrievals at about 40 km resolution with a sensing depth of 3 to 5 cm and a global revisit cycle of 3 days. The L-band radiometry is one of the optimal technologies widely accepted for SM estimation [9]. SMOS/SMAP SM products have been extensively validated and found suitable for climatology and large-scale hydrology purposes. Nonetheless, their typical spatial resolution of 40 km is too coarse for most hydro-agricultural applications [10–12].

Other remote sensing techniques such as radar or thermal imagery can provide SM information at a much higher spatial resolution than L-band radiometers. For instance, Landsat-8 thermal and Sentinel-1 C-band radar sensors achieve a spatial resolution of 100 and 20 m, respectively. Based on the assumption that the passive microwave-derived SM is accurate at low resolution and that relative SM information can be obtained at higher spatial resolution from radar/thermal sensors, various disaggregation approaches have been proposed [13,14]. On the one hand, the radar-based disaggregation technique combines the low-resolution L-band brightness temperature with fine resolution radar observations. In this vein, the SMAP satellite was originally dedicated to combining an L-band radiometer and an L-band radar to provide SM at 3 km resolution. However, due to the SMAP radar failure, currently, the SMAP mission provides SM at 9 km resolution on a global basis [15] by interpolating the brightness temperature of the L-band radiometer using the Backus-Gilbert method [16]. Another approach used by the SMAP mission is to combine the SMAP radiometer with the Sentinel-1 radar to provide SM at 9 and 3 km [17]. However, this approach is limited by the constraint of the need for quasi-simultaneous overlapping areas of SMAP and Sentinel-1 data.

On the other hand, the optical/thermal-based downscaling method generally relies on the relationship between passive microwave-derived SM and the evaporative fraction derived from the vegetation index (NDVI)-land surface temperature (LST) feature space [13,18–20]. The main advantage of optical-based over radar-based downscaling approaches is that the LST is less affected by the soil roughness [21] and vegetation structure [22] than the radar backscatter coefficient [23–25]. However, optical-based approaches are limited by (1) the low repeat cycle of currently available high-spatial-resolution thermal sensors, (2) the gaps in data coverage due to the presence of clouds, and (3) the underlying requirement of a large atmospheric evaporative demand at the time of thermal sensor overpass.

Radar data are primarily influenced by surface roughness [26], vegetation cover [27] and topography [28], making the direct estimation of SM from backscattering coefficients more difficult than from the SMOS/SMAP L-band brightness temperature. However, active microwave sensors are sensitive to SM [29,30] and C-band synthetic aperture radars (SAR) have the capability to provide SM data at high spatial resolution with a global

time coverage of 6–12 days with Sentinel-1, regardless of cloud coverage [31–33]. Various soil backscattering models [34], empirical and semi-empirical models [24,35,36] were developed to simulate the radar backscatter in the forward mode and to estimate SM from radar data in the retrieval mode. Because of water content in both the soil and vegetation components, estimating SM from the radar backscattering coefficient is a very complex task. The Water Cloud Model (WCM) [37] was developed to simulate the backscattering of the canopy. WCM is a simple mathematical model, and due to its simplicity, it is widely used in the forward or inverse mode [31,38–41]. The vegetation parameter in the WCM can be quantified using various vegetation descriptors such as the normalized difference vegetation index (NDVI), leaf area index (LAI), polarization ratio (PR), and the interferometric coherence (CO) [42–44].

Despite the pros and cons of the above SM retrieval techniques in terms of spatio-temporal resolution and their sensitivity to perturbing factors such as vegetation cover, soil roughness and meteorological conditions, there is currently no synergistic approach that takes advantage of all relevant remotely sensed data. To overcome the above-discussed limitations, this study aims to develop a new algorithm to provide SM at high spatio-temporal resolution without the need for in situ SM measurements for calibration of radar data. To do this, the new algorithm combines multi-resolution passive microwave, active microwave and optical/thermal data and an innovative calibration approach. As a first step, the DISPATCH algorithm is implemented at 100 m resolution to disaggregate the 36 km resolution SMAP SM at 100 m resolution on clear sky days [45]. DISPATCH is one of the reference disaggregation methods based on optical/thermal data [13,14,46,47]. As a second step, the 100 m resolution disaggregated SMAP SM data set is used to calibrate—on clear sky days with quasi-simultaneous overpasses of SMAP, Landsat, and Sentinel-1—two different C-band radar models: an empirical linear regression and a semi-empirical non-linear model based on the WCM formulation. In both (linear and non-linear) cases, three configurations are tested based on different vegetation descriptors in the model: the NDVI, PR, and CO separately. The different vegetation descriptors are used to evaluate the performance of each vegetation descriptor within the calibration/validation approach of the radar-based SM retrieval scheme. As a third and last step, both calibrated radar models are run in the inverse mode on all Sentinel-1 overpass dates to estimate the fine-scale SM at the temporal frequency of Sentinel-1.

Note that most past studies that have investigated soil moisture-related remote sensing tools such as SMAP, MODIS, Landsat and Sentinel-1, have compared the relative performance of individual techniques (e.g., [14,48,49]). Nevertheless, none of them have combined all the above sensors within a unique and spatially consistent method. To the knowledge of the authors, this study is the first to make synergistic use of SMAP, MODIS, Landsat and Sentinel-1 data to produce a single soil moisture data set at high spatio-temporal resolution. At the same time, recent research progresses present good direction for downscaling SMAP-like data using ancillary optical/thermal data [50–52]. However, such disaggregation approaches are still generally implemented at the 1 km resolution using MODIS or Sentinel-3 data [53–56]. Our study fundamentally differs from those previous approaches in that DISPATCH is implemented at 100 m resolution by using Landsat data, so that the spatial variability of SM is represented at a much finer scale, which is now consistent with the typical size of crop fields.

The proposed original disaggregation/calibration method for SM retrieval is tested over irrigated and rainfed wheat crop sites in the Haouz plain, central Morocco. In particular, the SM predicted by both models in different configurations are compared over the study area to analyze which retrieval approach performs better during the different stages of the agricultural season.

2. Materials and Methods

2.1. Study Area and In Situ Data

The study area comprises three experimental sites, namely the R3 irrigated zone and two (Sidi Rahal and Chichaoua) experimental crop fields, all located in the Haouz plain within a 100 km distance of Marrakesh city (see Figure 1). The Haouz plain has a semi-arid Mediterranean climate with an average annual precipitation of 250 mm [57,58] and an average evaporative demand of about 1600 mm/year [59]. The soil texture is clayey for the R3 irrigated zone, sandy for the Sidi Rahal site, and loamy-clayey for the Chichaoua site. The land of three experimental sites (R3 irrigated zone, Sidi Rahal and Chichaoua) are covered by agricultural crops, primarily cultivated with winter wheat.

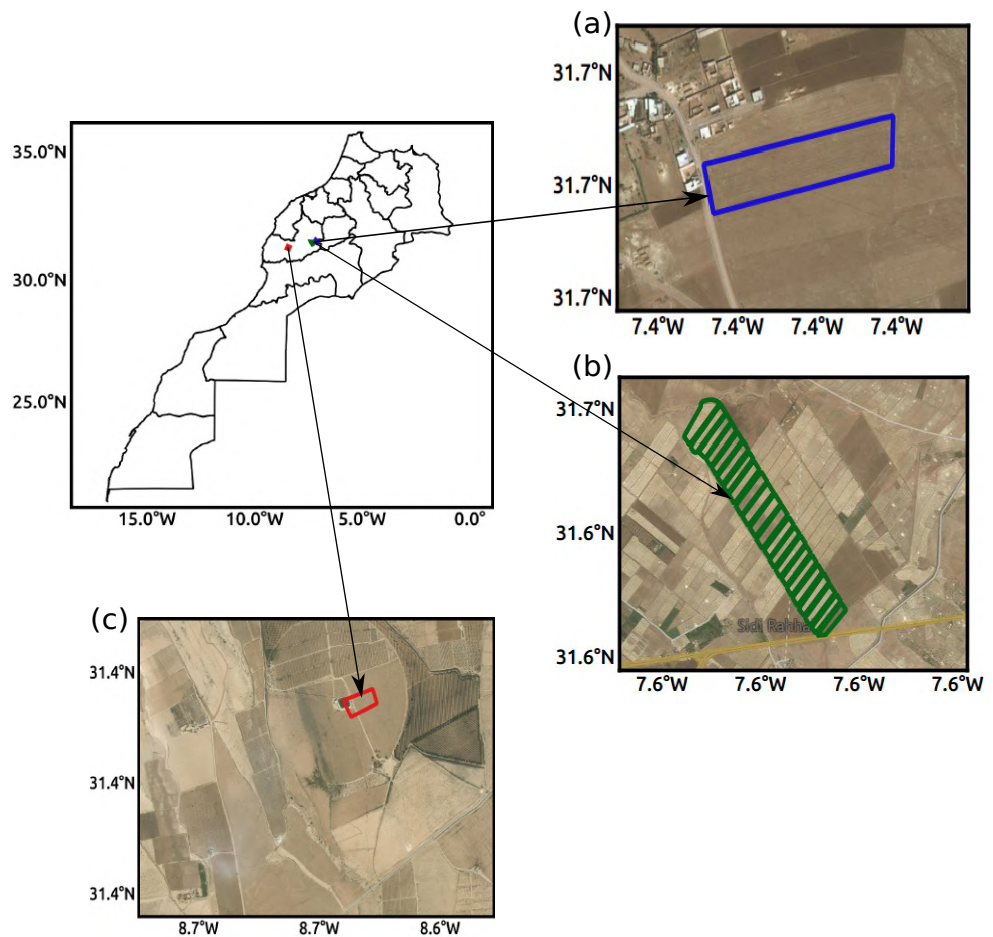


Figure 1. Location of the study area, including (a) Sidi Rahal, (b) R3 irrigated perimeter, (c) Chichaoua experimental sites.

The R3 irrigated study zone contains 22 irrigated (flood-irrigated) wheat parcels, with 3–4 ha each. The strategy for soil moisture sampling over R3 is explained in Amazirh et al. [21] and Ojha et al. [45]. In each of the 22 crop fields, 10 separate theta probe measurements were undertaken with 5 on a side of the field and 5 on the other side, by making sure that all measurements were taken sufficiently far (>5 m) from the field border for spatial representativeness issues. The field-scale in situ soil moisture data used in this paper were obtained by (1) calibrating the theta probe readings using gravimetric measurements and (2) averaging the 10 measurements for each field. Regarding the soil texture analysis, the samples were packed in plastic bags and properly marked for identification and analysis. A total of 20 g of the mixed soil was sampled for analyzing grain size distribution. These soil samples were air-dried and sieved into two fractions: (0.05–2 mm) to calculate the

percentage of sand content. The smaller fraction passed through a (0.05 mm) sieve was recovered and collected in a vial and then analyzed using pipette [60] and/or granulometry laser methods to measure coarse loam (20–50 μm), fine loam (2–20 μm) and clay content (<2 μm). In this study, five sampling days (day of year 14, 30, 38, 62, 78) in 2016 are used concurrently with Sentinel-1 overpasses.

Sidi Rahal and Chichaoua sites cover an area of 1 and 1.5 ha separately. In situ SM data were collected in both the sites every 30 min using time domain reflectometry (TDR) sensors. Sidi Rahal is a rainfed wheat site, and Chichaoua a drip-irrigated wheat site. At the Chichaoua site, two TDR sensors were mounted with one between and one under the drippers. The average TDR measured values were calibrated using the gravimetric method. More detailed information about the in situ data collection is presented in Rafi et al. [58], Amazirh et al. [21], Ouaadi et al. [61], Ait Hssaine et al. [62]. The SM data collected during the time period of 2017–2018 were used in this paper. Note that the irrigated crop in Chichaoua underwent controlled water stress during the 2018 agricultural season [58].

Note that data from Chichaoua and Sidi Rahal sites were used for calibration and validation in this paper. However, R3 irrigated zone datasets were used only for validation.

2.2. Remote Sensing Data

2.2.1. SMAP

The SMAP satellite was launched on 31 January 2015 by NASA [8]. SMAP is the first L-band satellite dedicated to provide SM at a resolution ranging from 3 to 36 km with a 2–3-day revisit cycle by incorporating both radar and radiometer. However, due to the failure of the SMAP radar, the SM generated by the SMAP processing chains is now defined at 36 and 9 km (by resampling technique) resolution. SMAP is a near-polar sun-synchronous orbit at an altitude of 658 km, with a descending/ascending overpass at 6:00 a.m./p.m. local time. To manage the SMAP radar failure, the SMAP mission has recently provided a product that combines SMAP and C-band Sentinel-1 radar data to provide an SM product at 1 km resolution. In this paper, the 36 km resolution SMAP level-3 version 005 product available on an EASE grid 2 at <https://nsidc.org/data/SPL3/SMP/versions/5> for a time period of 2016 to 2018 is used as input to the DISPATCH disaggregation method to provide SM data at 100 m resolution over the study areas.

2.2.2. MODIS

MODIS version 6 MOD11A1 and MOD13A2 products on ascending mode Terra overpass (10:30 a.m.) and MODIS version 6 MYD11A1 product on descending mode Aqua overpass (1 p.m.) were used in this paper. LST and enhanced vegetation index (EVI) data extracted from MOD11A1/MYD11A1 and MOD13A2 products, respectively, were used as input to the DISPATCH disaggregation method. In practice, the C4DIS processor is applied to SMAP level-3 data to disaggregate SM data at 1 km resolution [54,63].

2.2.3. Landsat

In this paper, optical/thermal data from Landsat-7 and Landsat-8, which have an offset of 8 days, were used as an input to the DISPATCH disaggregation method. The DISPATCH algorithm is applied to 1 km resolution disaggregated SMAP SM data using 100 m resolution Landsat LST/NDVI data to produce a disaggregated SM data set at 100 m resolution [45]. Landsat images are downloaded from the USGS website, which provides thermal radiance and surface reflectance data on a 30 m resolution sampling grid globally. Surface reflectance is aggregated at 100 m resolution and used to derive NDVI. The Landsat thermal radiance is used for the LST calculation using a single band algorithm from band-6 and band-10 of Landsat-7 and Landsat-8, respectively. The detailed description of the Landsat processing [64] is described in Ojha et al. [45].

2.2.4. Sentinel-1

Sentinel-1 is a C-band SAR mission that consists of two satellites, Sentinel-1 A (S1-A) launched in April 2014 and Sentinel-2 (S2-B) launched in April 2016. Sentinel-1 is a sun-synchronous near-polar orbit satellite with a revisit cycle of 12 days. In this paper, the radar-based SM retrieval models use VV polarization. As stated in Amazirh et al. [21] and Ouaadi et al. [31], VV polarization is a better indicator of SM than VH for the selected study area. Note that VH polarization is still used herein to estimate the PR defined as the ratio of backscattering coefficients in VH and VV polarizations.

In this paper, the Ground Range Detected (GRD) and Single Look Complex (SLC) products were downloaded from the Copernicus Sentinel hub. GRD products were used to compute the backscattering coefficient, whereas SLC products were used to calculate interferometric coherence. Sentinel-1 level-1 GRD products were processed in four steps: (1) removing thermal noise by removing the additive effect, (2) radiometric calibration to compute the backscattering coefficient by using sensor calibration parameters, (3) terrain correction by correcting the backscattering coefficient for the terrain and geometric effects using SRTM digital elevation model at 30 m resolution, and (4) reducing the speckle effects by using Lee speckle filter. The SLC products were also used to calculate the coherence from the SNAP platform in five successive steps: (1) applying an orbit file for a better estimation of position, (2) applying back-geocoding for co-registration, (3) running the “coherence module” to estimate coherence, (4) running the “TOPSAR-Deburst” module for removing the black band in SLC products, and (5) running the “Terrain correction” module using SRTM DEM.

The incidence angle for the product is 40 degrees for both R3 and Sidi Rahal sites and 35 degrees for the Chichaoua site Amazirh et al. [21], Ouaadi et al. [31]. Note that the 20 m resolution Sentinel-1 data were finally resampled at the field-crop scale.

2.2.5. Vegetation Descriptors

Vegetation descriptors depict the growth of vegetation, its density, and its impact on the radar backscatter. The accuracy and sensitivity of vegetation descriptors are essential for the correct estimation of SM throughout the agricultural season. Three different vegetation descriptors used as a proxy for vegetation in the linear and non-linear radar models are described below:

(1) NDVI is derived from Sentinel-2 surface reflectance—ESA launched the Sentinel-2 optical satellites S2-A and S2-B in 2015 and 2017, respectively. They provide optical images at 10–60 m resolution with a revisit cycle of 5 days. The Sentinel-2 level-2 product downloaded from the THEIA platform is used in this paper. Sentinel-2 product is orthorectified and corrected for the atmospheric effect using the MAJA processor [65] for cloud detection and atmosphere correction. NDVI is calculated from (near-infrared) band 8 and (red) band 4.

(2) PR is derived from Sentinel-1 data by taking the VH/VV polarization ratio.

(3) CO is calculated from S1A and S1B from two consecutive acquisitions of the same orbit (i.e., 6 days overpass with S1A and S1B)—the product of one SAR image with its complex conjugate of the second image from a local neighborhood [66,67].

Note that the vegetation indices NDVI, PR, and CO are resampled at the crop field scale and re-normalized by their minimum and maximum values obtained during the entire study period. The normalized NDVI, PR, and CO values thus lie in the range from 0 to 1.

2.3. Remote Sensing Method

2.3.1. DISPATCH

DISPATCH [46,47] is one downscaling reference algorithm that combines L-band passive microwave with optical/thermal data to provide SM at the optical/thermal spatial resolution. DISPATCH was initially developed using MODIS data at 1 km resolution. The algorithm computes the soil evaporative efficiency (*SEE*) from optical/thermal data. It dis-

tributes the 1 km disaggregated resolution SM by establishing a relationship between 40 km resolution SMOS/SMAP SM and 1 km resolution *SEE* estimates. *SEE* shows a quasi linear relationship with the soil temperature [68] retrieved from optical/thermal data. Note that the DISPATCH approach assumes that the spatial variability of SM does not significantly change between the SMOS/SMAP and optical/thermal overpasses. The C4DIS processor based on the DISPATCH algorithm was developed at Centre Aval de Traitement des Données SMOS (CATDS) to provide SM at 1 km resolution on a global and daily basis.

Recent improvements in the DISPATCH algorithm (named DISPATCH_{veg-ext}) allowed increasing its applicability domain by including densely vegetated areas and using the MODIS EVI instead of MODIS NDVI to increase its robustness over vegetated areas [54]. Herein, the DISPATCH_{veg-ext} algorithm is sequentially applied to 36 km resolution SMAP SM and to the 1 km resolution disaggregated SMAP SM using MODIS and Landsat LST/NDVI data, respectively. The two-step downscaling algorithm is fully described in Ojha et al. [45]. In practice, the 36 km resolution SMAP SM is disaggregated at 1 km resolution. The 1 km disaggregated data set is aggregated at an intermediate spatial resolution (ISR) of 10 km, and finally, the 10 km ISR data set is further disaggregated at 100 m resolution. The use of an ISR between the two disaggregation steps provides an optimal compromise—in terms of disaggregation efficiency at the target resolution—between scaling effects and the calibration performance of the contextual DISPATCH approach [45].

The general equation of the DISPATCH algorithm, which is implemented separately at 1 km and 100 m resolutions, is defined as follows:

$$SM_{HR} = SM_{LR} + \left(\frac{\delta SEE}{\delta SM} \right)_{LR}^{-1} * (SEE_{HR} - SEE_{LR}) \quad (1)$$

where SM_{LR} is SM at low (either SMAP or 10 km) resolution, SEE_{HR} is *SEE* at high (either MODIS or Landsat thermal) resolution calculated from MODIS/Landsat, and $\left(\frac{\delta SEE}{\delta SM} \right)_{LR}^{-1}$ is the inverse of the partial derivative of a *SEE*(SM) model calculated at *LR*. *SEE* is considered as a linear relationship with soil temperature and is written as:

$$SEE_{HR} = \frac{T_{s,max} - T_{s,HR}}{T_{s,max} - T_{s,min}} \quad (2)$$

where $T_{s,HR}$ is the soil temperature at HR, and $T_{s,max}$ and $T_{s,min}$ the soil temperature for fully dry ($SEE = 0$) and wet conditions ($SEE = 1$). More details are given in Ojha et al. [45] and Ojha et al. [54]. Note that the 100 m resolution DISPATCH SM data are finally resampled at the field crop scale for comparison with Sentinel-1-based estimates.

2.3.2. Active Microwave Radiative Transfer Models

The calibration/disaggregation scheme is tested with two formulations of radiative transfer model (RTM) for C-band radar data: an empirical multi-linear regression and a semi-empirical non-linear WCM-based formulation. The multi-linear RTM is expressed as:

$$\sigma_{VV,Linear} = a_{ML} * SM + b_{ML} * V + c_{ML} \quad (3)$$

with a_{ML} , b_{ML} and c_{ML} being three coefficients to be calibrated, and V the vegetation descriptor (NDVI, PR or CO). σ_{VV} is the backscattering coefficient calculated from Sentinel-1 is expressed in decibels (dB).

The non-linear RTM is derived from the WCM model of Attema and Ulaby [37]. The radar backscatter is written as the sum of the contributions from vegetation and from the soil attenuated by vegetation. The vegetation contribution is expressed as:

$$\sigma_{VV,veg} = A_{VV} * V_1 \cos \theta * (1 - T_{VV}^2) \quad (4)$$

$$T_{VV}^2 = e^{-2B_{VV}V_2\sec\theta} \quad (5)$$

where θ is the radar incidence angle, T_{VV}^2 is the two-way attenuation, V_1 and V_2 are the vegetation parameters and A_{VV} and B_{VV} are unknown coefficient parameters that are dependent on the vegetation characteristics. Here, $V_1 = V_2 = V$, where V can be either the normalized NDVI, normalized PR or normalized CO. In our case, the soil contribution is expressed as:

$$\sigma_{soil,VV} = a_{WC} * SM + c_{WC} \quad (6)$$

with a_{WC} and c_{WC} being two calibration parameters.

Using Equations (4)–(6), the non-linear RTM becomes:

$$\sigma_{VV,Non-linear} = A_{VV}V\cos\theta[(1 - e^{-2B_{VV}V\sec\theta})] + (e^{-2B_{VV}V\sec\theta})(a_{WC} * SM + c_{WC}) \quad (7)$$

where $A_{VV}\cos\theta$ and $2B_{VV}\sec\theta$ are assumed to be constant over each experimental site, and are hence considered as calibration parameters and defined as $A_{VV}\cos\theta = b_{WC}$ and $2B_{VV}\sec\theta = d_{WC}$. As a result, the non-linear WCM-based RTM has four parameters (a_{WC} , b_{WC} , c_{WC} and d_{WC}) to be calibrated:

$$\sigma_{VV,Non-linear} = b_{WC}V[(1 - e^{-d_{WC}V})] + (e^{-d_{WC}V})(a_{WC} * SM + c_{WC}) \quad (8)$$

Note that by neglecting the vegetation impact ($V = 0$), the non-linear model has the same expression as the linear one. The d_{WC} parameter represents here a non-linearity index of the vegetation impact on the radar backscatter. In the same vein, parameters a , b and c have the same meaning in both linear and non-linear RTM, so that their calibrated values over the same sites can be compared.

2.3.3. Coupling DISPATCH Data with Sentinel-1-Based SM Retrieval Algorithms

Figure 2 shows the schematic diagrams for the coupling of disaggregated SM with the SM retrieval algorithms based on the Sentinel-1 backscattering coefficient explained in three different steps. In the first step, a 100 m resolution SM data set is produced by disaggregating SMAP SM data at 100 m resolution. The disaggregation procedure consists of sequentially applying DISPATCH to 36 km resolution SMAP data using MODIS data and to 1 km resolution disaggregated SM using Landsat data [45]. In the second step, the previously derived 100 m resolution SM is used as a reference data set to calibrate the C-band RTM of Equations (3) and (8). In the third step, the so-calibrated RTM are run in the inverse mode to predict SM on each Sentinel-1 overpass date. The retrieved SM values are finally evaluated using the in situ SM measurements collected concurrently with Sentinel-1 data. Note that the main advantage of such a disaggregation/calibration coupling scheme is not requiring in situ data for calibrating radar models. Different configurations of radar models are tested in terms of the linear/non-linear representation of vegetation effects on the radar signal and the nature of vegetation descriptors (either NDVI, PR, or CO).

2.3.4. Calibration Parameters

The three calibration parameters (a_{ML} , b_{ML} and c_{ML}) of the linear RTM of Equation (3) and the four parameters (a_{WC} , b_{WC} , c_{WC} and d_{WC}) of the non-linear RTM of Equation (8) are calibrated using the 100 m disaggregated SMAP SM data set as a reference. To evaluate the impact of uncertainties in DISPATCH 100 m resolution data, the calibration procedure is also undertaken using in situ (instead of DISPATCH) SM. In both (calibration using DISPATCH or in situ SM) cases, and with both (linear and non-linear) RTM, three model configurations are investigated by selecting NDVI, PR or CO as the vegetation descriptor within the radar modeling.

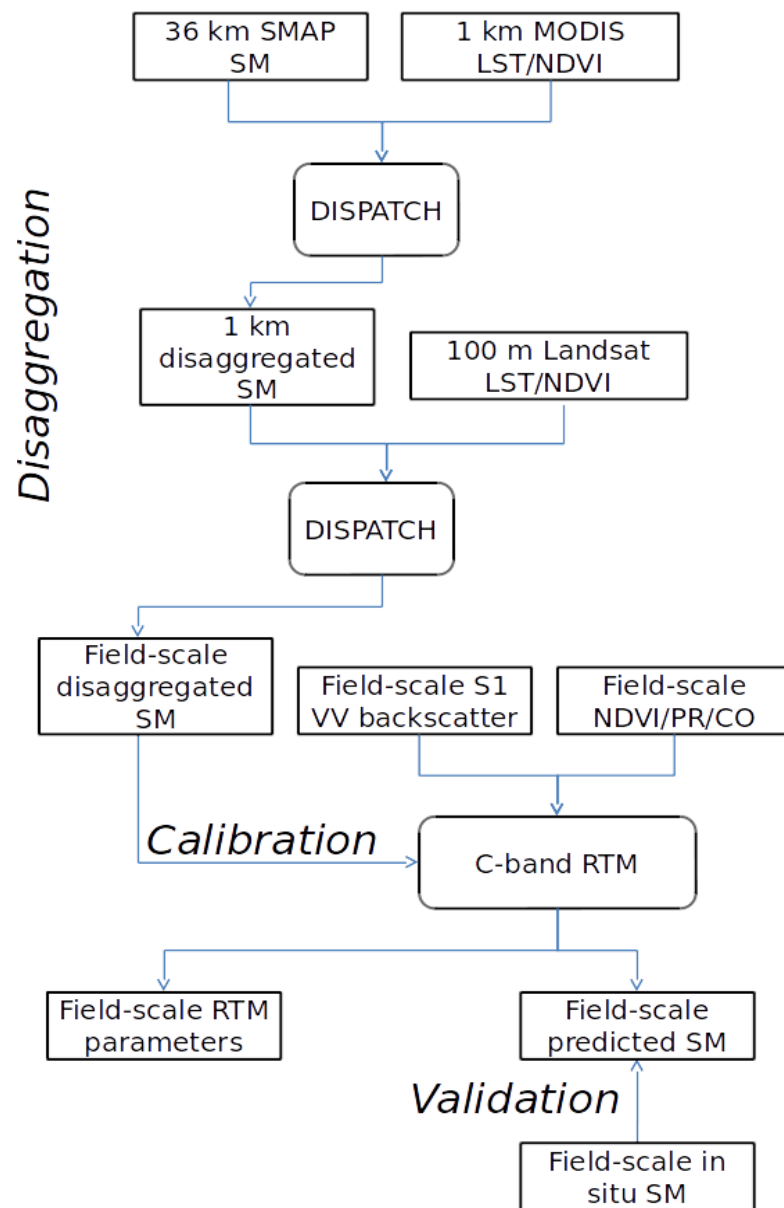


Figure 2. Schematic diagram of the calibration/disaggregation coupling scheme combining SMAP passive microwave, MODIS/Landsat optical/thermal and Sentinel-1 radar data at a range of spatial resolutions to provide an SM product at the field scale at the temporal frequency of Sentinel-1.

The calibration parameters for the linear RTM are estimated from the linear regression by using the ordinary least square method. The calibration parameter for the non-linear model is calculated from the non-linear least square method that is based on the Levenberg–Marquardt algorithm [69]. The optimization algorithm used here minimizes the squared error difference between the observed and predicted backscatter coefficient. For both linear and non-linear RTM, the covariance matrix is calculated. The standard error is calculated from the covariance matrix by the square root of the diagonal. The standard error of each calibration parameter is calculated to identify the uncertainty of the retrieved calibration parameters and possible compensation effects between retrieved parameters. Note that the standard error is systematically presented in terms of percentage relative to the retrieved parameter value.

For the calibration of a , b , c and d parameters, long time series of DISPATCH and Sentinel-1 data are preferred so as to cover a wide range of surface and vegetation conditions. This is the reason why the calibration procedure is undertaken herein only over Chichaoua and Sidi Rahal sites, where data were collected for more than one year. A calibration data set is derived for each site separately, while the R3 data set is kept for the e of the retrieved SM using a fully independent data set. The R3 data set covers only a few months during the agricultural season and is hence not fully relevant for calibration purposes. However, the in situ SM data distributed within the 22 crop fields of the R3 perimeter will be used to assess the performance of the approach in space at different times of the season. In practice, for the R3 application, the parameters used as input to the RTM are set to the average of the parameters retrieved over Chichaoua and Sidi Rahal sites.

Regarding the calibration strategy of the non-linear RTM, attention should be paid to the compensation effects between b_{WC} and d_{WC} parameters (not shown). Especially, when attempting to retrieve a_{WC} , b_{WC} , c_{WC} and d_{WC} parameters simultaneously using the brute-force method, large relative standard errors were systematically obtained for both vegetation parameters (b_{WC} and d_{WC}), notably when the retrieved d_{WC} was close to zero (low vegetation impact). This resulted in estimated percentage errors larger than 100%. Therefore, one parameter can be removed from the calibration without changing the results of the calibrated RTM model. Hence, a slightly different strategy was adopted by constraining the b_{WC} parameter of the non-linear RTM to be equal to the retrieved b_{ML} value in the linear RTM case. Consequently, the calibration of the RTM consists in retrieving, a_{WC} , c_{WC} and d_{WC} as free parameters while setting b_{WC} equal to an a priori value as an additional constraint for solving the ill-posed problem.

3. Results

In this section, the calibration approach is first applied to both (linear and non-linear) RTM in different configurations: using three vegetation descriptors (NDVI, PR, and CO) with two (in situ, DISPATCH) reference SM datasets separately. Then the calibrated parameters are used to estimate SM from Sentinel-1/2 data. Finally, in situ SM collected in Sidi Rahal, Chichaoua and R3 sites are used to analyze the accuracy of predicted SM.

3.1. Accuracy of DISPATCH SM

The accuracy of DISPATCH 100 m resolution SM is assessed with the in situ SM data set used in this study. Although, the objective herein is not to provide a full validation of the 100 m resolution disaggregated data set, it is still useful to first assess the uncertainty of this SM product with a view to better understand its possible impact on the calibration approach.

Figure 3 shows the scatter plots between DISPATCH and in situ SM (Chichaoua, Sidi Rahal). Chichaoua and Sidi Rahal sites show a correlation coefficient (R) value of 0.81 and 0.49, respectively. The mean bias (MB) at the Sidi Rahal site is relatively large whereas it is not significant at the Chichaoua site. Such a dry bias at Chichaoua can be due to uncertainties in SMAP data, in the DISPATCH methodology and/or its ancillary data as well as possibly the spatial heterogeneity of SM at a scale finer than 100 m. To try and explain the key reasons for the differences between Sidi Rahal and Chichaoua sites, the bias between remotely sensed and in situ SM was investigated in the original SMAP, the 1 km resolution DISPATCH and the 100 m resolution DISPATCH data sets separately. The bias in the original SMAP (and 1 km DISPATCH in parenthesis) SM is -0.06 (-0.06) m^3/m^3 and -0.02 (-0.05) m^3/m^3 at Sidi Rahal and Chichaoua sites, respectively.

Having a negative bias on low-resolution SM data at the Chichoua site is fully expected as the local irrigation makes the wheat field generally wetter than the surrounding area covered by the SMAP pixel. However, observing a negative bias in low-resolution SM data at the Sidi Rahal site (and even more negative than at the Chichaoua site) is unexpected. In fact, as a dryland site surrounded by irrigated areas in the west/east and bordered by the Atlas piedmont in the south, the Sidi Rahal site should be one of the driest part within the SMAP pixel. Therefore, the strong negative bias in 100 m resolution DISPATCH SM at Sidi

Rahal site is likely to be attributed to a negative bias in SMAP data over that area and/or a lack of representativeness of in situ measurements in terms of sensing depth (the surface TDR sensors are located in the 5–10 cm soil layer, whereas SMAP senses, on average, the 3–5 cm soil layer).

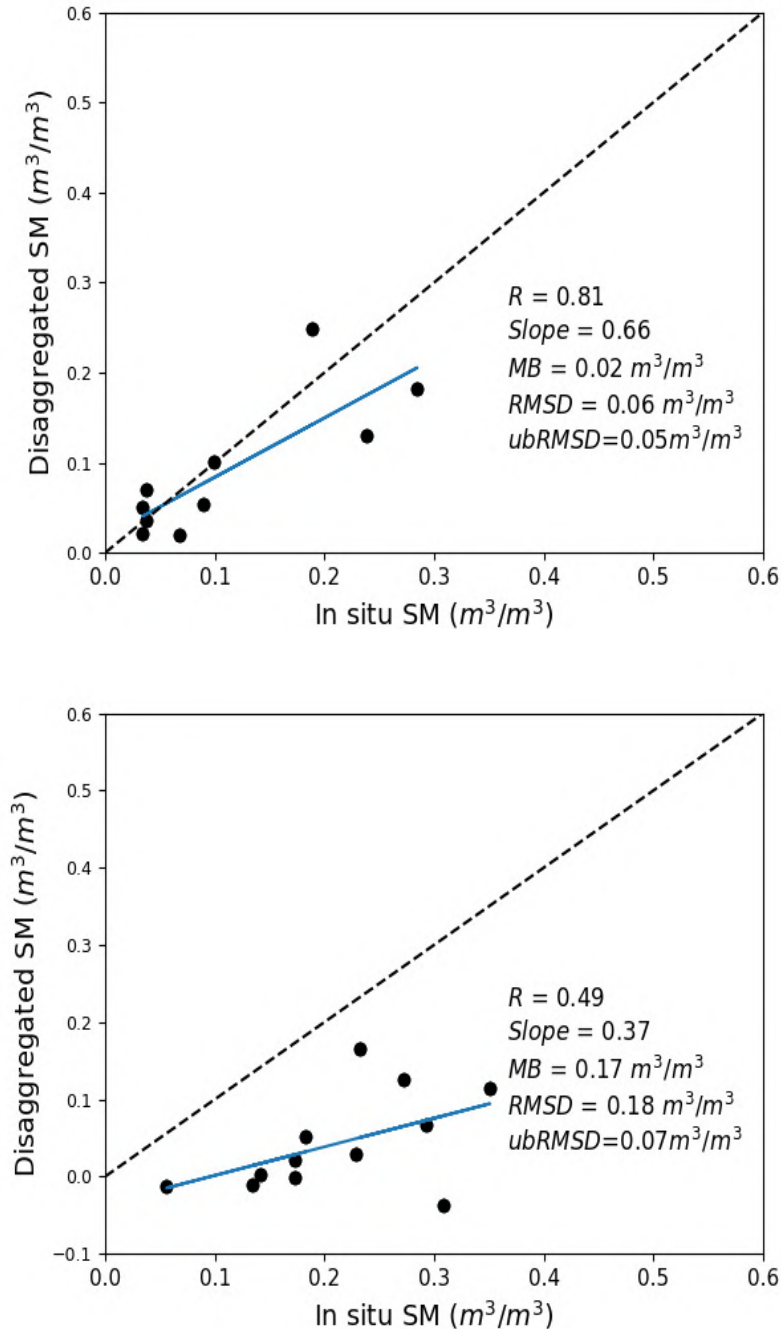


Figure 3. DISPATCH 100 m resolution disaggregated SM versus in situ measurements at Chichaoua (top) and Sidi Rahal (bottom) sites.

This brief evaluation of 100 m resolution DISPATCH SM indicates that the accuracy of the disaggregated dataset can be low due to the presence of bias. However, the disaggregated SMAP data set can capture most of the spatial variability of SM at 100 m resolution as well as the SM dynamics across the agricultural season from the early stage of the crop growth to the fully grown vegetation.

3.2. Evaluation of Calibration Parameters

Table 1 reports the value of calibrated parameters for Chichaoua and Sidi Rahal and their associated standard error for each (linear and non-linear) RTM, using in situ SM data sets as reference for the calibration. The calibration parameters (and their associated standard errors) of both RTM for the three vegetation descriptors (NDVI, PR, and CO) are compared.

Table 1. Values of the calibration parameters and their standard error for linear and non-linear RTM using NDVI, PR and CO as vegetation descriptor separately for Chichaoua (left) and Sidi Rahal (right) sites where in situ SM data are used for the calibration.

		Vegetation Descriptors	Chichaoua	Sidi Rahal
Linear	Calibration parameter $a_{ML}(\text{dB}\cdot\text{m}^3/\text{m}^3)/b_{ML}(\text{dB})/c_{ML}(\text{dB})$	NDVI	19/−3/−14	20/−0.7/−18
		PR	16/−6/−12	20/−4/−16
		CO	15/3/−16	17/3/−19
	Standard error percentage $\text{std}_{a_{ML}}(\%)/\text{std}_{b_{ML}}(\%)/\text{std}_{c_{ML}}(\%)$	NDVI	17/28/2	15/124/3
		PR	12/11/3	10/21/3
		CO	16/18/3	14/30/3
Non-linear	Calibration parameter $a_{WC}(\text{dB}\cdot\text{m}^3/\text{m}^3)/b_{WC}(\text{dB})/c_{WC}(\text{dB})/d_{WC}(\text{dB})$	NDVI	18/−3/−14/−0.28	19/−0.7/−18/−0.04
		PR	11/−6/−11/−0.9	17/−4/−16/−0.4
		CO	18/3/−17/0.2	18/3/−19/0.15
	Standard error percentage $\text{std}_{a_{WC}}(\%)/\text{std}_{b_{WC}}(\%)/\text{std}_{c_{WC}}(\%)/\text{std}_{d_{WC}}(\%)$	NDVI	13/28/2/21	14/124/3/175
		PR	11/11/4/12	11/21/4/26
		CO	14/18/3/14	14/30/4/33

Overall, the retrieved parameters are relatively consistent from one configuration (linear/non-linear RTM and vegetation descriptors) to the other and for both (Chichaoua and Sidi Rahal) sites. The only significant difference in the results between tested configurations is the change in the sign of the b parameter for the CO vegetation descriptor. Indeed, the backscattering coefficient is negatively correlated with NDVI and PR and positively correlated with CO. However, the absolute value is rather similar in all cases, which confirms that any of the three vegetation descriptors can be used to model the vegetation effect on a radar signal. Nonetheless, when looking at the standard error percentage on the retrieved parameters, significant differences appear between parameters and between configurations. For instance, the c parameter has a very small uncertainty (about 3%) in all cases. The uncertainty in the retrieved a parameter is relatively larger (about 13% on average for all cases), but it is quite stable and consistent in all cases. However, larger errors are obtained for the parameters b and d associated with the vegetation modeling. The overall uncertainty in b and d parameters is estimated as 39% and 47%, respectively. By removing the data associated with parameter values close to zero, the overall uncertainty drops to 21% and 18%, respectively. Interestingly, the relative error in retrieved parameters slightly varies with the vegetation descriptor used. It is minimum with PR, maximum with NDVI and intermediate with CO. This is valid for all configurations, including linear/non-linear RTM and both Chichaoua/Sidi Rahal sites. Similar to Table 1, Table 2 shows the value of the calibrated parameters but when the DISPATCH 100 m SM dataset is used as a reference in the calibration. As expected, the error in retrieved parameters increases when using remotely sensed (DISPATCH) instead of in situ SM data. For instance, the overall relative error in the c parameter is 9%, compared to 3% when using in situ data for calibration. By comparing results for the three vegetation descriptors, PR shows the

best performance with an average standard error (all parameters combined) of 20% and 25% over Chichaoua and 25% and 28% over Sidi Rahal, for the linear and non-linear RTM respectively. In addition, the retrieved values using DISPATCH data are closer to the in situ case for the PR configuration compared to NDVI and CO configurations. In particular, the CO configuration seems to be very sensitive to uncertainties in the reference calibration data set, resulting in relative errors of a parameter larger than 100% (see Table 2 for the Sidi Rahal site).

Table 2. Same as Table 1 where DISPATCH SM data are used for the calibration.

		Vegetation Descriptors	Chichaoua	Sidi Rahal
Linear	Calibration parameter $a_{ML}(\text{dB}\cdot\text{m}^3/\text{m}^3)/b_{ML}(\text{dB})/c_{ML}(\text{dB})$	NDVI	34/−7/−14	26/−4/−12
		PR	19/−9/−11	19/−6/−12
		CO	23/5/−18	11/4/−16
	Standard error percentage $\text{std}_{a_{ML}}(\%)/\text{std}_{b_{ML}}(\%)/\text{std}_{c_{ML}}(\%)$	NDVI	27/46/6	38/47/10
		PR	29/24/8	41/27/8
		CO	28/29/7	121/67/9
Non-linear	Calibration parameter $a_{WC}(\text{dB}\cdot\text{m}^3/\text{m}^3)/b_{WC}(\text{dB})/c_{WC}(\text{dB})/d_{WC}(\text{dB})$	NDVI	20/−7/−13/−0.76	19/−4/−12/−4
		PR	10/−9/−10/−2	14/−6/−11/−0.78
		CO	25/5/−18/0.27	12/4/−16/0.24
	Standard error percentage $\text{std}_{a_{WC}}(\%)/\text{std}_{b_{WC}}(\%)/\text{std}_{c_{WC}}(\%)/\text{std}_{d_{WC}}(\%)$	NDVI	25/46/6/41	41/47/11/54
		PR	32/24/12/31	44/27/9/31
		CO	29/29/8/30	122/67/9/67

Summarizing the results for two different (in situ, DISPATCH) calibration SM datasets, all three vegetation descriptors (NDVI, PR, CO) provide useful information about vegetation effects, which can be efficiently represented by a linear or a non-linear model. Nevertheless, the PR configuration shows slightly better results than the NDVI and CO configurations with smaller estimated uncertainties in the retrieved parameters, and with a better stability against errors and biases in DISPATCH data. Moreover, the consistency of parameter values indicates that DISPATCH data can be used for calibrating the RTM models, despite the errors in the remotely sensed SM that may compensate over relatively long time series. Finally, the parameter values are rather similar for both linear and non-linear RTM, so that, from the calibration point of view, both approaches are still relevant.

3.3. Evaluation of SM Estimates

Each calibrated parameter set is fed into the linear and non-linear RTM and the SM is derived from radar backscatter and vegetation descriptor observations by using the (linear/non-linear) RTM in the inverse mode: Formally, SM for the linear model is expressed as:

$$SM_{Linear} = (\sigma_{VV} - b_{ML} * V - c_{ML}) / a_{ML} \quad (9)$$

SM for a non-linear model is expressed as:

$$SM_{Non-linear} = ((\sigma_{VV} - b_{WC} * V) * e^{d_{WC}V} + (b_{WC} * V) - c_{WC}) / a_{WC} \quad (10)$$

The predicted SM is evaluated using in situ measurements collected over the R3 perimeter and at the Sidi Rahal and Chichaoua sites.

3.3.1. Temporal Analysis

SM is evaluated using two different calibration inputs (1) in situ SM and (2) DISPATCH SM at 100 m. Figure 4 plots predicted versus in situ SM in the case where in situ SM data are used to calibrate the RTM for three different vegetation descriptors (NDVI, PR, CO). For both sites (Chichaoua and Sidi Rahal), PR shows better performance with an R in the range 0.72–0.82 and 0.74–0.80 for linear and non-linear RTM, respectively. Note that the slope (S) and the bias for the linear case are equal to 1 and zero, respectively. It is because the same in situ SM data set is used for the calibration and validation. In general, the SM results are consistent with the previous study about calibration parameters as the PR configuration consistently provides a lower uncertainty in model parameters and more accurate estimates of SM.

Similar to Figure 4, Figure 5 shows the scatter plots between predicted and in situ SM, where DISPATCH SM data at 100 m resolution are used for calibration. When using DISPATCH SM data for calibration, the NDVI configuration shows a better performance for both linear and non-linear RTM models with R in the range 0.76–0.79 and 0.77–0.80 for both sites (Chichaoua and Sidi Rahal). Statistical results are significantly poorer for the CO configuration with an R in the range 0.64–0.68 for Chichaoua and Sidi Rahal, respectively.

Note that the MB in retrieved SM is quite large for Sidi Rahal. Such an MB was not observed when using in situ SM datasets for calibration. The bias is directly attributed to the dry bias in the SMAP disaggregated SM data sets (similar dry bias observed in the accuracy assessment of DISPATCH SM datasets). In general, the statistical results using DISPATCH instead of in situ SM data are degraded, but not in all cases, since with the NDVI configuration (for linear/non-linear RTM and both sites) the correlation is improved when using DISPATCH data as a reference data set. This observation is consistent with the good performance of DISPATCH over the Chichaoua site (see Figure 3). Note that part of the errors obtained in the comparison between the remotely sensed SM product and the localized TDR measurements may be attributed to the (not measured) possible variability of soil moisture within the field. However, given that the agricultural practices (including irrigation) are homogeneous at the field scale, this effect is assumed to be minor compared to other error sources.

3.3.2. Spatio-Temporal Analysis

Since the performance of the CO configuration is significantly weaker than both PR and NDVI configurations in terms of both RTM parameter uncertainties and the accuracy in predicted SM, only the NDVI and PR cases are implemented in the evaluation of the approach over the R3 study area. It is reminded that over R3, the linear and non-linear RTM are run using the parameters estimated as the average of those retrieved over Chichaoua and Sidi Rahal sites. The objective is to assess the robustness of the calibration strategy in space at different times of the season.

Figure 6 shows the scatter plots between predicted and in situ SM over R3 for spatio-temporal analysis, where in situ SM data are used to calibrate the RTM for two different vegetation descriptors (NDVI, PR). Here, the NDVI configuration shows a larger R for DOY 14, 30, and 38 in the range 0.53–0.74 by combining the quite similar result for both linear and non-linear RTM. Instead, the PR configuration shows better performance for DOY 62 and 78 with an R in the range 0.15–0.41 and 0.09–0.37 for linear and non-linear RTM, respectively. Note that the relatively poor performance on DOY 78 may be due to the time difference between SM sampling dates since ground measurements were undertaken on two successive days with one-half of the monitored crop fields on DOY 78 and the other half on the day after.

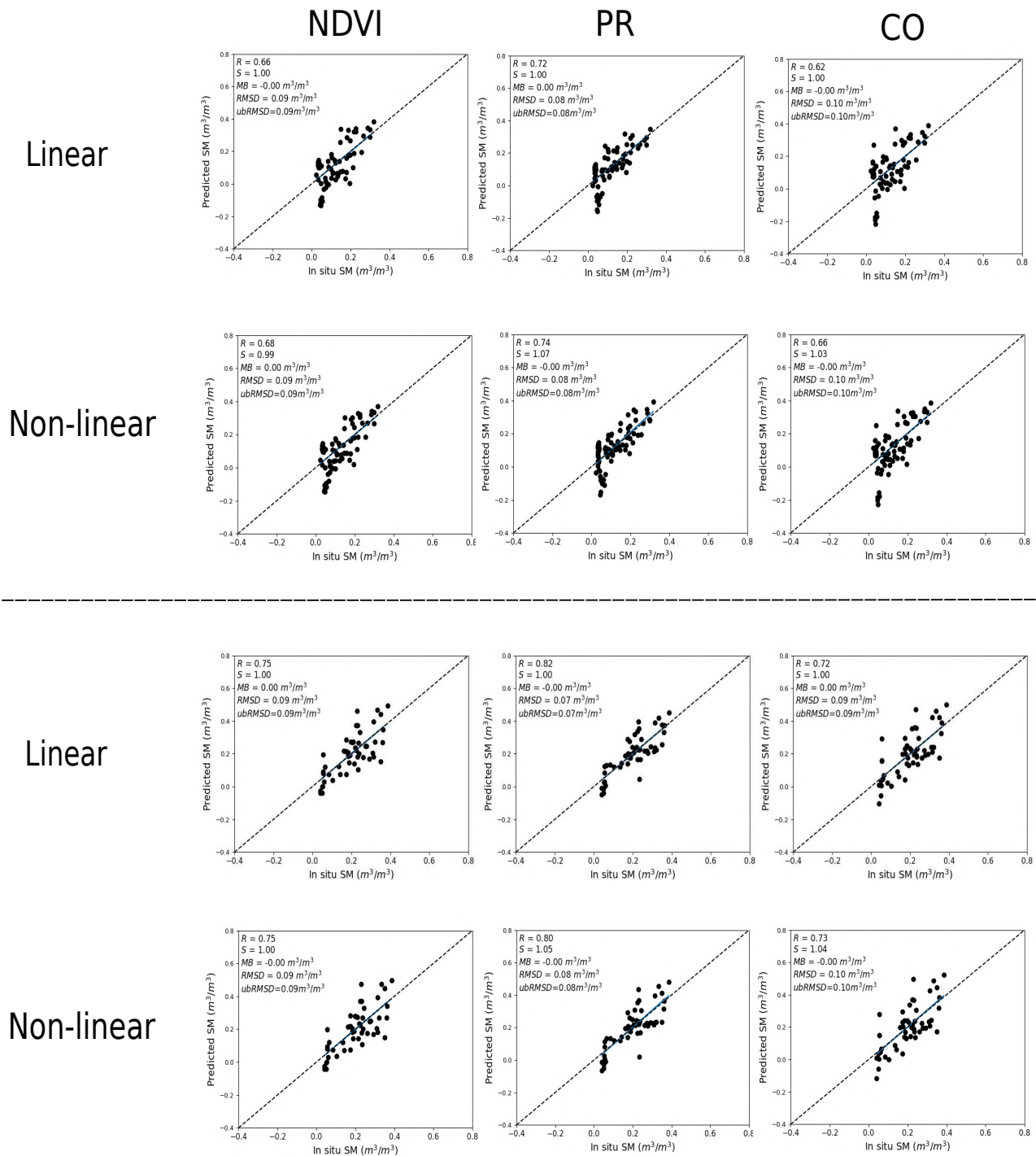


Figure 4. Scatter plot over Chichaoua (top) and Sidi Rahal (bottom) of predicted versus in situ SM, for linear and non-linear RTM with NDVI, PR and CO as vegetation descriptors separately where in situ SM data are used for calibration.

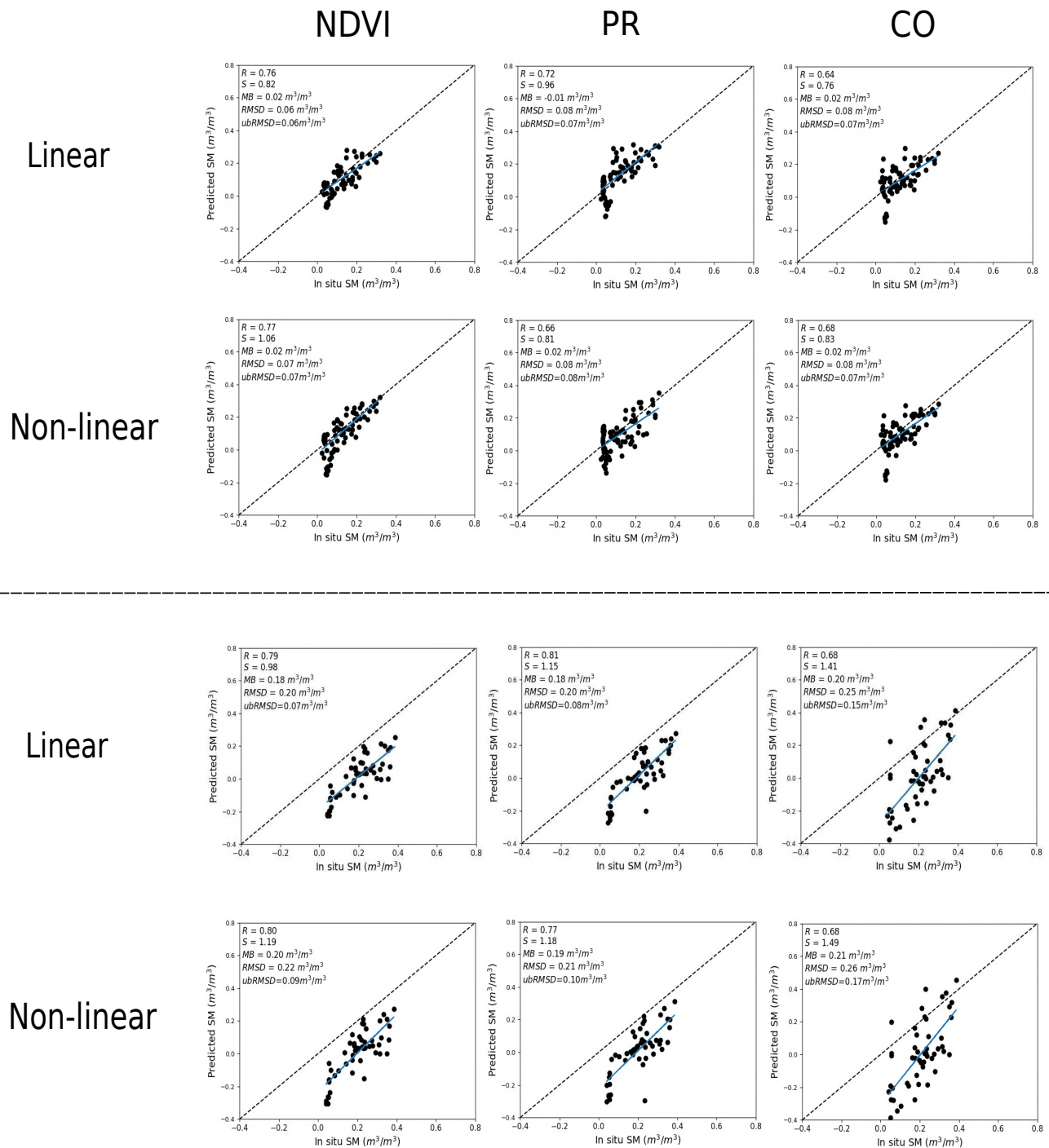


Figure 5. Same as Figure 4 but with DISPATCH SM data used for calibration.

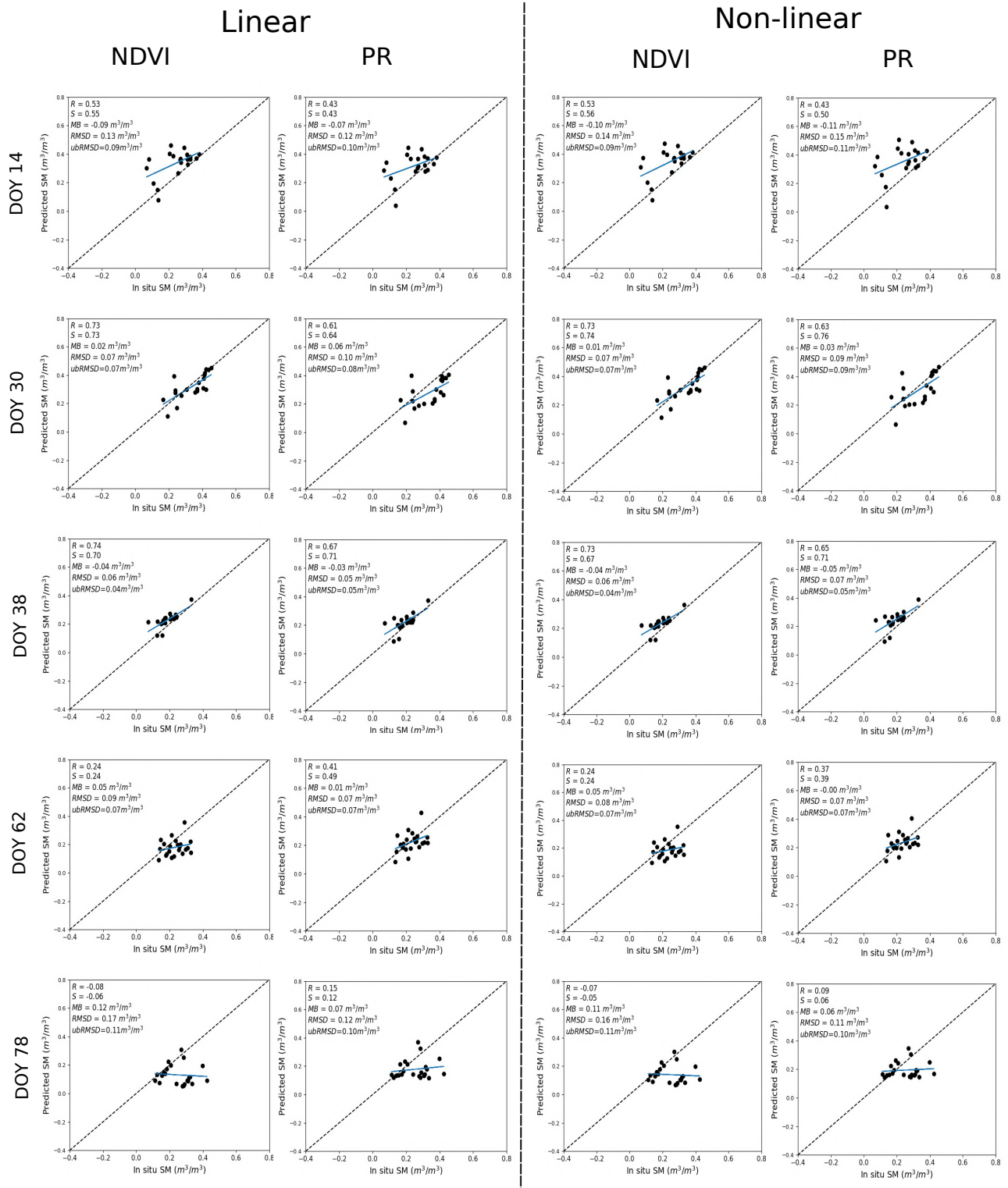


Figure 6. Scatter plot over the R3 irrigated parameter of predicted versus in situ SM, for linear (left) and non-linear (right) RTM with NDVI and PR as a vegetation descriptor separately where in situ SM data are used for calibration.

Figure 7 shows the time series of R and S between the predicted and in situ SM for both linear and non-linear RTM and for NDVI and PR vegetation descriptors separately. The graphs show that both (linear and non-linear) RTM with NDVI and PR vegetation descriptors behave similarly. R and S both increase during the early stages of the vegetation growth and then both decrease when the vegetation is fully developing. As the vegetation growth increases, the R decreases for both models, especially when the vegetation index is above 0.6 in-line with the study of Baghdadi et al. [70]. The time series of Figure 7 also illustrates that the NDVI as a vegetation descriptor shows better performance than the PR configuration during the early stage of the vegetation growth, but when vegetation is fully developed, the PR for both linear/non-linear models shows better performance. This is because NDVI is more sensitive than PR to small variabilities of vegetation cover during early stages of crops while it becomes saturated above a given threshold of biomass/LAI that is lower than the saturation threshold or PR [71,72]. The use of NDVI or PR as a vegetation descriptor is therefore a compromise between precision and accuracy in a range of crop covers.

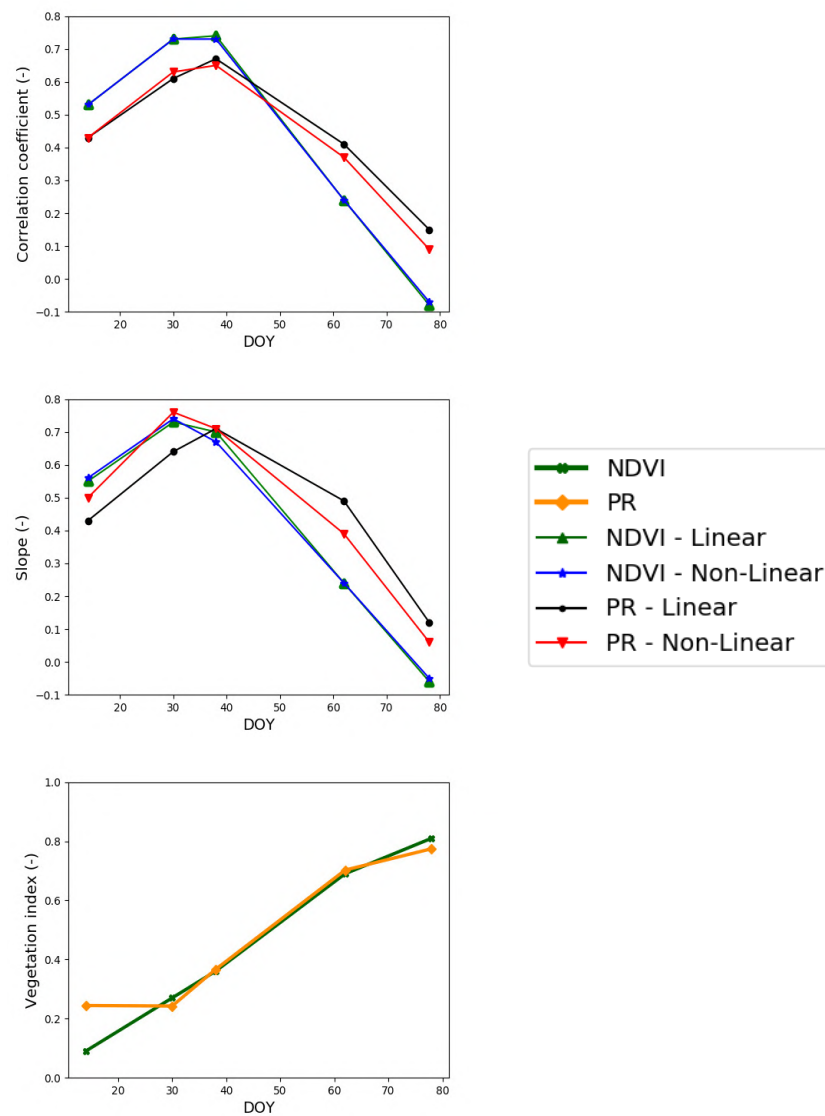


Figure 7. Time series of the correlation coefficient and slope of the linear regression between predicted and in situ SM for both (linear and non-linear) RTM, two vegetation descriptors (NDVI and PR) separately, and where in situ SM datasets are used for the calibration.

Figure 8 shows the scatter plot between predicted and in situ SM where DISPATCH 100 m SM data are used for calibration and in situ SM data for validation. On DOY 14, 30, 38, the NDVI configuration still shows a better performance with an R in the range 0.55–0.74 and 0.55–0.70 for linear and non-linear RTM, respectively. For DOY 62 and 78, the PR configuration better performs for the linear RTM, with an R in the range 0.36–0.50, but a more inadequate performance in non-linear RTM, whereas the NDVI shows an adequate configuration for the non-linear RTM, with an R in the range 0.20–0.41. The statistical results are consistent with the results obtained by using the in situ SM datasets for calibration, but with a dry bias in predicted SM associated with the dry bias in DISPATCH data over the Sidi Rahal site.

Table 3 reports the mean (average of all dates) statistical metrics in terms of R, S, MB, RMSD, and ubRMSD between predicted and in situ SM for both (linear and non-linear) RTM with their vegetation descriptors (NDVI, PR) and for both calibration strategies (using in situ and DISPATCH SM data separately for calibration). The overall results confirm the finding that the use of NDVI or PR as a vegetation descriptor and a linear or non-linear RTM is a trade-off between precision (as described by R) and accuracy (as described by S) all along the agricultural season. Based on our data set, the linear RTM using the PR as a vegetation descriptor offers a relatively good compromise in terms of robustness all throughout the season and simplicity with only three parameters to estimate.

Table 3. Mean statistical results over 22 parcels of R3 irrigated sites in terms of correlation coefficient (R), slope of the linear regression (S), mean bias (MB), RMSD, and ubRMSD between predicted and in situ SM, for linear and non-linear RTM with NDVI and PR as a vegetation descriptor and where in situ (left) and DISPATCH (right) SM datasets are used for calibration separately.

Calibration		In Situ SM Datasets					DISPATCH SM Datasets				
Model		R (-)	Slope (-)	MB (m ³ /m ³)	RMSD (m ³ /m ³)	ubRMSD (m ³ /m ³)	R (-)	Slope (-)	Absolute MB (m ³ /m ³)	RMSD (m ³ /m ³)	ubRMSD (m ³ /m ³)
Linear	NDVI	0.43	0.43	0.01	0.10	0.08	0.54	0.42	0.13	0.15	0.07
	PR	0.45	0.48	0.01	0.10	0.08	0.47	0.53	0.10	0.13	0.08
Non-linear	NDVI	0.43	0.43	0.01	0.10	0.08	0.51	0.50	0.11	0.14	0.07
	PR	0.43	0.48	0.01	0.10	0.08	0.33	0.40	0.10	0.14	0.09

Note that the in situ-based calibration shows better performance than the DISPATCH-based calibration. The point is that in situ data are in general extremely sparse and often simply unavailable so that such calibration cannot be undertaken continuously in space over a range of vegetation types and soil textures.

3.3.3. Gain in Accuracy at the Fine Scale Compared to SMAP

The proposed calibration-disaggregation coupling scheme applies the downscaling algorithm DISPATCH twice, uses as input a number of ancillary data sets including MODIS and Landsat data, and undertakes a calibration of a C-band radiative transfer model using Sentinel-1 backscatter data. All these successive steps are likely to introduce errors that may accumulate in cascade from the SMAP (40 km) resolution to the targeted 100 m resolution. This is all the more critical as DISPATCH introduces uncertainties through the (uncertain) downscaling relationship and through the errors in its input data. Nevertheless, downscaling algorithms especially aim to improve the spatial representativeness of SM estimates, meaning they provide fine scale information that is expected to improve the accuracy of the disaggregated data at the targeted resolution. In fact, there exists a trade-off in data disaggregation between the added uncertainty (which decreases data accuracy at the fine scale) and the improved spatial representativeness (which increases data accuracy at the fine scale). In our case, the uncertainty assessment is made more complex due to

the additional calibration step, as the disaggregated data set at 100 m resolution is not the final remote sensing product. It is only used to calibrate a Sentinel-1-based SM retrieval algorithm. Therefore, the random errors in the 100 m resolution disaggregated SM data are expected to have (and this assumption is verified in this study) a relatively small impact on the final Sentinel-1-based SM product.

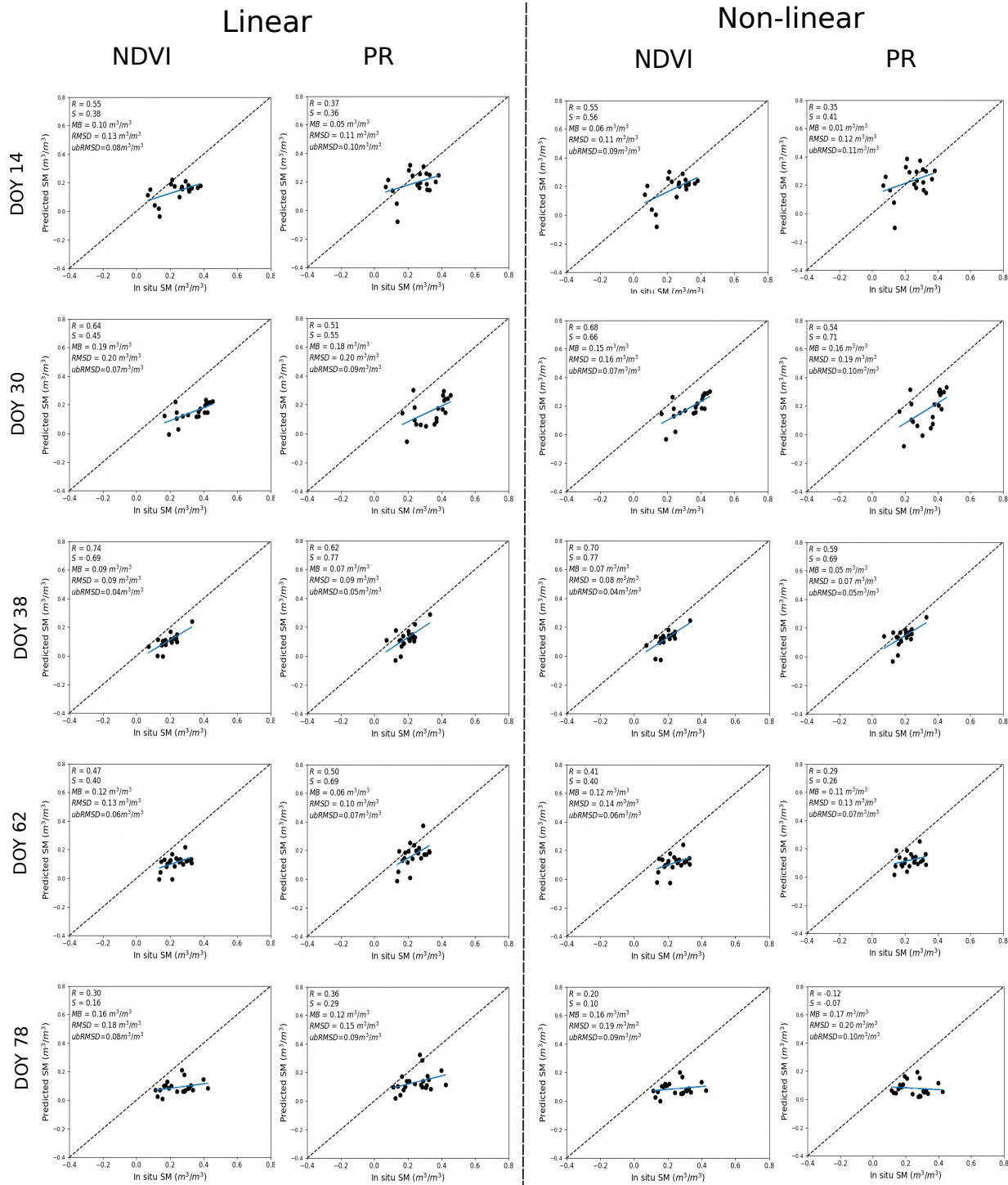


Figure 8. Same as Figure 6 but with DISPATCH SM data used for calibration.

One key issue is hence evaluating the accuracy of the 100 m resolution SM predicted by the calibration-disaggregation coupling scheme, compared to the original 40 km resolution SMAP SM estimate. A solution is to simply compare the performance of both products at the fine scale using localized in situ measurements [55]. Figure 9 compares the overall performance at the field scale of SMAP (original data without disaggregation and without synergy with Sentinel-1), the 1 km DISPATCH SM product and the calibration-disaggregation coupling scheme over Sidi Rahal and Chichaoua sites separately. In each case, the comparison between remotely sensed SM and in situ measurements was made on a point-by-point basis by extracting the pixel overlying the site. For clarity, in all cases, the remaining bias was removed and SM values below the residual SM (estimated as $0.02 \text{ m}^3/\text{m}^3$) were set to the residual SM. It is visible that the scatter of remotely sensed SM is generally larger for the calibration-disaggregation coupling scheme, as a result of the uncertainty added by the disaggregation and calibration steps. The point is that, and it is the main rationale for developing such a multi-sensor/multi-resolution approach, the spatial representativeness of the calibrated-disaggregated SM at the field scale is clearly superior to that of the original SMAP SM. In particular, the predicted range of SM values is much closer to that of in situ measurements in the calibration-disaggregation case, as supported by a slope of the linear regression between satellite and in situ SM significantly closer to 1. Note that the slope of the linear regression is a very relevant metric for evaluating the spatial representativeness of remote sensing data at a range of spatial scales because it combines both the correlation and the spatial variability indicators [55]. In all cases (both sites and linear/non-linear models), the calibrated-disaggregated outperforms the original SMAP SM estimates in terms of correlation coefficient, slope of the linear regression and unbiased root mean square error between satellite and in situ SM. Consequently, the added uncertainty due to the disaggregation and calibration steps is relatively small and still acceptable at 100 m resolution compared to the huge SM spatial variability over our study area, which is not represented by SMAP data.

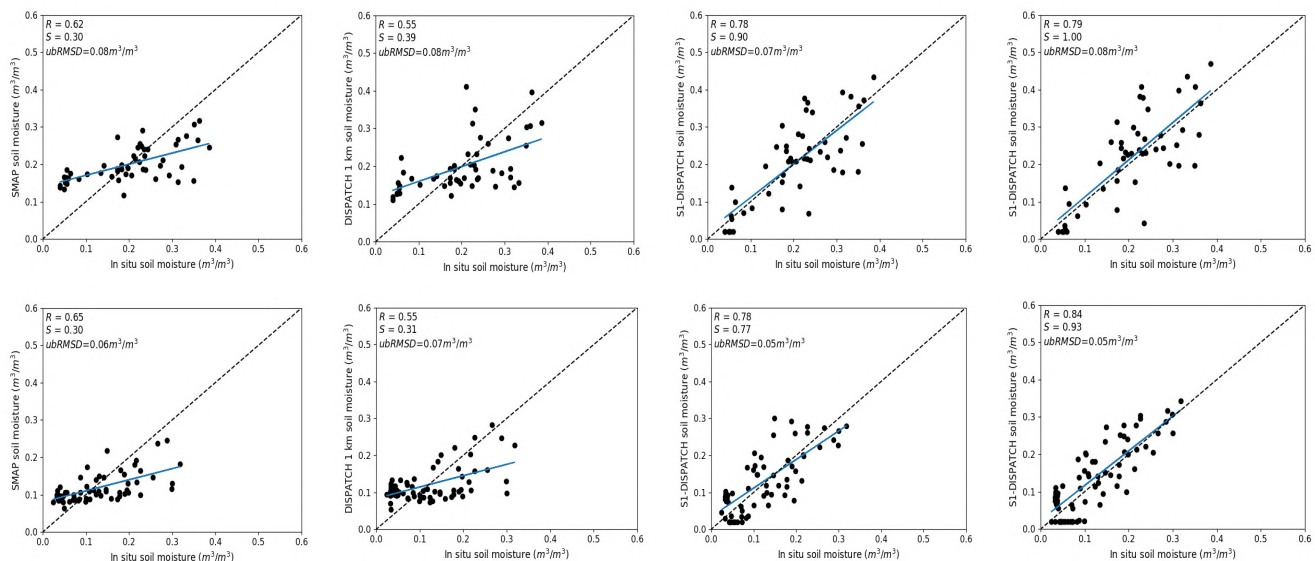


Figure 9. Scatter plots (from left to right) of the original 40 km resolution SMAP SM, the 1 km resolution DISPATCH SM, the 100 m resolution calibrated-disaggregated SM for the linear model and the 100 m resolution calibrated-disaggregated SM for the non-linear model versus in situ measurements, for Sidi Rahal (**top**) and Chichaoua (**bottom**) sites separately.

4. Conclusions

An original approach is developed to provide SM products at a high spatio-temporal resolution based on a synergy between multi-resolution passive microwave, active microwave, and optical/thermal data. It is a three-step procedure in which (1) the 36 km reso-

lution SMAP SM is disaggregated by DISPATCH at 100 m resolution using MODIS/Landsat optical/thermal data on clear sky days, (2) the 100 m resolution disaggregated SM data set is used to calibrate a radar-based SM retrieval model and (3) the so-calibrated radar model is run at field scale on each Sentinel-1 overpass. The calibration-disaggregation coupling approach is tested using two radar models (an empirical linear regression model and a non-linear semi-empirical formulation derived from the water cloud model) and three different vegetation descriptors (NDVI, PR, and CO). The retrieved SM values are finally evaluated over three sites (Chichaoua, Sidi Rahal and R3 perimeter) in central Morocco using the in situ SM measurements collected concurrently with Sentinel-1 data. A calibration data set is derived for Chichaoua and Sidi Rahal sites separately, where data were collected for more than one year, while the R3 data set is kept for the evaluation of the retrieved SM using a fully independent data set.

An evaluation of the retrieved parameters of the linear and non-linear RTM indicates that all three vegetation descriptors (NDVI, PR, CO) provide useful information about the vegetation effects on the radar signal, which can be efficiently represented in terms of model calibration, by a linear or a non-linear RTM. However, the PR configuration shows slightly better results than the NDVI and CO configurations with smaller estimated uncertainties in the retrieved parameters, and with a better stability against errors and biases in DISPATCH SM data.

In terms of predicted SM estimates, the temporal analysis (over Chichaoua and Sidi Rahal sites) indicates that the PR configuration shows better performance when in situ SM datasets are used for calibration. In contrast, the NDVI configuration shows slightly better performance when DISPATCH SM datasets are used for calibration. The spatio-temporal analysis (over R3 irrigated site) indicates that the NDVI configuration performs better (when calibration is undertaken using in situ or DISPATCH SM datasets), especially during the early stages of the agricultural season. However, the PR configuration still provides a more robust vegetation descriptor all throughout the agricultural season, consistent with the lower uncertainty in modeled parameters. In terms of linearity of the RTM, results are found very similar for both linear and non-linear formulations, so that the added complexity of the non-linear representation is not clearly justified by our data set.

The new calibration/disaggregation coupling scheme presented here does not require in situ data and has thus a strong potential for providing good quality and frequent SM data at a field scale over large areas for agricultural purposes. Despite the satisfying results obtained over the study sites in this paper, the 100 m resolution pixel may be relatively low compared to the typical size of crop fields in many regions. Two avenues are foreseen to help increase this resolution. The first avenue would be to consider the higher spatial resolution of Sentinel-1 data: the RTM parameters obtained at 100 m resolution from the synergy between DISPATCH and Sentinel-1 data, as presented in this paper, could be used at 20 m resolution to invert SM from Sentinel-1 at 20 m resolution. The second avenue would be to prepare for the near future advent of thermal infrared sensors with improved capacities in terms of spatial and temporal resolutions such as the TRISHNA mission [73]. In addition, a characterization of the error sources coming from the original SMAP data and from the DISPATCH methodology is necessary to assess their impact in the calibration procedure over a wider range of conditions. It is further reminded that both DISPATCH and Sentinel-1 data have intrinsic limitations, including the impact of cloud coverage (DISPATCH) and the lack of SM sensitivity over densely vegetated pixels (both DISPATCH and Sentinel-1). Nonetheless, further validation is needed to cover various incidence angles of Sentinel-1, crop types, and surface conditions in the future. In addition, a characterization of the error sources coming from the original SMAP data and from the DISPATCH methodology is necessary to assess their impact in the calibration procedure over a wider range of conditions. Furthermore, attention is drawn to one assumption underlying the temporal calibration strategy of the radar model: parameters were assumed to be constant in our study. The point is that soil roughness and vegetation parameters are likely to vary in time as a result of agricultural practices (notably, plowing and crop

rotation). Therefore, future studies should investigate the dynamical retrieval of model parameters over periods long enough to allow for an efficient calibration using a sufficient number of DISPATCH SM estimates concurrently with Sentinel-1 overpasses and, at the same time, short enough to represent possible changes in model parameters.

Author Contributions: Implementation, validation, investigation, visualization, data curation and writing original draft of the paper, N.O. (Nitu Ojha); supervision, reviewing and editing, O.M.; in situ soil moisture and Sentinel-1 data, A.A., N.O. (Nadia Ouadi); Landsat optical/thermal satellite data, V.R.; reviewing and editing, L.J., S.E.-R., M.J.E. All authors have read and agreed to the published version of the manuscript.

Funding: The study was supported by the Horizon 2020 ACCWA project (grant agreement # 823965) in the context of Marie Skłodowska-Curie research and the innovation staff exchange (RISE) program and by the IDEWA project (ANR-19-P026-003) of the Partnership for research and innovation in the Mediterranean area (PRIMA) program.

Institutional Review Board Statement: Not applicable.

Informed Consent Statement: Not applicable.

Data Availability Statement: Not applicable.

Acknowledgments: The author acknowledges NASA for freely available SMAP, MODIS, and Landsat satellite data. The author also likes to thank the THEIA platform for the availability of NDVI products from Sentinel-2 surface reflectance.

Conflicts of Interest: The authors declare no conflict of interest.

References

1. Robinson, D.; Campbell, C.; Hopmans, J.; Hornbuckle, B.K.; Jones, S.B.; Knight, R.; Ogden, F.; Selker, J.; Wendroth, O. Soil moisture measurement for ecological and hydrological watershed-scale observatories: A review. *Vadose Zone J.* **2008**, *7*, 358–389. [[CrossRef](#)]
2. Hanson, B.; Orloff, S.; Peters, D. Monitoring soil moisture helps refine irrigation management. *Calif. Agric.* **2000**, *54*, 38–42. [[CrossRef](#)]
3. Brocca, L.; Ciabatta, L.; Massari, C.; Camici, S.; Tarpanelli, A. Soil moisture for hydrological applications: Open questions and new opportunities. *Water* **2017**, *9*, 140. [[CrossRef](#)]
4. Wang, J.R.; O'Neill, P.E.; Jackson, T.J.; Engman, E.T. Multifrequency measurements of the effects of soil moisture, soil texture, and surface roughness. *IEEE Trans. Geosci. Remote Sens.* **1983**, *GE-21*, 44–51. [[CrossRef](#)]
5. Thompson, R.; Gallardo, M.; Valdez, L.; Fernández, M. Using plant water status to define threshold values for irrigation management of vegetable crops using soil moisture sensors. *Agric. Water Manag.* **2007**, *88*, 147–158. [[CrossRef](#)]
6. Pardossi, A.; Incrocci, L.; Incrocci, G.; Malorgio, F.; Battista, P.; Bacci, L.; Rapi, B.; Marzalletti, P.; Hemming, J.; Balendonck, J. Root zone sensors for irrigation management in intensive agriculture. *Sensors* **2009**, *9*, 2809–2835. [[CrossRef](#)] [[PubMed](#)]
7. Kerr, Y.H.; Waldteufel, P.; Richaume, P.; Wigneron, J.P.; Ferrazzoli, P.; Mahmoodi, A.; Al Bitar, A.; Cabot, F.; Gruhier, C.; Juglea, S.E.; et al. The SMOS soil moisture retrieval algorithm. *IEEE Trans. Geosci. Remote Sens.* **2012**, *50*, 1384–1403. [[CrossRef](#)]
8. Entekhabi, D.; Njoku, E.G.; O'Neill, P.E.; Kellogg, K.H.; Crow, W.T.; Edelstein, W.N.; Entin, J.K.; Goodman, S.D.; Jackson, T.J.; Johnson, J.; et al. The soil moisture active passive (SMAP) mission. *Proc. IEEE* **2010**, *98*, 704–716. [[CrossRef](#)]
9. Wigneron, J.P.; Jackson, T.; O'Neill, P.; De Lannoy, G.; De Rosnay, P.; Walker, J.; Ferrazzoli, P.; Mironov, V.; Bircher, S.; Grant, J.; et al. Modelling the passive microwave signature from land surfaces: A review of recent results and application to the L-band SMOS & SMAP soil moisture retrieval algorithms. *Remote Sens. Environ.* **2017**, *192*, 238–262.
10. Dari, J.; Quintana-Seguí, P.; Escorihuela, M.J.; Stefan, V.; Brocca, L.; Morbidelli, R. Detecting and mapping irrigated areas in a Mediterranean environment by using remote sensing soil moisture and a land surface model. *J. Hydrol.* **2021**, *596*, 126129. [[CrossRef](#)]
11. Lievens, H.; Tomer, S.K.; Al Bitar, A.; De Lannoy, G.J.; Drusch, M.; Dumedah, G.; Franssen, H.J.H.; Kerr, Y.H.; Martens, B.; Pan, M.; et al. SMOS soil moisture assimilation for improved hydrologic simulation in the Murray Darling Basin, Australia. *Remote Sens. Environ.* **2015**, *168*, 146–162. [[CrossRef](#)]
12. Wanders, N.; Bierkens, M.F.; de Jong, S.M.; de Roo, A.; Karssenbergh, D. The benefits of using remotely sensed soil moisture in parameter identification of large-scale hydrological models. *Water Resour. Res.* **2014**, *50*, 6874–6891. [[CrossRef](#)]
13. Peng, J.; Niesel, J.; Loew, A. Evaluation of soil moisture downscaling using a simple thermal-based proxy—The REMEDHUS network (Spain) example. *Hydrol. Earth Syst. Sci.* **2015**, *19*, 4765–4782. [[CrossRef](#)]
14. Sabaghy, S.; Walker, J.P.; Renzullo, L.J.; Akbar, R.; Chan, S.; Chaubell, J.; Das, N.; Dunbar, R.S.; Entekhabi, D.; Gevaert, A.; et al. Comprehensive analysis of alternative downscaled soil moisture products. *Remote Sens. Environ.* **2020**, *239*, 111586. [[CrossRef](#)]

Chapter 7

High-resolution soil moisture data at the daily scale using dynamic surface model

Contents

7.1	Introduction	152
7.2	Method	153
7.2.1	Force restore model	153
7.2.2	Assimilation techniques	153
7.3	Results	155
7.4	Conclusion	158

7.1 Introduction

Remote sensing data provide synoptic, spatially integrated, and temporally consistent information about the surface state. However, most of the Earth observation satellites use polar orbits so that the remotely sensed data have a repeat cycle of one day for medium resolution sensors, but usually one week or more for high-resolution sensors. For instance, the *DISPATCH*_{100m} algorithm presented in **Chapter 5** runs with Landsat optical/thermal data, with a frequency of one image every 16 days when using Landsat-8, and one image every eight days when combining both Landsat-7 and Landsat-8. Another example is given by the radar-based soil moisture (SM) retrieval approaches, with a potential frequency of SM data of 6 days by combining ascending and descending orbits and different incidence angles. The revisit time of about one week is still relatively long for quick processes like evaporation, and for related applications like irrigation monitoring and scheduling, for which data available every day would be most useful.

To overcome the frequency limitation of currently available remote sensing data, the assimilation of data in land surface models, which simulates the dynamics of flux and state variables like SM, is a physically-based, renowned and widely-used tool.

Data assimilation combines observation (in situ or satellite) information and a dynamic model (represented in a mathematical equation or land surface model) to provide the information with time continuously. SM is an essential variable in hydrological models. Hence hydrological models are generally used to integrate SM data within the modeled hydrological processes. However, hydrological processes are highly variable in 3 dimensions, so a complete assessment of all the variables in the hydrological model is challenging. For this reason, most of the studies focus on simpler 1D or 2D SM data assimilation.

The disaggregated SM product at 1 km resolution is sensitive to irrigation but with low spatial-temporal resolution. In contrast, the hydrological model provides SM on a daily temporal basis but is insensitive to irrigation. In this context, downscaled SM product at 1 km resolution is used in the hydrological model to provide SM on a daily temporal basis (Malbeteau et al., 2018) that is sensitive to irrigation. But the limitation still exists with a low spatial resolution for the use of irrigation purposes. The hydrological model used similar to (Malbeteau et al., 2018) to provide SM at the field scale to provide SM at a high spatial-temporal resolution.

This chapter presents an original case study in which the assimilation of remotely sensed data is undertaken over an irrigated crop where irrigation is unknown. The science question we propose to address is : Can a high-resolution SM data set be assimilated to compensate for errors in the model associated with a missing forcing? We set the assimilation configuration so that precipitation is included as input to the model but not irrigation. This issue is particularly relevant on an operational point of view since the water balance of irrigated crops is essentially dependent on irrigation, and this man-made flux is commonly (even over modern irrigation areas) unknown at fine space-time scales, whereas meteorological data are usually available nearby.

The assimilation approach is tested over two experimental fields named Foradada and Agramunt, located in the Urgell irrigation district in Spain. The Foradada and Agramunt field is 20 ha and 20.5 ha, and they are irrigated under the Segarra Garrigues system, where drip and sprinkler irrigation is used. The unique property of this area is that dryland areas surround it. So, during winter, the area is similar to the surrounding area, but when the site is irrigated in summer, the surrounding area remains dry. The irrigated area is not visible from the 1 km resolution

DISPATCH SM product (Fontanet et al., 2018). The area is so small that the 1 km resolution is too coarse and cannot differentiate between the irrigated and dry land areas. To assess the capability of the *DISPATCH*_{100m} SM dataset and to detect field-scale irrigation through the disaggregation-assimilation coupling scheme, the assimilation results are compared to the case when using the 1 km resolution DISPATCH SM as input to the same assimilation scheme still implemented at the field scale (either Foradada or Agramunt site).

7.2 Method

The model and assimilation scheme used are similar to the study of Malbeteau et al. (2018). However, the application context is quite different from that previous study. Indeed, Malbeteau et al. (2018) assimilated the 1 km resolution DISPATCH SM in a model implemented at the same resolution. Therefore, neither the observation nor the model grid size was able to resolve the field size so that field-scale irrigation events could not be detected. Instead, the irrigation could be somehow and indirectly quantified by the assimilation update of the root zone SM at the seasonal time scale. The material used to develop the assimilation scheme is presented in this section.

7.2.1 Force restore model

Deardorff (1977) established the force and restore model employed in this investigation to estimate surface SM. The model used in this study preserves the physics of the main interactions between the soil, vegetation, and atmosphere. In addition, the force and restore formulation of the soil component requires few input parameters. Therefore, it is a good compromise between the physical representation and its complexity.

In the force and restore model, the relation between SM, evaporation, and precipitation can be expressed by the following expression:

$$\frac{\delta\theta}{\delta t} = \frac{C_1}{\rho_w * d}(P - E) - \frac{C_2}{\tau}(\theta_1 - \theta_{eq}) \quad (7.1)$$

where, E is the evaporation of the soil surface, P is the precipitation, ρ_w is the density of the water, τ is the time constant, d is the normalization depth of 10 cm, C_1 and C_2 are the force and restore coefficients; θ_1 is the surface SM, and θ_{eq} is the SM at the equilibrium between the gravity and the capillary forces. The first term on the right hand side of the equation represents the forcing terms, where the coefficient C_1 drives the moisture exchange between the surface and the atmosphere. The other part of the equation is termed restore, representing the vertical diffusions between the root zone SM and surface layers. The parameter C_2 controls it, and it quantifies the rate at which SM at the root zone and external layer are restored to the SM at equilibrium. The model is characterized into the surface layer and the root zone layer. In this model, the surface SM layer is simulated, and the root zone SM layer is taken as a buffer variable to normalize the bias between the *DISPATCH*_{100m} SM and force-restore prediction.

7.2.2 Assimilation techniques

Data assimilation is a mathematical field that combines a numerical model (theory) with observations efficiently. This chapter uses data assimilation to integrate the data from the land surface

model and the observation (field or remote sensing satellite). Both model and observation are imperfect and, when used together, provide a more accurate estimation of products than when used individually. On the one hand, the model gives SM information on a geographic and temporal basis, with an inaccuracy, at the model resolution. On the other hand, remote sensing data offers near-surface SM information at a specific time. Since near-surface SM is highly variable in time and space, it isn't easy to encounter such high variability with either of them. So, the simulated SM from the model is combined with remote sensing observation to improve the accuracy and the frequency of the estimated SM.

Since we have a dynamic model, we need to find the best estimate for SM from the observation such that the error between the model and the observation is reduced. Based on this, two approaches are suggested 1) direct or sequential techniques 2) dynamic or variational techniques and are discussed in the following subsections.

Sequential assimilation

Sequential assimilation is primarily used in real-time analysis. It analyses the information based on the knowledge of the initial states and combines the model's data when the observation (i.e., satellite data) information is present and estimates a new value for the assimilation model. Since estimations are done for the model using current observation data, the assimilated model outputs real-time information. The estimated value is updated each time the observation information and the model information are present. Thus, the process of assimilation reduces the error between the observation and the model. The most commonly used sequential method is optimal interpolation and Kalman filter.

Kalman filter is a repetitive process that uses a set of mathematical equations to estimate the accurate values by considering a series of values from the model and observations values that contain random uncertainty. Kalman filter iteratively analyse the current estimate from the previous analysed model value and the current observation value (satellite or in situ) by giving higher weightage/certainty to the observation values.

In this study, we used a simplified one-dimensional Kalman filter expressed as:

$$X^a = X^b + K(y - X^b) \quad (7.2)$$

where X^a is the vector to be analyzed, X^b is the background state or model, y is the observation vector and K is the kalman gain.

This approach can update the estimates daily based on data availability and minimizes the error between the model and the observation. Moreover, it is a straightforward and computationally efficient algorithm that can be implemented easily in an assimilation system.

Variational assimilation

Variational assimilation is similar to an ensemble Kalman filter to analyze the information when the observation and model data are present within a time window. The variational assimilation technique solves the analytical problem by optimizing a specific criterion (minimizing so-called cost-function). In variational assimilation, a cost function reduces the error between the observed

and the model for accurate prediction of the assimilated data. In a variational method, the optimal weight (J) is derived by minimizing cost function between the model and the observation and is expressed as:

$$J(X) = 1/2(X^a - X^b)^T B^{-1}(X^a - X^b) + 1/2(y - H(X^a))^T R^{-1}(y - H(X^a)) \quad (7.3)$$

where B and R are the covariance matrices of the background and the observation, and H is the observation operator that transports the model or the background state into the observation space. A continuous line is drawn to analyze the model state variable based on the observation and model information. The assimilated observation is updated based on each observation of the model and observation.

2D(space and time)variational assimilation was first used by Mahfouf (1991) to analyze the estimated output from the 2m observation of SM and from a model. Later on, the 2D variational assimilation is simplified by Balsamo et al. (2004) to estimate the SM from the model and the observation by the linear minimization of the optimal weight from equation 7.3 and by assuming $\delta J(x)=0$. The H matrix is evaluated using the finite difference approach, and the analyzed state gives a final expression as:

$$X^a = X^b + K(y - X^b) \quad (7.4)$$

where

$$K = (BH^T)(HBH^T + R)^{-1} \quad (7.5)$$

and H is calculated by the ratio of observation error at time t and t-1.

A mixed sequential-variational assimilation

Herein, the 2D variational method is used to analyze the root zone SM from the surface. In fact, the root zone SM is used as a buffer variable to absorb the meteorological error (and the forcing error associated with the missing irrigation) and freely adjust the model's surface prediction. Variational assimilation is hence used to fit with the slow change in the root zone estimation, but it will not be helpful for the surface SM for the rapid change in the SM estimation. Instead, the sequential approach updates the surface SM for each interval when the satellite observation data is present. The sequential assimilation method can update the rapid change in the irrigation; the data present from disaggregated SM using DISPATCH algorithm, not in the surface model. So, the chosen assimilation technique is designed to take advantage of both assimilation methods (2D variational and sequential) and provides SM daily without losing the information about the irrigation, which is not present in the model.

7.3 Results

As a first assessment of SM estimates, the DISPATCH 1 km and 100 m SM products are separately evaluated with the in situ SM measurements collected over Foradada and Agramunt sites (shown in Figure 7.1).

We see that the number of observations available is much more significant for DISPATCH 1 km than for DISPATCH 100 m resolution data set, consistent with the observation frequency much higher for MODIS than for Landsat. An exciting feature is observed that the 100 m resolution

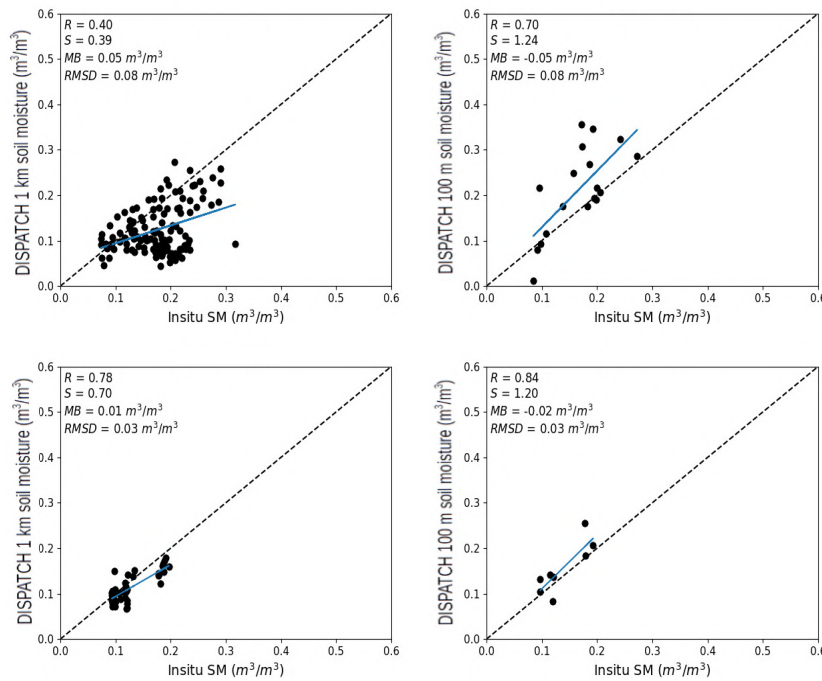


Figure 7.1: Scatter plot between DISPATCH and in situ SM for the 1 km (left) and 100 m (right) resolution satellite data and for Foradada (top) and Agramunt (bottom) sites.

DISPATCH SM shows better performance over the irrigated area with a correlation of 0.70 (0.84) compared to 0.40 (0.78) for the 1 km resolution DISPATCH SM case for Foradada (Agramunt), respectively. It is hypothesized that the 100 m resolution of the SM product is enough to catch the spatial variability of the agricultural land at the field scale. In contrast, the 1 km resolution SM product is too coarse to discriminate the wetter irrigated field from the dryland surrounding it.

Note that in the sprinkler irrigated field (Foradada), the 100 m resolution SM product is closer to in situ SM, whereas the 1 km resolution SM product is very far from in situ SM during the irrigation period. But in the drip-irrigated field (Agramunt), both 1 km and 100 m resolution DISPATCH SM products are close to in situ SM, as if the drip irrigation was not detectable from the remotely sensed near-surface SM data.

The assimilation approach is used to estimate SM at a daily time scale from 1 km and 100 m resolution DISPATCH SM products separately. The performance of the assimilation approach is assessed by comparing the time series of in situ SM, open-loop SM (the SM predicted by the land surface model without assimilation), and the re-analyzed SM for 1 km resolution and 100 m resolution DISPATCH SM products separately (shown in Figure 7.2). It is observed that the model predictions are closer to the satellite SM after the assimilation so that the re-analyzed SM is much closer to the in situ SM in the 100 m resolution DISPATCH SM case. Assimilation improves both 1 km and 100 m SM accuracy from the disaggregated SM product in both cases. In sprinkler irrigated areas, the predicted 100 m SM product is closer to in situ SM, whereas the predicted 1 km SM is far from in situ. But in drip-irrigated areas, both predicted 1 km and 100 m SM are closer to in situ SM. It is also worth mentioning that the assimilation reciprocally improves both remote sensing SM products at observation dates (statistical metrics are

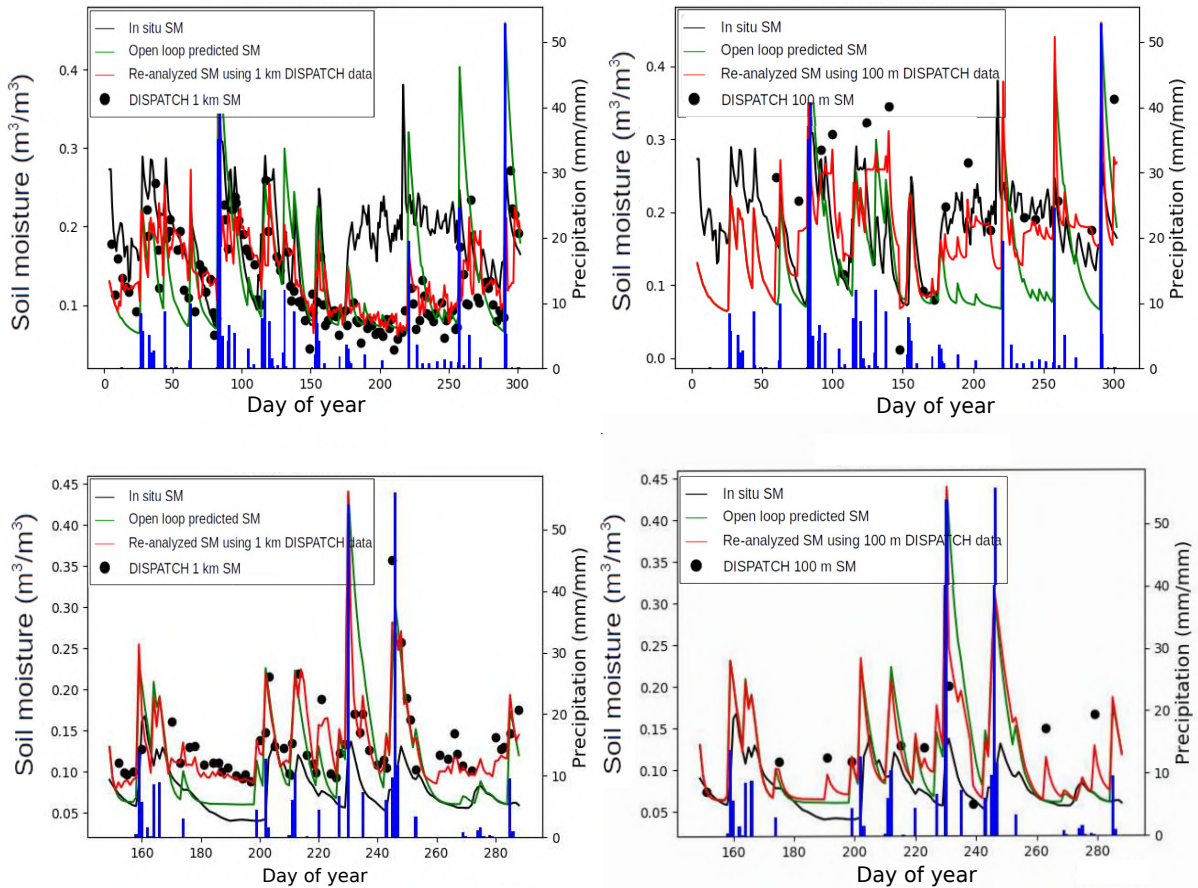


Figure 7.2: Time series of in situ SM, open loop predicted SM, re-analyzed SM using 1 km DISPATCH data and re-analyzed SM using 100 m DISPATCH data for Foradada (top) and Agramunt (bottom) sites.

systematically improved after assimilation). However, assimilation results are not significantly improved for the 1 km resolution DISPATCH product case. It is suggested that the disparity between the data resolution and the model grid size makes the assimilation scheme sub-optimal. This example illustrates very well the usefulness of disaggregation by making the readily available data compatible with the application scale.

A quantitative evaluation of the re-analyzed SM is provided in Figure 7.3. It is observed that the re-analyzed 100 m resolution SM product reduces the bias and RMSD as compared to the 1 km resolution re-analyzed SM product and shows an increase in performance with a correlation of 0.72 and 0.88 for Foradada and Agramunt, respectively.

Overall, results show that both 100 m resolution DISPATCH product and the re-analyzed SM after the assimilation of the 100 m resolution DISPATCH SM are sensitive to irrigation events and capture the spatial variability of the agricultural area at the field scale. Moreover, the 100 m resolution SM re-analyzed by the model is available on a daily temporal scale with an even improved performance and accuracy compared to DISPATCH product alone.

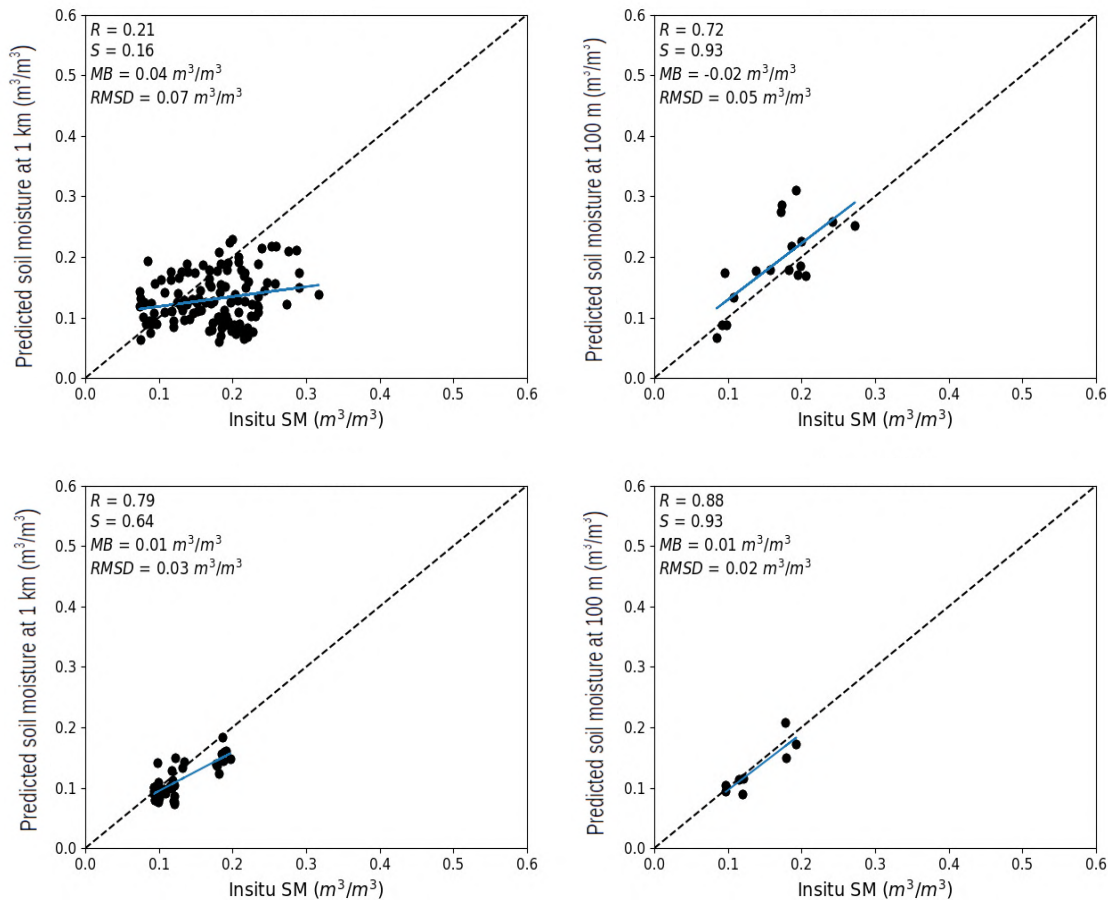


Figure 7.3: Scatter plot between re-analyzed and in situ SM for the assimilation of 1 km (left) and 100 m (right) resolution DISPATCH products and for Foradada (top) and Agramunt (bottom) sites.

7.4 Conclusion

Data assimilation combines observations and a dynamic land surface to provide the information continuously with time. This study set the assimilation configuration so that precipitation is included as input to the model but not irrigation, consistent with the general lack of knowledge about irrigation timing and amount at the fine space-time scales. The idea is to assimilate the 100 m resolution DISPATCH SM in a soil model and assess the disaggregation-assimilation scheme's capability to detect irrigation events. The approach is tested over two irrigated crop fields, in Foradada and Agramunt, irrigated by sprinkler and drip, respectively. The re-analyzed SM is evaluated against in situ SM measurements. Results are also compared with the assimilation of the 1 km resolution DISPATCH SM to assess the usefulness of the disaggregation to 100 m.

The approach is tested over two semi-arid irrigated areas of Spain, Fordada, and Agramunt. At first, time-series analysis is done for in situ SM, the model SM product, and the predicted SM products with 1 km and 100m DISPATCH SM products are analyzed separately.

The assimilation of DISPATCH SM products improves the SM's dynamics compared to both the SM observations and the SM predicted by the model in an open loop (without assimilation)

with a decrease in bias and RMSD, regardless of the spatial resolution (1 km or 100 m) at which the SM product is available. Statistical results indicate that the re-analyzed SM derived from the assimilation of 1 km DISPATCH SM is sensitive to rainfall, whereas the re-analyzed SM derived from the assimilation of 100 m DISPATCH SM is sensitive to both rainfall and irrigation. Overall, the 100 m resolution DISPATCH SM product can catch the spatial variability over the agricultural area at the field scale.

This disaggregation-assimilation coupling scheme provides SM data at the field scale on a daily temporal scale. This approach is easy to comprehend, computationally efficient, and can be applied operationally. Still, it is limited in its applicability due to the lack of thermal remote sensing data availability. In the near future, the approach should be tested using the SM data set derived from the synergy between *DISPATCH*_{100m} and Sentinel-1 radar data, as well as for different land covers and climatic conditions. In the medium term, this research will benefit from launching new thermal missions designed to provide data at high spatio-temporal resolution.

Chapter 8

General conclusions and perspectives

Contents

8.1	Summary of the main findings	162
8.2	Future researches on soil moisture monitoring and their applications	164

8.1 Summary of the main findings

Soil moisture (SM) data at different spatial and temporal resolutions are helpful for various applications such as climatology, hydrology, and agricultural purposes. Passive microwave sensors such as SMOS and SMAP provide global scale 40 km resolution surface (0-5 cm) SM data, which can be useful for meteorological and climatological applications. However, for many regional or local applications, SM data would be required at a higher (typically 100 m or finer) spatial resolution. Optical/thermal and radar sensors can be used as SM proxies to retrieve SM at such high spatial resolution, but both techniques have limitations. In particular, optical/thermal data are not available under clouds and under plant canopies, and radar data are sensitive to the soil roughness and vegetation structure, which are challenging to characterize from space.

The thesis aims to improve SM retrieval at multiple resolutions by developing a synergy between multi-sensor/multi-wavelength/multi-resolution remote sensing data. The synergistic approach based on multi-sensor data is a trend nowadays to try and resolve the spatial scale problem between the scale at which data are available and the application scale, and more generally to overcome the limitation of spaceborne sensors taken separately. The main goal of this approach is to combine multiple remote sensing data in order to obtain a better understanding of SM's spatial and temporal variability by accounting for the specific impact of soil, vegetation, and atmospheric conditions on satellite observations derived from various remote sensing techniques.

In practice, the guiding principle of the thesis is to propose a new approach combining active microwave, passive microwave, and optical/thermal sensors to provide SM data over large areas at 100 m resolution every day. Our assumption is first to rely on a disaggregation method (DISPATCH) of SMOS/SMAP SM data to meet the spatial resolution achieved by active microwave sensors. DISPATCH is based on a SM proxy called the soil evaporative efficiency (SEE) derived at high resolution from the LST and NDVI data (typically MODIS data) collected over partially vegetated pixels. The disaggregated SM data is then combined with a radar-based SM retrieval method to exploit the sensing capabilities of the Sentinel-1 radars. Finally, the usefulness of the assimilation of the satellite-based SM data in a simple soil model is assessed in terms of SM predictions at the 100 m resolution and daily temporal scale. The chosen study areas covering semi-arid and temperate sites are presented in **Chapter 2**, and the DISPATCH method is described in **Chapter 3**, while the new stepwise approach is described in **Chapter 4**, **Chapter 5**, **Chapter 6** and **Chapter 7**.

Chapter 4 describes a new and major improvement of DISPATCH when applied at the MODIS tile scale at 1 km resolution. This includes the application of the disaggregation method to fully vegetated pixels and the partial overcoming of the cloud cover limitation. The Temperature Vegetation Dryness Index (TVDI) is proposed as a surface SM proxy for highly vegetated pixels by assuming that the surface SM is spatially linked to the root zone SM within a SMOS/SMAP pixel. With the inclusion of the vegetated regions in the DISPATCH algorithm, the downscaled SM product increases the covered spatial extent by 58 to 86% over a given MODIS tile. In addition to this, the Enhanced Vegetation Index (EVI) is used instead of the NDVI to improve the robustness of DISPATCH over vegetated areas as EVI is supposedly less affected by soil and atmospheric effects and varies more linearly with vegetation cover. EVI improves DISPATCH's robustness in terms of downscaled SM accuracy by 7% in temperate and 1 to 4% in semi-arid areas.

The Sentinel-3 LST product is tested to overcome the limitation of cloud cover due to ear-

lier overpass of the satellite compared to MODIS by assuming that cloud cover is statistically smaller earlier in the morning. In general, the downscaled SM product from the improved version of the DISPATCH algorithm shows a significantly increased spatial extent and slightly better performance and accuracy than other SM products (SMAP/Sentinel-1, Copernicus Sentinel-1) available at 1 km resolution.

Given that the 1 km spatial resolution is still coarse for fine-scale applications -like water management over irrigated areas - **Chapter 5** is dedicated to develop a strategy for applying DISPATCH at 100 m resolution. A two-step downscaling algorithm is proposed to provide SM data at 100 m resolution using Landsat's LST and NDVI data. At first, 40 km resolution SM data from SMOS/SMAP is disaggregated at 1 km resolution following the approach described in **Chapter 4**. Then 1 km SM product is aggregated to an intermediate spatial resolution (ISR) of 10 km. Next, the ISR SM data are disaggregated at 100 m resolution using DISPATCH and the 100 m resolution NDVI and LST Landsat data. The ISR is set to 10 km in this case as a good compromise in terms of the encountered variability within a low resolution pixel (the larger the ISR, the more SM variability and the more robust DISPATCH is) and the gap between the low and high resolutions (the larger the gap, the more uncertain the disaggregation result is). The SM product at 100 m resolution is validated with in situ SM measurements collected over irrigated areas in Morocco, showing a daily spatial correlation in the range of 0.5-0.9.

SM products at high spatio-temporal resolution are essential from the agricultural point of view. Still, the applicability of the 100 m resolution DISPATCH SM for irrigation management is limited due to the low repeat cycle of high-spatial-resolution thermal sensors (16 days for Landsat) and cloud coverage. So, to provide SM data at the field scale in all weather conditions, **Chapter 6** proposes a synergy of the previous approaches with active microwave (radar) data. An algorithm is built on a synergy between the downscaled SM product at 100 m resolution and Sentinel-1 radar backscattering coefficient. In practice, the DISPATCH SM product available on clear sky days is used to calibrate a radar radiative transfer model in the direct mode. Then the calibrated radar radiative transfer model is used in the inverse method to estimate SM at the spatio-temporal resolution of Sentinel-1. This method is expected to reduce the impact of soil roughness and vegetation effects on the radar backscatter by incorporating independent remotely sensed data (provided by DISPATCH SM). The algorithm is tested for a constant incidence angle and VV polarization Sentinel-1 data, and by assuming that surface roughness is constant during the calibration period. This approach offers SM estimates at the crop field scale every six days. It is tested over several wheat crops in Morocco under drip and sprinkler irrigation. Results indicate a positive correlation between satellite and in situ measurements in the range of 0.66 to 0.81. A relatively good performance is obtained for a vegetation index lower than 0.6.

As a final step of this work, an initiative is taken in **Chapter 7** to improve the accuracy of the remotely sensed SM and its temporal frequency by combining this data set with a simple dynamic soil module extracted from the force-restore formulation of ISBA model. A 2D sequential-variational assimilation method is used to analyze the soil model predictions and the observed SM to provide reanalyzed SM data at the daily and crop field scale. The assimilation exercise is undertaken over irrigated crop fields in Spain, and two different cases are compared using the 1 km resolution and the 100 m resolution DISPATCH SM data as input. Results show that the analyzed SM product derived from the assimilation of 1 km resolution DISPATCH SM is sensitive to rainfall events but not to irrigation. In contrast, the dynamics of the analyzed SM product derived from the assimilation of 100 m resolution DISPATCH SM is consistent with irrigation events. Moreover, the analyzed SM data at the Landsat overpass time is more accurate

than the original 100 m resolution DISPATCH SM data. This approach can be readily applied over large areas given that all the required input (remote sensing and meteorological) data are available globally.

8.2 Future researches on soil moisture monitoring and their applications

This thesis has developed multiple algorithms building on synergies between active microwave, passive microwave, and optical/thermal data to estimate SM at high spatio-temporal resolution. According to my knowledge, this is the first time such a multi-spectral/multi-sensor synergy has been exploited, and this across an extensive range of scales from the SMOS/SMAP radiometer resolution (40 km) to the Sentinel-1 resolution (20 m). However, the methodology still has limitations such as uncertainties in low resolution SMOS/SMAP SM data, uncertainties in DISPATCH and more generally in downscaling procedures, the low repeat cycle of current high-resolution thermal sensors, uncertainties in the formulation of the radar radiative transfer, and the lack of sensitivity of radar data to SM for biomass above a given threshold (for $\text{NDVI} > 0.6$, see **Chapter 6**). Some of those limitations can potentially be lifted by future research and by the launch of new spaceborne sensors with improved capacities, which will foster the development of a more precise and robust high-resolution SM product at a global scale (Greifeneder et al., 2021). Meanwhile, another research avenue is using this high-resolution SM data set for thematic applications, like evapotranspiration and irrigation monitoring, studies on the land surface-atmosphere interactions, etc. The research perspectives that I have identified from my PhD work are listed below:

1) Keep improving downscaling algorithms to reduce uncertainties in downscaled SM data sets

A high resolution SM product has been produced by combining multi-sensor remote sensing data with different spatial and temporal resolutions, as shown in **Chapter 4** and **Chapter 5**. Since we rely on SMOS or SMAP SM data, any bias and uncertainty present in the low-resolution SM data will entirely contribute to errors in the high resolution downscaled SM product. Whereas many studies have addressed and are still addressing the error characterization of SMOS/SMAP-derived SM products (Kornelsen and Coulibaly, 2015; Lee et al., 2017; Zwieback et al., 2018; Lee and Ahn, 2019), the original requirement of an absolute error lower than $0.04 \text{ m}^3/\text{m}^3$ is not achieved globally. Moreover, part of the uncertainties in the disaggregated SM data at 1 km resolution and an expectedly even larger part of the uncertainties in the disaggregated DISPATCH SM data at 100 m resolution is attributed to the DISPATCH limitations. The former DISPATCH version was improved during my thesis, especially in terms of spatio-temporal coverage (notably by the use of TVDI). However, other aspects of DISPATCH should also be investigated. For instance, the relationship between SEE/TVDI and SM has been assumed to be linear, although it is known to be nonlinear (Merlin et al., 2013; Song and Zhang, 2021). In addition, the self-calibration of DISPATCH was done daily according to (Molero et al., 2016), but a recent study (Stefan et al., 2020) indicated that a yearly calibration of a nonlinear SEE model significantly outperforms the original configuration. Regarding the sequential application of DISPATCH at 1 km and 100 m resolutions, the use of an ISR set to 10 km needs to be confirmed by other studies undertaken in various surface conditions.

2) Towards an improved understanding of the radar signal parameterization and a dynamic calibration of time-varying parameters

Chapter 6 tested two different formulations of the relationship between the C-band radar backscatter, SM and a vegetation descriptor: a linear multi-linear model and a nonlinear model based on the Water Cloud Model (WCM) formulation. Contrary to expectations, the linear model provides results very similar to the WCM over the entire agricultural season. This raises a question about the understanding of the radar signal and its dependency on vegetation structure and water content. More research would hence be needed to characterize better the vegetation attenuation term, which is usually modeled using a (strongly nonlinear) exponential function. This issue is also naturally related to the vegetation descriptor (NDVI, PR, or CO) choice across various land covers and biomass values. In addition, the synergy between DISPATCH and radar-based SM data sets has been tested over wheat crop only, but with different soil types and different irrigation (drip or sprinkler) techniques. Before assessing the usefulness of such a complex approach over wide areas, the SM retrieval algorithm should be tested over various land covers, including different crop types and also orchards, as the physics of the radiative transfer is likely to differ significantly in three dimensional canopies.

Other research avenues concern the radar observing configuration and the time-varying parameters of the radar model. In my thesis, it was assumed that the calibration parameters and the incidence angle were constant. Sentinel-1 has a range of incidence angles. It would be useful to check the algorithm applicability using different incidence angles and how the retrieved parameters differ when changing the incidence angle. It was also assumed that the soil and vegetation parameters were constant during the entire study period. However, the soil parameters like roughness and vegetation parameters associated with the vegetation type may change, especially over agricultural areas with tillage and crop rotations. It will be thus necessary to integrate this constraint in the radar model. This actually is one strength of the developed disaggregation-calibration approach that can afford to make the radar parameters time-varying. It is just a matter of defining shorter calibration periods, provided that the frequency of concurrent thermal and radar data is sufficient to undertake the calibration with satisfying accuracy in retrieved parameters.

3) Building on future missions to develop original multi-sensor strategies

Scheduled for launch in 2025, the French-Indian TRISHNA (Thermal infraRed Imaging Satellite for High-resolution Natural resource Assessment) mission ([Lagouarde et al., 2018](#)) will provide LST data at 50 m spatial resolution with a revisit sub-cycle of 3 days in average. The advent of spaceborne LST data at such high spatial and temporal resolution will allow great progress on synergistic studies with other sensors, especially by maximizing the number of concurrent overpasses. The high temporal frequency of thermal is a major issue, compensate for the data gaps in current high-resolution LST images due to cloud cover. It is expected that the TRISHNA data will foster the development of our SM retrieval approach over large areas.

Meanwhile, it is worth mentioning that thermal missions generally use a polar orbit, apart from a couple of examples. This involves a relatively low temporal resolution (repeat cycle of one day or more), which implies a large impact of cloud cover on the spatial-temporal coverage of collected LST images. Instead, geostationary satellites with a measurement frequency of several minutes are more likely to provide cloud-free LST data. The use of thermal data from the geostationary satellites can significantly overcome the limitation of cloud cover. For instance, [Tagesson et al. \(2018\)](#) and [Piles et al. \(2016\)](#) used SEVERI satellite thermal data to downscale passive microwave-derived SM data. However, the currently available geostationary thermal sensors have a spatial resolution of 2-3 km at nadir, corresponding to a resolution of 4-5 km at

the latitude of the study areas of my thesis (see **Chapter 2**). In the more or less far future, the launch of geostationary satellites carrying thermal sensors with very high spatial resolution capabilities will be an asset to use thermal data on a quasi-systematic and more operational basis.

From a radar perspective, the L-band radar satellite named NASA-ISRO Synthetic Aperture Radar (NISAR) will be launched on 29 th January 2023. This satellite will be very useful as it will provide a spatial resolution of 3-5 m with a revisit cycle of 12 days with an ascending and descending overpass. This radar sensor will help implement the algorithm to provide SM globally. L-band has higher penetration within the vegetation canopy than c-band gives a strong potential in using NISAR data instead of (or complementarity to) Sentinel-1 data within our multi-sensor SM retrieval algorithm.

4) Application of high-resolution SM products to environmental and water management studies

Current remote sensing satellites provide coarse resolution SM at a global scale and are useful for climatic application. There are many other applications where SM is required at high resolution but limited by the unavailability of SM data at high resolution.

The existing numerical weather forecast (NWP) model uses the low resolution SM dataset for weather forecasts on a global scale. Integrating SM information in NWP models improves the weather forecast accuracy (Mahfouf, 2010; Carrera et al., 2019; Muñoz-Sabater et al., 2019). Currently, the approach is being adapted to integrate sub-kilometric resolution data, in order to keep improving the weather forecast at a regional scale, and to simulate the model output at a sub-kilometric scale; this requires SM data at high resolution.

SM data at high-resolution would also be helpful in climate research to better understand land-atmosphere processes (Taylor et al., 2012; Loew et al., 2013; Seneviratne et al., 2013). The coupling of SM with temperature and evapotranspiration (Lei et al., 2018) shows that SM is an essential metric in a transitional climatic zone (Hirschi et al., 2014).

The satellite-obtained SM data set is used for various hydrological purposes such as watershed management (Heimhuber et al., 2017), runoff modeling (Crow et al., 2018), evapotranspiration estimation (Lievens et al., 2017) etc., but it still generally applies to large river basins. To be useful for all the above applications at regional scale SM data are required at high resolution.

High resolution SM data at high temporal frequency is beneficial for agricultural purposes such as crop yield estimation (Holzman et al., 2014), monitoring irrigated areas (Fieuzal et al., 2011), monitoring irrigation volumes and dates, among others (Malbeteau et al., 2018; Ouaadi et al., 2020). It also gives valuable information for improving water management on a local and regional scale, particularly in regions facing water scarcity (Brocca et al., 2018; Zaussinger et al., 2019).

SM at high resolution can also be used for other applications such as identification of epidemic risk related to weather and environmental conditions (Peters et al., 2014), management of locust (Escorihuela et al., 2018), an indication of forest recovery after forest fires (Chu and Guo, 2014). The advent of SM data at improved spatio-temporal resolution is expected to further extend the application domain of SM information.

Chapitre 8

Conclusions générales et perspectives (français)

Contents

8.1	Résumé des principales conclusions	168
8.2	Recherches futures sur le suivi de l'humidité des sols et ses applications	170

8.1 Résumé des principales conclusions

Les données sur l'humidité du sol (SM) à différentes résolutions spatiales et temporelles sont utiles pour diverses applications telles que la climatologie, l'hydrologie et l'agriculture. Les capteurs passifs à micro-ondes tels que SMOS et SMAP fournissent des données sur l'humidité du sol à l'échelle mondiale avec une résolution de 40 km (0-5 cm), ce qui peut être utile pour les applications météorologiques et climatologiques. Cependant, pour de nombreuses applications régionales ou locales, des données SM sont nécessaires à une résolution spatiale plus élevée (typiquement 100 m ou plus fine). Les capteurs optiques/thermiques et les radars peuvent être utilisés comme des proxies de la SM pour récupérer la SM à cette haute résolution spatiale, mais les deux techniques ont des limites. En particulier, les données optiques/thermiques ne sont pas disponibles sous les nuages et sous les couverts végétaux, et les données radar sont sensibles à la rugosité du sol et à la structure de la végétation, qui sont difficiles à caractériser depuis l'espace.

La thèse vise à améliorer la récupération de la SM à de multiples résolutions en développant une synergie entre les données de télédétection multi-capteurs/multi-longueurs d'onde/multi-résolutions. L'approche synergique basée sur des données multi-capteurs est une tendance actuelle pour essayer de résoudre le problème d'échelle spatiale entre l'échelle à laquelle les données sont disponibles et l'échelle d'application, et plus généralement pour surmonter les limitations des capteurs spatiaux pris séparément. L'objectif principal de cette approche est de combiner plusieurs données de télédétection afin d'obtenir une meilleure compréhension de la variabilité spatiale et temporelle du SM en tenant compte de l'impact spécifique des conditions de sol, de végétation et d'atmosphère sur les observations satellitaires dérivées de diverses techniques de télédétection.

En pratique, le principe directeur de la thèse est de proposer une nouvelle approche combinant des capteurs actifs micro-ondes, passifs micro-ondes, et optiques/thermiques pour fournir des données SM sur de larges zones à une résolution de 100 m chaque jour. Notre hypothèse est d'abord de s'appuyer sur une méthode de désagrégation (DISPATCH) des données SMOS/SMAP pour atteindre la résolution spatiale obtenue par les capteurs micro-ondes actifs. DISPATCH est basé sur un proxy SM appelé l'efficacité évaporative du sol (SEE) dérivé à haute résolution des données LST et NDVI (typiquement des données MODIS) collectées sur des pixels partiellement végétalisés. Les données désagrégées de SM sont ensuite combinées avec une méthode d'extraction de SM basée sur un radar afin d'exploiter les capacités de détection des radars Sentinel-1. Enfin, l'utilité de l'assimilation des données SM satellitaires dans un modèle de sol simple est évaluée en termes de prédictions SM à une résolution de 100 m et à une échelle temporelle quotidienne. Les zones d'étude choisies, couvrant des sites semi-arides et tempérés, sont présentées au Chapitre 2. La méthode DISPATCH est décrite au Chapitre 3, tandis que la nouvelle approche par étapes est décrite aux Chapitres 4, 5, 6 et 7.

Le Chapitre 4 décrit une nouvelle et importante amélioration de DISPATCH lorsqu'elle est appliquée à l'échelle des tuiles MODIS à une résolution de 1 km. Cela comprend l'application de la méthode de désagrégation aux pixels entièrement végétalisés et le dépassement partiel de la limite de la couverture nuageuse. L'indice de température, de végétation et de sécheresse (TVDI) est proposé comme indicateur de la SM de surface pour les pixels fortement végétalisés, en supposant que la SM de surface est liée spatialement à la SM de la zone racinaire dans un pixel SMOS/SMAP. Avec l'inclusion des régions végétalisées dans l'algorithme DISPATCH, le produit SM à échelle réduite augmente l'étendue spatiale couverte de 58 à 86 % sur une tuile MODIS donnée. En outre, l'indice de végétation amélioré (EVI) est utilisé à la place du NDVI pour

améliorer la robustesse de DISPATCH sur les zones de végétation, car l'EVI est censé être moins affecté par les effets du sol et de l'atmosphère et varie plus linéairement avec la couverture végétale. L'EVI améliore la robustesse de DISPATCH en termes de précision de la réduction d'échelle SM de 7% dans les zones tempérées et de 1 à 4% dans les zones semi-arides.

Le produit LST de Sentinel-3 est testé pour surmonter la limitation de la couverture nuageuse due au survol plus précoce du satellite par rapport à MODIS en supposant que la couverture nuageuse est statistiquement plus faible plus tôt dans la matinée. En général, le produit SM réduit à partir de la version améliorée de l'algorithme DISPATCH montre une étendue spatiale significativement accrue et des performances et une précision légèrement meilleures que les autres produits SM (SMAP/Sentinel-1, Copernicus Sentinel-1) disponibles à une résolution de 1 km.

Étant donné que la résolution spatiale de 1 km est encore trop faible pour les applications à échelle fine, comme la gestion de l'eau dans les zones irriguées, le Chapitre 5 est consacré à l'élaboration d'une stratégie d'application de DISPATCH à une résolution de 100 m. Un algorithme de réduction d'échelle en deux étapes est proposé pour fournir des données SM à une résolution de 100 m en utilisant les données LST et NDVI de Landsat. Dans un premier temps, les données SM à résolution de 40 km provenant de SMOS/SMAP sont désagrégées à une résolution de 1 km selon l'approche décrite au Chapitre 4. Ensuite, le produit SM de 1 km est agrégé à une résolution spatiale intermédiaire (ISR) de 10 km. Ensuite, les données SM ISR sont désagrégées à une résolution de 100 m en utilisant DISPATCH et les données Landsat NDVI et LST à 100 m de résolution. L'ISR est fixé à 10 km dans ce cas comme un bon compromis en termes de variabilité rencontrée dans un pixel de basse résolution (plus l'ISR est grand, plus la variabilité SM est grande et plus DISPATCH est robuste) et l'écart entre les basses et hautes résolutions (plus l'écart est grand, plus le résultat de la désagrégation est incertain). Le produit SM à une résolution de 100 m est validé avec des mesures SM in situ collectées sur des zones irriguées au Maroc, montrant une corrélation spatiale quotidienne dans la gamme de 0,5-0,9.

Les produits SM à haute résolution spatio-temporelle sont essentiels du point de vue agricole. Pourtant, l'applicabilité de la résolution de 100 m de DISPATCH SM pour la gestion de l'irrigation est limitée en raison du faible cycle de répétition des capteurs thermiques à haute résolution spatiale (16 jours pour Landsat) et de la couverture nuageuse. Ainsi, pour fournir des données SM à l'échelle du champ dans toutes les conditions météorologiques, le Chapitre 6 propose une synergie des approches précédentes avec des données de micro-ondes actives (radar). Un algorithme est construit sur une synergie entre le produit SM réduit à une résolution de 100 m et le coefficient de rétrodiffusion du radar Sentinel-1. En pratique, le produit SM DISPATCH disponible les jours de ciel clair est utilisé pour calibrer un modèle de transfert radiatif radar en mode direct. Ensuite, le modèle de transfert radiatif radar calibré est utilisé dans la méthode inverse pour estimer le SM à la résolution spatio-temporelle de Sentinel-1. Cette méthode devrait permettre de réduire l'impact de la rugosité du sol et des effets de la végétation sur la rétrodiffusion radar en intégrant des données de télédétection indépendantes (fournies par DISPATCH SM). L'algorithme est testé pour un angle d'incidence constant et des données Sentinel-1 à polarisation VV, et en supposant que la rugosité de surface est constante pendant la période de calibration. Cette approche offre des estimations SM à l'échelle du champ de culture tous les six jours. Elle est testée sur plusieurs cultures de blé au Maroc sous irrigation par goutte à goutte et par aspersion. Les résultats indiquent une corrélation positive entre les mesures satellitaires et in situ de l'ordre de 0,66 à 0,81. Une performance relativement bonne est obtenue pour un indice de végétation inférieur à 0,6.

Comme étape finale de ce travail, une initiative est prise dans le Chapitre 7 pour améliorer la précision de la SM télédéetectée et sa fréquence temporelle en combinant cet ensemble de données avec un module de sol dynamique simple extrait de la formulation force-restauration du modèle ISBA. Une méthode d'assimilation séquentielle-variationnelle 2D est utilisée pour analyser les prédictions du modèle de sol et le SM observé afin de fournir des données SM réanalysées à l'échelle quotidienne et à l'échelle du champ de culture. L'exercice d'assimilation est entrepris sur des champs de cultures irriguées en Espagne, et deux cas différents sont comparés en utilisant les données SM DISPATCH de résolution 1 km et 100 m comme entrée. Les résultats montrent que le produit SM analysé dérivé de l'assimilation de DISPATCH SM à résolution de 1 km est sensible aux événements pluvieux mais pas à l'irrigation. En revanche, la dynamique du produit SM analysé dérivé de l'assimilation de DISPATCH SM avec une résolution de 100 m est cohérente avec les événements d'irrigation. De plus, les données SM analysées au moment du passage de Landsat sont plus précises que les données originales DISPATCH SM à 100 m de résolution. Cette approche peut être facilement appliquée à de vastes zones, étant donné que toutes les données d'entrée requises (télédétection et météorologie) sont disponibles à l'échelle mondiale.

8.2 Recherches futures sur le suivi de l'humidité des sols et ses applications

Cette thèse a développé de multiples algorithmes s'appuyant sur les synergies entre les données micro-ondes actives, micro-ondes passives, et optiques/thermiques pour estimer la SM à haute résolution spatio-temporelle. A ma connaissance, c'est la première fois qu'une telle synergie multi-spectrale/multi-capteur a été exploitée, et ce sur une large gamme d'échelles allant de la résolution du radiomètre SMOS/SMAP (40 km) à la résolution de Sentinel-1 (20 m). Cependant, la méthodologie présente encore des limites telles que les incertitudes des données SMOS/SMAP à faible résolution, les incertitudes de DISPATCH et plus généralement des procédures de réduction d'échelle, le faible cycle de répétition des capteurs thermiques haute résolution actuels, les incertitudes dans la formulation du transfert radiatif radar, et le manque de sensibilité des données radar au SM pour la biomasse au-dessus d'un seuil donné (pour $NDVI > 0,6$, voir Chapitre 6). Certaines de ces limitations peuvent potentiellement être levées par des recherches futures et par le lancement de nouveaux capteurs spatiaux aux capacités améliorées, ce qui favorisera le développement d'un produit SM haute résolution plus précis et plus robuste à l'échelle mondiale (Greifeneder et al., 2021). Parallèlement, une autre voie de recherche consiste à utiliser cet ensemble de données SM à haute résolution pour des applications thématiques, comme le suivi de l'évapotranspiration et de l'irrigation, les études sur les interactions entre la surface terrestre et l'atmosphère, etc. Les perspectives de recherche que j'ai identifiées à partir de mon travail de doctorat sont énumérées ci-dessous :

1) Continuer à améliorer les algorithmes de réduction d'échelle afin de réduire les incertitudes dans les jeux de données SM réduits

Un produit SM haute résolution a été obtenu en combinant des données de télédétection multi-capteurs avec différentes résolutions spatiales et temporelles, comme le montrent les Chapitres 4 et 5. Puisque nous nous basons sur les données SMOS ou SMAP SM, tout biais et toute incertitude présents dans les données SM à basse résolution contribueront entièrement aux erreurs dans le produit SM à haute résolution réduit à l'échelle. Alors que de nombreuses études ont abordé et abordent encore la caractérisation des erreurs des produits SM dérivés de SMOS/SMAP (Kornel-

sen and Coulibaly, 2015; Lee et al., 2017; Zwieback et al., 2018; Lee and Ahn, 2019), l'exigence initiale d'une erreur absolue inférieure à $0,04 \text{ m}^3/\text{m}^3$ n'est pas atteinte globalement. En outre, une partie des incertitudes des données SM désagrégées à une résolution de 1 km et une partie encore plus importante, selon les prévisions, des incertitudes des données SM désagrégées DISPATCH à une résolution de 100 m sont attribuées aux limitations de DISPATCH. L'ancienne version de DISPATCH a été améliorée au cours de ma thèse, notamment en termes de couverture spatio-temporelle (notamment par l'utilisation de TVDI). Cependant, d'autres aspects de DISPATCH devraient également être étudiés. Par exemple, la relation entre SEE/TVDI et SM a été supposée être linéaire, alors qu'elle est connue pour être non linéaire (Merlin et al., 2013; Song and Zhang, 2021). En outre, l'auto-calibration de DISPATCH a été effectuée quotidiennement selon (Molero et al., 2016), mais une étude récente (Stefan et al., 2020) a indiqué qu'une calibration annuelle d'un modèle SEE non linéaire surpasse significativement la configuration originale. En ce qui concerne l'application séquentielle de DISPATCH à des résolutions de 1 km et 100 m, l'utilisation d'un ESI réglé à 10 km doit être confirmée par d'autres études entreprises dans diverses conditions de surface.

2) Vers une meilleure compréhension de la paramétrisation du signal radar et une calibration dynamique des paramètres variant dans le temps

Le Chapitre 6 a testé deux formulations différentes de la relation entre la rétrodiffusion radar en bande C, le SM et un descripteur de végétation : un modèle linéaire multi-linéaire et un modèle non-linéaire basé sur la formulation du Water Cloud Model (WCM). Contrairement aux attentes, le modèle linéaire fournit des résultats très similaires au WCM sur l'ensemble de la saison agricole. Cela soulève une question sur la compréhension du signal radar et sa dépendance à la structure de la végétation et au contenu en eau. Des recherches supplémentaires seraient donc nécessaires pour mieux caractériser le terme d'atténuation de la végétation, qui est généralement modélisé à l'aide d'une fonction exponentielle (fortement non linéaire). Cette question est aussi naturellement liée au choix du descripteur de végétation (NDVI, PR ou CO) pour diverses couvertures terrestres et valeurs de biomasse. En outre, la synergie entre DISPATCH et les ensembles de données SM basés sur le radar a été testée sur une culture de blé uniquement, mais avec différents types de sol et différentes techniques d'irrigation (goutte à goutte ou aspersion). Avant d'évaluer l'utilité d'une approche aussi complexe sur de vastes zones, l'algorithme d'extraction SM devrait être testé sur diverses couvertures terrestres, y compris différents types de cultures et également des vergers, car la physique du transfert radiatif est susceptible de différer de manière significative dans les canopées tridimensionnelles.

D'autres pistes de recherche concernent la configuration d'observation du radar et les paramètres variables dans le temps du modèle radar. Dans ma thèse, il a été supposé que les paramètres de calibration et l'angle d'incidence étaient constants. Sentinel-1 possède une gamme d'angles d'incidence. Il serait utile de vérifier l'applicabilité de l'algorithme en utilisant différents angles d'incidence et de voir comment les paramètres récupérés diffèrent lorsque l'angle d'incidence change. On a également supposé que les paramètres du sol et de la végétation étaient constants pendant toute la période d'étude. Cependant, les paramètres du sol comme la rugosité et les paramètres de la végétation associés au type de végétation peuvent changer, en particulier sur les zones agricoles avec le travail du sol et la rotation des cultures. Il sera donc nécessaire d'intégrer cette contrainte dans le modèle radar. C'est en fait l'un des points forts de l'approche de désagrégation-calibration développée qui peut se permettre de faire varier les paramètres radar dans le temps. Il s'agit simplement de définir des périodes de calibration plus courtes, à condition que la fréquence des données thermiques et radar simultanées soit suffisante pour entreprendre

la calibration avec une précision satisfaisante des paramètres récupérés.

3) S'appuyer sur les missions futures pour développer des stratégies multi-capteurs originales

Prévue pour un lancement en 2025, la mission franco-indienne TRISHNA (Thermal infraRed Imaging Satellite for High-resolution Natural resource Assessment) (Lagouarde et al., 2018) fournira des données LST à 50 m de résolution spatiale avec un sous-cycle de revisite de 3 jours en moyenne. L'arrivée de données LST spatiales à si haute résolution spatiale et temporelle permettra de grands progrès sur les études synergiques avec d'autres capteurs, notamment en maximisant le nombre de passages simultanés. La fréquence temporelle élevée du thermique est un enjeu majeur, qui compense les lacunes des données dans les images LST actuelles à haute résolution dues à la couverture nuageuse. On s'attend à ce que les données TRISHNA favorisent le développement de notre approche d'extraction SM sur de grandes zones.

En attendant, il convient de mentionner que les missions thermiques utilisent généralement une orbite polaire, à l'exception de quelques exemples. Cela implique une résolution temporelle relativement faible (cycle de répétition d'un jour ou plus), ce qui implique un impact important de la couverture nuageuse sur la couverture spatio-temporelle des images LST collectées. Au contraire, les satellites géostationnaires avec une fréquence de mesure de plusieurs minutes sont plus susceptibles de fournir des données LST sans nuages. L'utilisation des données thermiques des satellites géostationnaires permet de surmonter les limites de la couverture nuageuse. Par exemple, Tagesson et al. (2018) et Piles et al. (2016)) ont utilisé les données thermiques du satellite SEVERI pour réduire l'échelle des données SM dérivées des micro-ondes passives. Cependant, les capteurs thermiques géostationnaires actuellement disponibles ont une résolution spatiale de 2-3 km au nadir, ce qui correspond à une résolution de 4-5 km à la latitude des zones d'étude de ma thèse (voir Chapitre 2). Dans un futur plus ou moins lointain, le lancement de satellites géostationnaires embarquant des capteurs thermiques à très haute résolution spatiale sera un atout pour exploiter les données thermiques de manière quasi-systématique et plus opérationnelle.

Du point de vue du radar, le satellite radar en bande L appelé NASA-ISRO Synthetic Aperture Radar (NISAR) sera lancé le 29 janvier 2023. Ce satellite sera très utile car il fournira une résolution spatiale de 3-5 m avec un cycle de revisite de 12 jours avec un passage ascendant et descendant. Ce capteur radar aidera à mettre en œuvre l'algorithme permettant de fournir un SM à l'échelle mondiale. La bande L a une pénétration plus élevée dans le couvert végétal que la bande C donne un fort potentiel d'utilisation des données NISAR à la place (ou en complément) des données Sentinel-1 dans notre algorithme d'extraction SM multi-capteurs.

4) Application des produits SM à haute résolution aux études environnementales et de gestion de l'eau

Les satellites de télédétection actuels fournissent une SM à résolution grossière à l'échelle mondiale et sont utiles pour les applications climatiques. Il existe de nombreuses autres applications pour lesquelles la SM est nécessaire à haute résolution, mais qui sont limitées par l'indisponibilité de données SM à haute résolution.

Le modèle actuel de prévision numérique du temps (PNT) utilise les données SM à faible résolution pour les prévisions météorologiques à l'échelle mondiale. L'intégration des informations SM dans les modèles NWP améliore la précision des prévisions météorologiques (Mahfouf, 2010; Carrera et al., 2019; Muñoz-Sabater et al., 2019). Actuellement, l'approche est adaptée pour

intégrer des données à résolution subkilométrique, afin de continuer à améliorer les prévisions météorologiques à l'échelle régionale, et de simuler la sortie du modèle à une échelle subkilométrique; cela nécessite des données SM à haute résolution.

Les données SM à haute résolution seraient également utiles dans la recherche climatique pour mieux comprendre les processus terre-atmosphère (Taylor et al., 2012; Loew et al., 2013; Senviratne et al., 2013). Le couplage du SM avec la température et l'évapotranspiration (Lei et al., 2018) montre que le SM est une métrique essentielle dans une zone climatique transitoire (Hirschi et al., 2014).

L'ensemble de données SM obtenues par satellite est utilisé à diverses fins hydrologiques, telles que la gestion des bassins versants (Heimhuber et al., 2017), la modélisation du ruissellement (Crow et al., 2018), l'estimation de l'évapotranspiration (Lievens et al., 2017) etc. mais il s'applique encore généralement aux grands bassins fluviaux. Pour être utiles à toutes les applications ci-dessus à l'échelle régionale, les données SM sont nécessaires à haute résolution.

Les données SM à haute résolution et à haute fréquence temporelle sont bénéfiques à des fins agricoles telles que l'estimation du rendement des cultures (Holzman et al., 2014), le suivi des zones irriguées (Fieuzal et al., 2011), le suivi des volumes et des dates d'irrigation, entre autres (Malbeteau et al., 2018; Ouaadi et al., 2020). Elle donne également des informations précieuses pour améliorer la gestion de l'eau à l'échelle locale et régionale, notamment dans les régions confrontées à une pénurie d'eau (Brocca et al., 2018; Zaussinger et al., 2019).

La SM à haute résolution peut également être utilisée pour d'autres applications telles que l'identification du risque d'épidémie lié aux conditions météorologiques et environnementales (Peters et al., 2014), la gestion des criquets (Escorihuela et al., 2018), une indication de la récupération des forêts après des feux de forêt (Chu and Guo, 2014). L'arrivée de données SM à une meilleure résolution spatio-temporelle devrait permettre d'étendre encore le domaine d'application des informations SM.

Bibliography

- Al Bitar, A., Leroux, D., Kerr, Y.H., Merlin, O., Richaume, P., Sahoo, A., Wood, E.F., 2012. Evaluation of smos soil moisture products over continental us using the scan/snotel network. *IEEE Transactions on Geoscience and Remote Sensing* 50, 1572–1586.
- Albergel, C., Rüdiger, C., Pellarin, T., Calvet, J.C., Fritz, N., Froissard, F., Suquia, D., Petitpa, A., Piguet, B., Martin, E., 2008. From near-surface to root-zone soil moisture using an exponential filter: an assessment of the method based on in-situ observations and model simulations. *Hydrology and Earth System Sciences* 12, 1323–1337.
- Allen, R.G., Pereira, L.S., Smith, M., Raes, D., Wright, J.L., 2005. Fao-56 dual crop coefficient method for estimating evaporation from soil and application extensions. *Journal of irrigation and drainage engineering* 131, 2–13.
- Amazirh, A., Merlin, O., Er-Raki, S., Gao, Q., Rivalland, V., Malbeteau, Y., Khabba, S., Escorihuela, M.J., 2018. Retrieving surface soil moisture at high spatio-temporal resolution from a synergy between sentinel-1 radar and landsat thermal data: A study case over bare soil. *Remote sensing of environment* 211, 321–337.
- Anderson, M., Norman, J., Diak, G., Kustas, W., Mecikalski, J., 1997. A two-source time-integrated model for estimating surface fluxes using thermal infrared remote sensing. *Remote sensing of environment* 60, 195–216.
- Anderson, M.C., Allen, R.G., Morse, A., Kustas, W.P., 2012. Use of landsat thermal imagery in monitoring evapotranspiration and managing water resources. *Remote Sensing of Environment* 122, 50–65.
- Andréassian, V., 2004. Waters and forests: from historical controversy to scientific debate. *Journal of hydrology* 291, 1–27.
- Attema, E., Ulaby, F.T., 1978. Vegetation modeled as a water cloud. *Radio science* 13, 357–364.
- Backus, G., Gilbert, F., 1970. Uniqueness in the inversion of inaccurate gross earth data. *Philosophical Transactions of the Royal Society of London. Series A, Mathematical and Physical Sciences* 266, 123–192.
- Baghdadi, N., Choker, M., Zribi, M., Hajj, M.E., Paloscia, S., Verhoest, N.E., Lievens, H., Baup, F., Mattia, F., 2016. A new empirical model for radar scattering from bare soil surfaces. *Remote Sensing* 8, 920.
- Baghdadi, N., Cresson, R., El Hajj, M., Ludwig, R., La Jeunesse, I., 2012. Soil parameters estimation over bare agriculture areas from c-band polarimetric sar data using neural networks. *Hydrology & Earth System Sciences Discussions* 9.

- Baghdadi, N., El Hajj, M., Zribi, M., Bousbih, S., 2017. Calibration of the water cloud model at c-band for winter crop fields and grasslands. *Remote Sensing* 9, 969.
- Baghdadi, N., Zribi, M., Loumagne, C., Ansart, P., Anguela, T.P., 2008. Analysis of terrasars-x data and their sensitivity to soil surface parameters over bare agricultural fields. *Remote sensing of environment* 112, 4370–4379.
- Balsamo, G., Bouyssel, F., Noilhan, J., 2004. A simplified bi-dimensional variational analysis of soil moisture from screen-level observations in a mesoscale numerical weather-prediction model. *Quarterly Journal of the Royal Meteorological Society: A journal of the atmospheric sciences, applied meteorology and physical oceanography* 130, 895–915.
- Baron, J.S., Poff, N.L., Angermeier, P.L., Dahm, C.N., Gleick, P.H., Hairston Jr, N.G., Jackson, R.B., Johnston, C.A., Richter, B.D., Steinman, A.D., 2002. Meeting ecological and societal needs for freshwater. *Ecological Applications* 12, 1247–1260.
- Bell, K.R., Blanchard, B., Schmutge, T., Witzczak, M., 1980. Analysis of surface moisture variations within large-field sites. *Water Resources Research* 16, 796–810.
- Berahmani, A., Faysse, N., Errahj, M., Gafsi, M., 2012. Chasing water: Diverging farmers' strategies to cope with the groundwater crisis in the coastal chaouia region in morocco. *Irrigation and drainage* 61, 673–681.
- Béziat, P., Ceschia, E., Dedieu, G., 2009. Carbon balance of a three crop succession over two cropland sites in south west france. *Agricultural and Forest Meteorology* 149, 1628–1645.
- Bhuiyan, H.A., McNairn, H., Powers, J., Friesen, M., Pacheco, A., Jackson, T.J., Cosh, M.H., Colliander, A., Berg, A., Rowlandson, T., et al., 2018. Assessing smap soil moisture scaling and retrieval in the carman (canada) study site. *Vadose Zone Journal* 17, 1–14.
- Bhumralkar, C.M., 1975. Numerical experiments on the computation of ground surface temperature in an atmospheric general circulation model. *Journal of Applied Meteorology and Climatology* 14, 1246–1258.
- Bindlish, R., Barros, A.P., 2001. Parameterization of vegetation backscatter in radar-based, soil moisture estimation. *Remote sensing of environment* 76, 130–137.
- Bircher, S., Skou, N., Jensen, K., Walker, J.P., Rasmussen, L., 2012. A soil moisture and temperature network for smos validation in western denmark. *Hydrology and Earth System Sciences* 16, 1445–1463.
- Boone, A., Calvet, J.C., Noilhan, J., 1999. Inclusion of a third soil layer in a land surface scheme using the force–restore method. *Journal of Applied Meteorology* 38, 1611–1630.
- Bouilloud, L., Delrieu, G., Boudevillain, B., Kirstetter, P.E., 2010. Radar rainfall estimation in the context of post-event analysis of flash-flood events. *Journal of Hydrology* 394, 17–27.
- Boulet, G., Chehbouni, A., Gentine, P., Duchemin, B., Ezzahar, J., Hadria, R., 2007. Monitoring water stress using time series of observed to unstressed surface temperature difference. *Agricultural and Forest Meteorology* 146, 159–172.
- Brocca, L., Melone, F., Moramarco, T., Morbidelli, R., 2010. Spatial-temporal variability of soil moisture and its estimation across scales. *Water Resources Research* 46.

- Brocca, L., Tarpanelli, A., Filippucci, P., Dorigo, W., Zaussinger, F., Gruber, A., Fernández-Prieto, D., 2018. How much water is used for irrigation? a new approach exploiting coarse resolution satellite soil moisture products. *International journal of applied earth observation and geoinformation* 73, 752–766.
- Byun, K., Liaqat, U.W., Choi, M., 2014. Dual-model approaches for evapotranspiration analyses over homo-and heterogeneous land surface conditions. *Agricultural and forest meteorology* 197, 169–187.
- Cai, X., Pan, M., Chaney, N.W., Colliander, A., Misra, S., Cosh, M.H., Crow, W.T., Jackson, T.J., Wood, E.F., 2017. Validation of smap soil moisture for the smapvex15 field campaign using a hyper-resolution model. *Water Resources Research* 53, 3013–3028.
- Calvet, J.C., Noilhan, J., Roujean, J.L., Bessemoulin, P., Cabelguenne, M., Olioso, A., Wigneron, J.P., 1998. An interactive vegetation svat model tested against data from six contrasting sites. *Agricultural and Forest Meteorology* 92, 73–95.
- Carrera, M.L., Bilodeau, B., Bélair, S., Abrahamowicz, M., Russell, A., Wang, X., 2019. Assimilation of passive l-band microwave brightness temperatures in the canadian land data assimilation system: Impacts on short-range warm season numerical weather prediction. *Journal of Hydrometeorology* 20, 1053–1079.
- Chandler, D., Seyfried, M., Murdock, M., McNamara, J., 2004. Field calibration of water content reflectometers. *Soil Science Society of America Journal* 68, 1501–1507.
- Chen, X.z., Chen, S.s., Zhong, R.f., Su, Y.x., Liao, J.s., Li, D., Han, L.s., Li, Y., Li, X., 2012. A semi-empirical inversion model for assessing surface soil moisture using amsr-e brightness temperatures. *Journal of Hydrology* 456, 1–11.
- Chitonge, H., 2020. Urbanisation and the water challenge in africa: Mapping out orders of water scarcity. *African Studies* 79, 192–211.
- Chu, T., Guo, X., 2014. Remote sensing techniques in monitoring post-fire effects and patterns of forest recovery in boreal forest regions: A review. *Remote Sensing* 6, 470–520.
- Colliander, A., Cosh, M.H., Misra, S., Jackson, T.J., Crow, W.T., Chan, S., Bindlish, R., Chae, C., Collins, C.H., Yueh, S.H., 2017a. Validation and scaling of soil moisture in a semi-arid environment: Smap validation experiment 2015 (smavex15). *Remote Sensing of Environment* 196, 101–112.
- Colliander, A., Cosh, M.H., Misra, S., Jackson, T.J., Crow, W.T., Powers, J., McNairn, H., Bullock, P., Berg, A., Magagi, R., et al., 2019. Comparison of high-resolution airborne soil moisture retrievals to smap soil moisture during the smap validation experiment 2016 (smavex16). *Remote Sensing of Environment* 227, 137–150.
- Colliander, A., Fisher, J.B., Halverson, G., Merlin, O., Misra, S., Bindlish, R., Jackson, T.J., Yueh, S., 2017b. Spatial downscaling of smap soil moisture using modis land surface temperature and ndvi during smavex15. *IEEE Geoscience and Remote Sensing Letters* 14, 2107–2111.
- Cosandey, C., Andréassian, V., Martin, C., Didon-Lescot, J.F., Lavabre, J., Folton, N., Mathys, N., Richard, D., 2005. The hydrological impact of the mediterranean forest: a review of french research. *Journal of Hydrology* 301, 235–249.

- Cramer, W., Guiot, J., Fader, M., Garrabou, J., Gattuso, J.P., Iglesias, A., Lange, M.A., Lionello, P., Llasat, M.C., Paz, S., et al., 2018. Climate change and interconnected risks to sustainable development in the mediterranean. *Nature Climate Change* 8, 972–980.
- Crow, W., Chen, F., Reichle, R., Xia, Y., Liu, Q., 2018. Exploiting soil moisture, precipitation, and streamflow observations to evaluate soil moisture/runoff coupling in land surface models. *Geophysical research letters* 45, 4869–4878.
- Dabrowska-Zielinska, K., Inoue, Y., Kowalik, W., Gruszczynska, M., 2007. Inferring the effect of plant and soil variables on c-and l-band sar backscatter over agricultural fields, based on model analysis. *Advances in Space Research* 39, 139–148.
- Das, N., Entekhabi, D., Dunbar, R., Kim, S., Yueh, S., Colliander, A., O’Neill, P., Jackson, T., 2018. Smap/sentinel-1 l2 radiometer/radar 30-second scene 3 km ease-grid soil moisture, version 2. NASA National Snow and Ice Data Center DAAC .
- Das, N.N., Entekhabi, D., Njoku, E.G., Shi, J.J., Johnson, J.T., Colliander, A., 2013. Tests of the smap combined radar and radiometer algorithm using airborne field campaign observations and simulated data. *IEEE Transactions on Geoscience and Remote Sensing* 52, 2018–2028.
- Deardorff, J., 1977. A parameterization of ground-surface moisture content for use in atmospheric prediction models. *Journal of Applied Meteorology* 16, 1182–1185.
- Deardorff, J.W., 1978. Efficient prediction of ground surface temperature and moisture, with inclusion of a layer of vegetation. *Journal of Geophysical Research: Oceans* 83, 1889–1903.
- Dente, L., Su, Z., Wen, J., 2012. Validation of smos soil moisture products over the maqu and twente regions. *Sensors* 12, 9965–9986.
- Dubois, P.C., Engman, T., et al., 1995. Corrections to” measuring soil moisture with imaging radars”. *IEEE Transactions on Geoscience and Remote Sensing* 33, 1340.
- Entekhabi, D., Njoku, E.G., O’Neill, P.E., Kellogg, K.H., Crow, W.T., Edelstein, W.N., Entin, J.K., Goodman, S.D., Jackson, T.J., Johnson, J., et al., 2010. The soil moisture active passive (smap) mission. *Proceedings of the IEEE* 98, 704–716.
- Entin, J.K., Robock, A., Vinnikov, K.Y., Hollinger, S.E., Liu, S., Namkhai, A., 2000. Temporal and spatial scales of observed soil moisture variations in the extratropics. *Journal of Geophysical Research: Atmospheres* 105, 11865–11877.
- Erlingsson, S., Baltzer, S., Baena, J., Bjarnason, G., 2009. Measurement techniques for water flow, in: *Water in road structures*. Springer, pp. 45–67.
- Escorihuela, M.J., Escorihuela, A., Richaume, P., Kerr, Y.H., 2012. Smos calibration and validation over the salar de uyuni, in: *2012 IEEE International Geoscience and Remote Sensing Symposium, IEEE*. pp. 1124–1126.
- Escorihuela, M.J., Merlin, O., Stefan, V., Moyano, G., Eweys, O.A., Zribi, M., Kamara, S., Benahi, A.S., Ebbe, M.A.B., Chihrane, J., et al., 2018. Smos based high resolution soil moisture estimates for desert locust preventive management. *Remote Sensing Applications: Society and Environment* 11, 140–150.
- Evaristo, J., Jasechko, S., McDonnell, J.J., 2015. Global separation of plant transpiration from groundwater and streamflow. *Nature* 525, 91–94.

- Evett, S., Parkin, G., 2005. Advances in soil water content sensing: The continuing maturation of technology and theory. *Vadose Zone Journal* 4, 986–991.
- Famiglietti, J.S., Ryu, D., Berg, A.A., Rodell, M., Jackson, T.J., 2008. Field observations of soil moisture variability across scales. *Water Resources Research* 44.
- Fang, B., Lakshmi, V., Bindlish, R., Jackson, T.J., Cosh, M., Basara, J., 2013. Passive microwave soil moisture downscaling using vegetation index and skin surface temperature. *Vadose Zone Journal* 12, vzj2013–05.
- Ferrara, G., Flore, J., 2003. Comparison between different methods for measuring transpiration in potted apple trees. *Biologia Plantarum* 46, 41–47.
- Fieuzal, R., Duchemin, B., Jarlan, L., Zribi, M., Baup, F., Merlin, O., Hagolle, O., Garatuza-Payan, J., 2011. Combined use of optical and radar satellite data for the monitoring of irrigation and soil moisture of wheat crops. *Hydrology and Earth System Sciences* 15, 1117–1129.
- Findell, K.L., Gentine, P., Lintner, B.R., Kerr, C., 2011. Probability of afternoon precipitation in eastern united states and mexico enhanced by high evaporation. *Nature Geoscience* 4, 434–439.
- Foley, J.A., DeFries, R., Asner, G.P., Barford, C., Bonan, G., Carpenter, S.R., Chapin, F.S., Coe, M.T., Daily, G.C., Gibbs, H.K., et al., 2005. Global consequences of land use. *science* 309, 570–574.
- Fontanet, M., Fernández-García, D., Ferrer, F., 2018. The value of satellite remote sensing soil moisture data and the dispatch algorithm in irrigation fields. *Hydrology and Earth System Sciences* 22, 5889–5900.
- Ford, T., Harris, E., Quiring, S., 2013. Estimating root zone soil moisture using near-surface observations from smos. *Hydrol. Earth Syst. Sci. Discuss* 10, 8325–8364.
- Fouillet, A., Rey, G., Laurent, F., Pavillon, G., Bellec, S., Guihenneuc-Jouyaux, C., Clavel, J., Jouglu, E., Hémon, D., 2006. Excess mortality related to the august 2003 heat wave in france. *International archives of occupational and environmental health* 80, 16–24.
- Fung, A.K., Li, Z., Chen, K.S., 1992. Backscattering from a randomly rough dielectric surface. *IEEE Transactions on Geoscience and remote sensing* 30, 356–369.
- Gao, Z., Gao, W., Chang, N.B., 2011. Integrating temperature vegetation dryness index (tvd) and regional water stress index (rws) for drought assessment with the aid of landsat tm/etm+ images. *International Journal of Applied Earth Observation and Geoinformation* 13, 495–503.
- Gao, Z., Xu, X., Wang, J., Yang, H., Huang, W., Feng, H., 2013. A method of estimating soil moisture based on the linear decomposition of mixture pixels. *Mathematical and Computer Modelling* 58, 606–613.
- Giorgi, F., 2006. Climate change hot-spots. *Geophysical research letters* 33.
- Giorgi, F., Lionello, P., 2008. Climate change projections for the mediterranean region. *Global and planetary change* 63, 90–104.
- Gitelson, A.A., 2004. Wide dynamic range vegetation index for remote quantification of biophysical characteristics of vegetation. *Journal of plant physiology* 161, 165–173.

- Greifeneder, F., Notarnicola, C., Wagner, W., 2021. A machine learning-based approach for surface soil moisture estimations with google earth engine. *Remote Sensing* 13, 2099.
- Van de Griend, A., Camillo, P., Gurney, R., 1985. Discrimination of soil physical parameters, thermal inertia, and soil moisture from diurnal surface temperature fluctuations. *Water Resources Research* 21, 997–1009.
- Habets, F., Noilhan, J., Golaz, C., Goutorbe, J., Lacarrere, P., Leblois, E., Ledoux, E., Martin, E., Oettle, C., Vidal-Madjar, D., 1999. The isba surface scheme in a macroscale hydrological model applied to the hapex-mobilhy area: Part i: Model and database. *Journal of Hydrology* 217, 75–96.
- Hallegatte, S., 2009. Strategies to adapt to an uncertain climate change. *Global environmental change* 19, 240–247.
- Heimhuber, V., Tulbure, M., Broich, M., 2017. Modeling multidecadal surface water inundation dynamics and key drivers on large river basin scale using multiple time series of earth-observation and river flow data. *Water Resources Research* 53, 1251–1269.
- Hinrichsen, D., Tacio, H., 2002. The coming freshwater crisis is already here. The linkages between population and water. Washington, DC: Woodrow Wilson International Center for Scholars , 1–26.
- Hirschi, M., Mueller, B., Dorigo, W., Seneviratne, S.I., 2014. Using remotely sensed soil moisture for land–atmosphere coupling diagnostics: The role of surface vs. root-zone soil moisture variability. *Remote sensing of environment* 154, 246–252.
- Holzman, M.E., Rivas, R., Piccolo, M.C., 2014. Estimating soil moisture and the relationship with crop yield using surface temperature and vegetation index. *International Journal of Applied Earth Observation and Geoinformation* 28, 181–192.
- Houborg, R., Fisher, J., Skidmore, A., 2015. Advances in remote sensing of vegetation function and traits: special issue of international journal of applied earth observation and geoinformation .
- Huete, A., Didan, K., Miura, T., Rodriguez, E.P., Gao, X., Ferreira, L.G., 2002. Overview of the radiometric and biophysical performance of the modis vegetation indices. *Remote sensing of environment* 83, 195–213.
- Jackson, T.J., 1993. Iii. measuring surface soil moisture using passive microwave remote sensing. *Hydrological processes* 7, 139–152.
- Jackson, T.J., Bindlish, R., Cosh, M.H., Zhao, T., Starks, P.J., Bosch, D.D., Seyfried, M., Moran, M.S., Goodrich, D.C., Kerr, Y.H., et al., 2011. Validation of soil moisture and ocean salinity (smos) soil moisture over watershed networks in the us. *IEEE Transactions on Geoscience and Remote Sensing* 50, 1530–1543.
- Jacob, D., Petersen, J., Eggert, B., Alias, A., Christensen, O.B., Bouwer, L.M., Braun, A., Colette, A., Déqué, M., Georgievski, G., et al., 2014. Euro-cordex: new high-resolution climate change projections for european impact research. *Regional environmental change* 14, 563–578.
- Jiang, L., Islam, S., 2003. An intercomparison of regional latent heat flux estimation using remote sensing data. *International Journal of Remote Sensing* 24, 2221–2236.

- Jiang, Z., Huete, A.R., Li, J., Chen, Y., 2006. An analysis of angle-based with ratio-based vegetation indices. *IEEE Transactions on Geoscience and Remote Sensing* 44, 2506–2513.
- de Jong, C., Lawler, D., Essery, R., 2009. Mountain hydroclimatology and snow seasonality-perspectives on climate impacts, snow seasonality and hydrological change in mountain environments. *Hydrological Processes* 23, 955.
- Jung, M., Reichstein, M., Ciais, P., Seneviratne, S.I., Sheffield, J., Goulden, M.L., Bonan, G., Cescatti, A., Chen, J., De Jeu, R., et al., 2010. Recent decline in the global land evapotranspiration trend due to limited moisture supply. *Nature* 467, 951–954.
- Kaheil, Y.H., Gill, M.K., McKee, M., Bastidas, L.A., Rosero, E., 2008. Downscaling and assimilation of surface soil moisture using ground truth measurements. *IEEE Transactions on Geoscience and Remote Sensing* 46, 1375–1384.
- Kerr, Y.H., Waldteufel, P., Wigneron, J.P., Delwart, S., Cabot, F., Boutin, J., Escorihuela, M.J., Font, J., Reul, N., Gruhier, C., et al., 2010. The smos mission: New tool for monitoring key elements of the global water cycle. *Proceedings of the IEEE* 98, 666–687.
- Kerr, Y.H., Waldteufel, P., Wigneron, J.P., Martinuzzi, J., Font, J., Berger, M., 2001. Soil moisture retrieval from space: The soil moisture and ocean salinity (smos) mission. *IEEE transactions on Geoscience and remote sensing* 39, 1729–1735.
- Kim, G., Barros, A.P., 2002. Downscaling of remotely sensed soil moisture with a modified fractal interpolation method using contraction mapping and ancillary data. *Remote Sensing of Environment* 83, 400–413.
- Komatsu, T.S., 2003. Toward a robust phenomenological expression of evaporation efficiency for unsaturated soil surfaces. *Journal of Applied Meteorology* 42, 1330–1334.
- Kornelsen, K.C., Coulibaly, P., 2013. Advances in soil moisture retrieval from synthetic aperture radar and hydrological applications. *Journal of Hydrology* 476, 460–489.
- Kornelsen, K.C., Coulibaly, P., 2015. Reducing multiplicative bias of satellite soil moisture retrievals. *Remote Sensing of Environment* 165, 109–122.
- Koster, R.D., Dirmeyer, P.A., Guo, Z., Bonan, G., Chan, E., Cox, P., Gordon, C., Kanae, S., Kowalczyk, E., Lawrence, D., et al., 2004. Regions of strong coupling between soil moisture and precipitation. *Science* 305, 1138–1140.
- Kuglitsch, F.G., Toreti, A., Xoplaki, E., Della-Marta, P.M., Zerefos, C.S., Türkeş, M., Luterbacher, J., 2010. Heat wave changes in the eastern mediterranean since 1960. *Geophysical Research Letters* 37.
- Lacava, T., Matgen, P., Brocca, L., Bittelli, M., Pergola, N., Moramarco, T., Tramutoli, V., 2012. A first assessment of the smos soil moisture product with in situ and modeled data in italy and luxembourg. *IEEE Transactions on Geoscience and Remote Sensing* 50, 1612–1622.
- Lagouarde, J.P., Bhattacharya, B.K., Crebassol, P., Gamet, P., Babu, S.S., Boulet, G., Briottet, X., Buddhiraju, K.M., Cherchali, S., Dadou, I., et al., 2018. The indian-french trishna mission: Earth observation in the thermal infrared with high spatio-temporal resolution, in: *IGARSS 2018-2018 IEEE International Geoscience and Remote Sensing Symposium, IEEE*. pp. 4078–4081.

- Lee, J.H., Ahn, C.K., 2019. Stochastic relaxation of nonlinear soil moisture ocean salinity (smos) soil moisture retrieval errors with maximal lyapunov exponent optimization. *Nonlinear Dynamics* 95, 653–667.
- Lee, J.H., Zhao, C., Kerr, Y., 2017. Stochastic bias correction and uncertainty estimation of satellite-retrieved soil moisture products. *Remote Sensing* 9, 847.
- Leflaive, X., 2012. Water outlook to 2050: The oecd calls for early and strategic action, in: *Global Water Forum*.
- Lei, F., Crow, W.T., Holmes, T.R., Hain, C., Anderson, M.C., 2018. Global investigation of soil moisture and latent heat flux coupling strength. *Water resources research* 54, 8196–8215.
- Lei, S.g., Bian, Z.f., Daniels, J.L., Liu, D.l., 2014. Improved spatial resolution in soil moisture retrieval at arid mining area using apparent thermal inertia. *Transactions of Nonferrous Metals Society of China* 24, 1866–1873.
- Lelieveld, J., Hadjinicolaou, P., Kostopoulou, E., Chenoweth, J., El Maayar, M., Giannakopoulos, C., Hannides, C., Lange, M., Tanarhte, M., Tyrllis, E., et al., 2012. Climate change and impacts in the eastern mediterranean and the middle east. *Climatic change* 114, 667–687.
- Li, B., Rodell, M., 2013. Spatial variability and its scale dependency of observed and modeled soil moisture over different climate regions. *Hydrology and Earth System Sciences* 17, 1177–1188.
- Li, J., Wang, S., 2018. Using sar-derived vegetation descriptors in a water cloud model to improve soil moisture retrieval. *Remote Sensing* 10, 1370.
- Lievens, H., Martens, B., Verhoest, N., Hahn, S., Reichle, R., Miralles, D.G., 2017. Assimilation of global radar backscatter and radiometer brightness temperature observations to improve soil moisture and land evaporation estimates. *Remote Sensing of Environment* 189, 194–210.
- Lionello, P., Scarascia, L., 2018. The relation between climate change in the mediterranean region and global warming. *Regional Environmental Change* 18, 1481–1493.
- Liu, H.Q., Huete, A., 1995. A feedback based modification of the ndvi to minimize canopy background and atmospheric noise. *IEEE transactions on geoscience and remote sensing* 33, 457–465.
- Lobell, D.B., Asner, G.P., 2002. Moisture effects on soil reflectance. *Soil Science Society of America Journal* 66, 722–727.
- Loew, A., Stacke, T., Dorigo, W., Jeu, R.d., Hagemann, S., 2013. Potential and limitations of multidecadal satellite soil moisture observations for selected climate model evaluation studies. *Hydrology and Earth System Sciences* 17, 3523–3542.
- López-Moreno, J., Goyette, S., Beniston, M., 2008. Climate change prediction over complex areas: spatial variability of uncertainties and predictions over the pyrenees from a set of regional climate models. *International Journal of Climatology: A Journal of the Royal Meteorological Society* 28, 1535–1550.
- Ma, C., Li, X., Wei, L., Wang, W., 2017. Multi-scale validation of smap soil moisture products over cold and arid regions in northwestern china using distributed ground observation data. *remote sensing* 9, 327.

- Mahfouf, J.F., 1991. Analysis of soil moisture from near-surface parameters: A feasibility study. *Journal of Applied Meteorology and Climatology* 30, 1534–1547.
- Mahfouf, J.F., 2010. Assimilation of satellite-derived soil moisture from ascat in a limited-area nwp model. *Quarterly Journal of the Royal Meteorological Society: A journal of the atmospheric sciences, applied meteorology and physical oceanography* 136, 784–798.
- Malbeteau, Y., Merlin, O., Balsamo, G., Er-Raki, S., Khabba, S., Walker, J., Jarlan, L., 2018. Toward a surface soil moisture product at high spatiotemporal resolution: temporally interpolated, spatially disaggregated smos data. *Journal of Hydrometeorology* 19, 183–200.
- Malbêteau, Y., Merlin, O., Molero, B., Rüdiger, C., Bacon, S., 2016. Dispatch as a tool to evaluate coarse-scale remotely sensed soil moisture using localized in situ measurements: Application to smos and amsr-e data in southeastern australia. *International Journal of Applied Earth Observation and Geoinformation* 45, 221–234.
- Maltese, A., Bates, P., Capodici, F., Cannarozzo, M., Ciruolo, G., La Loggia, G., 2013a. Critical analysis of thermal inertia approaches for surface soil water content retrieval. *Hydrological Sciences Journal* 58, 1144–1161.
- Maltese, A., Capodici, F., Ciruolo, G., La Loggia, G., 2013b. Mapping soil water content under sparse vegetation and changeable sky conditions: Comparison of two thermal inertia approaches. *Journal of Applied Remote Sensing* 7, 073548.
- Manabe, S., 1969. Climate and the ocean circulation: I. the atmospheric circulation and the hydrology of the earth's surface. *Monthly Weather Review* 97, 739–774.
- Matsushita, B., Yang, W., Chen, J., Onda, Y., Qiu, G., 2007. Sensitivity of the enhanced vegetation index (evi) and normalized difference vegetation index (ndvi) to topographic effects: a case study in high-density cypress forest. *Sensors* 7, 2636–2651.
- Mattia, F., Le Toan, T., Souyris, J.C., De Carolis, C., Floury, N., Posa, F., Pasquariello, N., 1997. The effect of surface roughness on multifrequency polarimetric sar data. *IEEE Transactions on Geoscience and Remote Sensing* 35, 954–966.
- Menenti, M., Bastiaanssen, W., Van Eick, D., Abd el Karim, M., 1989. Linear relationships between surface reflectance and temperature and their application to map actual evaporation of groundwater. *Advances in Space Research* 9, 165–176.
- Merlin, O., Al Bitar, A., Walker, J.P., Kerr, Y., 2009. A sequential model for disaggregating near-surface soil moisture observations using multi-resolution thermal sensors. *Remote Sensing of Environment* 113, 2275–2284.
- Merlin, O., Escorihuela, M.J., Mayoral, M.A., Hagolle, O., Al Bitar, A., Kerr, Y., 2013. Self-calibrated evaporation-based disaggregation of smos soil moisture: An evaluation study at 3 km and 100 m resolution in catalunya, spain. *Remote sensing of environment* 130, 25–38.
- Merlin, O., Rudiger, C., Al Bitar, A., Richaume, P., Walker, J.P., Kerr, Y.H., 2012. Disaggregation of smos soil moisture in southeastern australia. *IEEE Transactions on Geoscience and Remote Sensing* 50, 1556–1571.
- Merlin, O., Stefan, V.G., Amazirh, A., Chanzy, A., Ceschia, E., Er-Raki, S., Gentine, P., Tallec, T., Ezzahar, J., Bircher, S., et al., 2016. Modeling soil evaporation efficiency in a range of soil and atmospheric conditions using a meta-analysis approach. *Water Resources Research* 52, 3663–3684.

- Merlin, O., Walker, J., Panciera, R., Young, R., Kalma, J., Kim, E., 2007. Soil moisture measurement in heterogeneous terrain. *Proc. Int. Congr. MODSIM* , 2604–2610.
- Mishra, V., Ellenburg, W.L., Griffin, R.E., Mecikalski, J.R., Cruise, J.F., Hain, C.R., Anderson, M.C., 2018. An initial assessment of a smap soil moisture disaggregation scheme using tir surface evaporation data over the continental united states. *International journal of applied earth observation and geoinformation* 68, 92–104.
- Mohanty, B.P., Cosh, M.H., Lakshmi, V., Montzka, C., 2017. Soil moisture remote sensing: State-of-the-science. *Vadose Zone Journal* 16, 1–9.
- Mohanty, B.P., Skaggs, T., 2001. Spatio-temporal evolution and time-stable characteristics of soil moisture within remote sensing footprints with varying soil, slope, and vegetation. *Advances in water resources* 24, 1051–1067.
- Molero, B., Leroux, D., Richaume, P., Kerr, Y., Merlin, O., Cosh, M., Bindlish, R., 2018. Multi-timescale analysis of the spatial representativeness of in situ soil moisture data within satellite footprints. *Journal of Geophysical Research: Atmospheres* 123, 3–21.
- Molero, B., Merlin, O., Malbêteau, Y., Al Bitar, A., Cabot, F., Stefan, V., Kerr, Y., Bacon, S., Cosh, M., Bindlish, R., et al., 2016. Smos disaggregated soil moisture product at 1 km resolution: Processor overview and first validation results. *Remote Sensing of Environment* 180, 361–376.
- Moran, M., Clarke, T., Inoue, Y., Vidal, A., 1994. Estimating crop water deficit using the relation between surface-air temperature and spectral vegetation index. *Remote sensing of environment* 49, 246–263.
- Moran, M.S., Peters-Lidard, C.D., Watts, J.M., McElroy, S., 2004. Estimating soil moisture at the watershed scale with satellite-based radar and land surface models. *Canadian journal of remote sensing* 30, 805–826.
- Mu, Q., Heinsch, F.A., Zhao, M., Running, S.W., 2007. Development of a global evapotranspiration algorithm based on modis and global meteorology data. *Remote sensing of Environment* 111, 519–536.
- Muller, E., Decamps, H., 2001. Modeling soil moisture–reflectance. *Remote sensing of Environment* 76, 173–180.
- Muñoz-Carpena, R., 2004. Field devices for monitoring soil water content. *EDIS* 2004.
- Muñoz-Sabater, J., Lawrence, H., Albergel, C., Rosnay, P., Isaksen, L., Mecklenburg, S., Kerr, Y., Drusch, M., 2019. Assimilation of smos brightness temperatures in the ecmwf integrated forecasting system. *Quarterly Journal of the Royal Meteorological Society* 145, 2524–2548.
- Myers, N., 1990. The biodiversity challenge: expanded hot-spots analysis. *Environmentalist* 10, 243–256.
- Nielsen, D.R., Biggar, J.W., Erh, K.T., et al., 1973. Spatial variability of field-measured soil-water properties .
- Njoku, E.G., Entekhabi, D., 1996. Passive microwave remote sensing of soil moisture. *Journal of hydrology* 184, 101–129.

- Nocita, M., Stevens, A., Noon, C., van Wesemael, B., 2013. Prediction of soil organic carbon for different levels of soil moisture using vis-nir spectroscopy. *Geoderma* 199, 37–42.
- Noilhan, J., Planton, S., 1989. A simple parameterization of land surface processes for meteorological models. *Monthly weather review* 117, 536–549.
- Norman, J.M., Kustas, W.P., Humes, K.S., 1995. Source approach for estimating soil and vegetation energy fluxes in observations of directional radiometric surface temperature. *Agricultural and Forest Meteorology* 77, 263–293.
- Notarnicola, C., Solorza, R., 2014. Integration of remotely sensed images and electromagnetic models into a bayesian approach for soil moisture content retrieval: methodology and effect of prior information, in: *Dynamic Programming and Bayesian Inference, Concepts and Applications*. IntechOpen.
- Ochsner, E., Cosh, M.H., Cuenca, R., Hagimoto, Y., Kerr, Y., Njoku, E., Zreda, M., et al., 2013. State of the art in large-scale soil moisture monitoring. *Soil Science Society of America Journal*, 1–32.
- Oh, Y., 2004. Quantitative retrieval of soil moisture content and surface roughness from multipolarized radar observations of bare soil surfaces. *IEEE Transactions on Geoscience and Remote Sensing* 42, 596–601.
- Oh, Y., Sarabandi, K., Ulaby, F.T., et al., 1992. An empirical model and an inversion technique for radar scattering from bare soil surfaces. *IEEE transactions on Geoscience and Remote Sensing* 30, 370–381.
- Olsen, J.L., Ceccato, P., Proud, S.R., Fensholt, R., Grippa, M., Mougin, E., Ardö, J., Sandholt, I., 2013. Relation between seasonally detrended shortwave infrared reflectance data and land surface moisture in semi-arid sahel. *Remote Sensing* 5, 2898–2927.
- Ouaadi, N., Jarlan, L., Ezzahar, J., Zribi, M., Khabba, S., Bouras, E., Bousbih, S., Frison, P.L., 2020. Monitoring of wheat crops using the backscattering coefficient and the interferometric coherence derived from sentinel-1 in semi-arid areas. *Remote Sensing of Environment* 251, 112050.
- Owen, T., Carlson, T., Gillies, R., 1998. An assessment of satellite remotely-sensed land cover parameters in quantitatively describing the climatic effect of urbanization. *International journal of remote sensing* 19, 1663–1681.
- Pancieria, R., Walker, J.P., Kalma, J., Kim, E., 2011. A proposed extension to the soil moisture and ocean salinity level 2 algorithm for mixed forest and moderate vegetation pixels. *Remote Sensing of Environment* 115, 3343–3354.
- Peischl, S., Walker, J.P., Ye, N., Ryu, D., Kerr, Y., 2014. Sensitivity of multi-parameter soil moisture retrievals to incidence angle configuration. *Remote sensing of environment* 143, 64–72.
- Peng, J., Loew, A., Merlin, O., Verhoest, N.E., 2017. A review of spatial downscaling of satellite remotely sensed soil moisture. *Reviews of Geophysics* 55, 341–366.
- Peng, J., Niesel, J., Loew, A., 2015. Evaluation of soil moisture downscaling using a simple thermal-based proxy—the remedhus network (spain) example. *Hydrology and Earth System Sciences* 19, 4765–4782.

- Peters, J., Conte, A., Van Doninck, J., Verhoest, N.E., De Clercq, E., Goffredo, M., De Baets, B., Hendrickx, G., Ducheyne, E., 2014. On the relation between soil moisture dynamics and the geographical distribution of *culicoides imicola*. *Ecohydrology* 7, 622–632.
- Petropoulos, G.P., Ireland, G., Srivastava, P.K., Ioannou-Katidis, P., 2014. An appraisal of the accuracy of operational soil moisture estimates from smos miras using validated in situ observations acquired in a mediterranean environment. *International Journal of Remote Sensing* 35, 5239–5250.
- Piles, M., Petropoulos, G.P., Sánchez, N., González-Zamora, Á., Ireland, G., 2016. Towards improved spatio-temporal resolution soil moisture retrievals from the synergy of smos and msg seviri spaceborne observations. *Remote Sensing of Environment* 180, 403–417.
- Pisinaras, V., Petalas, C., Gikas, G.D., Gemitzi, A., Tsihrintzis, V.A., 2010. Hydrological and water quality modeling in a medium-sized basin using the soil and water assessment tool (swat). *Desalination* 250, 274–286.
- Pitman, A.J., 2003. The evolution of, and revolution in, land surface schemes designed for climate models. *International Journal of Climatology: A Journal of the Royal Meteorological Society* 23, 479–510.
- Qin, J., Yang, K., Lu, N., Chen, Y., Zhao, L., Han, M., 2013. Spatial upscaling of in-situ soil moisture measurements based on modis-derived apparent thermal inertia. *Remote Sensing of Environment* 138, 1–9.
- Qiu, Y., Fu, B., Wang, J., Chen, L., 2001. Soil moisture variation in relation to topography and land use in a hillslope catchment of the loess plateau, china. *Journal of Hydrology* 240, 243–263.
- Rao, B.H., Singh, D., 2011. Moisture content determination by tdr and capacitance techniques: a comparative study. *Int. J. Earth Sci. Eng* 4, 132–137.
- Robinson, D., Campbell, C., Hopmans, J., Hornbuckle, B.K., Jones, S.B., Knight, R., Ogden, F., Selker, J., Wendroth, O., 2008. Soil moisture measurement for ecological and hydrological watershed-scale observatories: A review. *Vadose Zone Journal* 7, 358–389.
- Roerink, G., Su, Z., Menenti, M., 2000. S-sebi: A simple remote sensing algorithm to estimate the surface energy balance. *Physics and Chemistry of the Earth, Part B: Hydrology, Oceans and Atmosphere* 25, 147–157.
- Romshoo, S.A., 2004. Geostatistical analysis of soil moisture measurements and remotely sensed data at different spatial scales. *Environmental Geology* 45, 339–349.
- Sánchez, N., Fernández, J.M., Ruiz, M.R., Belmonte, A.C., Álvarez, E.T., 2012. A simulation of soil water content based on remote sensing in a semi-arid mediterranean agricultural landscape. *Spanish journal of agricultural research* , 521–531.
- Sandholt, I., Rasmussen, K., Andersen, J., 2002. A simple interpretation of the surface temperature/vegetation index space for assessment of surface moisture status. *Remote Sensing of environment* 79, 213–224.
- Satalino, G., Mattia, F., Davidson, M.W., Le Toan, T., Pasquariello, G., Borgeaud, M., 2002. On current limits of soil moisture retrieval from ers-sar data. *IEEE Transactions on Geoscience and Remote Sensing* 40, 2438–2447.

- Schanda, E., 1987. On the contribution of volume scattering to the microwave backscattered signal from wet snow and wet soil. *International Journal of Remote Sensing* 8, 1489–1500.
- Schleussner, C.F., Lissner, T.K., Fischer, E.M., Wohland, J., Perrette, M., Golly, A., Rogelj, J., Childers, K., Schewe, J., Frieler, K., et al., 2016. Differential climate impacts for policy-relevant limits to global warming: the case of 1.5 c and 2 c. *Earth system dynamics* 7, 327–351.
- Schmugge, T., Jackson, T., McKim, H., 1980. Survey of methods for soil moisture determination. *Water Resources Research* 16, 961–979.
- Schmugge, T.J., Kustas, W.P., Ritchie, J.C., Jackson, T.J., Rango, A., 2002. Remote sensing in hydrology. *Advances in water resources* 25, 1367–1385.
- Sellers, P., Dickinson, R., Randall, D., Betts, A., Hall, F., Berry, J., Collatz, G., Denning, A., Mooney, H., Nobre, C., et al., 1997. Modeling the exchanges of energy, water, and carbon between continents and the atmosphere. *Science* 275, 502–509.
- Seneviratne, S.I., Corti, T., Davin, E.L., Hirschi, M., Jaeger, E.B., Lehner, I., Orlowsky, B., Teuling, A.J., 2010. Investigating soil moisture–climate interactions in a changing climate: A review. *Earth-Science Reviews* 99, 125–161.
- Seneviratne, S.I., Wilhelm, M., Stanelle, T., van den Hurk, B., Hagemann, S., Berg, A., Cheruy, F., Higgins, M.E., Meier, A., Brovkin, V., et al., 2013. Impact of soil moisture–climate feedbacks on cmip5 projections: First results from the glace-cmip5 experiment. *Geophysical Research Letters* 40, 5212–5217.
- Shi, J., Wang, J., Hsu, A.Y., O’Neill, P.E., Engman, E.T., 1997. Estimation of bare surface soil moisture and surface roughness parameter using l-band sar image data. *IEEE Transactions on Geoscience and Remote Sensing* 35, 1254–1266.
- Si, B.C., 2008. Spatial scaling analyses of soil physical properties: A review of spectral and wavelet methods. *Vadose Zone Journal* 7, 547–562.
- Sobrino, J.A., Jimenez-Munoz, J.C., Soria, G., Brockmann, C., Ruescas, A., Danne, O., North, P., Phillipe, P., Berger, M., Merchant, C., et al., 2015. A prototype algorithm for land surface temperature retrieval from sentinel-3 mission, in: *Sentinel-3 for Science Workshop*, p. 38.
- Song, C., Jia, L., Menenti, M., 2013. Retrieving high-resolution surface soil moisture by down-scaling amsr-e brightness temperature using modis lst and ndvi data. *IEEE Journal of Selected Topics in Applied Earth Observations and Remote Sensing* 7, 935–942.
- Song, P., Zhang, Y., 2021. An improved non-linear inter-calibration method on different radiometers for enhancing coverage of daily lst estimates in low latitudes. *Remote Sensing of Environment* 264, 112626.
- Srivastava, P.K., Han, D., Ramirez, M.A.R., Islam, T., 2013. Appraisal of smos soil moisture at a catchment scale in a temperate maritime climate. *Journal of Hydrology* 498, 292–304.
- Stefan, V.G., Merlin, O., Molero, B., Escorihuela, M.J., Er-Raki, S., 2020. On the calibration of an evaporation-based disaggregation method of SMOS soil moisture data. Technical Report. Copernicus Meetings.
- Stocker, T., Plattner, G.K., Dahe, Q., 2014. Ipcc climate change 2013: the physical science basis—findings and lessons learned, in: *EGU General Assembly Conference Abstracts*, p. 17003.

- Su, Z., 2002. The surface energy balance system (sebs) for estimation of turbulent heat fluxes. *Hydrology and earth system sciences* 6, 85–100.
- Tagesson, T., Horion, S., Nieto, H., Fornies, V.Z., González, G.M., Bulgin, C., Ghent, D., Fensholt, R., 2018. Disaggregation of smos soil moisture over west africa using the temperature and vegetation dryness index based on sevir land surface parameters. *Remote Sensing of Environment* 206, 424–441.
- Talleg, T., Béziat, P., Jarosz, N., Rivalland, V., Ceschia, E., 2013. Crops' water use efficiencies in temperate climate: Comparison of stand, ecosystem and agronomical approaches. *Agricultural and Forest Meteorology* 168, 69–81.
- Tang, R., Li, Z.L., Tang, B., 2010. An application of the ts–vi triangle method with enhanced edges determination for evapotranspiration estimation from modis data in arid and semi-arid regions: Implementation and validation. *Remote Sensing of Environment* 114, 540–551.
- Taylor, C.M., de Jeu, R.A., Guichard, F., Harris, P.P., Dorigo, W.A., 2012. Afternoon rain more likely over drier soils. *Nature* 489, 423–426.
- Teuling, A.J., Troch, P.A., 2005. Improved understanding of soil moisture variability dynamics. *Geophysical Research Letters* 32.
- Topp, G., Davis, J., 1985. Measurement of soil water content using time-domain reflectometry (tdr): A field evaluation. *Soil Science Society of America Journal* 49, 19–24.
- Tsimplis, M.N., Zervakis, V., Josey, S.A., Peneva, E.L., Struglia, M.V., Stanev, E.V., Theocharis, A., Lionello, P., Malanotte-Rizzoli, P., Artale, V., et al., 2006. Changes in the oceanography of the mediterranean sea and their link to climate variability, in: *Developments in earth and environmental sciences*. Elsevier. volume 4, pp. 227–282.
- Ulaby, F.T., Dobson, M.C., Brunfeldt, D.R., 1983. Improvement of moisture estimation accuracy of vegetation-covered soil by combined active/passive microwave remote sensing. *IEEE transactions on geoscience and remote sensing* , 300–307.
- Vanderlinden, K., Vereecken, H., Hardelauf, H., Herbst, M., Martínez, G., Cosh, M.H., Pachepsky, Y.A., 2012. Temporal stability of soil water contents: A review of data and analyses. *Vadose Zone Journal* 11, vzj2011–0178.
- Vereecken, H., Huisman, J., Pachepsky, Y., Montzka, C., Van Der Kruk, J., Bogaen, H., Weiermüller, L., Herbst, M., Martinez, G., Vanderborcht, J., 2014. On the spatio-temporal dynamics of soil moisture at the field scale. *Journal of Hydrology* 516, 76–96.
- Verhoest, N.E., Van Den Berg, M.J., Martens, B., Lievens, H., Wood, E.F., Pan, M., Kerr, Y.H., Al Bitar, A., Tomer, S.K., Drusch, M., et al., 2015. Copula-based downscaling of coarse-scale soil moisture observations with implicit bias correction. *IEEE Transactions on geoscience and remote sensing* 53, 3507–3521.
- Viviroli, D., Dürr, H.H., Messerli, B., Meybeck, M., Weingartner, R., 2007. Mountains of the world, water towers for humanity: Typology, mapping, and global significance. *Water resources research* 43.
- Viviroli, D., Weingartner, R., 2004. The hydrological significance of mountains: from regional to global scale. *Hydrology and earth system sciences* 8, 1017–1030.

- Vreugdenhil, M., Dorigo, W., Broer, M., Haas, P., Eder, A., Hogan, P., Blöschl, G., Wagner, W., 2013. Towards a high-density soil moisture network for the validation of smap in petzenkirchen, austria, in: 2013 IEEE International Geoscience and Remote Sensing Symposium-IGARSS, IEEE. pp. 1865–1868.
- Wagner, W., Blöschl, G., Pampaloni, P., Calvet, J.C., Bizzarri, B., Wigneron, J.P., Kerr, Y., 2007. Operational readiness of microwave remote sensing of soil moisture for hydrologic applications. *Hydrology Research* 38, 1–20.
- Wagner, W., Lemoine, G., Borgeaud, M., Rott, H., 1999. A study of vegetation cover effects on ers scatterometer data. *IEEE Transactions on Geoscience and Remote Sensing* 37, 938–948.
- Walker, J.P., Houser, P.R., 2004. Requirements of a global near-surface soil moisture satellite mission: accuracy, repeat time, and spatial resolution. *Advances in water resources* 27, 785–801.
- Walker, J.P., Willgoose, G.R., Kalma, J.D., 2004. In situ measurement of soil moisture: a comparison of techniques. *Journal of Hydrology* 293, 85–99.
- Wan, Z., Wang, P., Li, X., 2004. Using modis land surface temperature and normalized difference vegetation index products for monitoring drought in the southern great plains, usa. *International journal of remote sensing* 25, 61–72.
- Wang, T., 2014. Modeling the impacts of soil hydraulic properties on temporal stability of soil moisture under a semi-arid climate. *Journal of Hydrology* 519, 1214–1224.
- Wang, T., Franz, T.E., Zlotnik, V.A., You, J., Shulski, M.D., 2015. Investigating soil controls on soil moisture spatial variability: Numerical simulations and field observations. *Journal of Hydrology* 524, 576–586.
- Western, A.W., Grayson, R.B., Blöschl, G., 2002. Scaling of soil moisture: A hydrologic perspective. *Annual Review of Earth and Planetary Sciences* 30, 149–180.
- Western, A.W., Zhou, S.L., Grayson, R.B., McMahon, T.A., Blöschl, G., Wilson, D.J., 2004. Spatial correlation of soil moisture in small catchments and its relationship to dominant spatial hydrological processes. *Journal of Hydrology* 286, 113–134.
- Xoplaki, E., González-Rouco, J., Luterbacher, J., Wanner, H., 2004. Wet season mediterranean precipitation variability: influence of large-scale dynamics and trends. *Climate dynamics* 23, 63–78.
- Yoder, R., Johnson, D., Wilkerson, J., Yoder, D., 1998. Soilwater sensor performance. *Applied Engineering in Agriculture* 14, 121–133.
- Yves, T., Koutroulis, A., Samaniego, L., Vicente-Serrano, S.M., Volaire, F., Boone, A., Le Page, M., Llasat, M.C., Albergel, C., Burak, S., et al., 2020. Challenges for drought assessment in the mediterranean region under future climate scenarios. *Earth-Science Reviews* , 103348.
- Zaussinger, F., Dorigo, W., Gruber, A., Tarpanelli, A., Filippucci, P., Brocca, L., 2019. Estimating irrigation water use over the contiguous united states by combining satellite and reanalysis soil moisture data. *Hydrology and earth system sciences* 23, 897–923.
- Zhao, L., Yang, K., Qin, J., Chen, Y., Tang, W., Lu, H., Yang, Z.L., 2014. The scale-dependence of smos soil moisture accuracy and its improvement through land data assimilation in the central tibetan plateau. *Remote sensing of environment* 152, 345–355.

- Zhao, L., Yang, K., Qin, J., Chen, Y., Tang, W., Montzka, C., Wu, H., Lin, C., Han, M., Vereecken, H., 2013. Spatiotemporal analysis of soil moisture observations within a tibetan mesoscale area and its implication to regional soil moisture measurements. *Journal of Hydrology* 482, 92–104.
- Zhao, W., Li, Z.L., 2013. Sensitivity study of soil moisture on the temporal evolution of surface temperature over bare surfaces. *International Journal of Remote Sensing* 34, 3314–3331.
- Zribi, M., Baghdadi, N., Holah, N., Fafin, O., 2005. New methodology for soil surface moisture estimation and its application to envisat-asar multi-incidence data inversion. *Remote sensing of environment* 96, 485–496.
- Zribi, M., Dechambre, M., 2003. A new empirical model to retrieve soil moisture and roughness from c-band radar data. *Remote Sensing of Environment* 84, 42–52.
- Zwieback, S., Colliander, A., Cosh, M.H., Martínez-Fernández, J., McNairn, H., Starks, P.J., Thibeault, M., Berg, A., 2018. Estimating time-dependent vegetation biases in the smap soil moisture product. *Hydrology and Earth System Sciences* 22, 4473–4489.
- van Zyl, J.J., Chapman, B.D., Dubois, P., Shi, J., 1993. The effect of topography on sar calibration. *IEEE Transactions on Geoscience and Remote Sensing* 31, 1036–1043.